Washington University in St. Louis
Washington University Open Scholarship

All Theses and Dissertations (ETDs)

1-1-2011

Quantitative Perfusion-Sensitive Mri Phantoms

Jeff Anderson
Washington University in St. Louis

Follow this and additional works at: https://openscholarship.wustl.edu/etd

Recommended Citation
Anderson, Jeff, "Quantitative Perfusion-Sensitive Mri Phantoms" (2011). *All Theses and Dissertations (ETDs)*. 549.
https://openscholarship.wustl.edu/etd/549

This Dissertation is brought to you for free and open access by Washington University Open Scholarship. It has been accepted for inclusion in All Theses and Dissertations (ETDs) by an authorized administrator of Washington University Open Scholarship. For more information, please contact digital@wumail.wustl.edu.

WASHINGTON UNIVERSITY IN ST. LOUIS

Department of Chemisty

Dissertation Examination Committee:
Joseph Ackerman, Chair
Joel Garbow, Co-chair
Philip Bayly
John Bleeke
Mark Conradi
Dewey Holten

QUANTITATIVE PERFUSION-SENSITIVE MRI PHANTOMS

by

Jeff Richard Anderson

A dissertation presented to the
Graduate School of Arts and Sciences
of Washington University in
partial fulfillment of the
requirements for the degree
of Doctor of Philosophy

August 2011

Saint Louis, Missouri

ABSTRACT

Perfusion-sensitive MR methods are increasingly utilized in preclinical and clinical MR research studies with the promise of providing quantitative estimates of parameters that describe *in vivo* microvasculature. One of these techniques, dynamic contrast enhanced (DCE) MRI, has found particularly common use in oncology for the detection, staging, and monitoring of highly vascularized tumors. DCE-MRI has been qualitatively validated by various studies that show a high correlation between modeled parameters from DCE and histologically measured microvascular density (MVD). However, in the absence of a matching “gold-standard” technique, DCE-MRI has not yet been quantitatively validated (i.e., the accuracy of the estimated parameters is unknown). Partly because of this inability to determine the accuracy of the measured parameters, there remains debate in the literature about which DCE signal model(s) best reflect(s) experimental data.

In order to address these scientific challenges, realistic DCE tissue phantoms have been constructed. These phantoms implement semi-permeable hollow fibers, found commonly in commercial hemodialysis cartridges, to simulate “leaky” vasculature. Their design and construction are cataloged in this thesis. In addition, the phantoms have been experimentally characterized. In conjunction with these experiments, an interesting example of diffusion driven longitudinal relaxation was observed and is described herein. Lastly, the permeability of the fiber wall with respect to Gd-based contrast agents has been measured independently and compared with values derived from a mock-DCE experiment performed on the phantoms. In general, the results of these experiments support current DCE-MRI methods.

ACKNOWLEDGMENTS

For the completion of this major thesis project I would like to thank my wife, children, and parents for their support and inspiration.

I thank my advisors Joe Ackerman and Joel Garbow for their time, talents, insights, corrections, endless editing, and patience. I am grateful to them for taking interest in my research in the midst of many other responsibilities and commitments. Without their expertise and guidance this research would not have been possible.

I thank John Engelbach and Kassie Chaffee for their friendship and help. I thank others who have specifically contributed to publications resulting from this research: Jeffrey Arbeit, X. Jin, T.S. Lupu, Anthony Muslin, Jeff Neil, Michael Nelson, Yoel Sadovsky, Andrea Santeford, Andrew Siedlecki, Tracy Tomlinson, and Qingqing Ye. I thank the rest of my thesis committee; Phil Bayly, Mark Conradi, Lev Gelb, and Dewey Holten; for their time, direction, and for the review and editing of this thesis.

I thank Debra Brouk, Rachel Linck, Greg Noelken, Phyllis Noelken, Jessica Owens, Angie Stevens, Norma Taylor, and Barbara Tessmer for helping me to maneuver the less scientific side of science. I thank Larry Bretthorst for much help with the Bayesian analysis software and for his never-ending optimism. I thank Jim Linders for the machining of some of the apparatus used in this research. I thank Debasish Banerjee, Matt Budde, and Andy Prantner for answering a multitude of questions when I first arrived at the BMRL. I thank Alpay Ozcan for his technical support, patience, and stimulating conversation. I thank Dimitry Yablonskiy and Alex Sukstansky for help with math and concepts that, though simple to them, were difficult to me. I thank others who have been mentors to me: Mikhail Berezin, Ed Hiss, Josh Shimony, Victor Song, and Bill Spees. I thank all my fellow grad students for their friendship and support.

I acknowledge the support of the International Society of Magnetic Resonance in Medicine and the Gordon Research Conferences for providing student stipends to attend the 2010 annual meeting in Stockholm, Sweden and the 2008 semi-annual conference on *In Vivo Magnetic Resonance* in Andover, New Hampshire, respectively. I also acknowledge the generous

support of the National Institute of Health. This research has been supported by the following NIH grants: T90 DA22871, R01 EB002083, P30 CA9182, S10 RR022658, and S10 RR020916.

DEDICATION

Gloria, laus et honor

Tibi sit, Rex Christe, Redemptor:

Cui puerile decus prompsit

Hosanna pium.

Theodulph of Orleans (d. 821)

TABLE OF CONTENTS

LIST OF FIGURES

CHAPTER 1. INTRODUCTION

1.1. Abstract

Perfusion-sensitive imaging techniques attempt to probe the integrity of semi-permeable membranes *via* monitoring of endogenous or exogenous contrast agent perfusion. Dynamic contrast enhanced (DCE) MRI is one example. In DCE experiments, MRI is used to follow the perfusion of Gd-based contrast agents into tissue. The ultimate goal of DCE, and perfusion-sensitive imaging in general, is to quantitatively estimate parameters that 1) accurately describe tracer perfusion and 2) are meaningful biomarkers of insult, injury, or disease. Herein, DCE-MRI is described and examples of its application are given. In addition, attempts to validate the technique are briefly reviewed. Lastly, additional validation studies using realistic tissue phantoms, the main focus of this dissertation, are justified, and the contents of all subsequent chapters and appendices are outlined.

1.2. Motivation for monitoring, *via* imaging, semi-permeable membranes in biological systems

Semi-permeable membranes, barriers that allow passage of only certain molecules, are found extensively in biological systems. They, in concert with more complex active transport mechanisms, regulate chemical concentrations throughout the body. Examples of semi-permeable membranes include those found in the kidney that control the concentrations of different analytes in the blood, the blood brain barrier that prevents all but the most essential chemicals from passing from the blood to the cerebrospinal fluid, and, indeed, the entire capillary network where the exchange of analytes constantly occurs between blood and tissue. As semi-permeable membranes are thus found throughout the entire body, they provide an appealing target for the various imaging modalities.

In addition to being ubiquitous throughout biological systems, semi-permeable membranes provide further motivation for targeted examination *via* imaging as the integrity of semi-permeable membranes can be altered in response to stress and insult resulting from

disease, injury, or illness. Thus, semi-permeable membranes can potentially be used as a handle for indirectly monitoring these internal and external stressors.

Molecules preferentially cross a semi-permeable membrane in one direction in response to gradients; i.e., movement of molecules in both directions across the membrane, but a net movement of molecules in one direction. This transfer is defined as passive transport. The most common gradients that exist across semi-permeable membranes found in biological systems are gradients of potential, pressure, and concentration. In this dissertation, only concentration gradients are considered.

The general approach employed in the imaging sciences to probe semi-permeable membranes is to create a concentration gradient across a membrane of interest with a molecule that can be observed with the imaging modality of choice. These molecules are called contrast agents (CA) or tracers*. Magnetic resonance imaging (MRI) is one such imaging modality. It is based upon the well-known phenomenon of nuclear magnetic resonance (NMR). The interested reader is referred to one of many texts for an in-depth review of general NMR and MRI theory and procedures [1, 2, 3].

MR techniques that monitor the integrity of semi-permeable membranes (perfusion-sensitive MR) utilize endogenous or exogenous blood-born MR tracers to sensitize an image or group of images to perfusion (i.e., the perfusion of the tracer). This dissertation is concerned primarily with exogenous, Gd-based MR contrast agents and their use in a technique called dynamic contrast enhanced (DCE) MRI. Section 1.3 introduces these contrast agents and the basic theory surrounding their effects on MR. The implementation and potential impact of perfusion-sensitive MR methods are best demonstrated *via* examples. These examples also provide an effective venue for conceptually introducing DCE-MRI. Section 1.4 serves this dual purpose. Section 1.5 then discusses various approaches available to validate DCE-MRI and

* The terms contrast agent and tracer do not denote perfusion-sensitive methods, *per se*, but are more general. A more complete definition of a contrast agent/tracer is a molecule that increases the contrast in an image. An example of a contrast agent insensitive to semi-permeable membranes is barium, which is ingested in order to increase the contrast of the gastro-intestinal system to the rest of the internal organs (routinely used in conjunction with X-rays and computed tomography (CT) scans) [60].

justifies the necessity of further validation with MR phantoms, the focus of this dissertation. As a conclusion to chapter 1, section 1.6 further defines the scope of the dissertation and summarizes its contents.

1.3. MR contrast agents/tracers: theory

A spinning top has angular (rotational) momentum. Thus, when the axis of the top is tilted (not parallel with the force of gravity), the top precesses. This is in response to the torque applied by the constant force of gravity. In the absence of friction, this precession would be continuous resulting in a fixed rate of precession, i.e., frequency. Protons and neutrons within a nucleus also have angular momentum. However, this angular momentum does not result from the particles physically spinning, but is intrinsic. Despite this fact, the total angular momentum of a nucleus (resulting from the angular momenta of its protons and neutrons) is referred to as the nuclear spin.

Another distinction between the angular momentum of a spinning top and elementary particles is that the angular momenta of these particles are quantized. In other words, the angular momentum of the spinning top can be any value as dictated by the composition and shape of the top and how fast it is spinning, but the angular momentum of a proton can only be certain values as described by quantum mechanics. Subsequently, the nuclear spin can only be zero, half-integer, or integer. For those nuclei where the nuclear spin is non-zero, such as that of hydrogen, multiple values are possible for the z-component of the nuclear spin (e.g., +1/2 and -1/2 for ^{1}H).

A nuclear magnetic moment is associated with each individual nuclear spin. Thus, in a magnetic field, nuclear spins with different spin numbers correspond to different energy levels. The difference between these energy levels is proportional to the applied magnetic field. NMR and MRI probe these quantized energy levels. Relating this back to the example of the spinning top, within a magnetic field, nuclear spins precess at a frequency proportional to the applied magnetic field known as the Larmor frequency (the applied magnetic field exerting a torque on the nuclear spins). The classical representation of the entire system is a vector sum of the many nuclear spins within a sample. This vector, termed the magnetization, suffices to conceptually

understand the two relaxation processes associated with the return of the magnetization to equilibrium after perturbation.

At equilibrium, the magnetization lies coincident with the main magnetic field of the spectrometer/scanner. This axis, by convention, is labeled z. All MR experiments nutate or "tip" the magnetization away from the z-axis and into the xy-plane by applying electromagnetic radiation at an appropriate frequency (i.e., corresponding to the energy gap of the spin system) perpendicular to the z-axis. For MR, this electromagnetic radiation corresponds to radio frequencies (RF). In practice, these radiowaves are introduced into the sample by activating an RF transmitter for a short time (i.e., via an RF pulse).

After tipping the magnetization, one can consider the z-component and xy-component of the magnetization separately. The return to equilibrium of the z-component of the magnetization is called longitudinal relaxation and is described by the rate constant R_1 (the inverse of R_1 is the time constant T_1). The return to equilibrium of the xy-component of the magnetization is called transverse relaxation and is described by the rate constant R_2 (the inverse of R_2 is the time constant T_2). For a detailed analysis of the mechanisms by which these processes occur one is referred to the following reference [4]. A simplistic explanation is that energy is transferred from the nuclear spins to the system (the energy systems of multitude of the molecules within the sample) resulting in equilibration.

As mentioned, MRI techniques exist that utilize both exogenous and endogenous tracers (e.g., magnetically prepared areterial blood). Though the validation approach discussed in this dissertation (via MR perfusion phantoms, *vide infra*) can be of use to techniques that use either of these types of tracers, the focus is on exogenous MR contrast agents. Therefore, exogenous tracers are the sole focus of this conceptual introduction to contrast agents. The vast majority of all exogenous MR contrast agents, used both clinically and preclinically, utilize the gadolinium ion Gd^{3+}. These chelated gadolinium compounds alter the observed relaxation rate constants in homogeneous solutions and *in vivo*. In well mixed solutions the relationship is linear over a large range, i.e., R_1 and R_2 are linearly proportional to contrast agent concentration (see chapter 2). Examples of currently used chelates are shown in Figure 1-1. The mechanisms by which these

relaxation processes are altered hinge upon the quantum-mechanical coupling of the unpaired electrons of the gadolinium ion with the nuclear spins of the water protons. This coupling provides a more efficient mechanism of longitudinal and transverse relaxation for populations of spins associated with water than that found in their absence both in homogeneous solution and *in vivo* [5].

Interestingly, these types of MR contrast agents are not directly detected (MR-active), but rather their effects are indirectly observed. For example, a "contrast-enhanced" image sensitized to longitudinal relaxation (a contrast-enhanced "T_1-weighted" image) is an image of the bulk water where relatively high image intensity due to short water T_1 is potentially caused by high contrast agent concentration at that location (high image intensity could also be due to a short native T_1). Importantly, therefore, 1) signal will exist in regions void of CA, but filled with water, 2) the signal intensity observed in regions where CA is present will correspond to some combination of the native rate constant and that induced by the CA, and 3) both the exchange rates of water molecules and the CA may need to be considered (see chapter 2). All of these observations constitute both the benefits and challenges of exogenous MR contrast agents. For example, contrast-enhanced MR images of this type automatically include anatomical information, but signal intensity is not directly proportional to contrast agent concentration (points 1 and 2). Furthermore, dynamic data may include more information, but may be more difficult to interpret/resolve (point 3).

1.4. Examples of perfusion-sensitive imaging techniques and applications

As mentioned in the introduction to this chapter, the technique most discussed in this dissertation is dynamic contrast enhanced MRI. To understand DCE, however, it is best to first understand the utility of contrast enhancement in general. This utility is illustrated in the following example in which contrast agents are used to probe the semi-permeable barriers in the brain.

A well-known example of semi-permeable barrier breakdown is found in the response of the blood-brain barrier (BBB) to injury and disease. The blood-brain barrier is one of the most restrictive membranes in the body. In the brain, the endothelial cells lining the capillary network

are packed tightly together with only small passages remaining between the cells. These are known as tight junctions, and as their name implies, allow only the smallest of molecules; such as oxygen, carbon dioxide, and simple ions; to pass. This unique design protects the brain from most bacteria and foreign molecules. Case in point, when intact, the BBB will not allow Gd-based MR contrast agents to leave the blood.

Due to this complete impermeability of the healthy BBB to Gd-based CA, contrast enhancement in the brain is sometimes considered a binary function, i.e., either the BBB is intact or compromised. This information can be encoded into a single high-resolution, contrast-enhanced T_1-weighted image collected after (~30 min) a Gd-based contrast agent is injected intravenously. An example of this can be seen in Figure 1-2 where the insult to the BBB occurred due to tumorigenesis (panel D) [6]. The image is compared with an image collected with the same parameters in the absence of contrast agent (panel C). It is clear from this example that additional qualitative information can be obtained from contrast-enhanced images with exogenous Gd-based tracers. For instance, the tumor volume can be more clearly delineated, and heterogeneity within the tumor is evident with CA enhancement.

As useful as a single contrast-enhanced image is, more information can be gleaned by considering multiple images and, further, applying mathematical modeling to more fully capture or describe the perfusion of the tracer. In particular, two widely used techniques exist that extend the reach of contrast-enhanced MR. These are DCE-MRI and dynamic susceptibility contrast (DSC) MRI. As previously mentioned, the thesis research presented in this dissertation focuses primarily on DCE. Briefly, however, DSC consists of tracking the first passage of a bolus of intravenously injected Gd-based constast agent with time-resolved, T_2*-weighted MRI [7]. The utility of DCE compared with a simple contrast-enhanced T_1-weighted image is presented in the following examples (see appendices B and D).

Consider first, in contrast to the previous brain example, the semi-permeable membranes found in the kidney and their function. Though there are many different pathways, amino acids taken into the body, primarily from protein, are eventually converted to aspartate and glutamate

[8]. The nitrogen from the great majority of these two amino acids is then converted into urea by means of the urea cycle. The overall reaction can be written as:

$NH_3 + HCO_3^{\oplus}$ + aspartate + 3 ATP → urea + fumarate + 2 ADP + 2 P_i + AMP + PP_i

One of the nitrogens in urea comes from glutamate (by means of glutamate dehydrogenase; shown as ammonia above) and the other from aspartate [9]. This process occurs in the liver and the resulting urea travels in the bloodstream to the kidneys for removal from the body.

Blood is introduced into the kidneys via the renal artery and then proceeds to the glomerulus. The double cell layer surrounding the vasculature in each glomerulus consists of a fenestrated endothiluim on the interior of the vessels (pores of dia = 70 – 90 nm) and an epithelium striated with podocites on the exterior of the vessels, effectively forming filtration slits approximately 25 nm wide (Figure 1-3). These two cell layers form a semipermeable membrane allowing the passage of uncharged molecules below 8 nm in diameter in response to concentration gradients across the membrane. Thus, clearance of urea from the vasculature is realized as well as low molecular weight Gd-based contrast agents [10].

In the kidney, effective transfer, of urea and other molecules considered biological waste, across the semi-permeable membrane is the desired *mode d'emploi*. Therefore, unlike the brain, a healthy kidney will appear hyperintense in a contrast-enhanced image. In addition, although it is possible for a kidney to completely cease function, many maladies result in a gradual decrease in functionality of the kidney. In these cases, both the healthy and diseased kidney may show contrast enhancement. Furthermore, when kidney function has been compromised, it is of clinical importance to measure the extent to which functionality has been limited.

A common example of this type of gradual kidney deterioration is found in patients who have received a kidney transplant. In order to inhibit rejection of the kidney, an immunosuppresent, cyclosporin, is routinely administered at the time of transplantation and throughout the lifetime of the kidney. An ironic effect of this drug is eventual kidney failure. This pathway to kidney failure, which typically occurs ~3-5 years after transplantation, can be

reproduced over a period of several weeks in a mouse model [11]. In order to characterize 1) healthy kidney function, 2) the degree of functional loss in cyclosporine-damaged kidney, and 3) the degree of retention of function in unhealthy kidney protected by administration of a second drug, bosentin, Siedlecki *et al*., used DCE-MRI. In DCE-MRI, an exogenous tracer (most often Gd-based) is injected intravenously just as for a contrast-enhanced image. However, instead of just collecting a single image after the contrast agent has perfused into the system of interest, multiple T1-weighted images are collected before, during, and after injection of contrast agent. These images, consisting of a signal vs. time plot for each voxel in the field of view, record the perfusion of contrast agent into each voxel from the perspective of total signal enhancement due to contrast agent concentration in that voxel.

Examples of DCE data from the study of Siedlecki *et al*., are shown in Figure 1-4. In the DCE experiment, the extent of the loss of kidney functionality is reflected in the time-resolved data (right panels). A variety of approaches have been proposed for interpreting these data, or more clearly, for deriving useful biomarkers from these data. These range from simplistic shape recognition [12] to ad-hoc quantification [13] to full mathematical modeling [14, 15]. Seidlecki *et al*., used an ad-hoc, yet quantitative, approach for their study.

Despite the advantages of an ad-hoc, quantitative analysis of DCE-MRI data, parameter estimation of quantitative and physiologically meaningful metrics remains the ultimate goal. This type of parameter estimation requires two steps: 1) accurate conversion of signal intensity to concentration of contrast agent on a voxel by voxel basis, and 2) accurate modeling of the concentration vs. time data via a mathematical description (equation) of contrast agent perfusion. The common mathematical equations used in these two steps are presented in chapter 2. A conceptual introduction is presented in the following example.

The cervix of the uterus is interesting in that it is composed of two distinct regions of epithelial cells (one region of squamous epithelium and one region of columnar epithelium). The barrier between these regions is called the squamocolumnar junction or transformation zone and moves physical location (via metaplasia) throughout life both in response to normal development and pregnancy [16]. The entire uterus is well supplied with blood by a dense network of

subepithelial microvasculature. This blood supply facilitates placental growth during pregnancy, but, to quote Karram, also “accounts for [the cevix’s] ability to miraculously heal and to survive the worst kind of iatrogenic insults [17].”

Microvasculature networks are the source of one of the most common semi-permeable membranes found in the body, the capillary wall itself. Parallel networks of capillaries, the smallest blood vessels found in the circulatory system, connect arteries to veins and are the actual site of oxygen supply and carbon dioxide recovery to and from the interstitium. Structually, the vessels consist of a single layer of endothelial cells surrounded by a thin layer of basement membrane and sporadic peri-endothelium [18]. Their diameter ranges from 4 to 10 μm and the thickness of the vessel wall ranges from 0.1 to 3 μm [19]. Three types of capillaries exist, continuous, where the endothial cells line up side by side; fenestrated, where the endothelial cells have periodic orifices such as in the kidney (*vide supra*); and discontinuous, where sporadic, unusually large gaps exist between endothelial cells [18]. Clefts between endothelial cells in healthy continuous capillaries, such as those in the cervix, allow passage of water soluble molecules less than 4 nm in diameter [19].

The cervix is of great interest clinically due to the continued prevalence of cervical cancer worldwide. Cervical cancer is largely preventable as it can be detected premalignancy (e.g., *via* the Papanicolaou test). Screening is facilitated by unique progression from healthy to benign cancerous to malignant cancerous tissue in cervix. Briefly, human papillomavirus, if persistent increases the risk of cervical intraepithelial neoplasia (CIN). This growth of benign tumor cells originates in the transformation zone (intraepithelial) and progresses through three distinct stages. If CIN progresses to stage three, there is a greatly increased risk of malignancy.

Angiogenesis, the growth of blood vessels, accompanies cervical cancer and is believed to be progressive through the stages of CIN [20]. Blood vessels resulting from this angiogenesis have many differences from the existing capillaries, including that they are fenestrated, as shown in Figure 1-5 [21]. Thus, from the perspective of DCE, one would expect to see greater perfusion of contrast agent into cancerous tissue than in healthy tissue due to the larger gaps in the epithelium of the cancerous tissue.

Garbow, *et al*., used DCE to probe the permeability of the cervical vasculature in a mouse model of premalignant cervical dysplasia [22]. Figure 1-6 shows the DCE data from the cervix of a single mouse from this study. The model used to interpret the DCE data contained three physiological parameters quantifying both the permeability and density of the blood vessels. These parameters and the associated model are introduced in chapter 2. They appear in Figure 1-6 as the fitted smooth curve (red line) to the data (red circles).

The figure also illustrates an additional challenge to parameter estimation of DCE data. Namely, that it is necessary to measure or estimate the arterial (or vascular) input function (AIF or VIF). The AIF is a measure of the concentration of contrast agent in the vasculature vs. time. Its determination is not a trivial matter, especially in preclinical imaging of mice and other animals where physical dimensions are smaller. Furthermore, errors in the determination of the input function translate into errors in the estimation of model parameters [23]. Thus, various approaches have been suggested for determining/deriving the AIF in DCE, including: 1) assuming a global AIF [24], 2) measuring a global AIF from a large artery or vein (citation), 3) deriving a global AIF from a reference tissue [25], 4) deriving a semi-local "blind" AIF from a region of interest (i.e., fitting the AIF and the model parameters iteratively by assuming the AIF to be fixed over the region of interest) [26], and 5) modeling the AIF on a voxel-by-voxel basis [27]. The input function shown in Figure 1-6 (blue line) was derived from modeling the signal enhancement in a reference tissue (blue circles).

Both the ad-hoc and model-based approaches to DCE data analysis are important, and are expected to continue to be applied both preclinically and clinically. Further narrowing its scope, this dissertation will focus primarily on model-based parameter estimation. As noted, this type of parameter estimation requires two steps: 1) accurate conversion of signal intensity to concentration of contrast agent on a voxel-by-voxel basis, and 2) accurate modeling of the concentration vs. time data via a mathematical equation describing contrast agent perfusion. Hereafter, unless noted otherwise, all references to DCE data analysis will mean this more difficult and rigorous model-based approach.

1.5. Validation of DCE-MRI

The first published example of DCE-MRI was in 1991 [28]. Since then, the technique has found widespread use both preclinically and clinically. An internet-based literature search (Google Scholar) using the keywords “DCE” and “MRI” supports this statement and reveals a steady increase in the number of published scholarly articles relating to DCE-MRI over the last ten years (Figure 1-7). The relatively recent development of DCE, combined with an increasing interest in application of the procedure, underscores the importance of validating this technique.

A large body of research qualitatively validating DCE-MRI now exists, wherein parameter estimation *via* DCE has revealed differences between healthy and compromised tissue. That statistically significant differences between groups can be seen is important and argues the merits of the technique, but does not validate the quantitation of estimated parameters. In order for DCE-MRI to be quantitatively validated, both the accuracy (i.e., closeness to the actual or true value) and the precision (i.e., reproducibility of the measurement) of estimated parameters must be assessed. Traditionally, this type of validation is carried out by comparison of the estimated parameters to measurements made with “gold standards”.

Three potential gold standard measurements have been suggested for the validation of DCE-MRI: histologically measured microvessel density (MVD), positron emission tomography (PET), and dynamic contrast enhanced computed tomography (DCE-CT). The following discussion reviews the literature for validation studies using these techniques. Though correlations are seen between DCE and these techniques, further justifying the qualitative value of DCE, they cannot be considered gold standards (*vide infra*).

Microvessel density is a measure of the number of capillaries (or vessels below a certain threshold dimension) in a tissue. It is assessed by 1) immunohistochemically staining a tissue and 2) counting the number of vessels below a set threshold size [29]. All other variables held constant, tissue perfusion increases in concert with MVD (see equation 2-16, chapter 2).

Many attempts to validate DCE focus on its correlation with MVD [30, 31] and references therein. Given the proposed functional form of the modeled parameter K^{trans}, this is to be expected (see chapter 2). K^{trans}, the volume transfer constant of contrast agent from blood plasma

to the interstitial space, is scaled by the inverse of the fractional volume of the interstitial space. In DCE literature this fractional volume is labeled v_e. The subscript refers to the extravascular extracellular space (EES), the term given to the interstitial space in the DCE literature (emphasizing with its name that this volume does not include intracellular spaces). If the number of extravascular cells remains the same, then one would expect any increase in MVD to result in a decrease in v_e as the vessels would now occupy the volume previously ascribed to the EES. Interestingly, even though MVD has such a close relationship to v_e, papers citing MVD for DCE validation focus on correlation of K^{trans} or some ad-hoc parameter with the metric [30]. MVD cannot be considered a gold standard for K^{trans} as other parameters, e.g., flow, permeability, and vessel surface area, are understood to affect its value (see chapter 2). One notable exception is the manuscript recently published by Egeland *et al*. where estimated parameters, including v_e, were compared directly to histology [32].

Positron Emission Tomography (PET) has also been explored for validation of DCE. PET utilizes tracers that emit radiation via positron decay [33]. Although much more sensitive, the spatial resolution of PET is generally less than that of MRI. The majority of papers comparing PET to DCE use PET to measure flow and correlate that flow value with K^{trans} or some ad-hoc parameter [34, 35, 36, 37]. As with MVD, flow rate alone cannot serve as a gold standard as other parameters influence K^{trans}. An alternate approach is to carry out a DCE-like experiment with PET [38]. The potential advantage of this approach is that, unlike MRI, the conversion of signal intensity to contrast agent concentration is linear in PET. One, therefore, could assess errors in the conversion of the dynamic MRI signal intensity to tracer concentration. However, both techniques would presumably rely upon similar mathematical models of tracer perfusion. Thus, PET also cannot be considered a gold standard.

Lastly, in analogy with the comparison of dynamic PET studies with DCE-MRI, some have carried out the DCE experiment using CT instead of MRI [39, 40]. As the relationship between signal intensity and contrast agent concentration is a direct relationship in CT, errors can be assessed regarding the conversion of signal intensity to tracer concentration in DCE-MRI. However, as the mathematical models describing perfusion for both techniques rely upon the

same assumptions, such a comparison cannot elucidate the exact accuracy of estimated parameters via DCE-MRI. Therefore, DCE-CT cannot be considered a gold standard.

As no quantitative validation techniques currently exist *in vivo*, we decided to attempt to validate DCE-MRI *ex vivo* using realistic tissue phantoms. The design, construction, and testing of these phantoms are the major goal of the research described in this dissertation. The phantoms described herein share, as a major design feature, the use of semi-permeable hollow fibers to simulate vasculature (see chapter 3).

1.6. Scope and summary of dissertation

The scope of this dissertation is to describe the design and construction of these phantoms and the resultant attempts to validate DCE-MRI. Chapter 2 contains a mathematical introduction to the DCE data processing used *in vivo* as well as in the mock-DCE experiments carried out on *ex vivo* tissue phantoms. The starting point for the derivation of the mathematical models of perfusion in this chapter is Fick's Law for membranes. The derivation of this law from more fundamental concepts is included as Appendix A. Chapter 3 catalogs the design and construction of realistic, perfusion-sensitive tissue phantoms. In addition, the results of a number of control experiments are reported and discussed. Chapter 3 is currently in press in Concepts in Magnetic Resonance B, Magnetic Resonance Engineering. Chapter 4 discusses diffusion driven relaxation observed in one of these phantoms (the single fiber phantom). These observations and the ensuing discussion represent an example of the utility of these phantoms in elucidating potential challenges in perfusion-sensitive MRI. Chapter 4 is currently in press in NMR in Biomedicine. Chapter 5 decribes the mock-DCE experiment. It includes materials and methods, experimental results, and conclusions derived therefrom and is to be submitted for publication in the near future. Chapter 6 concludes this dissertation. Major results and conclusions are discussed as well as future research opportunities. Appendices B-D contain reprints that, though not the focus of this dissertation, utilized DCE-MRI. The author of this thesis made major contributions to each.

1.7. References

[1] M. Levitt, Spin dynamics: basics of nuclear magnetic resonance, 2nd ed., Chichester: John Wiley & Sons, 2008, p. 714.

[2] E. Fukushima and S. Roeder, Experimental pulse NMR: a nuts and bolts approach, Reading, MA: Addison-Wesley Pub. Co., 1981, p. 539.

[3] M. Haacke, Magnetic resonance imaging: physical principles and sequence design, New York, NY: Wiley, 1999, p. 914.

[4] R. van Eldik and I. Bertini, Eds., Advances in Inorganic Chemistry Including Bioinorganic Studies: Relaxometry of Water-Metal Ion Interactions, vol. 57, Amsterdam: Elsevier Inc., 2005, p. 485.

[5] S. Aime, M. Botta and E. Terreno, "Gd(III)-Based Contrast Agents for MRI," in *Advances in Inorganic Chemistry Including Bioinorganic Studies: Relaxomertry of Water-Metal Ion Interactions*, vol. 57, B. I. van Eldik R, Ed., Amsterdam, Elsevier Inc., 2005, pp. 173-238.

[6] C. Hess and D. Purcell, 5 August 2008. [Online]. Available: http://knol.google.com/k/christopher-p-hess-md-phd/brain-ct-mri/biWBkaDv/wqrGdg. [Accessed May 2011].

[7] R. Kennan and H. Jager, "T2- and T2*-w DCE-MRI: Blood Perfusion and Volume Estimation using Bolus Tracking," in *Quantitative MRI of the Brain*, P. Tofts, Ed., West Sussex, John Wiley & Sons Ltd, 2003, pp. 365-412.

[8] L. Cassimeris, V. Lingappa and G. Plopper, Eds., Lewin's Cells, 2nd ed., Sudburry, MA: Jones and Bartlett Publishers, 2011.

[9] H. Horton, L. Moran, R. Ochs, J. Rawn and K. Scrimgeour, Principles of Biochemistry, 3rd ed., Upper Saddle River, NJ: Prentice-Hall, Inc., 2002, p. 862.

[10] W. Boron and E. Boulpaep, Medical Physiology, 2nd ed., Philadelphia, PA: Saunders Elsevier, 2009.

[11] A. Siedlecki, J. Anderson, X. Jin, J. Garbow, T. Lupu and A. Muslin, "RGS4 Controls Renal

Blood Flow and Inhibits Cyclosporine-Mediated Nephrotoxicity," *American Journal of Transplantation,* vol. 10, no. 2, pp. 231-241, 2010.

[12] M. Knopp, F. Giesel, H. Marcos, H. von Tengg-Kobligk and P. Choyke, "Dynamic Contrast-Enhanced Magnetic Resonance Imaging in Oncology," *Topic in Magnetic Resonance Imaging,* vol. 12, no. 4, pp. 301-308, 2001.

[13] J. Evelhoch, "Key factors in the acquisition of contrast kinetic data for oncology," *Journal of Magnetic Resonance Imaging,* vol. 10, no. 3, pp. 254-259, 1999.

[14] P. Tofts, "Modeling tracer kinetics in dynamic Gd-DTPA MR imaging," *Journal of Magnetic Resonance Imaging,* vol. 7, no. 1, pp. 91-101, 1997.

[15] D. Buckley, "Uncertainty in the Analysis of Tracer Kinetics Using Dynamic Contrast-Enhanced T1-Weighted MRI," *Magnetic Resonance in Medicine,* vol. 47, pp. 601-606, 2002.

[16] J. Berek and E. Nocak, Berek & Novak's Gynecology, 14th ed., Philadelphia: Lippincott Williams, 2007.

[17] M. Baggish and M. Karram, Atlas of pelvic anatomy and gynecologic surgery, 3rd ed., Saint Louis, MO: Elsevier/Saunders, 2011.

[18] P. Vuong and C. Berry, The Pathology of Vessels, New York, NY: Springer, 2002.

[19] R. Hardaway, Capillary perfusion in health and disease, Mount Kisco, NY: Futura Pub. Co., 1981.

[20] J. Jordan, A. Singer, H. Jones and M. Shafi, The Cervix, 2nd ed., Malden, MA: Blackwell, 2006, p. 662.

[21] P. Baluk, H. Hashizume and D. McDonald, "Cellular abnormalities of blood vessels as targets in cancer," *Oncogenes and cell proliferation,* vol. 15, no. 1, pp. 102-111, 2005.

[22] J. Garbow, A. Santeford, J. Anderson, J. Engelbach and J. Arbeit, "Magnetic Resonance Imaging Defines Cervicovaginal Anatomy, Cancer, and VEGF Trap Antiangiogenic Efficacy in Estrogen-Treated K14-HPV16 Transgenic Mice," *Cancer Research,* vol. 69, no. 20, pp. 7945-7952, 2009.

[23] M. Cutajar, I. Mendichovszky, P. Tofts and I. Gordon, "The importance of AIF ROI selection in DCE-MRI renography: Reproducibility and variability of renal perfusion and filtration," *European Journal of Radiology,* vol. 74, no. 3, pp. e154-e160, 2010.

[24] G. Parker, C. Roberts, A. Macdonald, G. Buonaccorsi, S. Cheung, D. Buckley, A. Jackson, Y. Watson, K. Davies and G. Jayson, "Experimentally-derived functional form for a population-averaged high-temporal-resolution arterial input function for dynamic contrast-enhanced MRI," *Magnetic Resonance in Medicine,* vol. 56, no. 5, pp. 993-1000, 2006.

[25] T. Yankeelov, J. Luci, M. Lepage, R. Li, L. Debusk, P. Lin, R. Price and J. Gore, "Quantitative pharmacokinetic analysis of DCE-MRI data without an arterial input function: a rerefence region model," *Magnetic Resonance Imaging,* vol. 23, no. 4, pp. 519-529, 2005.

[26] M. Schabel, J. Fluckiger and E. DiBella, "A model-constrained Monte Carlo method for blind arterial input function estimation in dynamic contrast-enhanced MRI: I. Simulations," *Physics in Medicine and Biology,* vol. 55, pp. 4783-4806, 2010.

[27] J. Lee, L. Bretthorst, C. Derdeyn, W. Powers, T. Videen, A. Snyder, J. Markham and J. Shimony, "Dynamic susceptibility contrast MRI with localized arterial input functions," *Magnetic Resonance in Medicine,* vol. 63, no. 5, pp. 1305-1314, 2010.

[28] P. Tofts and A. Kermode, "Measurement of the blood-brain barrier permeability and leakage space using dynamic MR imaging. 1. Fundamental concepts," *Magnetic Resonance in Medicine,* vol. 17, no. 2, pp. 357-367, 1991.

[29] H. Turner and A. Harris, "Measurement of Microvessel Density in Primary Tumors," in *Methods in Molecular Medicine, vol. 57: Metastasis Research Protocols*, vol. 1, S. U. Brooks SA, Ed., Totowa, NJ: Humana Press Inc..

[30] A. Padhani and J. Husband, "Dynamic Contrast-enhanced MRI Studies in Oncology with an Emphsis on Quantification, Validation and Human Studies," *Clinical RAdiology,* vol. 56, no. 8, pp. 607-620, 2001.

[31] S. Rehman and G. Jayson, "Molecular Imaging of Antiangiogenic Agents," *The Oncologist,* vol. 10, no. 2, pp. 92-103, 2004.

[32] T. Egeland, T. Simonsen, J. Gaustad, C. Gulliksrud and E. Rofstad, "Dynamic Contrast-Enhanced Magnetic Resonance Imaging of Tumors: Preclinical Validation of Parametric Imaging," *Radiation Research,* vol. 172, no. 3, pp. 339-347, 2009.

[33] J. Prince and J. Links, Medical Imaging Signals and Systems, Upper Saddle River, NJ: Pearson Education, Inc., 2006.

[34] A. de Langen, V. van den Boogaart, J. Marcus and M. Lubberink, "Use of H2 15O-PET and DCE-MRI to Measure Tumor Blood Flow," *The Oncologist,* vol. 13, no. 6, pp. 631-644, 2008.

[35] J. Parkka, P. Niemi, A. Saraste, J. Koskenvuo, M. Komu, V. Oikonen, J. Toikka, T. Kiviniemi, J. Knutti, H. Sakuma and J. Hartiala, "Comparison of MRI and positron emission tomography for measutng myocardial perfusion researcve in healthy humans," *Magnetic Resonance in Medicine,* vol. 55, no. 4, pp. 772-779, 2006.

[36] C. Calcagno, J. Cornhily, F. Hyafil, J. Rudd, K. Briley-Saebo, V. Mani, G. Goldschlager, J. Machac, V. Fuster and Z. Fayad, "Detection of Neovessels in Atheroscerotic Plaques of Rabbits Using Dynamic Contrast Enhanced MRI and 18F-FDG PET," *Arteriosclerosis, Thrombosis, and Vascular Biology,* vol. 28, pp. 1311-1317, 2008.

[37] P. Eby, S. Partridge, S. White, R. Doot, L. Dunnwald, E. Schubert, B. Kurland, C. Lehman and D. Mankoff, "Metabolic and Vascular Features of Dynamic Contrast-enhnaced Breast Magnetic Resonance Imaging and 15O-Water Positron Emission Tomography Blood Flow in Breast Cancer," *Academic Radiology,* vol. 15, no. 10, pp. 1246-1254, 2008.

[38] M. Ferrier, H. Sarin, S. Fung, B. Schatlo, R. Pluta, S. Gupta, P. Choyke, E. Oldfield, D. Thomasson and J. Butman, "Validation of Dynamci Contrast-Enhanced Magnetic Resonance Imaging-Derived Vascular Permeability Measurements Using Quantitative Autoradiography in the RG2 Rat Brain Tumor Model," *Neoplasia,* vol. 9, no. 7, pp. 546-555, 2007.

[39] C. Yang, W. Stadler, G. Karczmar, M. Milosevic, I. Yeung and M. Haider, "Comparison of quantitative parameters in cervix cancer measured by dynamic contrast-enhanced MRI and CT," *Magnetic Resonance in Medicine,* vol. 63, no. 6, pp. 1601-1609, 2010.

[40] S. Donaldson, C. West, S. Davidson, B. Carrington, G. Hutchison, A. Jones, S. Sourbron and D. Buckley, "A Comparison of Tracer Kinetic Models for T1-Weighted Dynamic Contrast-Enhanced MRI: Application in Carcinoma of the Cervix," *Magnetic Resonance in Medicine,* vol. 63, no. 3, pp. 691-700, 2010.

1.7. Figures and captions

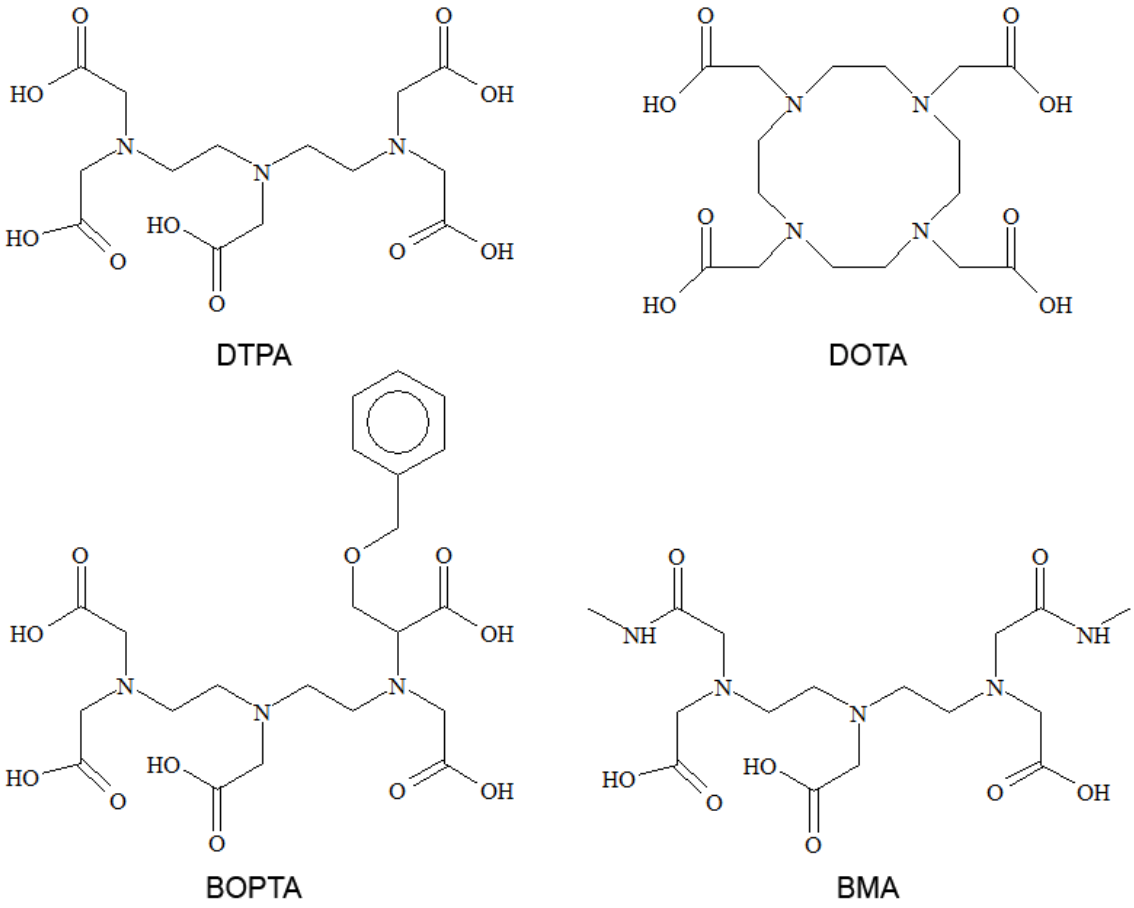

Figure 1-1. Example chelates for Gd-based contrast agents.

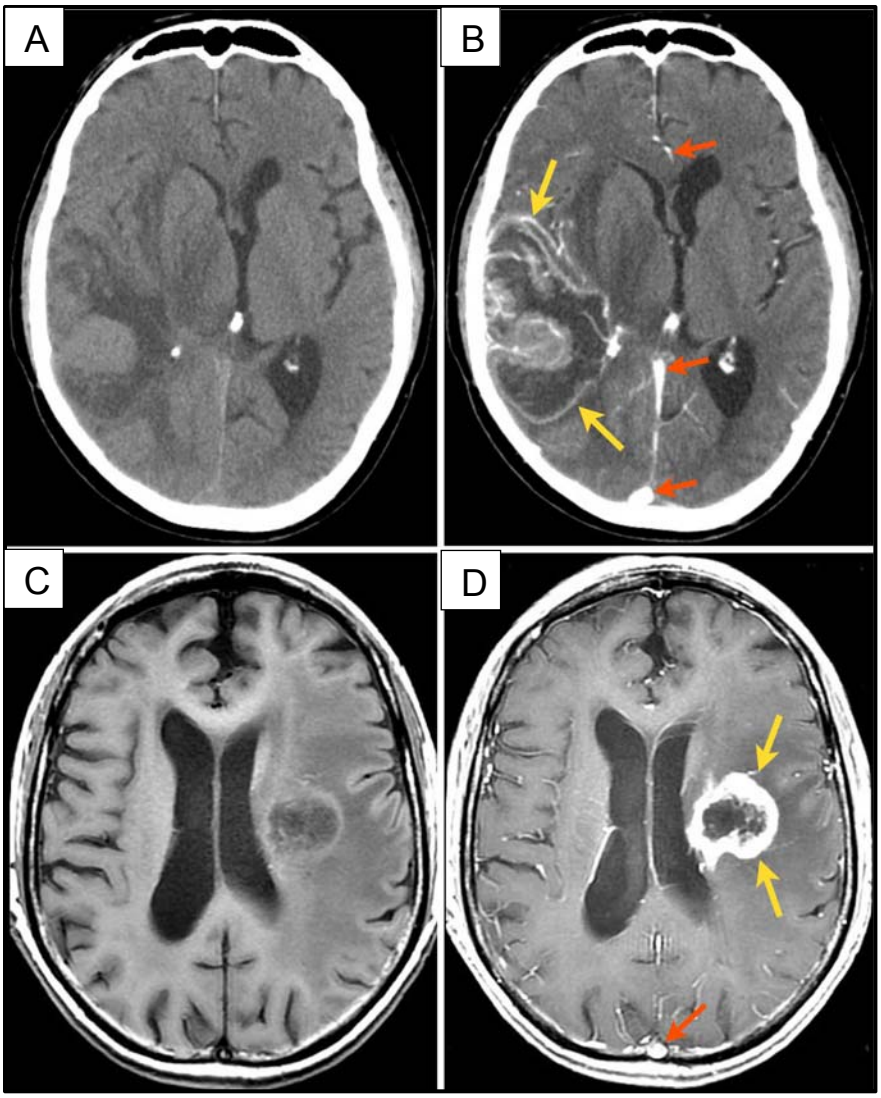

Figure 1-2. Examples of contrast enhanced images of brain tumors. Panels A and B were acquired with computed tomography (CT) before, A, and after, B, contrast agent administration. Panels C and D were acquired with magnetic resonance imaging (MRI) before, C, and after, D, contrast agent administration. A T_1-weighted acquisition was used. Red arrows show enhancement in the venous system. Yellow arrows show enhancement in vascularized regions of tumors where the blood brain barrier (BBB) has been compromised (C. Hess and D. Purcell, 5 August 2008. [Online]. Available: http://knol.google.com/k/christopher-p-hess-md-phd/brain-ct-mri/biWBkaDv/wqrGdg. [Accessed May 2011].).

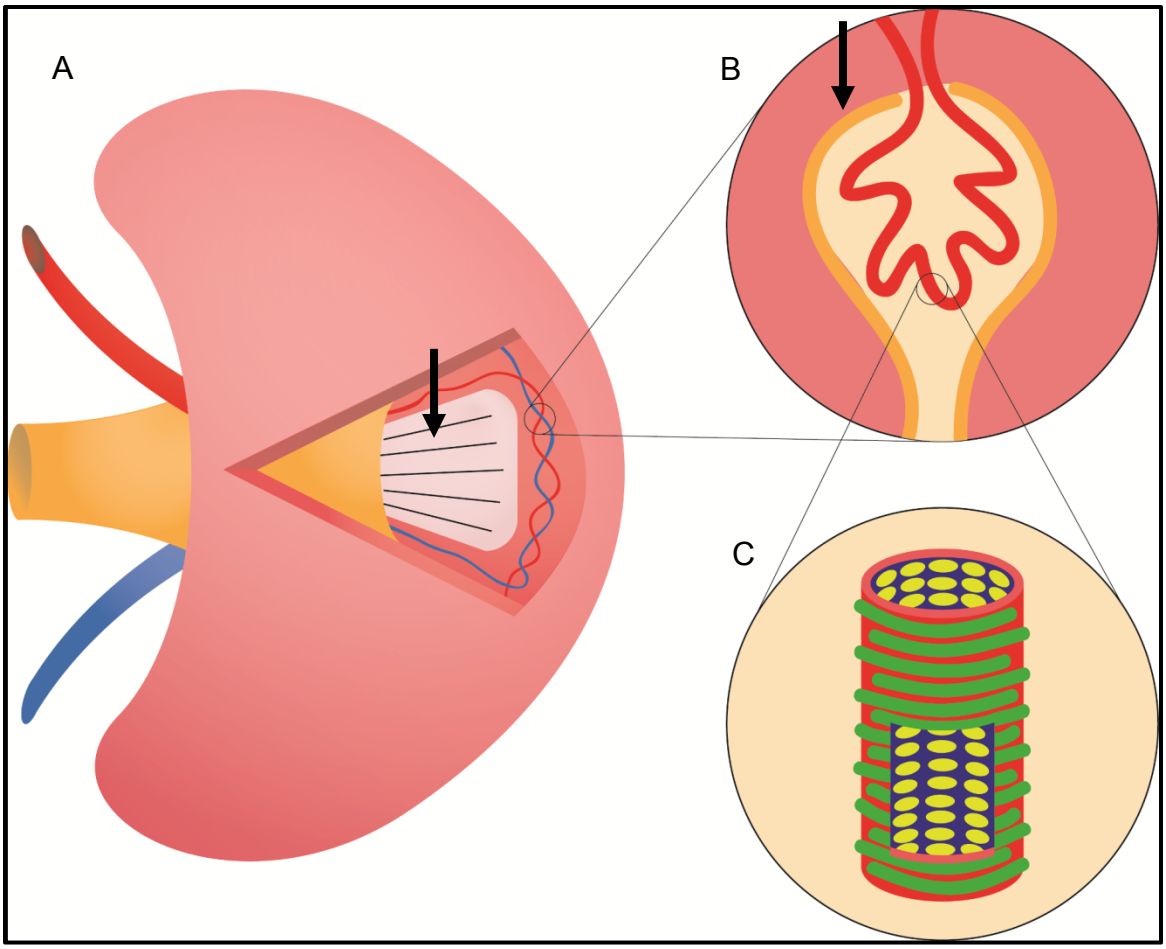

Figure 1-3. Schematic representation of the kidney. A) the kidney showing the renal artery (red) and vein (blue), the ureter (orange), a renal pyramid (black arrow), and representative internal vasculature in the cortex; B) Bowman's capsule (black arrow) containing a glomerulus; and C) a single arteriole within the glomerulus.

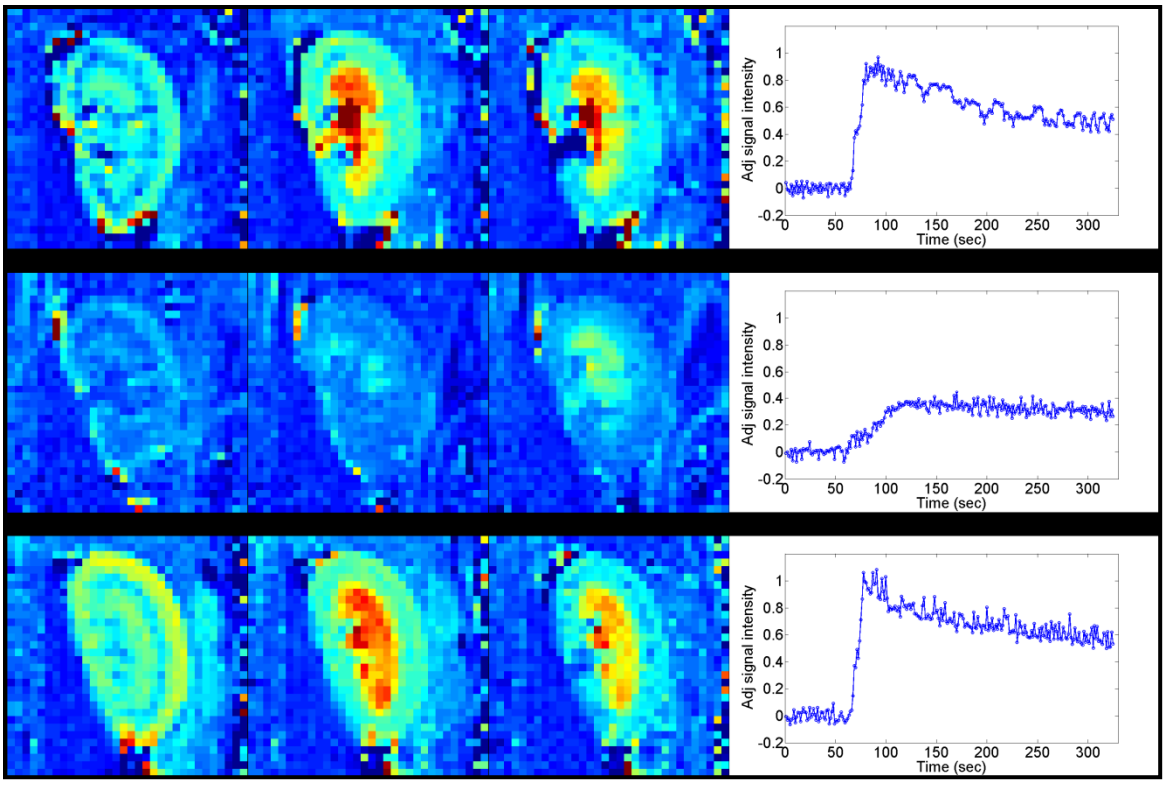

Figure 1-4. Dynamic contrast enhanced (DCE) MRI data in mouse kidneys collected following bolus injection of a low molecular weight, Gd-containing contrast agent. Selected images and adjusted signal intensity curves are shown for representative mice from three groups. These groups are, from top to bottom, control, compromised (cyclosporine treated), and protected (cyclosporine and bosentan treated). For each mouse, 250 images were collected with a temporal resolution of 1.3 s. Those images shown were collected at, from left to right, 12, 38, and 90 s post-contrast injection. At the right, in each panel are the complete adjusted signal intensity versus time curves for a medullary ROI for each of these mice (A. Siedlecki, J. Anderson, X. Jin, J. Garbow, T. Lupu and A. Muslin, "RGS4 Controls Renal Blood Flow and Inhibits Cyclosporine-Mediated Nephrotoxicity," *American Journal of Transplantation,* vol. 10, no. 2, pp. 231-241, 2010.).

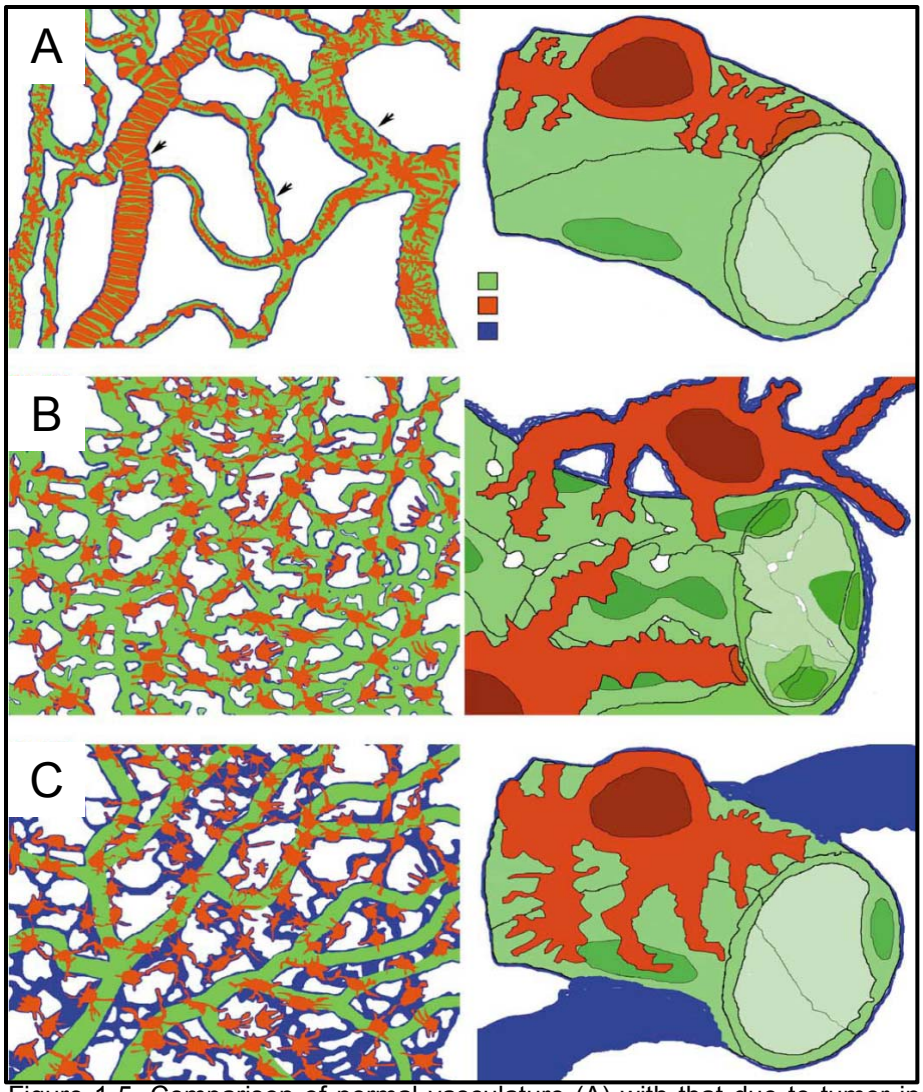

Figure 1-5. Comparison of normal vasculature (A) with that due to tumor induced angiogenesis before (B) and after (C) antiangiogenic therapy. Endothelial cells are green, pericytes are red, and basement membrane is blue. Note that the vasculature in B and C is random compared to the organized arteries, capillaries, and veins seen in A (arrows). Note also that B is fenestrated whereas both A and C are continuous (P. Baluk, H. Hashizume and D. McDonald, "Cellular abnormalities of blood vessels as targets in cancer," *Oncogenes and cell proliferation,* vol. 15, no. 1, pp. 102-111, 2005.).

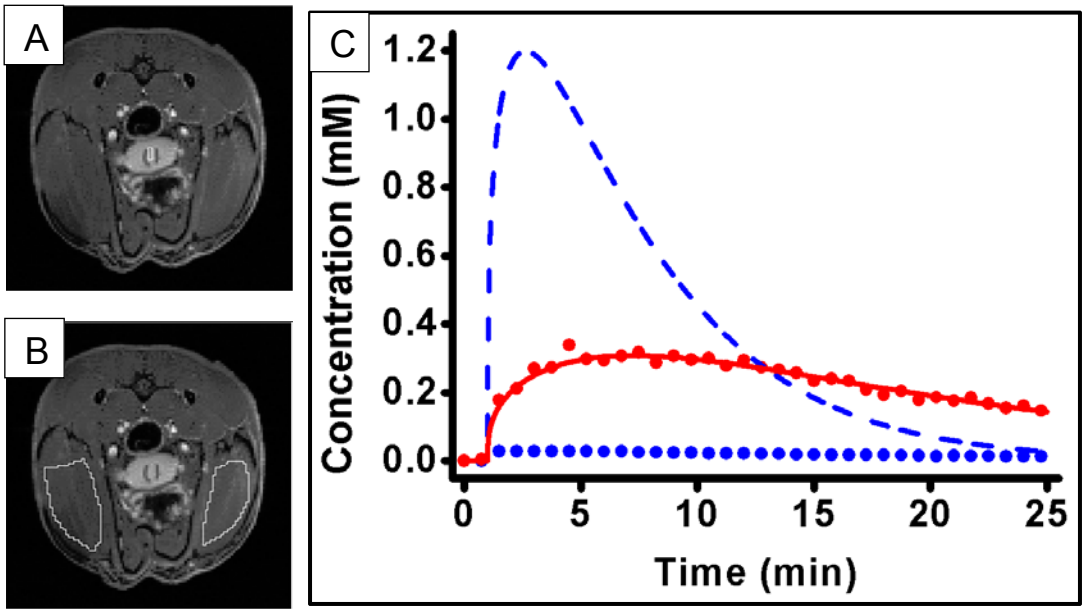

Figure 1-6. Representative DCE-MRI results in a mouse model of precancerous cervical dysplasia. Panels A and B show transaxial MRI images in mouse with regions of interest drawn over the cervix (A) and leg muscle (B). Panel C shows the resultant concentration time curves from these regions of interest (red dots – cervix; blue dots – muscle) as well as the modeled tracer perfusion in the cervix (red line) and the muscle-derived arterial input function (blue line) (J. Garbow, A. Santeford, J. Anderson, J. Engelbach and J. Arbeit, "Magnetic Resonance Imaging Defines Cervicovaginal Anatomy, Cancer, and VEGF Trap Antiangiogenic Efficacy in Estrogen-Treated K14-HPV16 Transgenic Mice," *Cancer Research,* vol. 69, no. 20, pp. 7945-7952, 2009.).

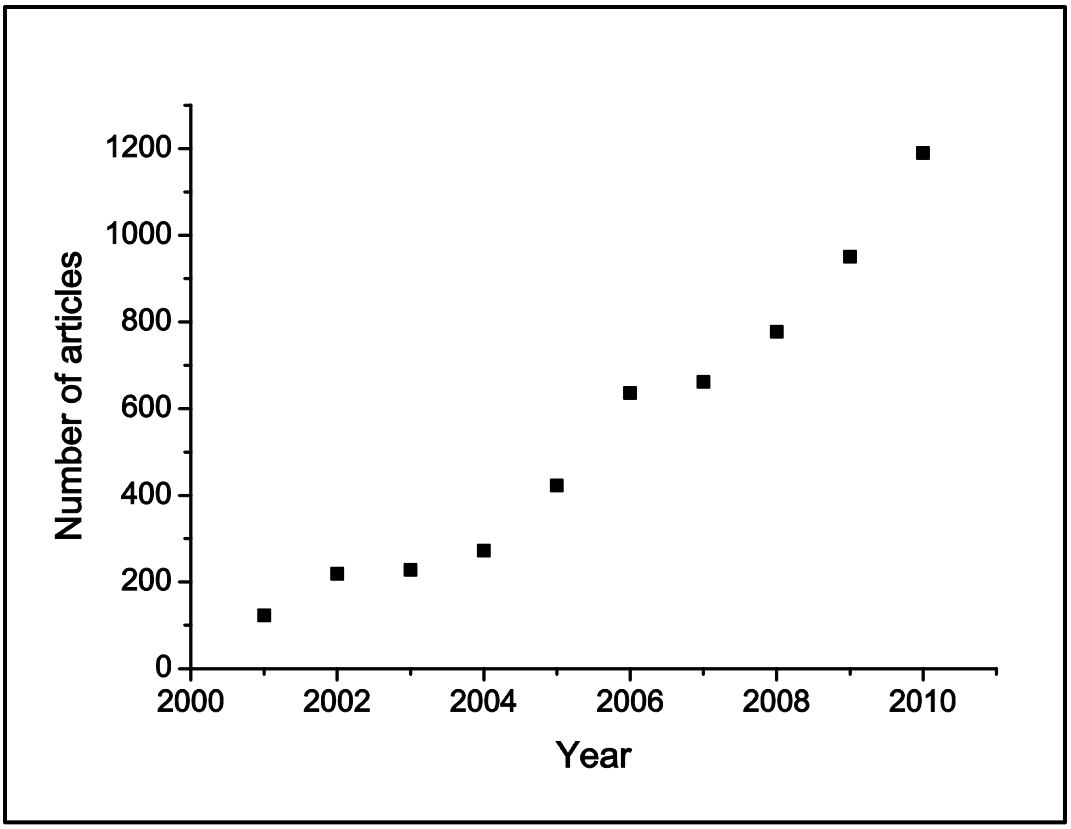

Figure 1-7. Scholarly article trends for DCE-MRI. Number of peer-reviewed articles published per year resulting from the search terms “DCE” and “MRI” using the Google scholar search engine.

CHAPTER 2. QUANTITATIVE DCE-MRI: THEORY

2.1. Abstract

Validation of DCE-MRI consists of validation of 1) the equations relating signal intensity to tracer concentration and 2) the equations describing contrast agent perfusion. Herein, these mathematical equations are cataloged and progressively explained. In the case of the contrast agent perfusion, the various iterations of these equations found in the literature are reviewed and described. Sample calculations for the processing of *in vivo* DCE-MRI data, as well as for phantom data from a mock-DCE experiment, are presented.

2.2. Introduction

DCE-MRI is an MRI experiment that involves the indirect detection of an intravenously injected contrast agent (CA). The data, which consist of a plot of signal intensity vs. time for each voxel in the image, reflect the response in different tissues to the injected CA, the impulse. To derive physiologically relevant parameters from these data, a number of critical steps must be followed. These are:

1. The signal intensities at each time point must be converted to R_1 values at each time point;
2. The R_1 values at each time point must be converted to concentrations of CA at each time point;
3. The concentration vs. time curves must be interpreted correctly by:
    a. Obtaining the impulse function, otherwise known as arterial input function (AIF), which is the concentration vs. time curve of the CA in the blood plasma;
    b. Analyzing the data with a mathematical model that correctly describes perfusion of the CA into the tissue.

Section 3 of this chapter presents the signal equations that relate R_1 to signal intensity. Section 4 describes the various approaches for relating CA concentration to R_1. Section 5 then reviews the various mathematical approaches found in the literature for modeling CA perfusion.

Lastly, section 6 gives an example of the entire process with data synthesized utilizing equations from the previous three steps.

2.3. Signal equations

Signal equations for a variety of experiments, including gradient-echo and spin-echo sequences, are described and derived in The MRI Pulse Sequence Handbook [1]

2.3.1. Signal equation parameters and units

Table 2-1. Parameter names, symbols, units, and descriptions used in the signal equations

Symbol[a]	Name	Units	Descriptions
S	Signal intensity	s	In spectroscopy, this is the area under a peak. In imaging, it corresponds to the brightness of the image at a given voxel.
M_z	Equilibrium longitudinal magnetization	AU	The net magnetization of a sample of nuclear spins. For NMR active nuclei this value is non-zero when the sample is in a magnetic field.
α	Flip angle	Degrees	A measure of the nutation of an MR sample by radiofrequency excitation. e.g., a 180° flip angle corresponds to complete inversion of M_z.
TR	Repetition time	s	The length (time) of a pulse sequence. When a pulse sequence is repeated multiple times this is the time from the start of one iteration to the next
TE	Echo time	s	The length of time in a pulse sequence between excitation of the sample and detection of the peak of the echo.
R_1	Longitudinal relaxation rate constant	s^{-1}	The rate constant describing longitudinal relaxation. This relaxation process involves the return of the longitudinal component of the net magnetization to M_z.

R_2	Transverse relaxation rate constant	s^{-1}	The rate constant describing transverse relaxation. This relaxation process involves the dephasing of the transverse component of the net magnetization.
R_2*	Apparent transverse relaxation rate constant	s^{-1}	The observed rate constant describing transverse dephasing of an MR signal that includes both R_2 and a R_2' (R_2* = R_2 + R_2') where R_2' reflects dephasing due to inhomogeneities in the static magnetic field, B_0

[a]Addition of a subscripted zero signifies a parameter in the absence of CA (i.e., pre-injection)

2.3.2. Spoiled gradient-echo signal equation

The most common approach to DCE data collection is to use a spoiled gradient-echo pulse sequence with a short TE, a short TR, and a relatively small flip angle. Spoiling is the act of destroying residual transverse phase coherence after the collection of a free induction decay (FID) and before any subsequent radiofrequency (RF) pulses. It can be carried out by applying gradients at the end of a pulse sequence and/or by cycling the phase of the RF pulses [1]. The practical result of spoiling is that no transverse steady state is established and the expression for signal intensity is somewhat simplified. The signal equation can be written as,

$$S = M_z \cdot \frac{\sin(\alpha)\cdot\left(1-e^{-TR\cdot R_1}\right)}{1-\cos(\alpha)\cdot e^{-TR\cdot R_1}}\cdot e^{-TE\cdot R_2{}^*}. \qquad (2\text{-}1)$$

Though void of transverse steady state terms, as these are assumed to be suppressed with spoiling, this equation essentially describes the longitudinal steady state of the signal (magnetization). In the limit of a very long TR and very short TE the signal equation yields the equilibrium magnetization M_z. As mentioned, DCE is usually carried out with a small TE and TR, which has the effect of minimizing the T_2*-dependent and maximizing the T_1-dependent portions of the signal equation, respectively. This highly T_1-weighted signal allows a further simplification of the signal equation by assuming negligible signal degradation due to T_2* effects. This simplification facilitates the conversion from signal intensity to tracer concentration (*vide infra*). The simplified signal equation is written as follows,

$$S = M_z \cdot \frac{\sin(\alpha)\left(1 - e^{-TR \cdot R_1}\right)}{1 - \cos(\alpha)\, e^{-TR \cdot R_1}}. \qquad (2\text{-}2)$$

The standard approach in DCE is to assume M_z is invariant with tracer concentration [2]. By taking the ratio of signal at an arbitrary CA concentration (S) and signal in the absence of CA (S_0), one can relate signal intensity to R_1 (which can be altered by a CA). The resultant signal equation, now relating S to S_0 and $R_{1,0}$ is,

$$S = S_0 \cdot \frac{\left(\frac{1 - e^{-TR \cdot R_1}}{1 - \cos(\alpha)\, e^{-TR \cdot R_1}}\right)}{\left(\frac{1 - e^{-TR \cdot R_{1,0}}}{1 - \cos(\alpha)\, e^{-TR \cdot R_{1,0}}}\right)}. \qquad (2\text{-}3)$$

To provide a measure of S_0, precontrast images are always collected before contrast agent administration in DCE. Equation 2-3 also reveals the necessity of acquiring, prior to contrast agent injection, an estimation of the native R_1 ($R_{1,0}$).

Equation 2-3 is shown graphically in figure 2-1 for various values of TR. The figure, calculated with S_0 set to 1, α set to 20°, and $R_{1,0}$ set to 1 s^{-1}, shows that these calibration curves (solid lines) are neither linear nor single valued (i.e., a given signal intensity can correspond to two different R_1 values). The dashed lines in figure 2-1 correspond to the full equation in which R_2* equal R_1 (this is a best case scenario as R_2* is usually greater than R_1). Graphical comparison of the signal equations with and without R_2* weighting reveals how crucial it is to assure the image is heavily T_1-weighted for all expected R_1 values [3].

2.3.3. Spin-echo pulse sequence

Signal-to-noise ratio (S/N) remains a challenge in DCE due to the demand for high temporally resolved data. Because of their lower S/N, spin-echo pulse sequences are not normally used in DCE-MRI. However, due to the unique design of the phantoms presented in this thesis, slice-selective spin-echo pulse sequences can be used. Thus, the spin-echo signal equation is presented here.

The spin-echo signal equation contains the same variables as that of the gradient-echo with one important exception. Signal loss is not dictated by T_2* decay. Instead, it is a function of true T_2 decay. The equation can be written as,

$$S = M_z \cdot \sin(\alpha_1) \sin^2\left(\frac{\alpha_2}{2}\right) \cdot \frac{\left(1 + \cos(\alpha_2 - 1)\, e^{-(TR-TE/2)R_1} - \cos(\alpha_2)\, e^{-TR \cdot R_1}\right)}{1 - \cos(\alpha_1)\cos(\alpha_2)\, e^{-TR \cdot R_1}} \cdot e^{-TE \cdot R_2} . \quad (2\text{-}4)$$

This complex equation can be greatly simplified when α_1 is set to 90° and α_2 to 180°:

$$S = M_z \cdot \left(1 - 2 \cdot e^{-(TR-TE/2)R_1} + e^{-TR \cdot R_1}\right) e^{-TE \cdot R_2} . \quad (2\text{-}5)$$

Similar to the gradient echo, for short TE experiments, it can be assumed that there is negligible signal decay due to T_2-weighting. However, unlike R_2*, R_2 can easily be related to tracer concentration. Thus, this simplifying assumption is not necessary as long as the transverse relaxivity, r_2, is known (*vide infra*). Taking the ratio of signal vs. initial signal, while including the R_2 term, results in the following signal equation,

$$S = S_0 \cdot \frac{\left(1 - 2 \cdot e^{-(TR-TE/2)R_1} + e^{-TR \cdot R_1}\right)}{\left(1 - 2 \cdot e^{-(TR-TE/2)R_{1,0}} + e^{-TR \cdot R_{1,0}}\right)} \cdot e^{-TE \cdot (R_2 - R_{2,0})} . \quad (2\text{-}6)$$

Equation 2-6 is shown graphically in figure 2-2 for different values of TR. The signal intensities in the figure, analogous to figure 2-1, were calculated with S_0 set to 1, $R_{1,0}$ set to 1 s^{-1}, and, for the dashed lines, R_2 set equal to R_1 (again, a best case scenario). Unlike the gradient-echo result, the calibration curves are nearly linear over the range shown. This is due to the use of such a large excitation flip angle (i.e., 90°). When T_2-weighting is assumed negligible, it is again important to assure that images are heavily T_1-weighted.

2.4. Determination of contrast agent concentrations from relaxation rate constants

The simplest, and by far the most common, approach for relating the signal intensity to tracer concentration in DCE is to assume a linear relationship between R_1 and the concentration of contrast agent in tissue (C_t) [2]. This assumption, carried over from studies of homogeneous

solutions, may not always be valid. At least one alternative approach has been proposed in the literature [4].

2.4.1. Homogeneous solutions and the fast exchange limit

Over a large range of concentrations, a linear relationship is observed in homogeneous solutions between tracer concentration ([CA]) and the relaxation rate constants R_1 and R_2 [2]. The equations describing these relationships are,

$$R_1 = R_{1,0} + r_1 \cdot [CA], \text{ and} \quad (2\text{-}7)$$

$$R_2 = R_{2,0} + r_2 \cdot [CA]. \quad (2\text{-}8)$$

The slopes in these equations are termed relaxivities; r_1 is the longitudinal relaxivity and r_2 is the transverse relaxivity. No such simple equation relates R_2^* and [CA] [5].

Most of the mathematical models used to describe tracer perfusion in DCE-MRI are built upon a two compartment model. These mathematical equations are presented in the next full section of this chapter. An understanding, however, of the actual compartments is required for the current discussion. As Gd-based tracers remain extracellular, the two compartments of general interest in DCE are the blood plasma compartment and the EES. Figure 2-3 shows a schematic of these compartments as well as a large intracellular compartment. The arrows are meant to indicate that contrast agent molecules can exchange only between the plasma and EES compartments.

Even though CA motion is restricted, water molecules are freely diffusible and can transfer between all compartments within the model. In principle, each compartment can have a different R_1 value. This is especially true in DCE as the contrast agent concentration can be unique in each of the three compartments during the DCE experiment. However, if water exchanges between the compartments on a timescale much faster than that of the NMR experiment (i.e., spin-echo or gradient-echo acquisition), then only a single, average R_1 value will be detected. This is known as the fast exchange limit [4]. Using equation 2-7 to convert from R_1 to tracer concentration is equivalent to assuming the FXL.

2.4.2. The slow exchange limit

The opposite of the fast exchange limit is the slow exchange limit (SXL), in which water in the different compartments does not communicate at all. In this limit, multiple R_1 values can theoretically be detected. For instance, for a two-compartment system in the slow exchange regime, the signal response to an inversion recovery experiment would be the following bi-exponential,

$$S = M_z \cdot \left[1 - 2\left(v_a \cdot e^{-TI \cdot R_{1,a}} + v_b \cdot e^{-TI \cdot R_{1,b}}\right)\right]. \quad (2\text{-}9)$$

The rate constants of the bi-exponential would correspond to the R_1 values of the two compartments (i.e., a and b). Furthermore, the amplitudes of the two exponentials would scale with the fractional volumes of the two compartments (lower case v). When the rate constants are similar to one another, it is difficult to resolve the different fractional components [6].

2.4.3. FXL vs. SXL

The validity of the FXL approximation is a function of both the rate of water exchange and the difference between the native R_1 values in the absence of exchange. For example, if the R_1 values in the two compartments are the same, then no exchange is necessary to achieve the FXL. (i.e., even in the absence of exchange only a single relaxation rate will be observed.) Similarly, if the R_1 values in the two compartments are close in value, then even a little exchange will be adequate to invoke the FXL. In contrast, if the R_1 values are very different, then a lot of exchange must occur for the FXL to be assumed. Accordingly, 1) the largest deviations from the FXL occur when high concentrations of CA are present and 2) the FXL is always assumed for precontrast R_1 acquisition (i.e., $R_{1,0}$).

Accordingly, one can define the FXL limit by relating the relaxation rates of the two compartments to the rate of exchange of the water between the compartments. Specifically, considering the generic compartments a and b, the FXL can be assumed when the following equation holds true [7],

$$k'_{ab} >> \left| R_{1,a} - R_{1,b} \right|. \quad (2\text{-}10)$$

The prime denotes that this is the rate constant of water exchange not CA exchange. The R_1 values are those in the absence of water exchange.

2.4.4. The fast and slow exchange regimes

The fast exchange regime (FXR) and slow exchange regime (SXR) both fall between the FXL and the SXL. Yankeelov *et al*. have proposed that assuming the EES and extravascular intracellular space (EIS) are in the FXR is more correct than assuming the FXL [4]. The fast exchange regime is based upon an alteration of equation 2-9. In the presence of water exchange, the amplitudes and exponential rate constants no longer represent the fractional volumes and rate constants of the two compartments, but instead, represent apparent values as follows,

$$S = M_z \cdot \left[1 - 2\left(a_S \cdot e^{-TI \cdot R_{1,S}} + a_L \cdot e^{-TI \cdot R_{1,L}} \right) \right]. \quad (2\text{-}11)$$

The subscripts S and L refer to small and large rate constants, and a denotes an apparent fractional volume. (Note that in the publication by Yankeelov *et al*., where the following equations are presented, S and L refer to short and long as the equations are written with time constants rather than rate constants.) In addition, if neither the fast exchange limit nor the slow exchange limit can be assumed, it has been proposed that the following equations can be applied for a two-compartment system (subscripted e and i in reference to the EES and EIS of relevance to DCE) [4]:

$$R_{1,S} = \frac{1}{2} \cdot \left\{ 2 \cdot R_{1,i} + r_1 \cdot C_e + \frac{R_{1,0} - \frac{1}{T_{1i}} R_{1,i} + k'_{ie}}{v_e} - \left[\left(2 \cdot k'_{ie} - r_1 \cdot C_e - \frac{R_{1,0} - R_{1,i} + k'_{ie}}{v_e} \right)^2 + \frac{4 \cdot k'_{ie} \cdot (1 - v_e)}{v_e} \right]^{\frac{1}{2}} \right\}, \quad (2\text{-}12)$$

$$R_{1,L} = \frac{1}{2} \cdot \left\{ 2 \cdot R_{1,i} + r_1 \cdot C_e + \frac{R_{1,0} - \frac{1}{T_{1i}} R_{1,i} + k'_{ie}}{v_e} + \left[\left(2 \cdot k'_{ie} - r_1 \cdot C_e - \frac{R_{1,0} - R_{1,i} + k'_{ie}}{v_e} \right)^2 + \frac{4 \cdot k'_{ie} \cdot (1 - v_e)}{v_e} \right]^{\frac{1}{2}} \right\}, \text{ and} \quad (2\text{-}13)$$

$$\frac{a_L}{a_L + a_S} = \frac{1}{2} - \frac{1}{2} \cdot \left\{ \frac{\left(\frac{R_{1,i} - R_{1,0}}{v_e} - r_{1e} \cdot C_e \right) \cdot (2 \cdot v_e - 1) + \frac{k'_{ie}}{v_e}}{\left[\left(2 \cdot k'_{ie} - r_1 \cdot C_e - \frac{R_{1,e} - R_{1,0} + k'_{ie}}{v_e} \right)^2 + \frac{4 \cdot k'_{ie} \cdot (1 - v_e)}{v_e} \right]^{\frac{1}{2}}} \right\}. \quad (2\text{-}14)$$

C represents the tracer concentration in a given compartment. If both $R_{1,L}$ and the $R_{1,S}$ are required for adequate fitting of the concentration curve then one is in the SXR and no closed form solution is available. However, if a single rate constant dominates then one is in the FXR. When this approach is applied to DCE, it is taken that the short rate constant dominates and the following equation can be used in the place of equation 2-7,

$$R_{1,obs} = \frac{1}{2} \cdot \left\{ \begin{array}{l} 2 \cdot \frac{1}{T_{1i}} R_{1,i} + r_1 \cdot C_e + \frac{R_{1,0} - R_{1,i} + k'_{ie}}{v_e} - \\ \left[\left(2 \cdot k'_{ie} - r_1 \cdot C_e - \frac{R_{1,0} - R_{1,i} + k'_{ie}}{v_e} \right)^2 + \frac{4 \cdot k'_{ie} \cdot (1 - v_e)}{v_e} \right]^{\frac{1}{2}} \end{array} \right\}. \quad (2\text{-}15)$$

2.4.5. More complex models

It is important to note that equation 2-15 ignores CA in the vasculature (i.e., the expression does not reference the plasma compartment). An even more complex set of equations results when all three compartments; the blood plasma, the EES, and the EIS; are considered in tandem. The interested reader is referred to the article by Springer *et al*. [8].

2.5. Mathematical equations describing contrast agent perfusion

As noted above, the mathematical equations used to describe tracer perfusion are based upon compartmental tissue models. These models share parameters which have been given standard names and symbols within the DCE literature [9]. The parameters, their symbols, and definitions are listed in the following subsection after which, the different models are described.

2.5.1.

Table 2-2. Parameter names, symbols, and units used in the DCE tracer perfusion equations. (For a more complete table see [9])

Symbol[a]	Name	Units	Symbol[a]	Name	Units
C_t	Total tissue concentration	mM	C_i	EIS concentration	mM
C_p	Blood plasma concentration	mM	C_e	EES concentration	mM
v_p	Fractional blood plasma volume[a]	Unitless	v_e	Fractional volume of the EES	Unitless
k_{ep}	Rate constant of flux of an agent from blood plasma to EES	min^{-1}	K^{trans}	Transfer constant of flux of an agent from blood plasma to EES	min^{-1}

[a] v_p is, to a good approximation, equal to one minus the hematocrit (Hct)

2.5.2 The modified Tofts model

The most commonly used model for DCE data analysis is referred to as the modified Tofts model. This model is derived from more fundamental physical principles in Appendix A and is rewritten with the symbols listed above as,

$$C_t(t) = v_p \cdot C_p(t) + K^{trans} \cdot e^{-k_{ep} \cdot t} \otimes C_p(t). \quad (2\text{-}16)$$

The symbol $\otimes$ denotes the convolution operation (see Appendix A). This equation derives from the two compartment model (with respect to CA) shown in figure 2-3 and is similar to the equation originally utilized by Tofts and known as the standard Tofts model [10]. Note that K^{trans} is equal to $k_{ep} \cdot v_e$. Tofts has shown that this model is mathematically equivalent to the models used by Brix and by Larsson [11]. Note that in order to determine v_p, K^{trans}, and k_{ep}; both $C_t(t)$ and $C_p(t)$ must be known. $C_p(t)$ is the AIF (in terms of concentration vs. time) and must be assumed or measured (*vide infra*). Also note that the equation does not depend upon any specific functional

form for the AIF. However, if a functional form can be assumed then it is sometimes possible to explicitly solve the convolution integral (*vide infra*).

Equation 2-16 can be explained in broad terms by referring to the following equation which can be found as an intermediary in its derivation,

$$C_t(t) = v_p \cdot C_p(t) + v_e \cdot C_e(t). \quad (2\text{-}17)$$

Equation 2-17 states that the concentration of CA in the tissue equals the weighted concentration of CA in the blood plasma plus the weighted concentration of the CA in the EES. Equation 2-16 is derived by setting $C_e(t)$ equal to the response of the system to the impulse $C_p(t)$. In other words, the convolution of $C_p(t)$ and $k_{ep} \cdot e^{-kep \cdot t}$. The product of v_e and k_{ep} is normally expressed as a single constant, K^{trans}.

The validity of the modified Tofts equation rests on several assumptions which are listed below [11].

1. The compartmental model shown in figure 2-3 is accurate
    a. All compartments are well mixed
    b. CA is found only in the EES and the plasma compartments
    c. Any CA in the EES originated from the plasma compartment
2. Fick's law for membranes holds and is time dependent (equation A-14)
    a. Complex transport mechanisms and multiple transport boundaries can be expressed by one effective permeability
    b. Intercompartmental flux is linear and is determined solely from concentrations on each side of the compartmental barrier
3. $C_e(0)$ is equal to zero

In addition, there is the implicit assumption in data processing that the discrete data (i.e., the sampled time course) are of sufficiently fast temporal resolution to accurately reproduce the continuous concentration curves $C_p(t)$ and $C_t(t)$. Including additional assumptions will generally produce a less complex model; removing or partially removing assumptions will result in a more complex model.

2.5.3. Less complex models

There are two additional assumptions sometimes added to the list above. By understanding these assumptions, one can more clearly understand their judicious application.

2.5.3.1. No vascular component

The vascular component of the tissue concentration is expressed as v_p multiplied by $C_p(t)$. This value is equal to zero if v_p is equal to zero or if $C_p(t)$ is equal to zero. Neither of these conditions is true after contrast agent injection in a DCE experiment. However, this assumption is effectively achieved if the quantity $v_pC_p(t)$ is much less than $v_eC_e(t)$. Alternatively, this can be achieved experimentally if signal corresponding to plasma tracer is not detected (e.g., due to time-of-flight or T_2* effects).

As $C_p(t)$ and $C_e(t)$ both change over the time course of the DCE experiment, the validity of this assumption can change as the experiment progresses. If a bolus injection of CA is used, then at short times C_p is much larger than C_t, and at long times (after leakage has occurred) C_p and C_t are closer in value. Thus, this assumption is least valid at short times and most valid at long times. Also, the smaller the value of K^{trans} (the less leaky the vasculature), the longer the potential invalidity of the assumption persists.

The general solution, under the assumption of no vascular component of tissue concentration is known as the standard Tofts model [11] and simplifies to,

$$C_t(t) = K^{trans} \cdot e^{-k_{ep} \cdot t} \otimes C_p(t). \quad (2\text{-}18)$$

2.5.3.2. k_{ep} equals zero

Expressing k_{ep} as the ratio of K^{trans} and v_e, one can see that the assumption that k_{ep} is zero is never achieved, as both K^{trans} and v_e are positive by definition and non-zero in practice. However, it is effectively true if k_{ep} is very small. Therefore, this assumption becomes increasingly valid in the limit of small K^{trans} and/or large v_e. Under this assumption, the resulting equation is known as the Patlak model [12], and the solution can be written as,

$$C_t(t) = v_p \cdot C_p(t) + K^{trans} \otimes C_p(t). \quad (2\text{-}19)$$

As K^{trans} is a constant, this equation is equivalent to:

$$C_t(t) = v_p \cdot C_p(t) + K^{trans} \int_0^t C_p(\tau) d\tau. \quad (2\text{-}20)$$

These assumptions and the resultant general solutions are summarized in Table 2-3.

Table 2-3. Summary of compartmental model assumptions, solutions, and modeled parameters

	Assumptions		General solution	Modeled parameters
1			$C_t(t) = v_p \cdot C_p(t) + K^{trans} \cdot e^{-k_{ep} \cdot t} \otimes C_p(t)$	v_p, K^{trans}, and k_{ep}
2	$C_t=v_eC_e$		$C_t(t) = K^{trans} \cdot e^{-k_{ep} \cdot t} \otimes C_p(t)$	K^{trans} and k_{ep}
3		$k_{ep}=0$	$C_t(t) = v_p \cdot C_p(t) + K^{trans} \int_0^t C_p(\tau) d\tau$	v_p and K^{trans}
4	$C_t=v_eC_e$	$k_{ep}=0$	$C_t(t) = K^{trans} \int_0^t C_p(\tau) d\tau$	K^{trans}

2.5.4. More complex models

As mentioned, more complex physiological models result from removing or relaxing restrictions imposed by the modified Tofts model. The advantage to additional complexity is the potential of more accurately describing tissue perfusion. A number of such models are presented here.

2.5.4.1. The concentration of contrast agent in the plasma compartment is not homogeneous (i.e., the compartment is not well mixed), but instead is represented by a concentration gradient from higher arterial concentrations to lower venous concentrations

It has been shown that the parameter K^{trans} can be written in terms of more fundamental constants [9, 13]. The general form is as follows,

$$K^{trans} = E \cdot f \cdot \rho \cdot (1 - Hct). \quad (2\text{-}21)$$

The parameter f is blood flow per unit mass of tissue (ml/g/min), Hct is the hematocrit (which is assumed to be invariant and homogeneous within the voxel throughout the time course of the experiment), ρ is the density of the tissue (g/ml), and E is the initial extraction ratio which is defined as the fraction of contrast agent that is removed from the arterial blood supply as it passes through the tissue. Despite this analytical expression for K^{trans}, one cannot decompose the transfer constant into its more basic components with a two compartment model (see table 2). Instead, one must use a more complex kinetic model such as the one proposed by St. Lawrence and Lee, the tracer kinetic model [14].

Recall that the two compartment model assumed well-mixed compartments. Restated for the plasma compartment, the model assumes that the contrast agent mixes instantaneously within the vasculature after injection and that arterial and venous concentrations are the same. The tracer kinetic model addresses this assumption by allowing a spatial gradation of concentration along the "temporal" axis of the vasculature (from higher, arterial to lower, venous concentrations) as is shown in block diagram in figure 2-4.

An analytical solution to the concentration of contrast agent in the the tissue can only be obtained by making an additional constraining assumption on the system, namely,

$$\left|\frac{dC_p}{dt}\right| >> \left|\frac{dC_e}{dt}\right|. \quad (2\text{-}22)$$

This is the known as the adiabatic approximation and states that the time rate of change in concentration in the plasma is much greater than the change in concentration in the EES. Under this assumption, the concentration of contrast agent in the tissue can be written as:

$$C_t(t) = \frac{K^{trans}}{E} \int_0^{T_c} C_p(t-\tau) d\tau + K^{trans} \int_{T_c}^{t} C_p(\tau) \cdot e^{-k_{ep} \cdot (t - T_c - \tau)} d\tau. \quad (2\text{-}23)$$

T_c is called the mean capillary transit time (s); functionally it represents the average time for a bolus of CA to traverse the vascular bed within the voxel (i.e., come into and pass out of the vascular compartment). If one assumes that Hct and ρ are known, then flow can be derived by

applying equation 2-21. This is made clear by rewriting equation 2-23 as a function of F and E rather than K^{trans} and E (6),

$$C_t(t) = f \cdot \rho \cdot (1 - Hct) \int_0^{T_c} C_p(t-\tau) d\tau + E \cdot f \cdot \rho \cdot (1 - Hct) \int_{T_c}^{t} C_p(\tau) \cdot e^{-k_{ep} \cdot (t - T_c - \tau)} d\tau. \qquad (2\text{-}24)$$

Furthermore, it can be shown that this equation reduces to equation 2-16 when $t>T_c$ [14]. The same modification to account for incomplete mixing can be applied to the other models of table 2 that contain the term v_pC_p.

The appropriateness of this model hinges upon the validity of the adiabatic assumption. The change in CA concentration in the plasma with respect to time depends largely on the clearance of the contrast agent from the body. The change in CA concentration in the EES with respect to time, however, is described by the modeled vascular parameters. Therefore, the validity of the assumption increases as K^{trans} decreases and as v_e increases. In addition, for this model to be applied, the temporal resolution and S/N of the collected data must be very high. This is stated as an assumption for all the models (see section 2.5.2), but is particularly important here, as the time period $0<t<T_c$ must be well sampled for both C_t and C_p.

2.5.4.2. The plasma compartment is not well mixed during the first pass of the CA, but is represented instead as a distribution of concentration gradients during the first pass

Koh et al. expanded the work of St. Lawrence and Lee by allowing for a distribution of capillary transit times [15]. The single T_c value, introduced by St. Lawrence and Lee, results from treating all the blood vessels within the voxel as one compartment or, equivalently, as one central vessel. Allowing for a distribution of T_c values, therefore, is to model the blood compartment as numerous smaller compartments or vessels with different T_c values. The mean value of this distribution of vessels is equal to the single T_c obtained by taking all the vessels as one. This effect is introduced into equation 2-24 by means of a normalized probability density function, $g(T_c,\mu,\sigma)$ where μ and σ are the mean and standard deviation, respectively, describing the probability of all possible correlation times. The expression thus becomes [15]:

$$C_t(t) = f \cdot \rho \cdot (1 - Hct) \int_0^{T_c} C_p(t-\tau) \cdot \left(1 - \int_0^t g(T_c, \mu, \sigma) dT_c\right) d\tau$$
$$+ E \cdot f \cdot \rho \cdot (1 - Hct) \int_{T_c}^{t} C_p(t-\tau) \cdot \left(e^{-k_{ep} \cdot \tau} \int_0^t g(T_c, \mu, \sigma) \cdot e^{k_{ep} \cdot T_c} dT_c\right) d\tau. \quad (2\text{-}25)$$

In Koh's paper, both a Gaussian and a similar, but slightly asymmetric, function were introduced as possible probability density functions. This model is most valid in the same situations as equation 2-24. However, for the addition of two modeled parameters to be justified, the concentration from $0<t<T_c$ must have strong deviations from equation 2-24 (manifested as a curve near time $t=T_c$ instead of a sharp drop [15]) and the experiment must have adequate temporal resolution to sample effectively such deviations.

2.6. Sample data processing

As a final example, the general two compartment equation (equation 2-16), the FXL equation for R_1 (equation 2-7), and the full gradient echo signal equation (equation 2-3) are combined into a single function expressing signal intensity vs. time in terms of MRI and DCE parameters as well as the input function $C_p(t)$. Pros and cons of this approach are discussed, after which, a stepwise data analysis of a simulated data set is demonstrated.

2.6.1. Combined signal equation

Equation 2-7 can be substituted into equation 2-3 to yield the following equation,

$$S = \frac{S_0}{\left(\frac{1 - e^{-TR \cdot R_{1,0}}}{1 - \cos(\alpha) \cdot e^{-TR \cdot R_{1,0}}}\right)} \cdot \left(\frac{1 - e^{-TR \cdot (R_{1,0} + r_1 \cdot [CA])}}{1 - \cos(\alpha) \cdot e^{-TR \cdot (R_{1,0} + r_1 \cdot [CA])}}\right). \quad (2\text{-}26)$$

In order to apply this equation in a time-resolved manner to DCE data, one additional assumption must be made. Recall that equation 2-3 describes a steady state signal. During a DCE experiment, signal intensity changes in response to changing contrast agent concentration (resulting from the perfusion of a bolus of intravenously injected contrast agent). After any change in contrast agent concentration, the signal requires some equilibration time before steady state is

again reached [1]. However, as the change in concentration is gradual throughout the entire experiment, the signal intensity can be treated as if it is continually at steady state. This assumption is most strongly challenged when large changes in concentration occur between consecutive data points, a situation most likely to occur with a large TR and during the initial uptake of contrast agent. Expressing [CA] as $C_t(t)$ yields,

$$S_t(t) = \frac{S_0}{\left(\frac{1-e^{-TR\cdot R_{1,0}}}{1-\cos(\alpha)\cdot e^{-TR\cdot R_{1,0}}}\right)} \cdot \left(\frac{1-e^{-TR\cdot\left(R_{1,0}+r_1\cdot C_t(t)\right)}}{1-\cos(\alpha)\cdot e^{-TR\cdot\left(R_{1,0}+r_1\cdot C_t(t)\right)}}\right). \quad (2\text{-}27)$$

Equation 2-16 can now be substituted directly into equation 2-27,

$$S_t(t) = \frac{S_0}{\left(\frac{1-e^{-TR\cdot R_{1,0}}}{1-\cos(\alpha)\cdot e^{-TR\cdot R_{1,0}}}\right)} \cdot \left(\frac{1-e^{-TR\cdot\left(R_{1,0}+r_1\cdot v_p\cdot C_p(t)+r_1\cdot K^{trans}\cdot e^{-k_{ep}\cdot t}\otimes C_p(t)\right)}}{1-\cos(\alpha)\cdot e^{-TR\cdot\left(R_{1,0}+r_1\cdot v_p\cdot C_p(t)+r_1\cdot K^{trans}\cdot e^{-k_{ep}\cdot t}\otimes C_p(t)\right)}}\right). \quad (2\text{-}28)$$

In practice, the input function is assumed, measured in a major artery, or derived from reference tissue [16]. If the AIF is measured in a major artery, then equation 2-27 is used to convert $S_p(t)$ to $C_p(t)$ as well as $S_t(t)$ to $C_t(t)$. If a reference tissue is used, then $C_p(t)$ is derived by assuming perfusion parameters for the reference tissue and using an equation such as 2-16 [17].

2.6.2. Explicit solutions to the arterial input function

The convolution of the exponential and $C_p(t)$, as seen in equation 2-28, can be expressed in full integral form as,

$$C_e(t) = k_{ep}\cdot e^{-k_{ep}\cdot t} \otimes C_p(t) = k_{ep}\cdot\int_0^t C_p(\tau)\cdot e^{-k_{ep}\cdot(t-\tau)}\cdot d\tau\,. \quad (2\text{-}29)$$

If a functional form for the input function is assumed, this integral can potentially be explicitly solved. For instance, if the arterial input function is a square function that changes from 0 mM CA to $C_{p,max}$ and back, then equation 2-29 can be written as a set of three equations. The first describes the signal intensity from time $t=t_0$ (the beginning of the experiment) to time $t=t_a$ (the front edge of the square function). The second describes the signal intensity from time $t=t_a$ to $t=t_b$ (the back edge of the square function). The third describes the signal intensity from time $t=t_b$ to

infinity. This approach is used in the ideal mock-DCE experiment described in chapters 4 and 5 of this dissertation. This set of equations is,

$$\frac{C_e(t)}{k_{ep}} = \begin{cases} 0, & \text{if } t < t_a \\ C_{p,\max} \cdot \left(1 - e^{-k_{ep}\cdot(t-t_a)}\right), & \text{if } t_a \le t < t_b \\ C_{p,\max} \cdot \left(1 - e^{-k_{ep}\cdot(t_b-t_a)}\right) \cdot e^{-k_{ep}\cdot(t-t_b)}, & \text{if } t \ge t_b \end{cases}. \quad (2\text{-}30)$$

With current DCE injection protocols, a square input function would not be observed *in vivo*. Most rely on a bolus injection of contrast agent. Perhaps the simplest functional form that could be applied to the resultant input function would be a single exponential decay from some maximum tracer concentration $C_{p,max}$ (where $C_{p,max}$ is less than or equal to the injected CA concentration). The set of equations resulting from this assumed functional form, i.e., $C_p(t)=C_{p,max}\cdot\exp(-k_{AIF}\cdot t)$, are,

$$\frac{C_e(t)}{k_{ep}} = \begin{cases} 0, & \text{if } t < t_a \\ C_{p,\max} \cdot \left(\dfrac{e^{-k_{AIF}\cdot(t-t_a)} - e^{-k_{ep}\cdot(t-t_a)}}{k_{ep} - k_{AIF}} \right), & \text{if } t \ge t_a \end{cases}. \quad (2\text{-}31)$$

Potentially, as more parameters are added to the equation describing the AIF, it more realistically reflects the shape of a measured input function. For example, adding a third parameter, one could use the equation $A\cdot(\exp(-k_{AIF,1}\cdot t)-\exp(-k_{AIF,2}\cdot t))$ to describe the input function. This would give,

$$\frac{C_e(t)}{k_{ep}} = \begin{cases} 0, & \text{if } t < t_a \\ A \cdot \left(\dfrac{e^{-k_{ep}\cdot(t-t_a)} - e^{-k_{AIF,1}\cdot(t-t_a)}}{k_{AIF,1} - k_{ep}} - \dfrac{e^{-k_{ep}\cdot(t-t_a)} - e^{-k_{AIF,2}\cdot(t-t_a)}}{k_{AIF,2} - k_{ep}} \right), & \text{if } t \ge t_a \end{cases}. \quad (2\text{-}32)$$

Many other more advanced ad-hoc functional forms for the AIF could also be applied [18, 19, 20]. Advantages to using an ad-hoc equation for the input function include: 1) one can avoid numerical convolution/deconvolution techniques and 2) modeling of the input function can be performed on a voxel-by-voxel basis [21]. A significant disadvantage is that DCE data processing, requires mathematical modeling of the AIF.

Whether or not modeling of the input function is part of the DCE analysis, there is at least one potential reason to avoid completing the analysis in a single step. When this is done, the

calculated concentrations in the tissue (C_t) and the blood plasma (C_p) are not available individually for inspection. Though maximum concentration values for the tissue or input function are not known *a priori*, they should be equal to or less than the concentration of the injected solution. Similarly, both values should be less than or equal to the concentration of the injected solution diluted by the total blood volume of the patient or animal, and $C_{p,max}$ should be greater than or equal to $C_{t,max}$.

2.6.4. Simulated data example

A simulated signal vs. time curve is shown in figure 2-5 as well as an accompanying AIF. TR and α are assumed to be 0.025 s and 20°, respectively. The temporal resolution was set to 6.4 s which corresponds to an imaging experiment having a TR of 0.025 s, a field of view of 64×64, and collecting four averages for each image. Figure 2-6 shows the concentration vs. time curves that result by applying equation 2-27 with these parameters. As the relationship between tracer concentration and signal intensity is not single valued, a look up table was prepared for the expected concentration range of the experiment as opposed to algebraically reformulating the equation. Lookup tables were made using $R_{1,0,t} = 1\ s^{-1}$, $R_{1,0,p} = 0.5\ s^{-1}$, and $r_1 = 5\ mM^{-1}\ s^{-1}$. S_0 was set to the mean value of the first 20 data points.

Lastly, using the "conv" function in Matlab, the signal concentration curve was fitted iteratively to minimize the mean residual using equation 2-16. The modeled results are presented in figure 2-7. The actual kinetic parameters vs. fitted parameters are given in table 2-4.

Table 2-4. Results from the DCE analysis of a simulated data set.

	K^{trans}	k_{ep}	v_p	v_e
True	0.10	0.50	0.050	0.20
Model	0.10	0.46	0.038	0.22

2.7. References

[1] M. Bernstein, K. King and Z. Zhou, Handbook of MRI Pulse Sequences, Burlington, MA: Elsevier, 2004.

[2] G. Parker and D. Buckley, "Phamacokinetic Modelling of Contrast Kinetics in Dynamic Studies," in *Dynamic Contrast Enhanced Magnetic Resonance Imaging in Oncology*, Berlin, Springer, 2005.

[3] J. Evelhoch, "Key factors in the acquisition of contrast kinetic data for oncology," *Journal of Magnetic Resonance Imaging,* vol. 10, no. 3, pp. 254-259, 1999.

[4] T. Yankeelov, W. Rooney, X. Li and C. J. Springer, "Variation of the Relaxographic "Shutter Speed" forTtranscytolemmal Water Exchange Affects the CR Bolus Tracking Curve Shape," *Magnetic Resonance in Medicine,* vol. 50, no. 6, pp. 1151-1169, 2003.

[5] D. Yablonskiy and E. Haacke, "Theory of NMR Signal Behavior in Magnetically Inhomogeneous Tissues: The Static Dephasing Regime," *Magnetic Resonance in Medicine,* vol. 32, pp. 749-763, 1994.

[6] G. Bretthorst, W. Hutton, J. Garbow and J. Ackerman, "Exponential parameter estimation (in NMR) using Bayesian probability theory," *Concepts in Magnetic Resonance Part A,* vol. 27A, no. 2, pp. 55-63, 2005.

[7] G. Moran and F. Prato, "Modeling (1H) Exchange: an Estimate of the Error Introduced in MRI by Assuming the Fast Exchange Limit in Bolus Tracking," *Magnetic Resonance in Medicine,* vol. 50, no. 6, pp. 1151-1169, 2003.

[8] C. J. Springer, W. Rooney and L. Xin, "The Effects of Equilibrium Transcytolemmal Water Exchange in Medicine," *Magnetic Resonance in Medicine,* vol. 47, no. 2, pp. 422-424, 2002.

[9] P. Tofts, G. Brix, D. Buckley, J. Evelhoch, E. Henderson, M. Knopp, H. Larsson, T. Lee, N. Mayr, G. Parker, R. Port, J. Taylor and R. Weisskoff, "Estimating Kinetic Parameters from Dynamic Contrast-Enhanced R(1)-Weighted MRI of a Diffusable Tracer: Standardized Quantities and Symbols," *Journal of Magnetic Resonance Imaging,* vol. 10, no. 3, pp. 223-

232, 1999.

[10] H. Larsson and P. Tofts, "Measurement of Blood-Brain Barrier Permeability Using Dynamic Gd-DTPA Scanning -- A Comparison of Methods," *Magnetic Resonance in Medicine,* vol. 24, no. 1, pp. 174-176, 1992.

[11] P. Tofts, "Modeling Tracer Kinetics in Dynamic Gd-DTPA MR Imaging," *Journal of Magnetic Resonance Imaging,* vol. 7, no. 1, pp. 91-101, 1997.

[12] J. Ewing, R. Knight, T. Nagaraja, J. Yee, V. Nagesh, P. Whitton, L. Li and J. Fenstermacher, "Patlak plots of Gd-DTPA MRI data yiled blood-brain trasfer constants concordant with those of 14C-sucrose in areas of blood-brain opening," *Magnetic Resonance in Medicine,* vol. 50, no. 2, pp. 283-292, 2003.

[13] G. Parker, "T1-w DCE-MRI: T1-weighted Dynamic Contrast-enhanced MRI," in *Quantitative MRI of the Brain*, T. PS, Ed., West Sussex, Wiley, 2004, pp. 341-364.

[14] K. St. Lawrence and T. Lee, "An Adiabatic Approximation to the Tissue Homogeneity Model of Water Exchange in the Brain," *Journal of Cerebral Blood Flow and Metabolism,* vol. 18, no. 12, pp. 1365-1377, 1998.

[15] T. Koh, V. Zeman, J. Darko, T. Lee, M. Milosevic, M. Haider, P. Warde and I. Yeung, "The Inclusion of Capillary Distribution in the Adiabatic Tissue Homogeneity Model of Blood Flow," *Physics in Medicine & Biology,* vol. 46, no. 5, pp. 1519-1538, 2001.

[16] G. Parker and D. Buckley, "Quantification of Contrast-Enhancement in Dynamic Studies," in *Dynamic Contrast Enhanced Magnetic Resonance Imaging in Oncology*, Berlin, Springer, 2005.

[17] T. Yankeelov, J. Luci, M. Lepage, R. Li, L. Debusk, P. Lin, R. Price and J. Gore, "Quantitative pharmacokinetic analysis of DCE-MRI data without an arterial input function: a rerefence region model," *Magnetic Resonance Imaging,* vol. 23, no. 4, pp. 519-529, 2005.

[18] S. Schabel and D. Parker, "Uncertainty and bias in contrast concentration measurements using spoiled gradient echo pulse sequences," *Physics in Medicine and Biology,* vol. 53, no.

9, pp. 2345-2373, 2008.

[19] M. Schabel, J. Fluckiger and E. DiBella, "A model-constrained Monte Carlo method for blind arterial input function estimation in dynamic contrast-enhanced MRI: I. Simulations," *Physics in Medicine and Biology,* vol. 55, pp. 4783-4806, 2010.

[20] G. Parker, C. Roberts, A. Macdonald, G. Buonaccorsi, D. Buckley, A. Jackson, Y. Watson, K. Davies and G. Jayson, "Experimentally-derived functional form for a population-averaged high-temporal-resolution arterial input function for dynamic contrast-enhanced MRI," *Magnetic Resonance in Medicine,* vol. 56, no. 5, pp. 993-1000, 2006.

[21] J. Lee, L. Bretthorst, C. Derdeyn, W. Powers, T. Videen, A. Snyder, J. Markham and J. Shimony, "Dynamic susceptibility contrast MRI with localized arterial input functions," *Magnetic Resonance in Medicine,* vol. 63, no. 5, pp. 1305-1314, 2010.

2.8. Figures and captions

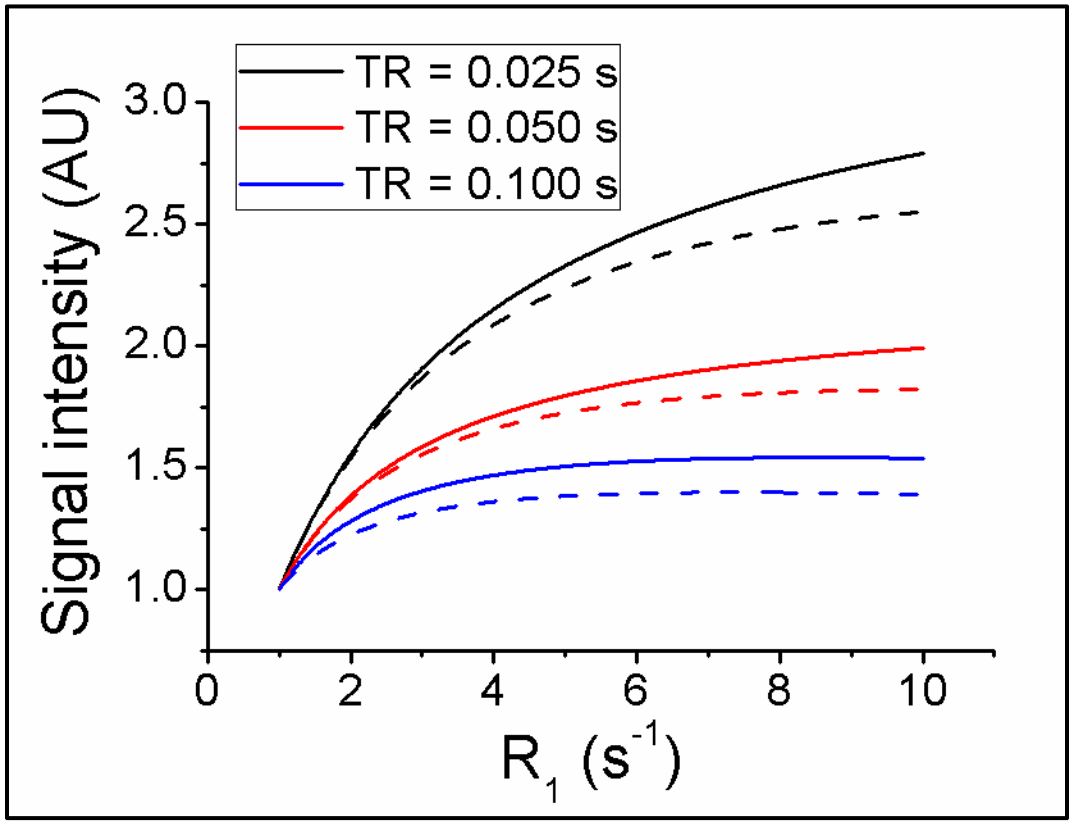

Figure 2-1. Calibration curves for a gradient-echo pulse sequence. The relationship between signal intensity and the longitudinal relaxation rate constant (R_1) is shown for various values of TR. Solid lines assume no T_2*-weighting. Dashed lines assume R_2* is equal to R_1 (best case scenario).

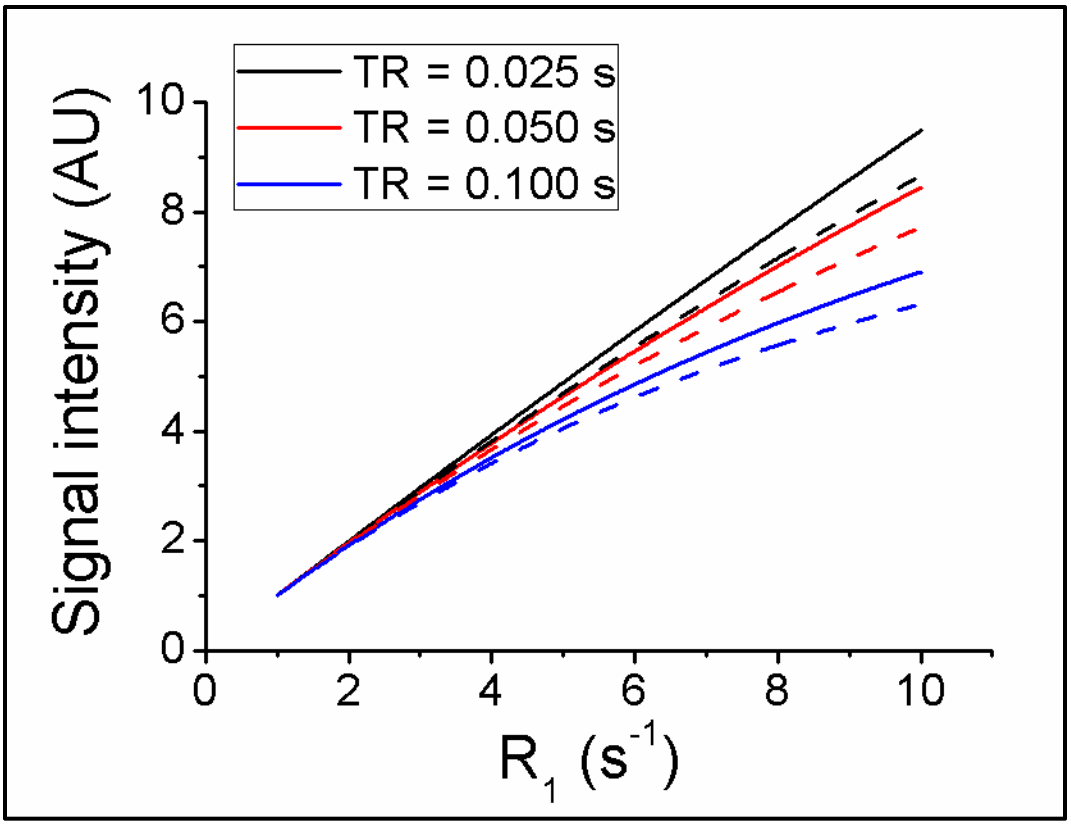

Figure 2-2. Calibration curves for a spin-echo pulse sequence. The relationship between signal intensity and the longitudinal relaxation rate constant (R_1) is shown for various values of TR. Solid lines assume no T_2-weighting. Dashed lines assume R_2 is equal to R_1 (best case scenario).

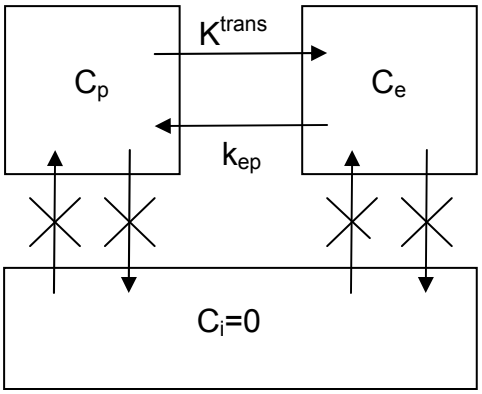

Figure 2-3. Diagram of a three compartment system. C stands for concentration of CA; p, e, and i denote the plasma, extravascular extracellular, and extravascular intracellular spaces respectively; K^{trans} is the transfer constant of CA from p to e; and k_{ep} is the rate constant of CA from e to p. The crossed out arrows indicate that CA cannot cross the cell wall even though water and other analytes do transfer across the barrier.

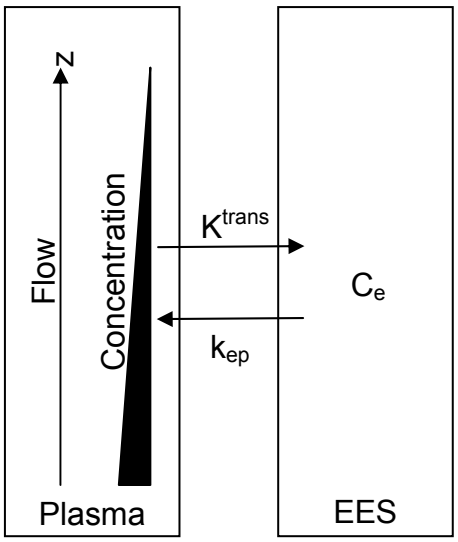

Figure 2-4. Block diagram for the tracer kinetic model. This model does not assume a well mixed plasma compartment, but instead, assumes a linear gradient along the effective length of the "vessel" (the "z axis" runs from arterial to venous ends of the vasculature).

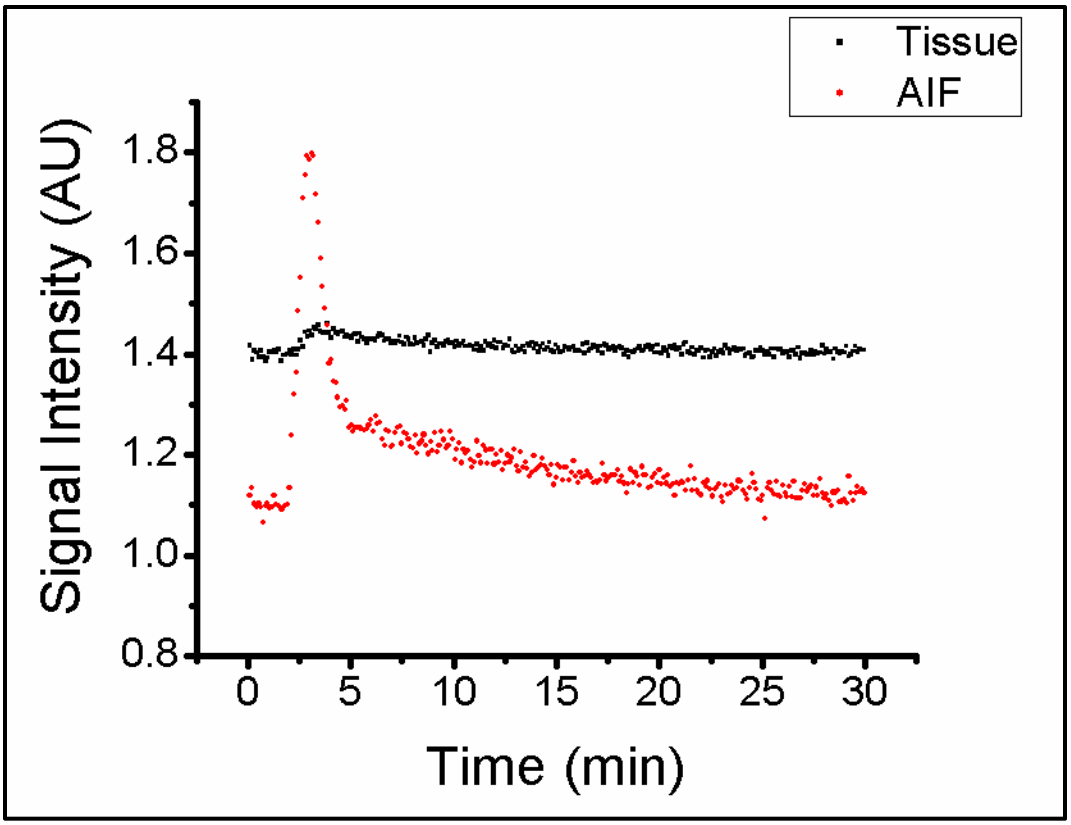

Figure 2-5. Simulated DCE-MRI signal intensity data. The black points correspond to temporally resolved signal intensities measured in a tissue of interest. The red points correspond to temporally resolved signal intensities measured in an artery feeding the tissue of interest, the arterial input function (AIF).

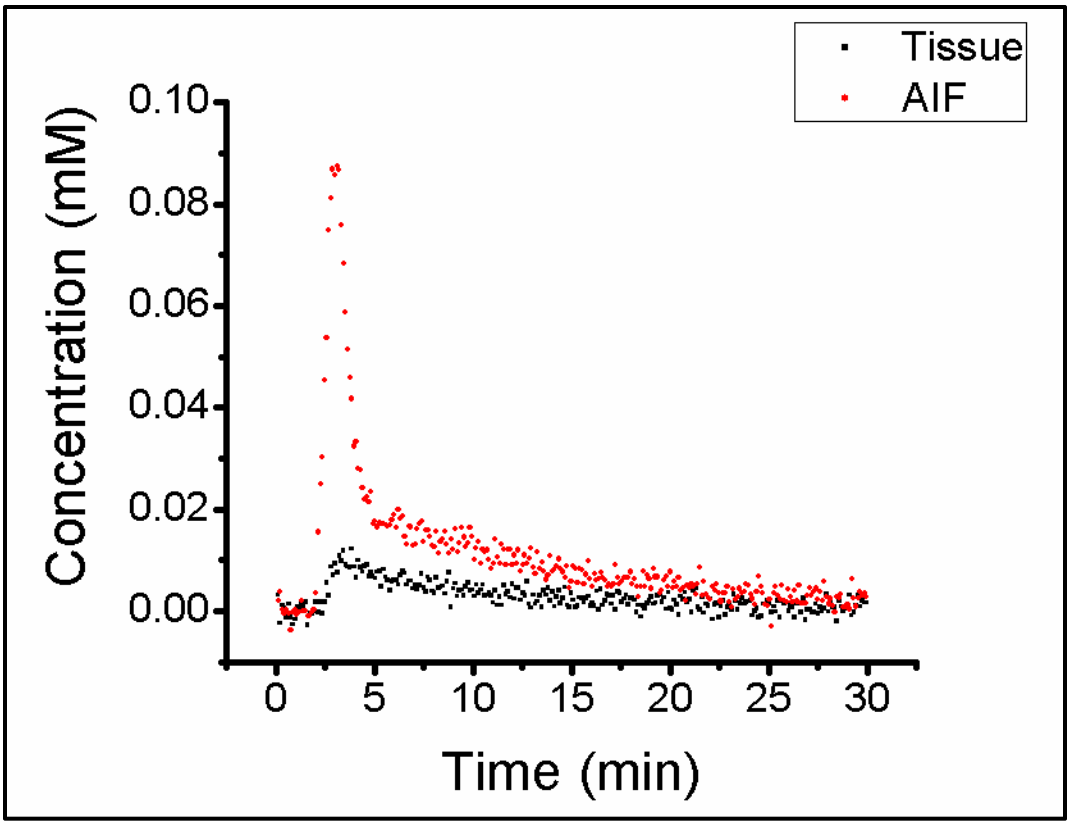

Figure 2-6. Simulated DCE-MRI concentration data derived from signal intensities shown in figure 2-5. The black points correspond to a tissue of interest. The red points correspond to the arterial input function (AIF).

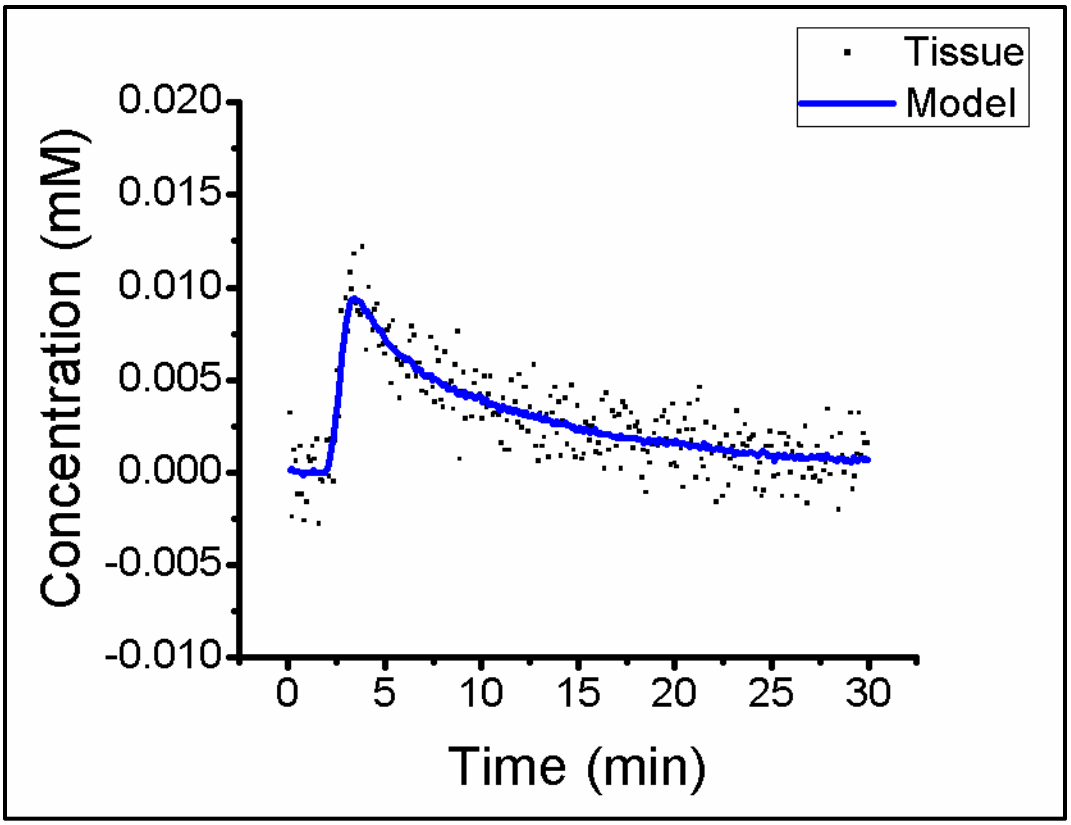

Figure 2-7. Simulated DCE-MRI concentration data derived from signal intensities shown in figure 2-5 corresponding to a tissue of interest. The blue line represents the fitted parameter model.

CHAPTER 3. SEMI-PERMEABLE HOLLOW FIBER PHANTOMS

3.1. Abstract

Two semi-permeable, hollow-fiber phantoms for the validation of perfusion-sensitive MR methods and signal models are described. Semi-permeable hollow fibers harvested from a standard commercial hemodialysis cartridge serve to mimic tissue capillary function. Flow of aqueous media through the fiber lumen is achieved with a laboratory-grade peristaltic pump. Diffusion of water and solute species (e.g., Gd-based contrast agent) occurs across the fiber wall, allowing exchange between the lumen and the extra-lumenal space. Phantom design attributes include: (i) small physical size, (ii) easy and low-cost construction, (iii) definable compartment volumes, and (iv) experimental control over media content and flow rate.

3.2. Publication information

3.2.1. Status

In Press

3.2.2 Journal

Concepts in Magnetic Resonance Part B (Magnetic Resonance Engineering)

3.2.3. Title

Semi-permeable Hollow-Fiber Phantoms for Development and Validation of Perfusion-Sensitive MR Methods and Signal Models

3.2.4. Authors

J. R. Anderson[a], J. J. H. Ackerman[a,b,c], J. R. Garbow[b]

3.2.5. Affiliations

Departments of [a]Chemistry, [b]Radiology, and [c]Internal Medicine; Washington University;

1 Brookings Drive; St. Louis, MO 63130; USA

3.2.6. Corresponding author

Joel R. Garbow, Ph.D.

Biomedical Magnetic Resonance Laboratory

Campus Box 8227

Mallinckrodt Institute of Radiology

Washington University School of Medicine

660 South Euclid Avenue

St. Louis, MO 63110

USA

Email: garbow@wustl.edu

Phoned: 314-362-9949

Fax: 314-362-0526

3.2.7. Keywords

MR phantom design, Hollow fiber bioreactor, Dialyzer, Perfusion, Semi-permeable hollow fiber

3.3. Introduction

Perfusion-sensitive magnetic resonance (MR) techniques, such as dynamic contrast enhanced (DCE) and arterial spin labeled (ASL) MR, are powerful methods for defining and monitoring tissue vascular status, and changes therein, in the face of physiologic challenge, normal and pathologic. DCE and ASL MR methods employ exogenous and endogenous MR-sensitive diffusible tracers, respectively. Analysis of the DCE or ASL MR signal characterizes tissue vasculature by estimating parameters associated with multi-compartment kinetic models, which seek to describe the relevant biophysical properties of a given tissue's vascular system. Quantitative validation of a particular DCE or ASL MR method and its related signal model is

difficult, often impossible, *in vivo*. Phantoms, designed to mimic salient properties of tissue vasculature, provide a platform for validation of perfusion-sensitive MR methods and signal models. Importantly, phantoms allow MR-derived kinetic parameters to be compared with alternative, "gold standard" measurements of these same parameters.

The ideal MR perfusion phantom should contain simulated vasculature enabling (i) lumenal flow, i.e., media flow through the interior of the mock capillaries, and (ii) diffusion of water and solutes (e.g., Gd-based contrast agent) across the vessel wall, i.e., exchange of water and solutes between lumenal and extra-lumenal spaces. The phantom should allow independent determination of parameters characterizing the relevant kinetic model, such as the DCE model's volume wash-in transfer constant (K^{trans}) and wash-out rate constant (k_{ep}), and the ASL model's perfusion rate (f) and mean transit time (MTT).

MR methods and signal-model validation would be enabled by a simple multi-compartment phantom constructed of spaces with known dimensions, as fractional volumes are often important model parameters. Likewise, MR-independent knowledge of experimental parameters would allow quantitative comparison to MR-derived signal/kinetic model-parameter values. These include, for example, media flow rate and velocity, contrast-agent "arterial" input function, and diffusivity of water and contrast agent across the fiber wall. Lastly, a phantom requiring only inexpensive, simple components and construction methods, while maintaining an overall diameter of a few centimeters or less, would facilitate testing/validation of a broad range of perfusion-sensitive MR techniques on pre-clinical (small-animal) MRI scanners.

Hollow fiber modules (HFM), in the form of commercial hemodialyzers (e.g., Fresenius Medical Care AG & Co., Bad Homberg, Germany; Baxter International Inc., Deerfield, IL, USA), hollow-fiber bioreactors, and small-volume filtration and concentration systems (e.g., Spectrum Laboratories Inc., Rancho Dominguez, CA, USA; FiberCell Systems Inc., Frederick, MD, USA) could potentially serve as such phantoms. HFM contain semi-permeable hollow fibers that mimic vasculature. The straw-like polymer fibers permit restricted diffusion of small molecules across the fiber wall, while blocking passage of larger particles such as cells, hence the term "semi-

permeable". The design of HFM permit media flow; thus, simulated perfusion experiments are possible.

MR imaging and spectroscopy studies of HFM have been published, including one in which a commercial dialyzer was used as a phantom for validation of perfusion measurements[1]. However, most imaging studies have focused on testing and improving the efficacy of dialyzers by directly measuring flow (velocity) within the dialysis fibers to probe homogeneous fluid transport[2-9] and assess the impact of different design innovations[10,11]. MR imaging and spectroscopy studies of HFM bioreactors have also been reported. As the native application of bioreactors is support of cell cultures, the majority of this literature is focused on monitoring and characterizing cell growth within the bioreactor *via* diffusion weighting, velocity encoding, or contrast enhancement[12-14]. HFM perfusion measurements employing spectroscopic methods have also been reported[9,15-17].

Despite the many advantages of commercial HFM, there are limitations to their use as perfusion-sensitive MR phantoms. HFM fiber-packing density is fixed by the manufacturer for optimal hemodialysis/micro filtration-concentration/cell growth, limiting the options available for perfusion-sensitive MR phantoms. The chemical composition of the semi-permeable hollow fibers, and thus the porosity/molecular weight cutoff, is likewise fixed by the manufacturer. We further note that human dialyzer HFM, manufactured with clinical efficiency in mind, have a relatively large size that constrains both MR protocols (e.g., field-of-view (FOV) *vs.* spatial resolution) and access to smaller magnet-bore scanners.

Herein, we present the design and construction of two perfusion-sensitive MR phantoms. These laboratory constructed phantoms can be designed with specific fiber dimensions and numbers, allowing accurate calculation of fractional compartment volumes. Further, fibers of various compositions can be obtained from commercial suppliers, allowing selection of permeability characteristics appropriate for the research question of interest. Finally, other parameters salient to perfusion-sensitive MR techniques; including media flow rate, velocity, and input function, can be controlled experimentally. The phantoms are of small dimensions, thereby facilitating high spatial-resolution imaging on preclinical MR imaging scanners by permitting the

use of small, high sensitivity volume coils. Ebrahimi et. al., recently presented a phantom with microfluidic channels[18]. The “vessels” (channels) of the phantom are similar in size to those found *in vivo*. The phantoms presented in this manuscript contain “vessels” of larger dimensions that, unlike microfluidic channels, allow diffusion of water and other molecules through the fiber wall.

Demonstrating two extremes, one phantom consists of a single fiber suspended through the center of a capillary tube; the other phantom consists of multiple fibers densely packed in heat-shrink tubing. Both phantoms permit lumenal and, if desired, extra-lumenal flow/access. Uniformity of commercial fibers allows controlled “gold standard” experiments on a single or a small number of fibers, e.g., measurement of the diffusivity or permeability of water or contrast agent across the fiber wall.

3.4. Phantom Design

3.4.1. Single-fiber Phantom Overview

The overall design of the single-fiber phantom is shown in Fig. 1. The phantom consists of a single, semi-permeable hollow fiber (inner diameter (ID) = 0.20 mm; thickness (TH) of the wall = 0.04 mm) suspended in a capillary tube (ID = 1.00 mm). The fiber was harvested from a commercial HFM used for clinical hemodialysis, *vide infra*. Three physical compartments exist within the phantom: the fiber lumen, the fiber wall, and the extra-fiber space. For many experiments (e.g., T_1 in the absence of lumenal flow or with respect to a molecule that is freely diffusible in both the fiber wall and the extra-lumenal space), the fiber wall and the extra-fiber space constitute a single compartment, collectively referred to as the extra-lumenal space.

In the single-fiber phantom, the lumenal and extra-fiber compartments are independently accessible. For the fiber lumen, access is provided by Luer fittings, mounted directly on the two ends of the capillary tube (Fig. 1), through which a single hollow fiber passes. For the extra-fiber space, access is *via* a catheter, consisting of a 10” piece of tubing (ID = 0.20 mm; TH = 0.10 mm) with an attached Luer fitting. The lumenal and extra-fiber compartments communicate only through the wall of the fiber. The connectors allow for efficient purging of these compartments, as

well as flow in either compartment during experimentation. In our experiments, flow was achieved with a standard laboratory peristaltic pump, *vide infra*.

A design feature of the single-fiber phantom is the ability to control the relative sizes of the lumenal and extra-fiber compartments by changing capillary tubes. The phantom shown in Fig. 1 employs a capillary tube with ID = 1.00 mm; we have also constructed phantoms using capillary tubes with ID = 0.50 mm. These two arrangements result in lumen:fiber wall:extra-fiber space fractional volumes of 0.16:0.15:0.69 and 0.04:0.04:0.92, respectively. The length of the phantom can also be adjusted as required. Typically, capillary tubes for our phantoms are approximately 3 cm long.

3.4.2. Multi-fiber Phantom Overview

The overall design of the multi-fiber phantom is shown in Figs. 2 and 3. The phantom consists of multiple semi-permeable fibers bundled inside heat-shrink tubing (ID = 2.6 mm after shrinkage). As with the single-fiber phantom, three physical compartments exist within the multi-fiber phantom: the fiber lumen, the fiber wall, and the extra-fiber space. Again, under many experimental conditions, the fiber wall and the extra-fiber space can be considered as a single compartment, the extra-lumenal space.

External access to compartments is shown in two different configurations in Figs. 2 and 3. Figure 2 shows the geometry more commonly used in our lab. In this configuration, external access is available only to the lumenal compartment, *via* Luer fittings mounted directly on the two ends of the heat shrink tubing. Figure 3 presents a second geometry, in which both the fiber lumen and the extra-fiber space are accessible externally.

The relative ratios of the different compartments can be altered by changing (i) the number of fibers in the bundle and/or (ii) the diameter of the heat-shrink tubing, as illustrated in two example setups (Figs. 4 and 5, panels C and D). In one case (panel C), 75 fibers placed into heat-shrink tubing that is then contracted produce a densely-packed fiber-bundle phantom having an inner diameter (ID) of 2.6 mm and lumen:fiber wall:extra-fiber space fractional volumes of 0.44:0.43:0.13. In a second case (panel D), 50 fibers placed into 4.0 mm ID heat-shrink tubing

that is not further contracted produce a loosely-packed fiber-bundle phantom with lumen:fiber wall:extra-fiber fractional volumes 0.13:0.12:0.75. Multi-fiber phantoms have been constructed with heat-shrink tubing lengths from 5 cm to 10 cm.

3.5. Construction of phantoms

3.5.1. General Considerations

Devcon 5 Minute Epoxy was used for the construction of all phantoms (ITW Devcon; Danvers, MA, USA). To facilitate precision application of epoxy, a 10 mL syringe with a 19G blunt-tipped needle was used to first draw and then apply the freshly mixed epoxy. Care was taken not to plug the ends of catheters and fibers used in phantoms with epoxy. All fibers used were harvested from a Fresenius Optiflux F-160NR dialyzer. Fibers were cut with a razor blade.

3.5.2. Single-fiber Phantom

In preparation for phantom construction, two Luer-lock end pieces were fashioned from 1 mL Luer-Lok syringes (P/N 309628; Beckton, Dickinson and Company; Franklin Lakes, NJ, USA). The syringes were cut to size (~1.5 cm) and 1.0 mm diameter holes were drilled at an approximately 45° angle, as shown in the left inset of Fig. 1. Mouse tail-vein catheters (MTV-01; Strategic Applications Inc.; Libertyville, IL, USA) were threaded through the holes.

A semi-permeable hollow fiber (length: ~15 cm) was threaded through a capillary tube cut to the desired length. The tips of the two catheters, providing access to the extra-lumenal space, *vide supra*, were inserted ~0.5 cm into opposite ends of the capillary tube. After axially centering the fiber in the capillary, the fiber and catheter tips were fixed in place with epoxy while applying gentle tension to the fiber. Once the epoxy cured, the ends of the semi-permeable hollow fiber were carefully trimmed, leaving ~0.2 cm extending from the capillary on each side. Next, the two Luer-lock end pieces were centered axially on the ends of the capillary and fixed in place with epoxy. Lastly, the holes in the end pieces, through which the catheters were fed, were filled with epoxy.

3.5.3. Multi-fiber Phantom

Value Plastics “Build-A-Part” components (Value Plastics, Inc.; Fort Collins, CO, USA) were used to construct the Luer-lock connectors for the multi-fiber phantoms. These preformed building-block components can be connected to each other, using a small amount of acetone, to form various parts. The “Build-A-Part” components used in these phantoms consisted primarily of cubes with various pass-through holes, as seen in both Figs. 2 and 3. The end connectors for the multi-fiber phantom shown in Fig. 2 were constructed from “Build-A-Part” components before assembly of the phantom, but those used in the multi-fiber phantom shown in Fig. 3 were assembled as part of the phantom-building process, as noted below.

The phantom shown in Fig. 2 was constructed by first bundling together seventy-five fibers with a small amount of fishing line and then threading the fiber bundle through generic 1/8” polyolefin heat-shrink tubing. Epoxy was carefully, but liberally, applied on and around the fibers at one end of the phantom. The epoxy was allowed to seep ~0.5 cm (axially) into the heat-shrink tubing and to completely cover the fibers extending outside of the tubing, also a length of ~0.5 cm. After the epoxy cured for 40 minutes, the fibers at the epoxied end were carefully trimmed with a razor blade, leaving ~0.2 cm exposed beyond the edge of the heat-shrink tubing. Trimming fibers that have been completely encased in epoxy results in a very clean cut and ensures little to no fiber occlusions (Fig. 2, panel D). Next, the heat-shrink tubing was gently contracted with a heat gun. The exposed portions of the fibers were covered with aluminum foil to prevent potential heat damage. Epoxy was then applied to the opposite end of the phantom, allowed to cure, and the fibers trimmed. Lastly, the Luer-lock connectors were fixed to the ends of the phantom with epoxy, taking care not to bend or otherwise constrict any of the fiber tips.

Construction of the multi-fiber phantom shown in Fig. 3 was somewhat more challenging. To ensure that the phantom had a uniform, cylindrical shape, a length of 1/4” heat-shrink tubing was “pre-conditioned” by contracting it around a 4-mm outer-diameter glass rod, which was then removed from the tubing. (A light coating of glycerin applied to the 4-mm glass rod prior to contracting the tubing made it easier to withdraw the rod.) Fifty fibers were bundled and fed

through the “pre-conditioned” (now 4-mm ID) heat-shrink tubing. The bundle of fibers was then threaded through the first “Build-A-Part” component (Fig. 3, right side) until ~0.2 cm of the heat-shrink tubing was nested inside the “Build-A-Part” component. The heat-shrink tubing was fixed to the “Build-A-Part” component with epoxy, taking care to avoid applying any epoxy to the fibers. The fibers were carefully fed through the second component (Fig. 3, center), which was then connected to the first. The fibers were fixed to each other, and then to the inside of the second component with epoxy, and were trimmed to leave ~0.2 cm exposed. Finally, the third “Build-A-Part” component was connected (Fig. 3, left side).

Persistent air bubbles, remaining in the interior of the phantoms after being filled with media, were flushed out using the following two-step procedure. First, the phantom was gradually submerged in a 250 mL Erlenmeyer flask with a sidearm and placed under house vacuum. While under vacuum, the phantom was agitated gently by tapping the flask. Second, the phantom was placed inline and purged with media for 10 to 60 min, as required.

3.6. Materials and methods

3.6.1. Peristaltic Pumping

Peristaltic pumps (single-fiber phantom: Carter Manostat Cassette Pump; Thermo Scientific-Barnant, Barrington, IL, USA; multi-fiber phantom: Masterflex L/S Digital Economy Drive; Cole-Parmer Instrument Company; Vernon Hills, IL, USA) were placed just outside the 5-G line of the magnet’s fringe field. To minimize peristalsis, pump heads with 8 and 6 rollers were used for the single- and multi-fiber phantoms, respectively. Also, small-diameter pump tubing was used to facilitate increased pump-head speeds. Pump tubing with an ID of 0.25 mm was used with the single-fiber phantom (Masterflex Santoprene Tubing; Cole-Parmer; Vernon Hills, IL, USA), while tubing with an ID of 1.6 mm was used with the multi-fiber phantom (Masterflex Tygon Tubing; Cole-Parmer).

3.6.2. MR Imaging

Images were collected on scanners employing Oxford Instruments 4.7-T horizontal-bore magnets of either 33 or 40 cm clear bore (Oxford Instruments; Oxford, UK). Both scanners are interfaced with Agilent/Varian DirectDrive^{TM} consoles, and Agilent/Magnex gradient coil assemblies (Agilent Technologies; Santa Clara, CA, USA). The gradient-coil assemblies have the following respective characteristics: bore IDs = 12 and 21 cm; max gradient amplitudes = 58 and 28 G/cm; and rise times = 295 and 650 μs. Slice-selective gradient-echo images were acquired without lumenal flow, while spin-echo images were acquired with lumenal flow; flow rate = 0.65 mL/min for single-fiber phantoms and 50 mL/min for multi-fiber phantoms. The experimental imaging parameters were: repetition time (TR) = 500 ms, echo time (TE) = 10/13.5 ms (gradient-echo/spin-echo), TH of slice = 1.00 mm, and number of transients (NT) = 32. Although the in-plane FOV varied from 6.4 x 0.8 mm^2 (Figs. 4 and 5, panel A) to 6.4 x 6.4 mm^2 (Figs. 4 and 5, panel D), in-plane voxel dimensions were fixed for all images at 25 x 25 μm^2.

3.6.3. Contrast-Agent Enhancement

To mimic a DCE-MRI experiment, a low molecular weight Gd-based contrast agent was "injected" into the lumenal compartment of the multi-fiber phantom (ID = 2.6 mm; 75 fibers). This "injection" was achieved by means of a 4-way valve located near the phantom that rapidly switched the flowing lumenal solution between pure water and an aqueous solution containing 0.2 mM Gd-BOPTA (gadobenate dimeglumine; MultiHance; Bracco Diagnostics Inc.; Princeton, NJ, USA). The switching apparatus, shown in Figs. 6 and 7, consists of the valve, located immediately adjacent to the phantom, and the actuating handle, located outside the bore of the magnet. A "dummy" phantom was added to the setup, as shown in Fig. 7, so that the pressure in both lines was equivalent. Slice-selective, spin-echo spectroscopy was used to monitor signal intensity *vs.* time as the flowing media was cycled from water (60 sec) to 0.2 mM Gd-BOPTA (60 sec) and back to water (60 sec). The acquisition parameters were: TR = 50 ms, TE = 10 ms, TH = 1.00 mm, and NT = 4. The flow rate was 55 mL/min.

The longitudinal relaxivity of Gd-BOPTA (r_1, mM^{-1} s^{-1}) was determined for the multi-fiber phantom. Media Gd-BOPTA concentrations of 0, 0.25, 0.50, 0.75, and 1 mM were allowed to

completely equilibrate throughout all compartments of the phantom prior to relaxation measurements. At each equilibrated Gd-BOPTA concentration, the longitudinal relaxation rate constant (R_1; s^{-1}) was determined *via* inversion-recovery, spin-echo MR *spectroscopy* experiments without and with lumenal flow (10 mL/min). The experimental parameters were: TE = 10.0 ms, TH = 1.00 mm, NT = 4, number of steady-state scans (SS) = 5, and spectral width (SW) = 4006 Hz. For each experiment, the relaxation pre-delay (PD) was set to at least five times the inverse of R_1, (5 x T_1 (s)). Table 1 lists these PD values and the inversion times (TI) used. Inversion-recovery time-course experiments were repeated three times at each Gd-BOPTA concentration and the R_1 values estimated with Bayesian analysis methods developed in our lab (software available for free download; see Bayesian Analysis of Common NMR Problems; http://bayesiananalysis.wustl.edu/index.html)[19].

The mock-DCE experiment was repeated with the following additional contrast agents: 0.2 mM $GdCl_3$ (gadolinium (III) chloride hexahydrate; P/N G7532; Sigma-Aldrich, St. Louis, MO, USA), 0.2 mM Gd-DTPA-BMA (gadodiamide; Omniscan; GE Healthcare, Piscataway, NJ, USA), and 0.02 mM Gd-DTPA-BSA[20]. Signal intensities were converted to concentrations via the signal equation, measured relaxivities, and the T_1 of bulk water in the presence of flow[21,22]. The uptake curves were quantitatively compared by calculating the initial slope from the first 20 data points immediately following contrast agent “injection”.

3.7. Results

Figure 4 shows representative gradient-echo transaxial images from two single-fiber phantoms (panels A and B) and two multi-fiber phantoms (panels C and D). Due to differences in proton density, the fiber walls appear hypointense in these images. R_1-mapping has established that, in the absence of lumenal flow, there is no significant difference in longitudinal rate constant in the fiber wall compared to homogeneous solution[23]. Figure 5 shows representative spin-echo transaxial images from the same phantoms as in Fig. 4. Flow has suppressed signal in the lumenal compartment in these images *via* time-of-flight effects. The fibers in this figure appear

hyperintense; the region of hyperintensity extends into the extra-fiber space. This interesting effect is due to diffusion-driven longitudinal relaxation (vida infra)[23].

No fluid leakage was observed from any of the phantoms and no diminution of signal was seen in compartments assumed to be non-flowing (i.e., the extra-lumen space). Following a period of several days of being continuously filled with water, the fiber within the single-fiber phantom, which had originally been taught, appeared flaccid. This change in physical appearance was accompanied by a decrease in proton-density contrast between the fiber wall and the extra-fiber space (data not shown). As a consequence, we routinely use a new phantom for each set of experiments. Nonetheless, this effect did not impact any of our individual experiments, the longest of which lasted 15 hours[23].

The results of a mock DCE-MRI experiment with Gd-BOPTA are shown in Fig. 8. Short-lived transients in the highly time-resolved (TR = 50 ms) signal profile accompany each "switching" of the flowing media (with/without contrast agent). These transients provide a convenient time stamp and can be seen in Fig. 8 at the 1- and 2-minute marks of the signal profile.

The expected linear relationship between concentration of contrast agent and R_1 of the equilibrated extra-fiber space was verified, both in the absence and presence of lumenal flow (Fig. 9). However, while the slopes of this relationship, r_1, are equivalent in the absence and presence of flow, the intercepts ($R_{1,0} = R_1$ at 0 mM contrast agent) are different. This is because, in a slice-selective protocol, the flowing media brings fully polarized water ^1H magnetization into the slice, which, during the TI period of the relaxation experiment, exchanges by diffusion with magnetization-perturbed water in the extra-fiber space. (Recall, lumenal water is not observed directly due to time-of-flight effects.) As noted, this diffusion-driven relaxation effect, a phenomenon described in more detail elsewhere, can also be seen in Fig. 5 as an increase in signal amplitude within the fiber wall and in the extra-fiber space near the fiber wall[23].

Concentration vs. time curves from the mock-DCE experiment are shown in figure 10. Clearly, extravasation of contrast agent from the lumenal compartment to the extra-lumenal compartment is a function of the size of the contrast agent, with $GdCl_3$ leaking the most rapidly

and Gd-DTPA-BSA not diffusing through the fiber wall at all. The rate of contrast agent extravasation is compared quantitatively in table 2 via the initial slope of the concentration uptake curve. These simple examples demonstrate the utility of the perfusion-sensitive MR phantom in revealing phenomena, perhaps unanticipated, that can impact various MR protocols and accompanying kinetic models.

3.8. Conclusions

Design and construction details for two semi-permeable hollow-fiber phantoms, useful for testing and validation of perfusion-sensitive MR protocols and signal models, are described. The phantoms, single- and multi-fiber, are robust and allow control over the fractional volumes of the lumenal and extra-fiber compartments. The phantoms' small sizes allow high spatial resolution to be achieved with small, high sensitivity volume coils on preclinical MR imaging scanners, resolving individual compartments: fiber lumen, fiber wall, extra-fiber space. The small size also facilitates purging of air bubbles within the phantom, as the entire phantom can easily be submerged under vacuum. Complete suppression of lumenal signal can be achieved, if desired, with slice-selective, spin-echo protocols *via* time-of-flight. Mock-DCE experiments clearly demonstrate extravasation of low molecular-weight contrast agents from lumenal to extra-fiber compartments. While the expected linear relationship between concentration of contrast agent and longitudinal relaxation rate constant is demonstrated, modification of this linear relationship by flow-enabled, diffusion-driven relaxation is revealed. These phantoms will contribute to efforts, ongoing in many laboratories, to develop, test, and validate, quantitative perfusion-sensitive MRI methods and associated signal models.

3.9. References

1. Wang Y, Kim SE, DiBella EV, Parker DL. 2010 Flow measurement in MRI using arterial spin labeling with cumulative readout pulses--theory and validation. Med Phys 37:5801-5810.

2. Osuga T, Obata T, Ikehira H. 2004 Detection of small degree of nonuniformity in dialysate flow in hollow-fiber dialyzer using proton magnetic resonance imaging. Magn Reson Imag 22:417-420.

3. Osuga T, Obata T, Ikehira H. 2004 Proton magnetic resonance imaging of flow motion of heavy water injected into a hollow fiber dialyzer filled with saline. Magn Reson Imaging 22:413-416.

4. Hardy PA, Poh CK, Liao Z, Clark WR, Gao D. 2002 The use of magnetic resonance imaging to measure the local ultrafiltration rate in hemodialyzers. J Membr Sci 204:195-205.

5. Laukemper-Ostendorf S, Lemke HD, Blümler P, Blümich B. 1998 NMR imaging of flow in hollow fiber hemodialyzers. J Membr Sci 138:287-295.

6. Pangrle BJ, Walsh EG, Moore S, DiBiasio D. 1989 Investigation of fluid flow patterns in a hollow fiber module using magnetic resonance velocity imaging. Biotechnol Tech 3:67-72.

7. Poh CK, Hardy PA, Liao Z, Clark WR, Gao D, Dibakar B, Butterfield DA. 2003. Membrane and Science Technology Series. New Insights into Membrane Science and Technology: Polymeric and Biofunctional Membranes. Dibakar Bhattacharyya and D. Allan Butterfield. Editors. Elsevier Science B.V., Amsterdam, The Netherlands. pp. 89-122.

8. Zhang J, Parker DL, Leypoldt JK. 1995 Flow Distributions in Hollow Fiber Hemodialyzers Using Magnetic Resonance Fourier Velocity Imaging. ASAIO J 41:M678-M682.

9. Heese F, Robson P, Hall LD. 2005 Quantification of fluid flow through a clinical blood filter and kidney dialyzer using magnetic resonance imaging. IEEE Sens J 5:273-276.

10. Poh CK, Hardy PA, Liao Z, Huang Z, Clark WR, Gao D. 2003 Effect of flow baffles on the dialysate flow distribution of hollow-fiber hemodialyzers: a nonintrusive experimental study using MRI. J Biomech Eng 125:481-489.

11. Poh CK, Hardy PA, Liao Z, Huang Z, Clark WR, Gao D. 2003 Effect of spacer yarns on the dialysate flow distribution of hemodialyzers: a magnetic resonance imaging study. ASAIO J 49:440-448.

12. Donoghue C, Brideau M, Newcomer P, Pangrle B, DiBiasio D, Walsh E, Moore S. 1992 Use of magnetic resonance imaging to analyze the performance of hollow-fiber bioreactors. Ann N Y Acad Sci 665:285-300.

13. Galons JP, Lope-Piedrafita S, Divijak JL, Corum C, Gillies RJ, Trouard TP. 2005 Uncovering of intracellular water in cultured cells. Magn Reson Med 54:79-86.

14. Thelwall PE, Neves AA, Brindle KM. 2001 Measurement of bioreactor perfusion using dynamic contrast agent-enhanced magnetic resonance imaging. Biotechnol Bioeng 75:682-690.

15. Heilmann M, Vautier J, Robert P, Volk A. 2009 In vitro setup to study permeability characteristics of contrast agents by MRI. Contrast Med Mol Imaging 4:66-72.

16. Planchamp C, Gex-Fabry M, Dornier C, Quadri R, Reist M, Ivancevic MK, Vallee JP, Pochon S, Terrier F, Balant L and others. 2004 Gd-BOPTA transport into rat hepatocytes: pharmacokinetic analysis of dynamic magnetic resonance images using a hollow-fiber bioreactor. Invest Radiol 39:506-15.

17. Van As H, Lens P. 2001 Use of 1H NMR to study transport processes in porous biosystems. J Ind Microbiol Biotechnol 26:43-52.

18. Ebrahimi B, Swanson SD, Chupp TE. 2010 A Microfabricated Phantom for Quantitative MR Perfusion Measurements: Validation of Singular Value Decomposition Deconvolution Method. IEEE Biomed Eng 57:2730-2736.

19. Bretthorst GL, Hutton WC, Garbow JR, Ackerman JJH. 2005 Exponential parameter estimation (in NMR) using Bayesian probability theory. Concepts Magn Reson Part A 27:55-63.

20. Dafni H, Landsman L, Schechter B, Kohen F, Neeman M. 2002 MRI and fluorescence microscopy of the acute vascular response to VEGF165: vasodilation, hyper-permeability

and lymphatic uptake, followed by rapid inactivation of the growth factor. NMR Biomed 15:120-131.

21. Bernstein MA, King KF, Zhou ZJ. 2004. Handbook of MRI Pulse Sequences. Amsterdam, Boston: Academic Press. p 1017.

22. Jackson A, Buckley D, Parker GJM, eds. 2003. Dynamic Contrast-Enhanced Magnetic Resonance Imaging in Oncology. Berlin, New York: Springer.

23. Anderson JR, Ye Q, Neil JJ, Ackerman JJH, Garbow JR. 2011 Diffusion Effects on Longitudinal Relaxation in Poorly Mixed Compartments. J Magn Reson 211:30-36.

3.10. Figures and captions

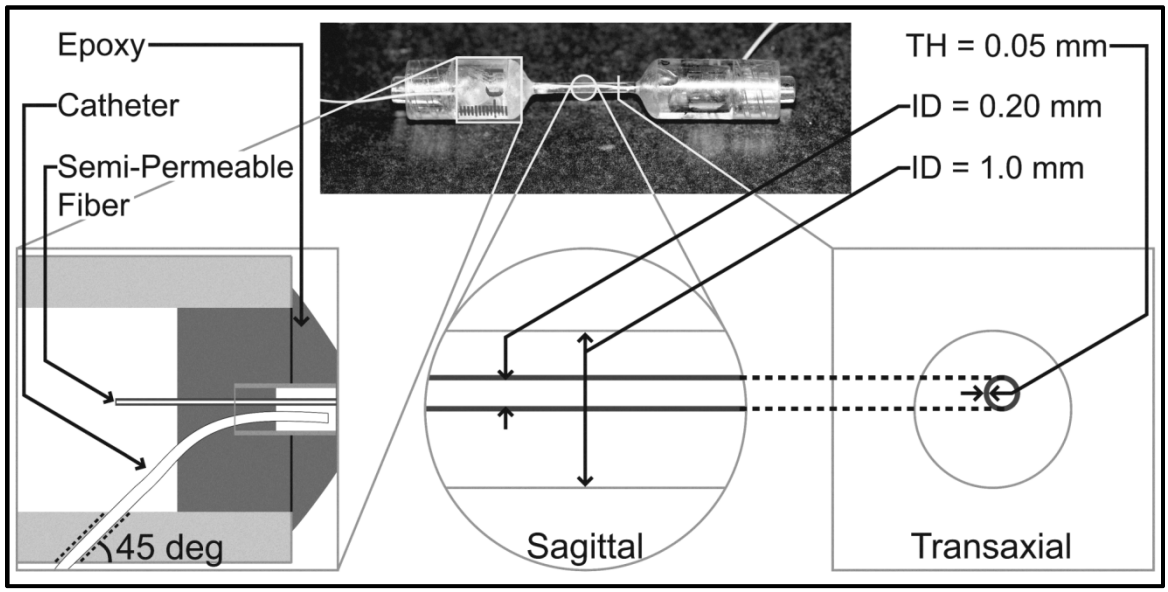

Figure 3-1. Single-fiber phantom. Left inset: schematic of the interior of the Luer-lock end piece. Center inset: schematic interior of the center portion of the phantom; sagittal view. Right inset: schematic interior of the center portion of the phantom; transaxial view.

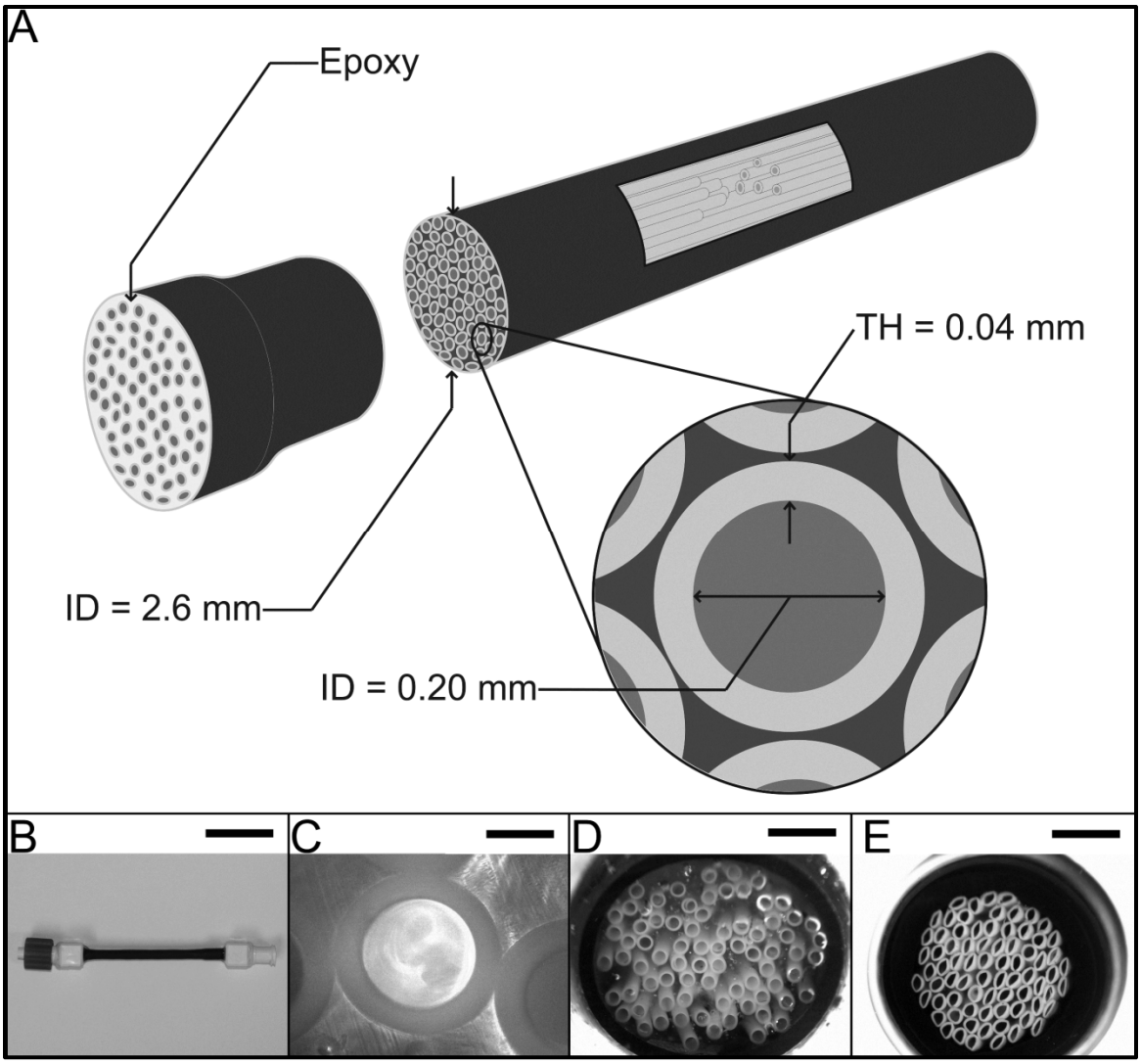

Figure 3-2. Multi-fiber phantom; lumenal compartment access only. Panel A: schematic of the design and dimensions of the multi-fiber phantom. Panel B: photograph of the multi-fiber phantom (scale bar = 2.50 cm). Panel C: microscope image of a transaxial cross-section of a single fiber (40X magnification, scale bar = 100 μm). Panel D: microscope image of a transaxial cross-section of the end of the phantom, i.e., fibers fixed in epoxy (4X magnification, scale bar = 1 mm). Panel E: microscope image of a transaxial cross-section of the center portion of the phantom; fibers tightly bundled (4X, scale bar = 1 mm). Note: the slight deformity seen in some fibers in panel E occurred while cutting the phantom for the microscope image.

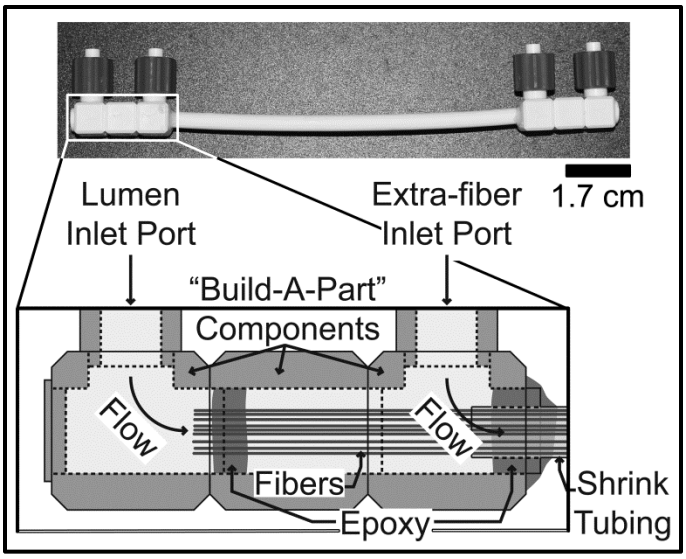

Figure 3-3. Multi-fiber phantom with lumenal and extra-fiber compartment access. Inset: schematic of the interior of the "Build-A-Part" Luer-lock connector.

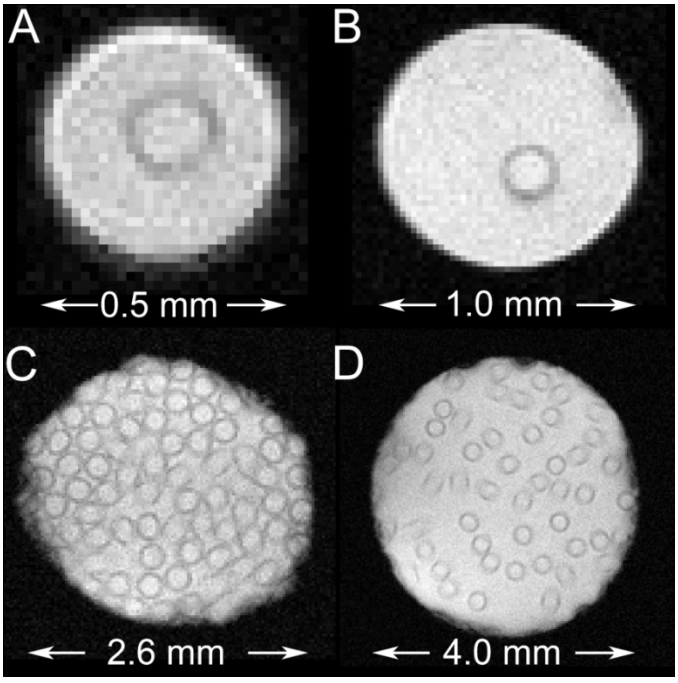

Figure 3-4. Gradient-echo images of various semi-permeable hollow-fiber phantoms, without lumenal flow. Panel A: single-fiber phantom; ID = 0.5 mm. Panel B: single-fiber phantom; ID = 1.0 mm. Panel C: multi-fiber phantom; 75 fibers; ID = 2.6 mm. Panel D: multi-fiber phantom; 50 fibers; ID = 4.0 mm.

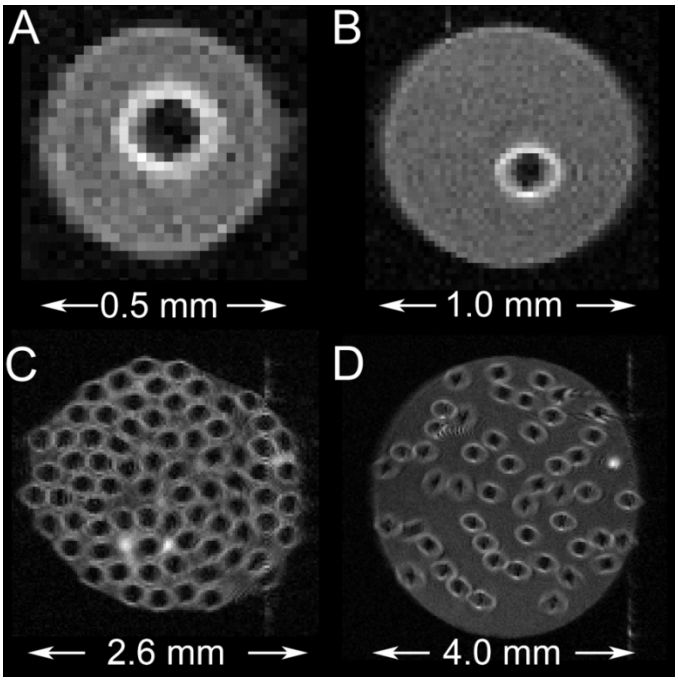

Figure 3-5. Spin-echo images of various semi-permeable hollow-fiber phantoms with lumenal flow. Panel A: single-fiber phantom; ID = 0.5 mm. Panel B: single-fiber phantom; ID = 1.0 mm. Panel C: multi-fiber phantom; 75 fibers; ID = 2.6 mm. Panel D: multi-fiber phantom; 50 fibers; ID = 4.0 mm.

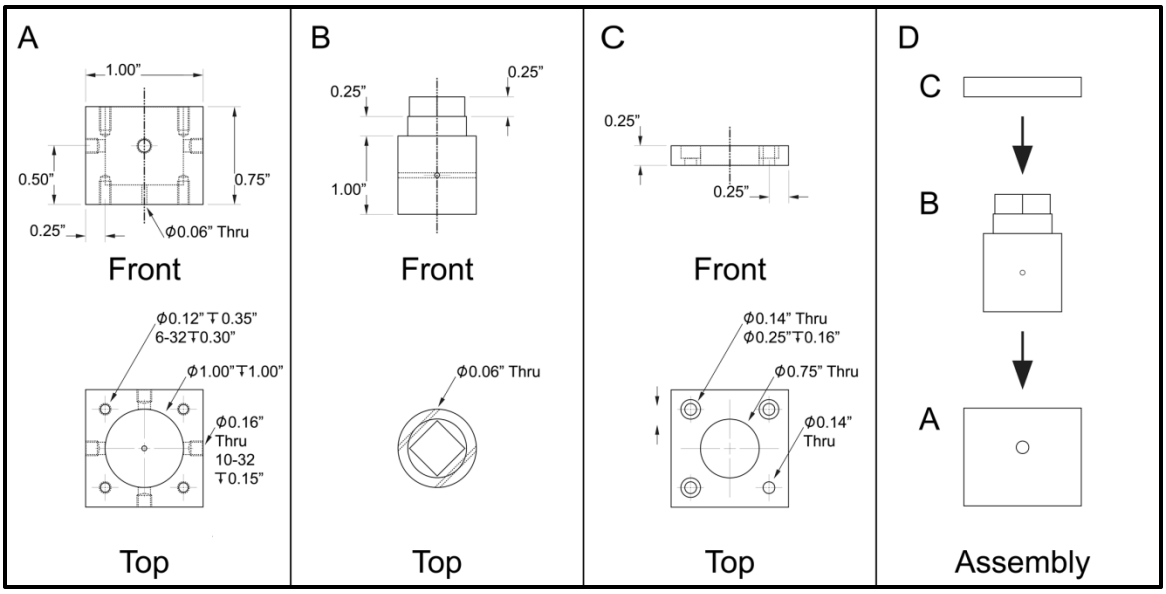

Figure 3-6. Four-way valve used in the switching apparatus. Panel A: polyoxymethylene (Delrin) valve-chamber casing. The eight threaded holes are for attaching the valve lid to the valve casing (top four) and for securing the valve to the switching apparatus (bottom four). Panel B: polyoxymethylene valve plug. Panel C: polyoxymethylene valve chamber lid. Note that one of the four small through-holes has no counterbore. The screw at this position, which can be seen in Fig. 7, is used as a guide for switch actuation. Panel D: Assembly of the valve. Assembly was aided by applying a thin layer of high vacuum grease (Dow Corning Corporation; Midland, MI, USA) between the valve chamber casing and the valve plug.

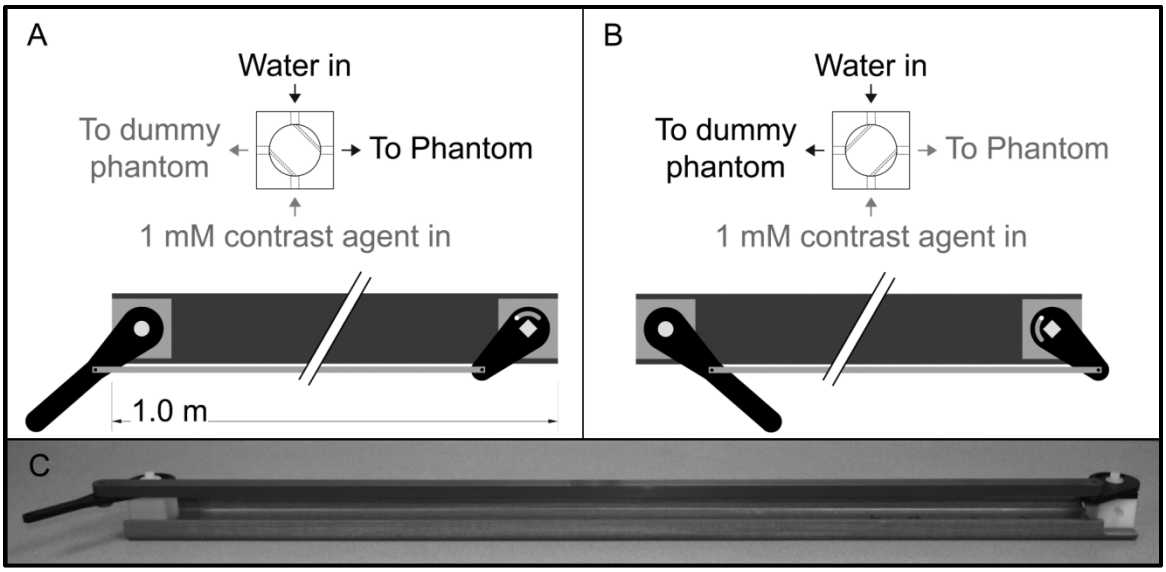

Figure 3-7. Switching apparatus used to rapidly switch the lumenal media between water and contrast agent in the mock-DCE experiment (Fig. 8). Panel A: The apparatus in position one, with water flowing to the phantom. Panel B: The apparatus in position two, with 1 mM contrast agent flowing to the phantom. Panel C: photograph of the switching apparatus.

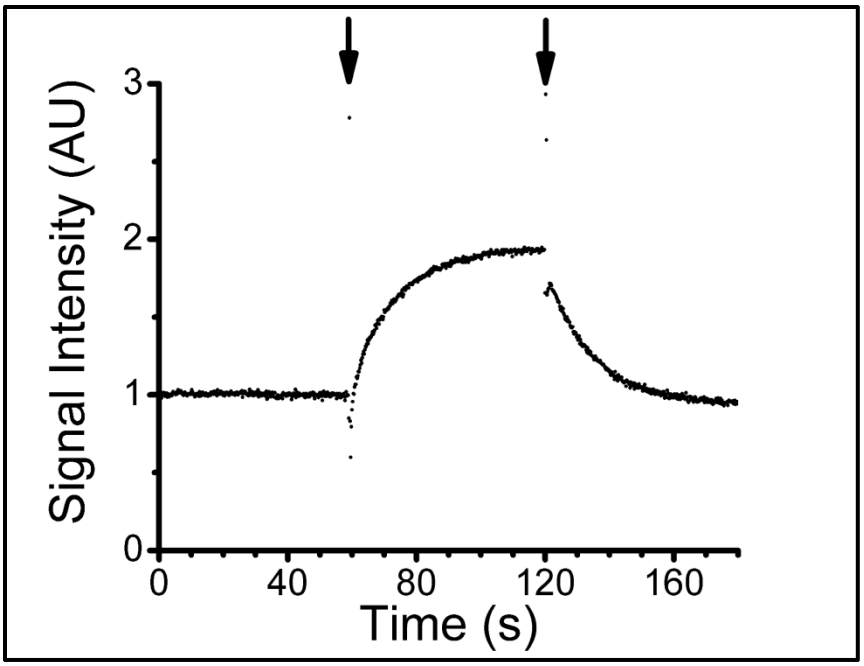

Figure 3-8. Mock-DCE experiment, as measured in the multi-fiber phantom. Signal intensity was monitored as a function of time, while lumenal media was cycled from water (duration ~60 s) to 0.2 mM Gd-BOPTA (duration ~60) and back to water (duration ~60 s). Short-lived transients, observed coincident with media switching, are highlighted with arrows.

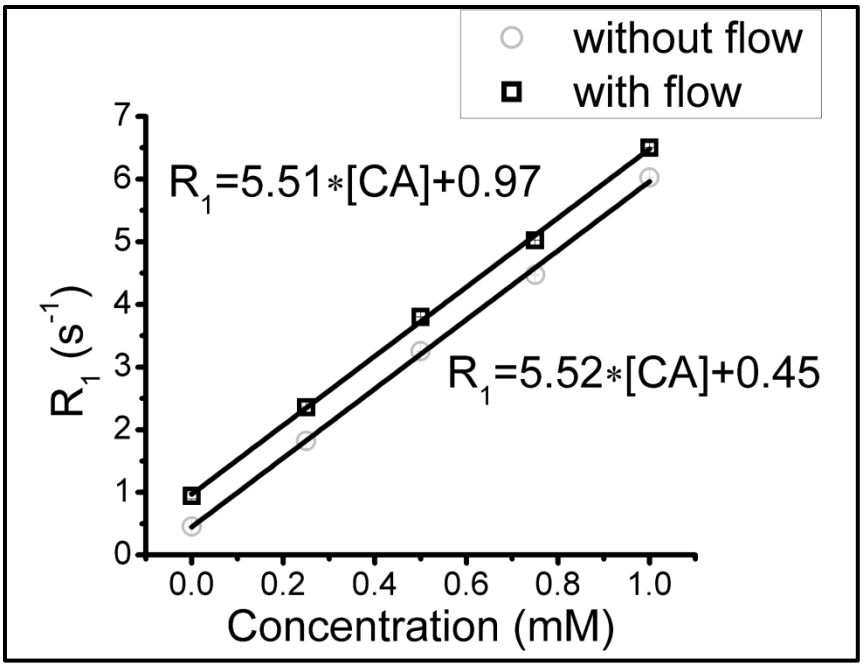

Figure 3-9. . Longitudinal relaxation rate (R_1; s^{-1}) measured in the multi-fiber phantom, as a function of Gd-BOPTA concentration, with (squares) and without (circles) lumenal flow. Linear regression fits, used to derive relaxivity values (r_1, s^{-1} mM^{-1}), are shown.

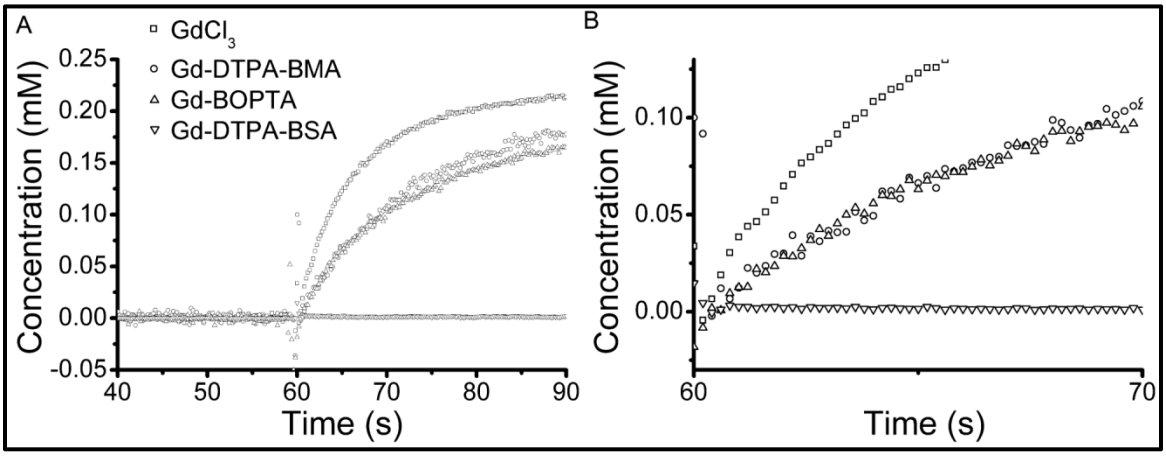

Figure 3-10. Mock-DCE experimental results for $GdCl_3$ (squares), Gd-DTPA-BMA (circles), Gd-BOPTA (up-pointing triangles), and Gd-DTPA-BSA (down-pointing triangles). The concentration of contrast agent in the extra-lumenal compartment (mM) was derived from dynamic signal intensity in the presence of lumenal flow (see Materials and Methods). Panel B is an expanded view of panel A that highlights the initial contrast agent uptake, or, in the case of Gd-DTPA-BSA, the lack thereof.

3.11. Tables

Table 1. Additional experimental parameters, not noted in the text, corresponding to Fig. 6.

Concentration of Gd-BOPTA	**Pre-delay (PD)**	**First inversion time (TI_{first})[a]**	**Last inversion time (TI_{last})[a]**
0.00 mM	11.50 s	0.23 s	11.50 s
0.25 mM	3.00 s	0.05 s	3.00 s
0.50 mM	1.75 s	0.03 s	1.75 s
0.75 mM	1.25 s	0.02 s	1.25 s
1.00 mM	1.00 s	0.02 s	1.00 s

[a]Thirty TI values were used spaced logarithmically from TI_{first} to TI_{last}

Table 2. Initial slopes calculated from the various contrast-agent uptake curves shown in Fig. 10.

Contrast agent	**$GdCl_3$**	**Gd-DTPA-BMA**	**Gd-BOPTA**	**Gd-DTPA-BSA**
Molecular weight	157 Da[a]	574 Da	668 Da[a]	~68 kDa
Initial slope	0.024 mM/s	0.013 mM/s	0.015 mM/s	0.000 mM/s

[a]Molecular weight without counterion

CHAPTER 4. SINGLE-FIBER PHANTOM

4.1. Abstract

Diffusion of spins between physical or virtual, communicating compartments having different states of longitudinal magnetization leads to diffusion-driven longitudinal relaxation. Herein, in two model systems, the effects of diffusion-driven longitudinal relaxation are explored experimentally and analyzed quantitatively. In the first case, longitudinal relaxation in a single slice of a water phantom is monitored spectroscopically as a function of slice thickness. In the second case, mimicking vascular flow/diffusion effects, longitudinal relaxation is monitored in a two-compartment, semi-permeable fiber phantom. In both cases, apparent longitudinal relaxation, though clearly multi-exponential, is well-modeled as bi-exponential.

4.2. Publication information

4.2.1. Status

Published: 2011, 211:30-36

4.2.2. Title

Diffusion Effects on Longitudinal Relaxation in Poorly Mixed Compartments

4.2.3. Authors

J. R. Anderson[a], Q. Ye[a], J. J. Neil[b,c,d], J. J. H. Ackerman[a,b,e], J. R. Garbow[b]

4.2.4. Affiliation

Department of [a]Chemistry; Washington University; 1 Brookings Drive; St. Louis, MO 63130; USA

Departments of [b]Radiology, [c]Neurology, [d]Pediatrics, and [e]Internal Medicine, Washington University School of Medicine, 660 South Euclid Ave., St. Louis, MO 63110; USA

4.2.5. Keywords

NMR, MRI, flow, thin slice, semi-permeable fiber

4.3. Introduction

The remarkable performance capabilities of modern MR scanners are redefining the limits of spatial resolution, signal sensitivity, and data interpretation. Data are often of such high quality that subtle signal characteristics, ones that could previously be safely ignored, must now be recognized in accurate signal-modeling and parameter estimation. This is especially true when testing signal models against “ideal” data obtained from phantoms and phantom-like systems.

This laboratory has, for some time, been interested in signal models that describe systems characterized by coherent and incoherent displacement motions, e.g., flow, perfusion, and diffusion. Despite the multi-compartment complexity of most tissues, data modeling is typically performed using relatively simple mathematical representations of the signal. The utility of the resulting parametric maps depends upon the validity of the underlying simplifying assumptions, which can be difficult to assess. Recently, while pursuing control experiments with phantoms, we encountered diffusion-driven relaxation, a phenomenon that could, if unrecognized, compromise data interpretation.

Diffusion of spins between physical or virtual, communicating compartments having different states of longitudinal magnetization leads to diffusion-driven longitudinal relaxation [1-5]. The population of spins in one physical or virtual compartment will demonstrate altered longitudinal relaxation when exchanging, *via* diffusion, with a population of spins of different magnetization state from a communicating second compartment.

Herein, deviations from mono-exponential longitudinal relaxation due to diffusion-driven relaxation are examined in two limiting cases. In the first case, a sample consisting of a single physical compartment is divided, by slice selection, into two virtual compartments. Experiments are performed in which signal is only detected from one compartment - the selected slice. In the second case, a two-compartment, semi-permeable fiber phantom is constructed. Experiments are performed in which, due to time-of-flight flow effects, signal is only detected from one of the two

compartments - the extra-lumenal compartment. The effects of diffusion between virtual and physical communicating compartments are observed and modeled, and the implications of diffusion-driven relaxation are discussed.

4.4. Materials and methods

4.4.1. Longitudinal Relaxation Rate Constant Determination

All longitudinal relaxation rate constants were measured with a modified fast inversion recovery (MFIR) pulse sequence [6]. MFIR is a variation on the standard inversion recovery experiment, in which images are collected at different inversion times (TI), where the repetition time (TR) is fixed at a value that is shorter than required for full recovery of longitudinal magnetization. This method realizes a portion of the time savings of fast inversion recovery (FIR), for which both TI and TR are varied in concert in order to fix the pre-delay, but, unlike FIR, can be modeled even in the presence of imperfect flip angles by the following three parameter equation,

$$S(TI) = A + B \exp(-R_1 \cdot TI), \qquad [1]$$

where S(TI) is the signal intensity for inversion time TI and R_1 is the longitudinal relaxation rate constant, the inverse of the time constant, T_1 [7,8].

4.4.2. Slice Thickness Experiments

Apparent longitudinal relaxation was monitored in a water-filled, 1.0-mm ID capillary tube *via* a slice-selective (transverse to the tube's long axis), spin-echo, MFIR spectroscopy experiment. To observe the effect of diffusion on the measurement, experiments were performed with four different slice thicknesses (TH): 1.00, 0.500, 0.250 and 0.125 mm. Crafted 90° and 180° pulses, similar in shape to SLR pulses, were used to minimize imperfections in slice profile [9,10]. To this same end, symmetric left and right crusher ("butterfly") gradients were implemented with both the inversion and refocusing 180° pulses.

For all slice thicknesses, the acquisition parameters were: TR = 20.0 s, TE = 10.67 ms, and spectral width (SW) = 4006 Hz. To compare data at similar signal-to-noise ratio (SNR), the

number of transients (NT) was varied: NT = 1 (TH =1.00 mm), 4 (TH = 0.500 mm), 16 (TH = 0.250 mm), and 64 (TH = 0.125 mm). In addition, a single relaxation data set was acquired at higher SNR with TH = 10.0 mm and NT = 4, a slice thickness greater than the active region of the coil. Thirty logarithmically spaced TI values ranging from 0.01 – 15 s were employed throughout.

Signal amplitudes were calculated from the total integrated intensity of the water ^{1}H resonance *via* in-house programs developed using Matlab (Mathworks; Natick, MA, USA). Relaxation data were modeled as exponential functions by Bayesian analysis methods developed in our lab (Bayesian Analysis of Common NMR Problems; http://bayesiananalysis.wustl.edu/index.html) [11,12].

4.4.3. Non-permeable and Semi-permeable Fiber Phantom Design

A non-permeable hollow fiber (polyurethane catheter; ID = 300 μm, OD = 400 μm) or semi-permeable hollow fiber (polysulfone dialyzer; ID = 200 μm, OD = 280 μm) was suspended through the middle of a capillary tube (ID = 1.0 mm) and held in place with epoxy applied at the ends of the capillary tube. (Note: in this paper, semi-permeable denotes a material allowing free diffusion of water and allowing, but potentially slowing, diffusion of aqueous Gd-based contrast agents; and non-permeable denotes a material completely blocking diffusion of both water and aqueous Gd-based contrast agents.) The phantom consisted of two physical compartments, the lumen, i.e., the interior of the fiber, and the extra-lumenal space. The phantom design allowed controlled flow of media in the fiber lumen. The semi-permeable hollow fiber, similar to those used in hollow-fiber bioreactors, was harvested from a commercial dialyzer (Optiflux F-160NR; Fresenius Medical Care AG & Co., Bad Homburg, Germany). As the extra-lumenal space was closed and water is an incompressible fluid, there were no pressure gradients across the transverse axis of the phantom (i.e., between lumenal and extra-lumenal compartments).

Lumenal flow was achieved *via* a peristaltic pump. Flow rates were periodically measured just downstream of the phantom to assure constant flow velocities throughout the experiment.

4.4.4. Non-Permeable and Semi-permeable Fiber Phantom Experiments

For both the semi-permeable and non-permeable fiber phantoms, T_1 maps were obtained with and without aqueous flow at 0 and 1 mM concentrations of Omniscan (gadodiamide; Gd-DTPA-BMA; GE Healthcare, Piscataway, USA). A flow rate of 0.4 mL/min was maintained during experiments requiring flow. If plug flow is assumed, this flow rate corresponded to a lumenal velocity of 0.2 mm/ms, translating to clearance of lumenal spins within TE/2 when TE = 10 ms and TH = 1 mm. Experiments with aqueous gadodiamide solution allowed sufficient equilibration time to ensure homogeneous distribution of gadodiamide (1 mM) throughout the extra-lumenal space.

Four single-slice images (transverse to the fiber's long axis) were acquired to monitor longitudinal relaxation, with TI values 0.002, 0.080, 2.500, and 8.000 s for 0 mM gadodiamide experiments and 0.002, 0.025, 0.080, 0.250 s for 1 mM gadodiamide experiments. To ensure images at each TI had approximately the same SNR, variable numbers of transients (NT) were averaged for each image, corresponding, respectively, to the different TI values: NT = 8, 16, 32, and 8. To assure that no steady-state transverse magnetization was present during the MFIR experiment, the shortest value of Δ = TR-TI was set equal to three times the transverse relaxation time constant (T_2) of the bulk (non-flowing) solution: TR = 13.5 s for 0 mM gadodiamide experiments and 0.8 s for 1 mM gadodiamide experiments [8]. (Note: T_2 was measured independently for 0 mM and 1 mM gadodiamide solutions *via* spectroscopic methods with a standard CPMG sequence.) All images were acquired with the following parameters: TH = 1 mm; TE = 10 ms; in-plane field of view, 5.12 x 1.28 mm^2; in-plane voxel dimensions, 20 x 20 μm^2.

Modeling of the data was carried out using signal intensities from phased (absorption mode) images [13,14]. Parameters A, B, and R_1 (Eq. [1]) were estimated from the phased images by non-linear least-squares analysis in Matlab. The image acquired at the longest TI was used for thresholding prior to modeling the relaxation data. R_1 values were only estimated for those voxels in which the signal intensity was greater than five times the standard deviation of the noise.

To identify regions corresponding to the fiber wall, proton-density weighted, gradient-echo images of the semi-permeable fiber phantom were acquired without flow (TR = 500 ms; TE

= 9.7 ms; NT = 256; and flip angle, α = 20°). These images were collected with the same field of view, slice thickness, and in-plane voxel dimensions as the images acquired for R_1 analysis.

A region of interest (ROI) consisting of voxels with different R_1 values would be expected to exhibit non-mono-exponential relaxation behavior. To examine this phenomenon, an ROI covering one sixteenth of the entire image (0.64 x 0.64 mm^2) was selected with the fiber at its center; lumenal voxels were discarded (976 voxels selected after thresholding). For each extra-lumenal voxel within the ROI, mono-exponential relaxation recovery curves (Eq. [1]) were derived based on the measured voxel intensities at the four TI values. These simulated relaxation recovery data sets, one for each voxel within the ROI, were averaged to derive a single relaxation recovery data set for the ROI as a whole, sampled at ten logarithmically-spaced TI values ranging from 0.017 to 15 s. Bayesian analysis was then applied to this derived, single ROI relaxation data set to compare the probabilities of mono-, bi-, and tri-exponential models [11].

4.5. Results

4.5.1. Slice Thickness Experiments

As shown in Fig. 1, the MFIR relaxation time course observed for a 1-mm thick slice was well-modeled as mono-exponential, yielding an estimated T_1 essentially equal to that estimated for the bulk sample, 2.8 s *vs.* 2.7 s, respectively. However, deviation from mono-exponential relaxation became increasingly apparent as slice thickness decreased. This can be illustrated using standard deviations of the residuals from these fits as a goodness-of-fit metric (Table 1). Further, Bayesian analysis was used to determine the probabilities of mono-, bi-, and tri-exponential models for each data set. A mono-exponential model was the most probable for data obtained at slice thicknesses of 1.00 and 0.500 mm, and a bi-exponential model was most probable for data obtained at slice thicknesses of 0.250 and 0.125 mm (Table 1). This bi-exponentiality is clearly illustrated in Fig. 2 (TH = 0.125 mm). Apparent longitudinal relaxation time constants, computed from mono-exponential and bi-exponential fits to the MFIR data obtained from slices with different thicknesses, are shown in Table 2.

Within a thin slice, the observed relaxation time course was non-mono-exponential. While such time-course data are well-modeled as bi-exponential (Fig. 2, Tables 1 and 2), neither of the bi-exponential decay time constants corresponds to the "true" longitudinal relaxation time constant. For example, bi-exponential modeling of MFIR data from a 0.125-mm thick slice yielded time-constant estimates of 2.2 ± 0.2 s and 0.17 ± 0.02 s with component fractional amplitudes of 0.68 and 0.32, respectively. Both time-constant estimates are substantially different from the bulk sample T_1, 2.7 s.

4.5.2. Fiber Phantom Experiments

Non-permeable Fiber:

For the non-permeable fiber phantom, water ^1H T_1 maps of the region surrounding the fiber (extra-fiber space) in the presence or absence of lumenal gadodiamide solution (0 and 1 mM) were homogeneous, with a mean relaxation time constant that agreed with spectroscopic (non-imaging) measurements (~3 s and ~0.2 s, respectively). In the presence of lumenal flow, the lumenal water spin-echo signal intensity decreased to the noise level, independent of lumenal gadodiamide concentration (0 and 1 mM).

Semi-permeable Fiber / Absence of Flow:

For the semi-permeable fiber phantom in the absence of flow, water ^1H T_1 maps of the region surrounding the fiber lumen (extra-lumenal space, which includes the fiber wall and the extra-fiber region) in the absence or presence of gadodiamide solution (0 and 1 mM) were homogeneous. As expected, T_1 was markedly shortened in the presence of 1-mM gadodiamide solution (~0.2 s). Proton-density weighted images and the individual images acquired for T_1-mapping clearly defined the region of the fiber wall (e.g., Fig. 3, panel C).

Semi-permeable Fiber / Presence of Flow / Absence of Gadodiamide:

For the semi-permeable fiber phantom in the presence of flow but without gadodiamide, apparent T_1 values varied as a function of voxel distance from the lumen boundary. Figure 3 shows a T_1 map, as well as a gradient-echo image identifying fiber-wall position. Compared to T_1 measured in the absence of flow, the presence of lumenal flow results in shorter T_1 values in

voxels near the fiber, an effect most pronounced within the fiber wall. Moving radially away from the fiber wall, voxel T_1 values lengthen, returning to 95% of that observed in the absence of flow at a distance of 120 μm from the outer edge of the fiber wall. The lengthening of T_1 showed a mono-exponential dependence on radial distance from the fiber wall. The distance-rate constant governing this spatial change in T_1 (modeled from the combined data shown in Fig. 3, Panel B; solid line) was 0.018 ± 0.003 μm^{-1} (or equivalently, 0.36 ± 0.05 $voxel^{-1}$).

As described in the Methods Section, an ROI covering one sixteenth of the entire image (0.64 x 0.64 mm^2; 976 voxels after thresholding to remove lumenal voxels) was selected, with the fiber at its center, and the relaxation time course for this entire ROI was derived from knowledge of the individual voxel T_1 values, Fig. 4. The derived ROI relaxation time-course data were preferentially modeled as bi-exponential. Bayesian model selection probabilities (P), expressed as natural log P, were -7.78, -0.232, -1.63, and -4.95 for mono-, bi-, tri- and quad-exponential models, corresponding to probabilities of ~ 0, 79, 20, and 1% respectively.

Semi-permeable Fiber / Presence of Flow and Gadodiamide:

For the semi-permeable fiber phantom in the presence of lumenal flow and gadodiamide (1 mM), variation in voxel T_1 with distance from the fiber was not observed, i.e., T_1 was homogeneous throughout. However, as for the no-flow case, voxel T_1 values were shortened markedly (~0.2 s) compared with the situation in which gadodiamide was absent (~3 s).

4.6. Discussion

Perfusion-sensitive MR methods, such as arterial spin labeling (ASL) and dynamic contrast enhanced (DCE) MRI, are valuable techniques for the detection and staging of illness and disease. However, these techniques only reach their full potential when derived parameter estimates are quantitative (i.e., accurate and precise). When using a signal model employing a single R_1 value (i.e., mono-exponential longitudinal relaxation), both ASL and DCE-MRI implicitly assume the presence of well-mixed compartments. Errors in parameter estimates occur with deviations from mono-exponential relaxation. As described previously by others, such deviations are observed for systems in which the detected signal arises from multiple, internally well-mixed

compartments that are not in fast exchange [15-17]. The examples presented in this paper demonstrate that deviations from mono-exponential longitudinal relaxation can also be detected when the signal arises from a poorly mixed single compartment, due to diffusion of spins from a communicating second compartment (physical or virtual).

The slice-thickness experiment separated a homogeneous phantom (single physical compartment) into two virtual compartments, consisting of spins either initially inside or outside the selected inversion slice. Deviations from mono-exponential longitudinal relaxation were most dramatic when TH = 0.125 mm (Fig. 2). These deviations were not due to errors in slice profile, which were themselves minimized by crusher gradients and shaped RF pulses, as residual errors in slice profile would not result in non-mono-exponential relaxation with MFIR [7]. Rather, non-mono-exponential longitudinal relaxation occurred due to diffusion of thermal-equilibrium-state (non-inverted) spins from the second, virtual compartment into the selected slice and, correspondingly, diffusion of non-thermal-equilibrium-state (inverted) spins out of the slice. Decreasing the slice thickness decreased the number of spins initially in the slice, increasing the population of detected spins originating from outside the slice relative to the population of detected spins originating and remaining inside the slice. With decreasing slice thickness, Bayesian model selection analysis increasingly favors (more probable model) a bi-exponential characterization of the relaxation data, Table 1. Indeed, for the 0.250 and 0.125 mm thick slices, Bayesian model selection overwhelmingly favors the bi-exponential relaxation model compared to mono- or tri-exponential models. Likewise, consistent with the Bayesian model selection, qualitative examination of the residuals, presented in Table 1, illustrates that there is no improvement in bi-exponential *vs.* mono-exponential fitting of the thick-slice relaxation data, but marked improvement for the thin-slice relaxation data.

This example of diffusion-driven longitudinal relaxation is expected to result in a broad distribution of relaxation rates, with spin populations at the very edge of the slice having the greatest diffusion-driven-contribution to relaxation and those spin populations in the middle of the slice having the least diffusion-driven-contribution to relaxation. Although a broad distribution of relaxation rates is expected, the single-slice-relaxation spectroscopy data (sum of all spin

populations) are remarkably well-modeled as “simply” bi-exponential, even for the thinnest slice examined (TH = 0.125 mm). It is worth noting that for the thinnest slice, TH = 0.125, neither exponential time constant, 2.2 ± 0.2 s nor 0.17 ± 0.02 s, corresponds to the true spin-lattice relaxation time constant, 2.7 s. Furthermore, the measured fractional amplitudes and component time constants depend upon slice thickness. As slice thickness increases and diffusion-driven relaxation becomes less significant, the fractional amplitude of the rapidly relaxing component decreases toward zero, the time constant for the slowly relaxing component approaches that of the true spin-lattice relaxation time constant, and relaxation appears mono-exponential (Table 2).

While the manner in which a bi-exponential function can well-approximate signals that are, *a priori*, more complex, is a recurring theme in MR data analysis, diffusion-driven bi-exponential relaxation is not limited to experiments utilizing thin slices, as is demonstrated herein with thick slices and the semi-permeable fiber phantom.

Control experiments with the non-permeable fiber phantom in the presence and absence of flow and the semi-permeable fiber phantom in the absence of flow were well-characterized by spatially homogeneous, mono-exponential relaxation maps of the extra-fiber space (more precisely, in the case of the semi-permeable fiber phantom, extra-lumenal space). Further, imaging-derived voxel T_1 values agreed with T_1 values obtained by spectroscopic methods. Likewise, the semi-permeable fiber phantom in the presence of flow and 1 mM gadodiamide was well-characterized by a spatially homogeneous, mono-exponential, relaxation map of the extra-lumenal space with voxel T_1 values markedly shortened (~0.2 s) from values obtained in the absence of gadodiamide (~3 s). Thus, (i) in the absence of flow or (ii) in the presence of flow but the absence of diffusion-driven magnetization exchange or (iii) when *de novo* relaxation is sufficiently rapid relative to exchange between compartments (*vide infra*), irrespective of the presence of flow or diffusion-driven magnetization exchange, extra-fiber relaxation is spatially uniform and mono-exponential in nature.

The situation is quite different for the case of the semi-permeable fiber phantom in the presence of flow, but the absence of gadodiamide. Here, spatially-inhomogeneous relaxation is observed for the extra-lumenal space, with T_1 values dependent on the distance from the lumenal

boundary (see Fig. 3 panel B, modeled curve). Recall that no signal is observed for spins remaining within the lumen because of time-of-flight, spin-echo signal suppression. Variations in T_1 are, therefore, due to diffusion of thermal-equilibrium-state spin populations from the lumenal compartment to the extra-lumenal compartment and concomitant diffusion of partially saturated spin populations from the extra-lumenal compartment to the lumenal compartment. T_1 shortening is most pronounced in the fiber wall and dies away with increasing radial distance from the lumen boundary. This effect is independent of slice thickness.

The summed signal from an ROI with the fiber at its center (see Materials and Methods) will include voxels having different T_1 values and, thus, will be characterized, *a priori*, by multi-exponential relaxation behavior. Nevertheless, the derived ROI data are seen to be fit preferentially to a bi-exponential model. It is worth noting that neither resulting exponential time constant, 2.5 s nor 0.82 s, corresponds to the true spin-lattice relaxation time constant, 2.7 s. Likewise, the fractional amplitudes and component time constants will vary with the size and position of the ROI relative to the fiber location.

Returning briefly to the case of the semi-permeable fiber in the presence of flow and gadodiamide, recall that, for parallel kinetic processes, rate constants (not time constants) are additive. The presence of 1 mM gadodiamide dominates water relaxation to the extent that the additional relaxation pathway provided by diffusion-driven exchange makes only a minor, essentially undetectable, contribution. For example, consider the innermost voxels associate with the fiber wall, where diffusion-driven relaxation contribution is maximal (Fig. 3.). In the absence of gadodiamide but in the presence of flow, the longitudinal relaxation rate constant increased from 0.38 s^{-1} to 1.88 s^{-1}, an additive diffusion-driven contribution of 1.50 s^{-1}. In the presence of 1 mM gadodiamide and flow, this additive diffusion-driven relaxation contribution is predicted to increase the rate constant from 4.3 s^{-1} to 5.8 s^{-1}, a decrease to the time constant of 0.06 s. However, for the semi-permeable fiber in the absence of flow but in the presence of gadodiamide, the average T_1 in the extra-lumenal space was 0.23 ± 0.06 s. Thus, in the presence of 1 mM gadodiamide, the expected maximal relaxation contribution from diffusion in the presence of flow falls within the error of the measurement in the absence of flow (i.e., is undetectable).

4.7. Conclusions

As scanner technology advances, MR experiments performed with phantoms allow for the testing and modeling of biophysical phenomena with unprecedented accuracy and precision. The two “simple” phantoms and associated experiments described herein are part of such an effort, relating to dynamic contrast enhancement and flow/perfusion measurement protocols. However, even such simple phantoms and relatively uncomplicated MR protocols yield multi-exponential relaxation data. Further, the data -- while *a priori* clearly multi-exponential -- are well approximated as bi-exponential, a consistent theme with MR relaxation data of realistic SNR.

These experiments specifically highlight the effects of diffusion-driven exchange on careful relaxation measurements and serve as another cautionary reminder about the risks of over-interpretation of bi-exponential data [18,19]. When bi-exponential signals are observed in MR, it is tempting to ascribe physical/physiologic significance -- such as unique compartments -- to the component fractional amplitudes and decay-rate constants. As demonstrated in both the thin-slice and single-fiber experiments, this need not be the case.

4.8. Acknowledgements

Support from NIH grants T90 DA22871, R01 EB002083, P30 CA91842, S10 RR022658, and S10 RR020916 is gratefully acknowledged.

4.9. References

[1] M.D. Does, C. Beaulieu, P.S. Allen, and R.E. Snyder, Multi-component T1 relaxation and magnetisation transfer in peripheral nerve. Magn. Reson. Imaging 16 (1998) 1033-1041.

[2] M.D. Does, and J.C. Gore, Compartmental study of T1 and T2 in rat brain and trigeminal nerve in vivo. Magn. Reson. Med. 47 (2002) 274-283.

[3] W.B. Hyslop, and P.C. Lauterbur, Effects of restricted diffusion on microscopic NMR imaging. J. Magn. Reson. 94 (1991) 501-510.

[4] H.D. Morris, W.B. Hyslop, and P.C. Lauterbur, Diffusion-Enhanced NMR Microscopy, Proc. Soc. Magn. Reson., San Francisco, 1994, pp. 376.

[5] A.M. Prantner, G.L. Bretthorst, J.J. Neil, J.R. Garbow, and J.J.H. Ackerman, Magnetization transfer induced biexponential longitudinal relaxation. Magn. Reson. Med. 60 (2008) 555-563.

[6] R.K. Gupta, J.A. ferretti, E.D. Becker, and G.H. Weiss, A modified fast inversion-recovery technique for spin-lattice relaxation measurements. J. Magn. Reson. 38 (1980) 447-452.

[7] J.L. Evelhoch, and J.J.H. Ackerman, NMR T1 measurements in inhomogeneous B1 with surface coils. J. Magn. Reson. 53 (1983) 52-64.

[8] P.B. Kingsley, Methods of measuring spin-lattice (T1) relaxation times: An annotated bibliography. Concepts Magn. Reson. 11 (1999) 243-276.

[9] M.A. Bernstein, K.F. King, and X.J. Zhou, Handbook of MRI pulse sequences, Academic Press, Amsterdam; Boston, 2004.

[10] M. Shinnar, L. Bolinger, and J.S. Leigh, The synthesis of soft pulses with a specified frequency response. Magn. Reson. Med. 12 (1989) 88-92.

[11] G.L. Bretthorst, W.C. Hutton, J.R. Garbow, and J.J.H. Ackerman, Exponential parameter estimation (in NMR) using Bayesian probability theory. Concepts Magn. Reson. A (Magn. Reson. Eng.) 27A (2005) 55-63.

[12] G.L. Bretthorst, W.C. Hutton, J.R. Garbow, and J.J.H. Ackerman, Exponential model selection (in NMR) using Bayesian probability theory. Concepts Magn. Reson. A (Magn. Reson. Eng.) 27A (2005) 64-72.

[13] G. Larry Bretthorst, Automatic phasing of MR images. Part I: Linearly varying phase. J. Magn. Reson. 191 (2008) 184-192.

[14] G. Larry Bretthorst, Automatic phasing of MR images. Part II: Voxel-wise phase estimation. J. Magn. Reson. 191 (2008) 193-201.

[15] K.M. Donahue, R.M. Weisskoff, and D. Burstein, Water diffusion and exchange as they influence contrast enhancement. J. Magn. Reson. Imaging 7 (1997) 102-10.

[16] T.E. Yankeelov, W.D. Rooney, X. Li, and C.S. Springer, Jr., Variation of the relaxographic "shutter-speed" for transcytolemmal water exchange affects the CR bolus-tracking curve shape. Magn. Reson. Med. 50 (2003) 1151-69.

[17] X. Li, W.D. Rooney, and C.S. Springer, Jr., A unified magnetic resonance imaging pharmacokinetic theory: intravascular and extracellular contrast reagents. Magn. Reson. Med. 54 (2005) 1351-9.

[18] D.A. Yablonskiy, G.L. Bretthorst, and J.J. Ackerman, Statistical model for diffusion attenuated MR signal. Magn. Reson. Med. 50 (2003) 664-9.

[19] M.L. Milne, and M.S. Conradi, Multi-exponential signal decay from diffusion in a single compartment. J. Magn. Reson. 197 (2009) 87-90.

4.10. Figures and captions

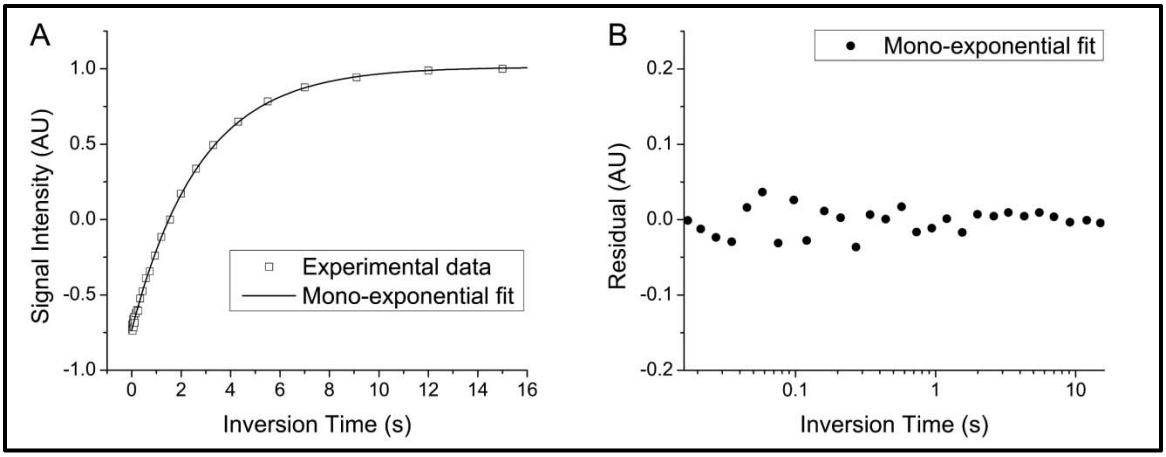

Figure 4-1. Slice selection experiment: thick slice (TH = 1.00 mm). A: Signal intensity *vs.* inversion time (TI); squares are experimental data values and the solid line corresponds to a mono-exponential model: $SI(TI) = 1.012 - 1.744 \cdot e^{-TI/2.76}$. B: Residuals from panel A *vs*. inversion time. (Note: inversion time axis is logarithmic.)

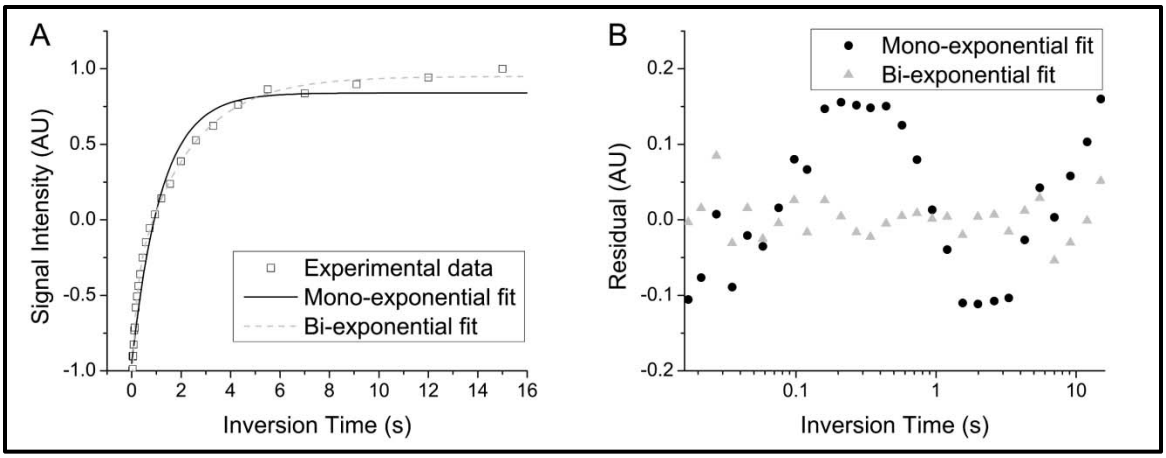

Figure 4-2. Slice selection experiment: thin slice (TH = 0.125 mm). A: Signal intensity *vs.* inversion time; squares are data values, the solid line corresponds to a mono-exponential model: $SI(TI) = 0.84 - 1.79 \cdot e^{-TI/1.2}$ and the dashed line corresponds to a bi-exponential model: $SI(TI) = 0.95 - 1.40 \cdot e^{-TI/2.2} - 0.65 \cdot e^{-TI/0.17}$. B: Residuals from panel A *vs.* inversion time; circles denote the mono-exponential model and triangles the bi-exponential model. (Note: inversion time axis is logarithmic.)

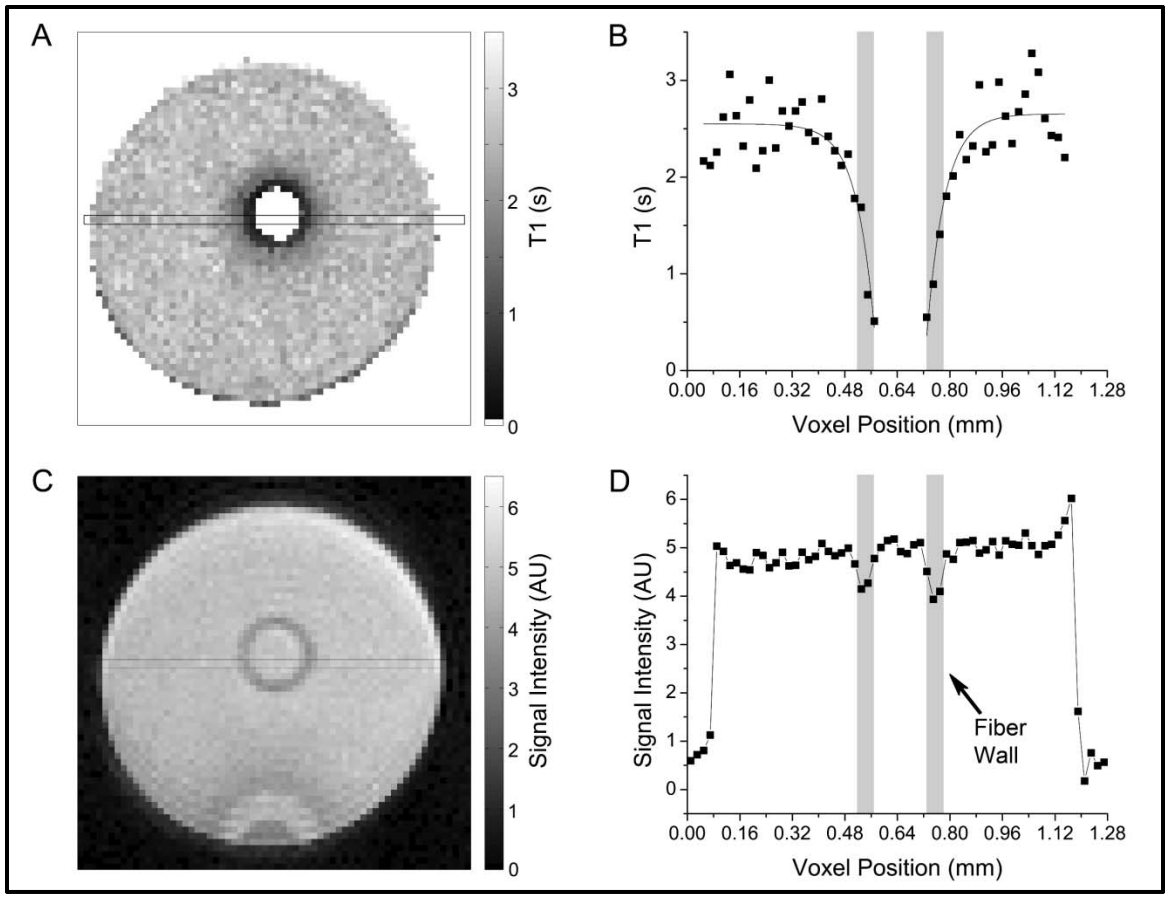

Figure 4-3. Semi-permeable fiber (absence of gadodiamide). A: Longitudinal relaxation time-constant (units expressed as s) map of the phantom with lumenal flow. B: Longitudinal relaxation time constant *vs.* voxel position from a single line of the image as indicated in panel A where the data selected are within the outlined narrow-rectangle. A mono-exponential fit (solid line in panel B; left side, $2.54 - 2.1 \cdot e^{-0.018 \cdot x}$; right side, $2.64 - 2.3 \cdot e^{-0.018 \cdot x}$) and gray shading rectangles denoting the location of the fiber walls are also shown. C: Proton-density-weighted gradient echo image of the same phantom, without lumenal flow, included for visualization of the fiber wall. (Artifact at bottom of image is from susceptibility effect of an out-of-slice air bubble attached to wall of capillary tube.) D: Signal intensity *vs.* voxel position from a single line of the image shown in panel C where the selected data are within the outlined narrow rectangle. Gray shading rectangles denote the location of the fiber wall.

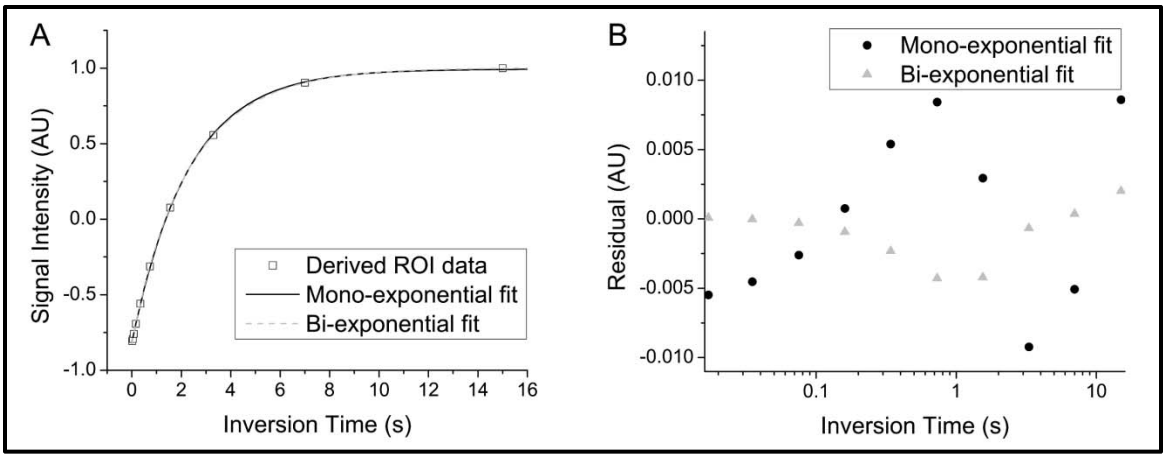

Figure 4-4. Semi-permeable fiber (presence of flow, absence of gadodiamide) derived ROI data. A: derived ROI signal-intensity *vs.* inversion time; squares are derived data values, the solid line corresponds to a mono-exponential model: $SI(TI) = 0.998 - 1.811 \cdot e^{-TI/2.34}$, and the dashed line corresponds to a bi-exponential model: $SI(TI) = 1.0034 - 1.67 \cdot e^{-TI/2.487} - 0.15 \cdot e^{-TI/0.97}$. B: Residuals from panel A *vs.* inversion time; circles denote the mono-exponential model and triangles the bi-exponential model. (Note: inversion time axis is logarithmic.)

4.11. Tables

Table 1. Goodness-of-fit, expressed as the residual standard deviation, assuming either mono-exponential or bi-exponential fits to the data, for different slice thicknesses. A decrease in the residual standard deviation corresponds to a better fit. A decrease in the ratio of the values corresponds to the mono-exponential being preferred (more probable model).

$\sigma_{residual}$	**TH = 1.00 mm**	**TH = 0.500 mm**	**TH = 0.250 mm**	**TH = 0.125 mm**
Mono-exp	0.0196 ± 0.0005	0.0169 ± 0.0004	0.047 ± 0.001	0.110 ± 0.003
Bi-exp	0.0197 ± 0.0005	0.0156 ± 0.0006	0.029 ± 0.001	0.033 ± 0.001
Ratio[a]	1.0	1.1	1.6	3.3
Probability$_{bi}$[b,c]	-3.8×10^{-3}	-7.1×10^{-3}	-8.5	-8.5
Probability$_{mono}$[b,c]	-8.5	-8.5	-2.8×10^{-2}	9.2×10^{-3}
Probability$_{tri}$[b,c]	-8.5	-8.5	-3.7	-4.9

[a]The ratio of the standard deviation of the residual with a mono-exponential fit to the standard deviation of the residual with a bi-exponential fit.

[b]Probabilities are those estimated by Bayesian analysis.

[c]Expressed as log base e of the probability.

Table 2. Apparent longitudinal relaxation time constants, assuming either mono-exponential or bi-exponential fits to the data, for different slice thicknesses. These values are to be compared with the "true" T_1 value of 2.708 ± 0.002 s.

$T_{1,app}$	**TH = 1.00 mm**	**TH = 0.500 mm**	**TH = 0.250 mm**	**TH = 0.125 mm**
Mono-exp	2.76 ± 0.05 s	2.56 ± 0.04 s	2.00 ± 0.09 s	1.2 ± 0.1 s
Bi-exp	3 ± 1 s	2.7 ± 0.5 s	2.9 ± 0.4 s	2.2 ± 0.1 s
	1.1 ± 0.8 s	0.5 ± 0.5 s	0.6 ± 0.1 s	0.17 ± 0.02 s

CHAPTER 5. MULTI-FIBER PHANTOM

5.1. Abstract

DCE-MRI was carried out in a multi-fiber tissue phantom and the results compared to gold standard measurements to assess the precision of estimated parameters. Both experiments are described as well as control experiments that characterized the shape of the contrast agent input function. The DCE-estimated rate constant describing contrast agent extravasation was found to be marginally dependent upon flow rate. General agreement of estimated parameters, however, was found comparing DCE-MRI with gold standard measurements.

5.2. Materials and methods

5.2.1. Gold standard measurements

The permeability coefficient of the fiber with respect to the Gd-based contrast agent Gd-BOPTA was measured in a single fiber. The experimental setup is shown schematically in figure 5-1. Briefly, a single fiber was suspended in a vial such that 1) lumenal flow was permitted in the fiber, and 2) exchange of water and contrast agent molecules could occur between the fiber lumen compartment and the vial compartment *via* diffusion through the fiber wall.

For the experiment, the vial was filled with a known volume of water. Then, 1 mM Gd-BOPTA (gadobenate dimeglumine, MultiHance, Bracco Diagnostics Inc., Princeton, NJ, USA) was continuously introduced into the system *via* lumenal flow at a flow rate of 0.2 mL/min. To monitor contrast agent concentrations in the two compartments, 100 μL aliquots were sampled during the time course from both the exit port of the fiber (the effluent) and the internal compartment of the vial. The solution in the vial was continuously stirred with a magnetic spin bar throughout the experiment.

To assure that exchange between the compartments only occurred due to diffusion, the system was sealed from the atmosphere. This fixes the pressure in both compartments at the same value. Aliquots from the vial were sampled through a septa with a syringe. Also, when the

aliquot was taken from the vial, the total volume of the vial was physically decreased by the volume of the aliquot (*via* partial insertion of a threaded screw; see figure 5-1).

Contrast agent concentrations in the sampled aliquots were determined by measuring the longitudinal rate constant R_1 at a temperature of 4° C and at a field strength of 0.55 T with an Oxford Instruments MARAN Ultra NMR spectrometer (Oxford Instruments, Oxfordshire, UK). A calibration curve was prepared with the following contrast agent concentrations as standards: 0, 0.2, 0.4, 0.6, 0.8, and 1 mM Gd-BOPTA as shown in figure 5-2 (see equation 2-7). Triplicate samples were prepared at each concentration. Inversion recovery experiments were used to measure R_1. To balance signal-to-noise and scan time, the predelay (PD) on the spectrometer was always set to 1.4 times the reported T_1 (where $T_1 = 1/R_1$). For each T_1 measurement, 20 data points were acquired with inversion times spaced exponentially from $0.1 \cdot T_1$ to $5 \cdot T_1$. Additional acquisition parameters were as follows: dwell time = 10 μs, number of transients (NT) = 4, spectral width (SW) = 100 KHz, number of complex points (NP) = 1024 points, steady state scans (SS) = 4. A representative signal response from one of these inversion recovery experiments is shown in figure 5-3.

The concentration of contrast agent in the vial vs. time was plotted. These data were modeled as a mono-exponential assuming an asymptotic ($t = \infty$) value equal to the average lumenal contrast agent concentration along the length of the fiber within the vial. This walue was approximated as the mean of the measured value in the effluent and the known value of the stock lumenal solution (1 mM) feeding the fiber (entry value). The total surface area of the suspended fiber within the vial was calculated using fiber dimensions obtained from the manufacturer and measured vial dimensions. The fiber permeability coefficient of Gd-BOPTA was derived from the estimated mono-exponential rate constant according to equation 5-1 (see Appendix A):

$$k_{ep} = \frac{S \cdot P}{V_e}. \qquad (5\text{-}1)$$

S equals surface area, P equals permeability coefficient, and V_e equals the volume of the external compartment.

5.2.2. DCE-MRI of the multi-fiber phantom

DCE-MRI was performed in accordance with the technique described in chapter 4. The contrast agent input function for the experiment was a step function from 0 to 0.1 mM Gd-BOPTA. Thus, the following equation was used for calculation of rate constant k_{ep} (see chapter 2):

$$C_e(t) = \begin{cases} 0, & \text{if } t < t_a \\ C_{p,\max} \cdot \left(1 - e^{-k_{ep} \cdot (t - t_a)}\right), & \text{if } t \geq t_a \end{cases}. \quad (5\text{-}2)$$

A slice selective spin-echo pulse sequence was used to collect 3,600 temporally resolved spectra during the experiment (at 4.7 T). All slice selective spectroscopy as well as all imaging experiments were performed with an Oxford Instruments (Oxford Instruments, Oxfordshire, UK) magnet with a 40 cm clear bore equipped with 21 cm gradient-coil (max gradient amplitude = 28 G/cm and rise time = 650 μs). The scanner was operated with an Agilent/Varian DirectDrive™ console (Agilent Technologies, Santa Clara, CA, USA).

The MRI acquisition parameters for the experiment were: repetition time (TR) = 50 ms, echo time (TE) = 10 ms, slice thickness (TH) = 1 mm, NT = 1, SS = 200, SW = 8.012 MHz, NP = 128, and acquisition time (AT) = 15.97 ms. The effective NT was increased to 4 post acquisition by a simple averaging of signal intensities. The leading edge of the input function occurred roughly 1 minute after commencement of the experiment. The experiment was repeated three times at lumenal flow rates: 56 mL/min, 62 mL/min, and 68 mL/min with three different phantoms each (i.e., nine experiments in total).

Data were analyzed from these experiments as follows. Each spectrum was individually phased and the signal intensity estimated by taking the numerical integral. Temporally resolved signal intensities were converted to contrast agent concentrations employing equations 2-6 and 2-7 (*via* a look-up table). As is illustrated in figure 5-4, the relaxivity used for this conversion was obtained from spectroscopic measurements of homogeneous standards, whereas, the $R_{1,0}$ was determined in the presence of lumenal flow immediately prior to the DCE experiment and under matched experimental conditions to the DCE experiment (i.e., matched TE, TH, flow rate, etc.). All R_1 measurements were achieved with an inversion recovery approach (see chapter 3).

The contrast agent concentration time course data were modeled with equation 5-2. Bayesian analysis methods developed in our lab were used for these parameter estimations (software available for free download; see Bayesian Analysis of Common NMR Problems; http://bayesiananalysis.wustl.edu/index.html) [2]. Permeability coefficients were then derived according to equation 5-1. Data acquired in the first few seconds after "injection" of contrast agent were often affected by deviations in the input function from its assumed shape (*vide infra*). Accordingly, the "outlier" functionality available in the Bayesian software was implemented. This option within the software looks for outliers from the mathematical model on a point by point basis.

5.2.3. Input function validation

Equations 5-2 assumes a stepped contrast agent input function. Validation experiments were carried out to investigate this assumption for the DCE experiment. A high molecular weight contrast agent, Gd-DTPA-BSA (MW ≈ 68 kDa), was synthesized as described in the literature [3]. Four transaxial spin-echo images were acquired from a multi-fiber phantom without lumenal flow. The first two images were acquired sequentially; they were collected immediately after 30 minutes of lumenal CA perfusion and 1 additional minute of water perfusion, respectively. The second two images were also acquired sequentially; they were collected immediately following 3 days of lumenal CA perfusion and 1 additional minute of water perfusion, respectively. The relevant acquisition parameters for all images were: TR = 500 ms, TE = 13.5 ms, TH = 1 mm, NT = 16, in-plane field of view = 6.4 mm × 3.2 mm, and in-plane voxel dimensions = 25 μm × 25 μm. In addition, a single experiment, identical in form to the DCE experiment described above, was carried out with Gd-DTPA-BSA as the contrast agent.

5.3. Results

5.3.1. Gold standard measurements

The inner and outer diameter of each fiber was reported by Fresenius to be 200 μm and 280 μm, respectively. The diameter of a representative multi-fiber phantom was 2.6 mm (see chapter 3). As the phantom contained 75 fibers, the extralumenal volume was 3.2×10^{-3} cm^3 (for a 1 mm slice) and the fractional volumes were 0.43:0.57 (lumenal:extralumenal compartments). The surface area of the 75 fibers, for a 1 mm slice, was 0.47 cm^2.

The volume in the experimental apparatus shown in figure 5-1 was 16.1 cm^3 (a density of 1 mg/mL was assumed for water). The length of the suspended fiber within the apparatus was measured to be 2.42 cm resulting in a surface area of 0.152 cm^2.

Figure 5-5 shows the results of this experiment. The average measured contrast agent concentration of fiber effluent was 0.94 mM, thus, the asymptote was set to 0.97 mM. The rate constant for contrast agent extravasation was 0.00025 min^{-1}. As expected, this value was well approximated by taking the slope of the first two measured points (truncated Taylor series expansion): 0.00025 min^{-1}. The permeability coefficient of the fiber with respect to Gd-BOPTA was thus found to be 0.00045 cm s^{-1} (0.00044 cm s^{-1} from the Taylor series approximation).

5.3.2. DCE-MRI of the multi-fiber phantom

A representative concentration vs. time curve can be found in figure 5-6. The modeled results for this data set as well as the residual between data and model are also plotted. The average rate constants and permeability coefficients resulting from all DCE experiments are given in table 5-1. As can be seen in figure 5-6, outliers from the model were identified only within the first couple of seconds following injection. This trend was rigidly consistent throughout all data sets.

5.3.3. Input function validation

Spin-echo images are shown of multi-fiber phantoms after various stages of perfusion with Gd-DTPA-BSA in figure 5-7. In addition, the signal response from a DCE experiment using Gd-DTPA-BSA is shown in figure 5-8. It should be noted that, although a slight increase in signal

intensity is observed after contrast agent administration, this does not correspond to an appreciable increase in concentration (see figure 3-10).

5.4. Discussion

5.4.1. Gold standards

The data from the gold standard experiment were well modeled by a mono-exponential (figure 5-5). Furthermore, the rate constant was well estimated by a first order approximation of a Taylor expansion (initial slope). The concentration of contrast agent measured at the exit port of the single fiber was very close to the concentration of the stock solution, with measurements made throughout the time course randomly scattered about a mean value. Thus, the lumenal flow rate is sufficiently fast enough, relative to the rate of contrast agent extravasation, to assume that exchange kinetics are defined by the “PS-limited” regime [4].

5.4.2. DCE-MRI of the multi-fiber phantom

It should first be noted that the calculated asymptotic concentration was consistently underestimated (see figure 5-6). On average, this value was found to be 0.08 ± 0.02 mM (as compared with a known value of 1 mM). The origin of this incorrect conversion from signal intensity to concentration is unknown at the time of this writing. One potential source of error may be residual transverse magnetization between sequentially acquired data points. Although routinely ignored when using a spin-echo imaging sequence, the abnormally short TR (desired for high T_1-weighting and temporal resolution) may require more careful consideration here. These errors are expected to add random noise and bias to the measured permeability coefficients.

A slight dependence of measured permeability coefficient on lumenal velocity was seen (see table 5-1). While it is possible that flow rates are not sufficiently rapid to completely ensure PS-limited exchange kinetics, the origin of this unexpected result is unknown at this writing. It

may be due non-idealities in data acquisition or modeling (e.g., deviations from the assumption of total suppression of the lumenal signal).

5.4.3. Input function validation

Recall that the analysis of the DCE data using equations 5-2 is only valid if the assumed stepped shape of the contrast agent input function is correct. In the case of strong deviations from this ideal input function, the derived exchange rate constant will be substantially dependent upon the actual shape of the input function. Thus, defining/confirming the actual shape of the input function is of import. The contrast agent Gd-DTPA-BSA was used to interrogate the input function as its high molecular weight, ~68 kDa, prevents it from diffusing through the walls of the fibers which have a molecular weight cutoff ≈ 40 kDa. Both the impermeability of the fibers to Gd-DTPA-BSA and the shape of the input function were validated as follows.

First, consider figure 5-7. If a contrast agent were to pass readily from the lumenal space to the extralumenal space, then one would expect a homogeneously enhanced image after total equilibration. Panel A shows that after a half an hour this equilibration is not reached. If any small amount of contrast agent had permeated the fiber wall in that half an hour, then panel B should reveal it. One would expect that if this were the case, the image in panel B would reveal fiber lumens (corresponding to pure water) less intense then the extralumenal space (corresponding to some small concentration of CA). However, in contrast, a homogenous image is observed. Panels C and D emphasize and repeat these results over a much longer period of time.

Having shown that the fiber is not at all permeable with respect to Gd-DTPA-BSA, the increase in signal intensity observed in figure 5-8 must correspond to another phenomenon. One possible explanation is that this slight signal increase is a manifestation of small deviations from plug flow. In a laminar flow regime the velocity on the outermost rim of the tubing is considerably slower than that toward the center of the tubing. Due to the very small diameter of the fibers, the calculated Reynolds number (Re) is very small (~0.01; $Re = \rho \cdot v \cdot d/\mu = 1 \cdot 0.05 \cdot 0.0002/0.001$ where ρ, v, d, and μ are density (kg/m^3), velocity (m/s), diameter (m), and viscosity (m^2/s), respectively). Thus, deviations from plug flow could be expected.

However, regardless of the mechanism, when coupled with figure 5-7 it is clear that the features in figure 5-8 correspond to changes in lumenal contrast agent concentration. Figure 5-8 reveals that peak concentration in the lumen is achieved after just a few seconds. With the kinetics of contrast agent extravasation being on the order of minutes, e.g., asymptotic values are reached ~1 min post contrast agent initiation, the assumption of a stepped input function is reasonable as long as the initial couple of seconds of time course data are ignored, especially the large deviations from ideal model behavior immediately following switching from contrast agent free media to media with contrast agent (see chapter 3).

5.4.4. Comparison of gold standard techniques with DCE-MRI

Generally good agreement is seen between the DCE-estimated and the gold standard determined permeability coefficients. However, there is some, as yet not fully understood, apparent flow-rate dependence to the permeability coefficients derived by DCE-MRI. DCE-estimated permeability coefficients mores closely approach the gold standard value as flow rate increases. We hypothesize that this high flow rate behavior reflects a closer approach to PS-limited kinetic modeling where negligible flow rate independence is postulated.

5.5. Conclusions

The rate constant governing the extravasation of contrast agent from the lumenal to extra-lumenal compartments was estimated in two different experimental systems. One method mimicked DCE-MRI, while the other was meant to be a “gold standard.” Extravasation occurred due to diffusion (in response to a concentration gradient) through the wall of semi-permeable hollow fibers. From this rate constant the permeability of the fiber wall, with respect to the contrast agent Gd-BOPTA, was calculated and compared. A slight apparent dependence on flow rate was seen in the DCE experiment suggesting the PS-limited regime had not been fully accessed at the flow rates employed. Nonetheless, general agreement (within one to two standard deviations) was seen between the two methods at all flow rates.

Though potential biases were evidenced in the current experiment, this stands as the first quantitative validation of the accuracy of DCE-MRI. In addition, this approach can be modified, in future experiments, to further test the technique. For instance, one could introduce cells into the extralumenal space and probe the correctness of assumptions surrounding fast and slow exchange of extra and intra-cellular water populations (see chapter 2).

5.6. References

[1] J. Anderson, Q. Ye, J. Neil, J. Ackerman and J. Garbow, "Diffusion effects on longitudinal relaxation in poorly mixed compartments," *Journal of Magnetic Resonance,* vol. 211, no. 1, pp. 30-36, 2011.

[2] G. Bretthorst, W. Hutton, J. Garbow and J. Ackerman, "Exponential parameter estimation (in NMR) using Bayesian probability theory," *Concepts in Magnetic Resonance Part A,* vol. 27A, no. 2, pp. 55-63, 2005.

[3] H. Dafni, L. Landsman, B. Schechter, F. Kohen and M. Neeman, "MRI and fluorescence microscopy of the acute vascular response to VEGF165: vasodilation, hyper-permeability and lymphatic uptake, followed by rapid inactivation of the growth factor," *NMR in Biomedicine,* vol. 15, no. 2, pp. 120-131, 2002.

[4] P. Tofts, G. Brix, D. Buckley, J. Evelhoch, E. Henderson, M. Knopp, H. Larsson, T. Lee, N. Mayr, G. Parker, R. Port, J. Taylor and R. Weisskoff, "Estimating Kinetic Parameters from Dynamic Contrast-Enhanced R(1)-Weighted MRI of a Diffusable Tracer: Standardized Quantities and Symbols," *Journal of Magnetic Resonance Imaging,* vol. 10, no. 3, pp. 223-232, 1999.

5.7. Figures and captions

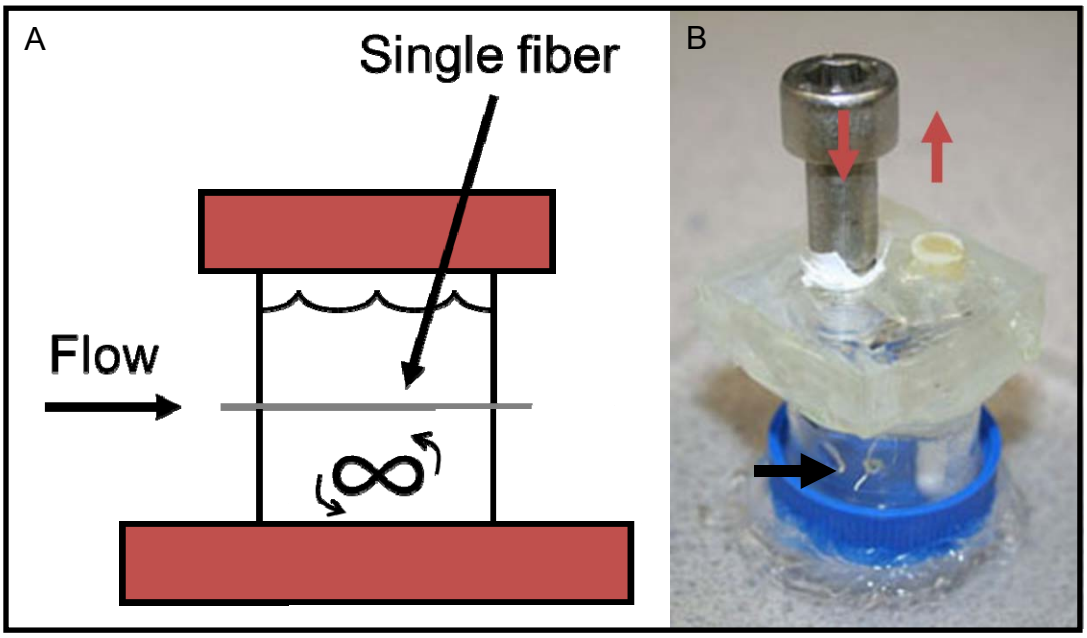

Figure 5-1. Experimental setup for the gold standard experiment. Panel A, schematic showing the suspended fiber, lumenal flow, and internal stirring. Panel B, photograph highlighting the method for aliquot sampling: in order to draw a sample and keep the pressure in the vial constant, the screw is inserted (down red arrow) and the aliquot sampled (up red arrow) simultaneously. The exit port of the semi-permeable hollow fiber is also visible in this panel (black arrow)

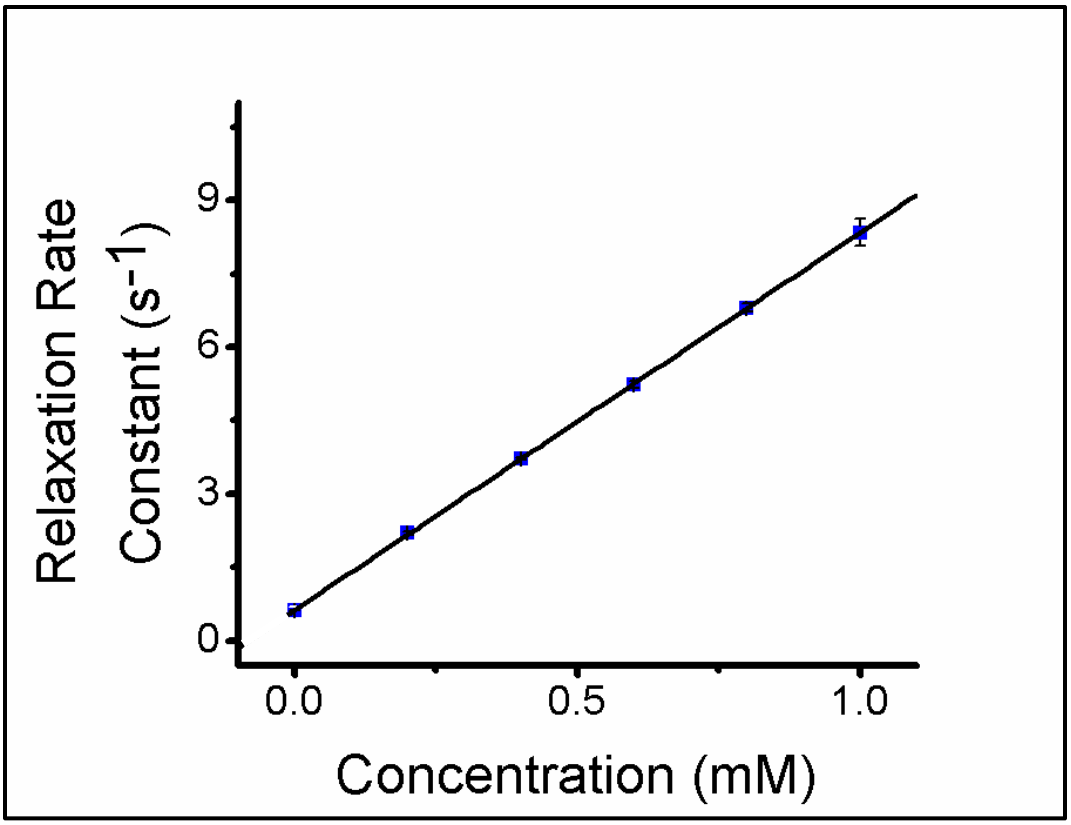

Figure 5-2. Longitudinal relaxation rate calibration curve at 0.55 T. A linear dependence is seen for the longitudinal relaxation rate constant (R_1) measured at six different concentrations of contrast agent.

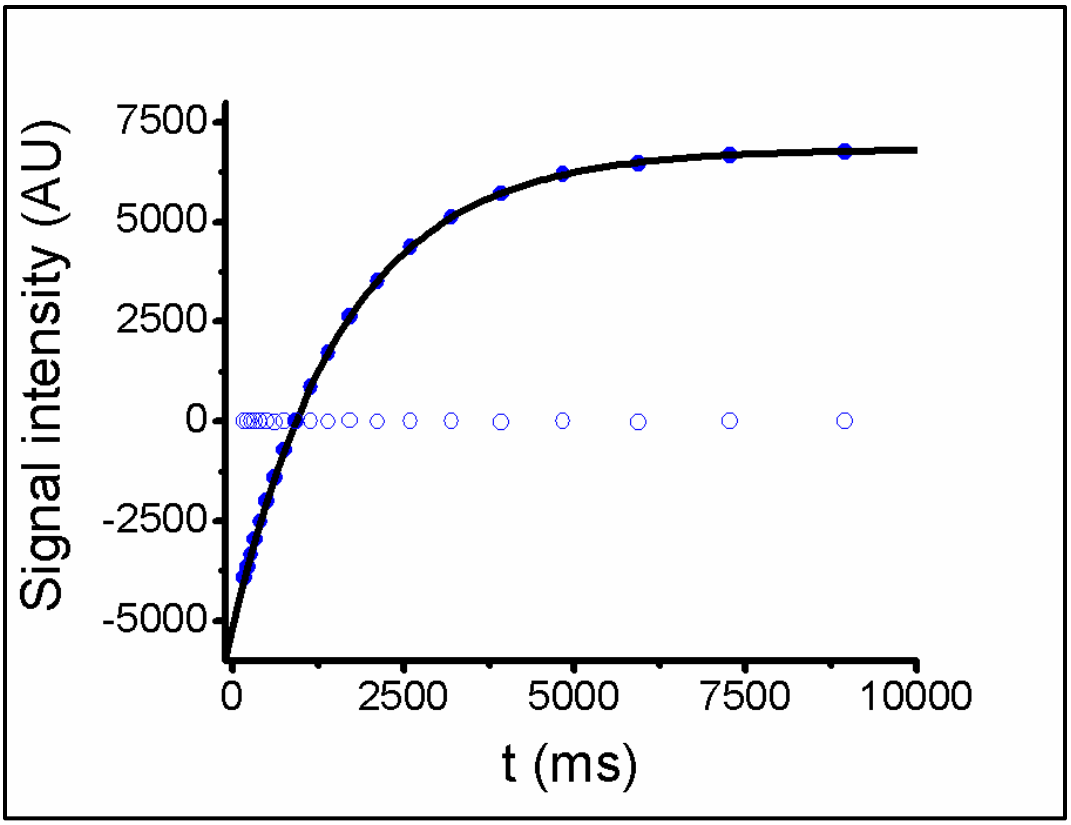

Figure 5-3. Sample inversion recovery at 0.55 T. This measurement corresponds to the rate constants seen in Figure 5-2 (plotted vs. concentration of contrast agent). The modeled inversion recovery equation is -3919 + 6814·exp(-1639·TI), therefore, the rate constant for this sample is 0.6101 s^{-1} (i.e., 1/1.639 s). The inversion recovery data show no apparent deviations from the applied monoexponetial signal model.

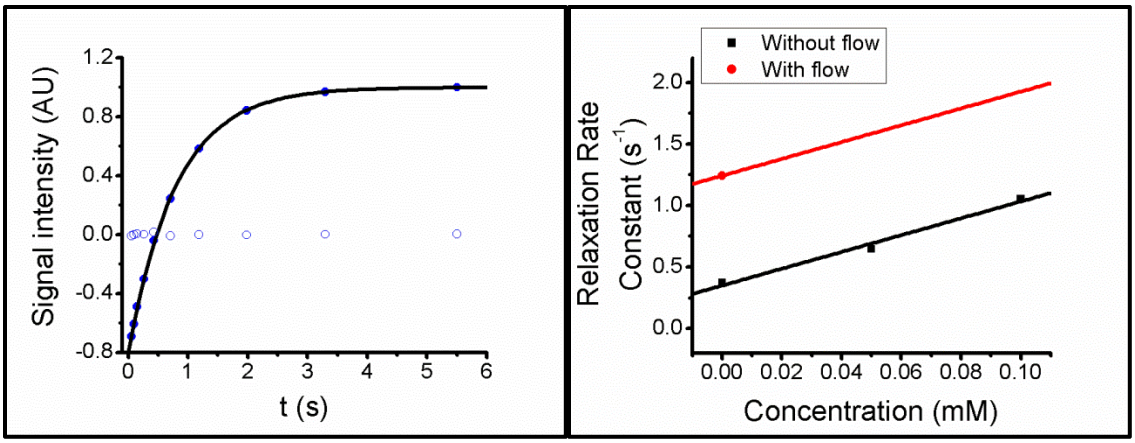

Figure 5-4. Sample inversion recovery (panel A) and calibration curve (panel B) at 4.7 T. Panel A: The inversion recovery data show no apparent deviations from the applied monoexponential signal model. Panel B: The calibration curve with flow (red line) was constructed with the relaxivity (slope) from the curve without flow (black line). Assuming that the slopes of the two calibration curves, with and without flow, are equivalent is justified in chapter 3 where multiple data points were collected for each curve. In practice, this technique allows individual calibration curves to be constructed for each individual DCE-MRI experiment with little difficulty/additional scan time.

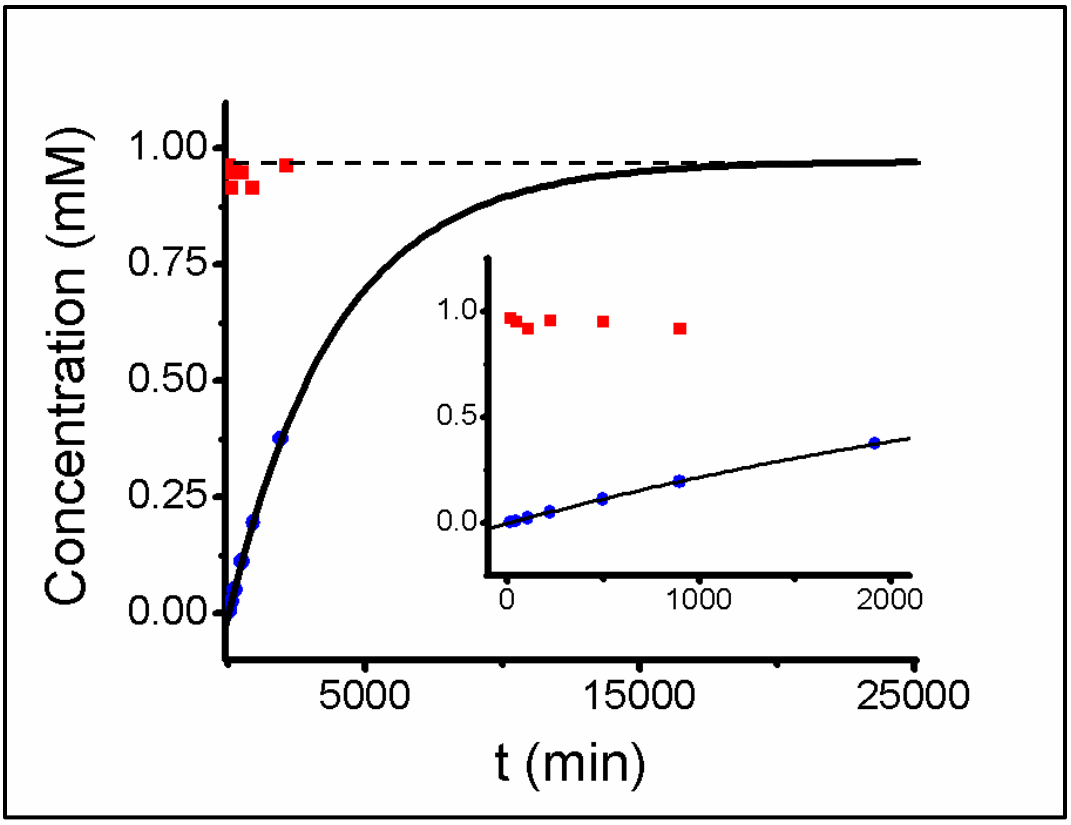

Figure 5-5. Results from the gold standard experiment to measure the fiber permeability coefficient with respect to Gd-BOPTA. Red squares correspond to aliquots sampled from the exit port of the suspended fiber (see figure 5-1). Blue circles correspond to aliquots sampled from the interior of the vial. The solid line corresponds to the modeled fit: 0.97-0.97·exp(-0.00025·t).

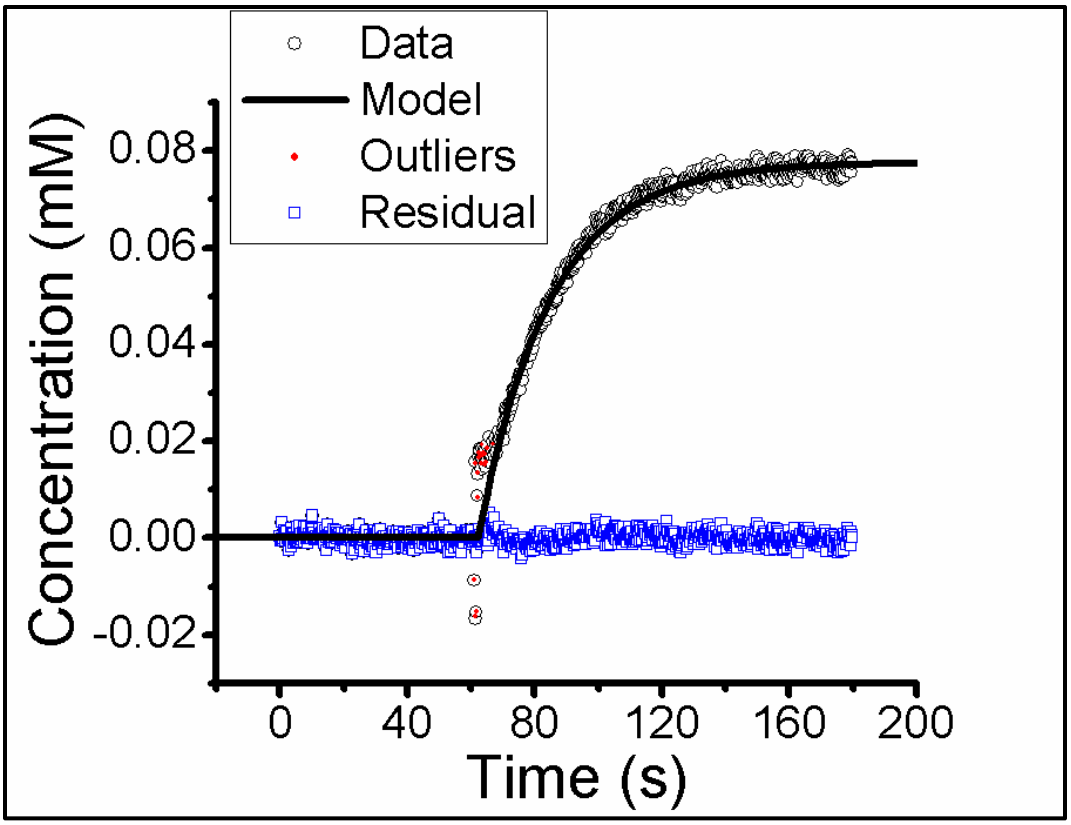

Figure 5-6. Results from a representative DCE experiment with the multi-fiber phantom. The black circles correspond to data points. The black line is the applied mathematical model describing the contrast agent extravasation/kinetics. As noted in the text, deviations from the model occur in the first few data points following the indroduction of contrast agent into the lumenal solution (t~60 s). Therefore, the software used to model the data was configured to reject any outliers from the model. Those data points recognized as outliers are shown in red. The residuals (differences between the data and model) are shown as blue squares. The modeled equation is 0.078-0.078·exp(¯0.044·(t-62)).

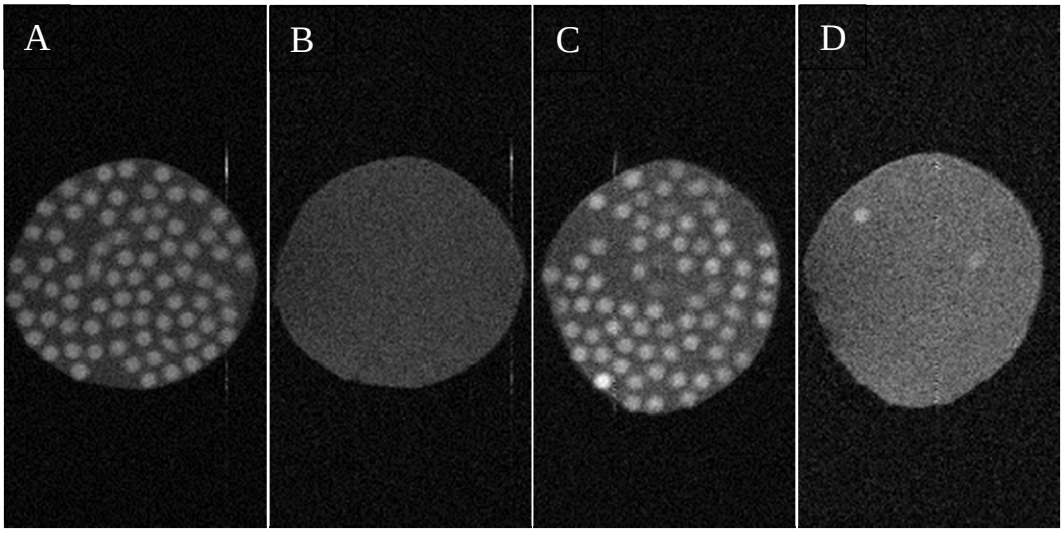

Figure 5-7. Spin-echo images of a multi-fiber phantom immediately after perfusion with Gd-DTPA-BSA (panels A and C) and following subsequent perfusion with water (B and D). All images were acquired without flow. Panel A was acquired immediately after Gd-DTPA-BSA perfusion of the phantom for 30 minutes, and panel B was acquired after one additional minute of water perfusion. Panel C was acquired immediately after Gd-DTPA-BSA perfusion of the phantom for 3 days, and panel D was acquired after one additional minute of water perfusion. Intensity scales are the same for panels A and B and panels C and D.

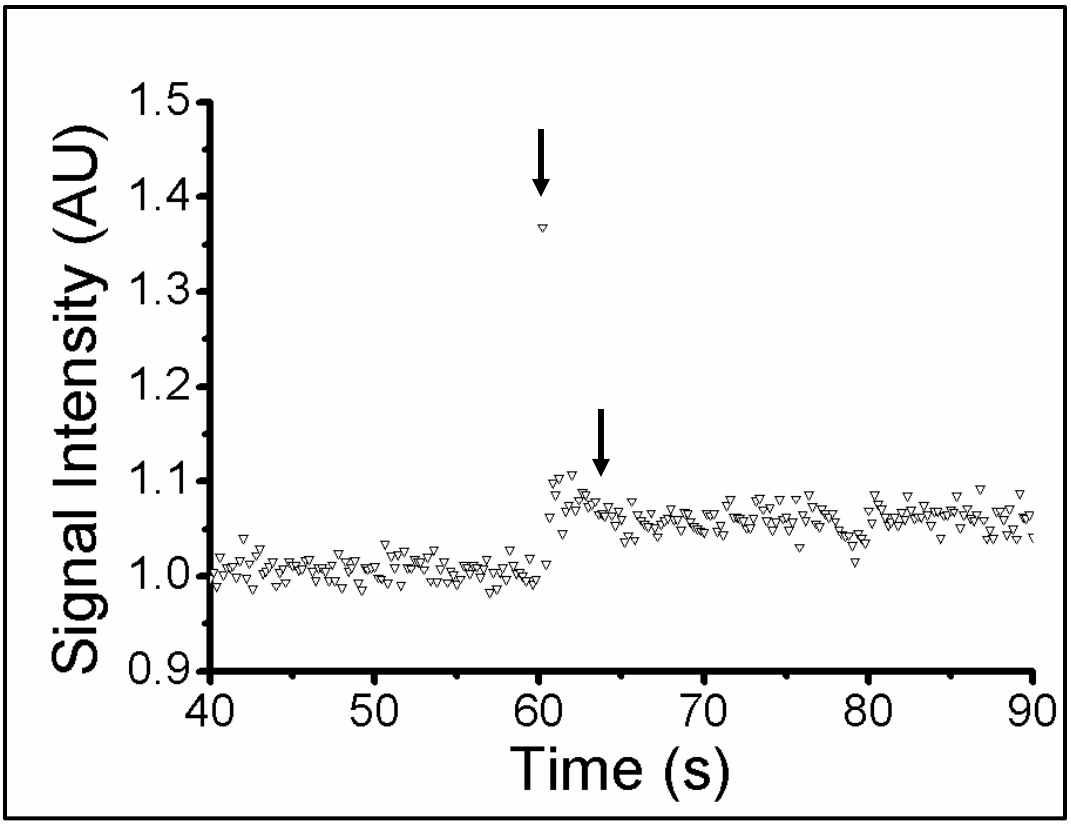

Figure 5-8. Results from a DCE experiment with Gd-DTPA-BSA. Though no extravasation of contrast agent occurred (i.e., diffusion of the contrast agent from the lumenal to the extra-lumenal compartment), a slight increase in signal intensity is seen coincident with contrast agent "injection". Arrows denote the time period (2-3 seconds) over which the deviations occur from the assumed stepped input function.

5.8. Tables

Table 5-1. Averaged results from DCE-MRI

Flow rate	Lumenal velocity	Rate constant	Permeability coefficient
56 mL/min	48 mm s^{-1}	0.051 ± 0.007 s^{-1}	0.00035 ± 0.00005 cm s^{-1}
62 mL/min	44 mm s^{-1}	0.06 ± 0.01 s^{-1}	0.00039 ± 0.00009 cm s^{-1}
68 mL/min	40 mm s^{-1}	0.066 ± 0.008 s^{-1}	0.00045 ± 0.00005 cm s^{-1}

CHAPTER 6. CONCLUSION

6.1. Summary of major findings

A review of the literature finds that DCE-MRI is 1) well established and 2) qualitatively validated by, among other methods, comparison with histologically determined microvascular density. Nevertheless, quantitative validation of the technique remains a challenge as determining the accuracy of estimated parameters is difficult (i.e., generally impossible *in vivo*). A first step toward this quantitative validation has been presented herein utilizing realistic tissue models (phantoms) that contain semi-permeable hollow fibers.

Two types of phantoms were described, single and multi-fiber. Their design and construction offer many benefits including: low cost and simple construction, small physical size (facilitating high spatially resolved imaging), controlled lumenal flow, and compartmental access. These phantoms are expected to aid in validation and control experiments for various perfusion-sensitive techniques employing different imaging modalities.

An example of their utility was given by demonstrating, with single-fiber phantoms, diffusion driven longitudinal relaxation. In this experiment, the measured longitudinal relaxation rate constant in a single physical compartment was influenced by the diffusion of spins from another compartment. The effect was shown to result theoretically in a multi-exponential response to an inversion recovery experiment. However, interestingly, the data were well modeled by a simple bi-exponential function. A second example of diffusion driven longitudinal relaxation was also given, this time in a simple capillary tube in response to decreasing the slice thickness. An analogous bi-exponential response was observed. In addition to demonstrating the utility of such phantoms to probe basic science questions, these examples also stand as a cautionary example to the overestimation of multi-exponential relaxation data in MRI.

Finally, a mock-DCE experiment was validated and demonstrated in multi-fiber phantoms. Due to control of key aspects of experimental design, the DCE experiment was reduced in complexity. These aspects included, stepped or square contrast agent input functions, detection of signal from a single compartment due to time-of-flight effects, and use of a highly time slice-selective spectroscopy protocol rather than an imaging experiment. Ideally shaped

contrast agent input functions were realized by fast switching within the magnet using a four-way valve. Deviations from these ideal shapes were transient when compared to the time scale of the entire experiment. When contrast agents of differing molecular weights were qualitatively compared, correlation was seen between molecular weight and the rate of contrast agent extravasation (see chapter 3). Last, comparison with gold standard measurements for a single contrast agent, Gd-BOPTA, demonstrated for the first time the accuracy of parameters estimated by DCE-MRI (see chapter 5).

6.2. Future work

Though the outcomes of the various experiments were positive, further corrections must be made to the experimental design of the mock-DCE experiment. Foremost among these is diagnosing the underlying cause of and correcting for the error in estimation of contrast agent concentration from signal intensities. Currently, asymptotic ($t = \infty$) concentrations in the DCE experiment are underestimated by up to 20%. Potentially, this underestimation is not due to faulty experimental design, but physical phenomena not currently addressed in the DCE-modeling. If this be the case then an altered model should be constructed and proposed.

Future work also includes carrying out the phantom-DCE experiment under less ideal circumstances. For instance, as cited in chapter 5, one could grow cells in the extralumenal space of the multi-fiber phantom. This would result in a three compartment system with respect to water (lumenal, extralumenal extracellular, and extralumenal intracellular) and a two compartment system with repect to CA (lumenal and extralumenal extracellular). This is more representative of the compartmental environment found *in vivo*. Currently, disagreement exists concerning the correct modeling of water exchange between these compartments *via* DCE-MRI.

APPENDIX A. DERIVATION OF DCE COMPARTMENTAL MODELS

A.1. Abstract

Analysis of dynamic contrast enhanced (DCE) MRI data relies upon mathematical modeling of contrast agent perfusion. Current models describe *in vivo* physiology as multiple compartments that communicate via semi-permeable barriers. Derivation from Fick's law of diffusion is herein presented.

A.2. Derivation of the modified Tofts DCE model from Fick's law of diffusion

A.2.1. Fick's law of diffusion

Much of the following derivation follows that presented in Cellular Biophysics by Thomas Fisher Weiss (8). The phenomenological relationship known as Fick's law of diffusion is expressed in one dimension as,

$$J(x,t) = -D\frac{\partial C(x,t)}{\partial x}. \qquad \text{(A-1)}$$

J is flux (molecules m^{-2} s^{-1}), x is position in one dimension (m), t is time (s), D is the diffusion coefficient (m^2 s^{-1}) of the diffusing molecule in the appropriate solvent, and C is concentration (molecules m^{-3}) of the diffusing molecule. This equation states that flux of particles will occur in response to a concentration gradient at a rate determined by the diffusion coefficient in the direction to minimize the concentration gradient.

A.2.2. The continuity relation

Next, the continuity relation must be justified. Consider the volume in figure A-1 of width Δx, influx J(x,t), outflux J(x+Δx,t), and surface area A (m^2) of the face orthogonal to the flux.

Let Δx be small enough that the change in concentration from left to right is negligible. The net flux of particles into the volume in time Δt is thus,

$$N = \left[J(x,t) - J(x+\Delta x,t)\right]\cdot A\cdot \Delta t\,. \qquad \text{(A-2)}$$

N is the net increase of molecules in the volume. An alternative representation is,

$$N = \left[C\left(x + \frac{\Delta x}{2}, t + \Delta t \right) - C\left(x + \frac{\Delta x}{2}, t \right) \right] \cdot A \cdot \Delta x \,. \tag{A-3}$$

Here, the average concentration has been taken as that in the middle of the voxel. Equating these two and taking the limit as Δx and Δt go to zero one obtains the continuity equation,

$$\frac{\partial J(x,t)}{\partial x} = -\frac{\partial C(x,t)}{\partial t} \,. \tag{A-4}$$

In three dimensions this relationship is,

$$\nabla \cdot J(x,y,z,t) = -\frac{\partial C(x,y,z,t)}{\partial t} \,. \tag{A-5}$$

Integration yields,

$$J(x,y,z,t) = -\frac{V}{A} \cdot \frac{dC(x,y,z,t)}{dt} \,. \tag{A-6}$$

V is volume (m^3) and Gauss's integral theorem was used to make the following substitution,

$$\int \nabla \cdot J \cdot dV = \oint J \cdot dA \,. \tag{A-7}$$

A.2.3. Steady state diffusion

Assuming steady state diffusion is tantamount to taking both flux and concentrations as invariant with respect to time. Under this assumption, the continuity relationship then implies,

$$\frac{\partial J(x,t)}{\partial x} = -\frac{\partial C(x,t)}{\partial t} = 0 \,. \tag{A-8}$$

In other words, it implies that flux is invariant with respect to position as well as time. In this situation Fick's first law reduces to,

$$J = const. = -D \frac{dC(x)}{dx} \,. \tag{A-9}$$

Furthermore, if D does not equal zero then,

$$C(x) = C(x_o) - \frac{J}{D} \cdot (x - x_o) \,. \tag{A-10}$$

$C(x_o)$ is a known concentration at reference point x_o.

A.2.4. Steady state diffusion across a membrane

Consider now steady state diffusion across a membrane according to figure A-2 where C_1 (the concentration of compartment 1; molecules m^{-3}) and C_2 (the concentration of compartment 2; molecules m^{-3}) are two well mixed pools (no spatial concentration dependence within the compartment) of constant concentration with respect to time. If C(0) is taken as a reference point the previous equation evaluated at x=d is,

$$C(d) = C(0) - \frac{J_{12} \cdot d}{D}. \qquad \text{(A-11)}$$

D is the diffusion coefficient ($m^2\ s^{-1}$) within the membrane. Rearrangement yields,

$$J_{12} = \frac{D}{d} \cdot [C(0) - C(d)]. \qquad \text{(A-12)}$$

J_{12} is the flux from compartment 1 to compartment 2 (positive if flux is from 1 to 2 and negative if flux is from 2 to 1 as D is always positive).

Boundary conditions can be imposed by defining the partition coefficient as,

$$z = \frac{C(0)}{C_1} = \frac{C(d)}{C_2} \qquad 0 \le z \le 1. \qquad \text{(A-13)}$$

The partition coefficient is thus unitless and allows rearrangement of the previous equation to yield what is know as Fick's law for membranes,

$$J_{12} = P \cdot (C_1 - C_2). \qquad \text{(A-14)}$$

P is the permeability ($m\ s^{-1}$) and is defined by the following relationship,

$$P = \frac{D \cdot z}{d}. \qquad \text{(A-15)}$$

The above relation holds for the situation where the only transport process is simple diffusion through a single permeable membrane. If the membrane is porous or if transport is not active then the analytical expression for P becomes more complex or possibly nonanalytical.

A.2.5. Generalization of Fick's law for membranes

Fick's law for membranes can be generalized for application in the DCE-MRI experiment of interest. In this experiment there is not a steady state as concentrations in the compartments vary and concentrations within the compartments may not be homogeneous, there is not a single membrane, and there is the possibility of multiple transport processes (2). Thus a simple analytical form of P is insufficient. Fortunately, with a few additional assumptions the general form of Fick's law for membranes is conserved.

First, one must address the issue of permeability. If the membrane actually consists of multiple transport mechanisms then one can assume that the total permeability for the membrane (P_{mem}; m s^{-1}) is equal to the n individual permeabilities (P_i; m s^{-1}) in parallel which gives (2),

$$P_{mem} = \sum_{i}^{n} P_i \ . \tag{A-16}$$

Second, if there are multiple membranes we will assume that the total permeability of m overlapped complex membranes (P_{tot}; m s^{-1}) is equal to all the individual membrane permeabilities (P_{mem}; m s^{-1}) in series which yields (2),

$$\frac{1}{P_{tot}} = \sum_{i}^{m} \frac{1}{P_{mem}} . \tag{A-17}$$

Thus, Fick's law for membranes becomes,

$$J_{12} = P_{tot} \cdot \left(C_1 - C_2\right). \tag{A-18}$$

P_{tot} can be considered the effective permeability of these multiple complex membranes over an effective surface area S (m^2).

To address the issue of steady state it is required that one assumes: (1) concentration within each compartment is uniform, i.e., the contrast agent is well mixed within each compartment, and (2) clearance time of contrast agent from the vascular compartment is orders of magnitude longer than the time that it takes to reach steady state within the membrane, i.e., the intercompartmental flux is linear with respect to space (in figure A-2 with respect to the x axis)

If these two assumptions are met then one can reintroduce time dependence upon both concentration and flux yielding,

$$J_{12}\left(t\right) = P_{tot} \cdot \left[C_1\left(t\right) - C_2\left(t\right)\right]. \tag{A-19}$$

Combination with the continuity relation, introduction of the general rate constant k_{12} (s^{-1}), and rearrangement renders the working form of the equation,

$$\frac{dC_1(t)}{dt} = k_{12} \cdot [C_2(t) - C_1(t)], \quad \text{(A-20)}$$

or, with respect to compartment two,

$$\frac{dC_2(t)}{dt} = k_{21} \cdot [C_1(t) - C_2(t)]. \quad \text{(A-21)}$$

The rate constants are defined by the following relationships,

$$k_{12} = \frac{S \cdot P_{tot}}{V_1}, \text{ and } k_{21} = \frac{S \cdot P_{tot}}{V_2}. \quad \text{(A-22)}$$

V_1 being the volume of compartment one and S being the effective surface area referred to above. In this form it is evident that in the development an additional assumption was implied, namely that P_{12} is equal to P_{21}.

It is noteworthy that sometimes an alternate form of equation A-19 is seen in DCE literature (2). In the alternate form, P is replaced by P·S. In this formulation it should be remembered that flux is defined as the physical amount of substance that diffuses through the whole membrane of interest, i.e., the flux is not scaled, but is the flux of the system.

A.2.6. Solution to the general rate equation in terms of the total concentration

Consider first the three compartment system as shown in figure A-3 in accordance with the DCE experiment. Generally, one cannot monitor the concentrations C_1, C_2, and C_3 individually; rather, one can only monitor C_t (total concentration; molecules m^{-3}). Therefore, the analysis must be further developed in terms of C_t. Starting with the relationship,

$$C_t = \frac{V_1}{V_t} \cdot C_1 + \frac{V_2}{V_t} \cdot C_2 + \frac{V_3}{V_t} \cdot C_3 = v_1 \cdot C_1 + v_2 \cdot C_2 + v_3 \cdot C_3. \quad \text{(A-23)}$$

V_t is the total tissue volume (m^3); v_1, v_2, and v_3 are the fractional volumes of compartments one and two and three respectively; and C_3 is the concentration in compartment three (molecules m^{-3}). If C_3 is equal to zero then,

$$C_t = v_1 \cdot C_1 + v_2 \cdot C_2 . \tag{A-24}$$

This is essentially a two compartment system where the partial volumes of the two active compartments do not add up to 1, i.e. v_3 does not equal zero which leads to,

$$v_1 + v_2 + v_3 = 1 \quad \rightarrow \quad v_1 + v_2 = 1 - v_3 . \tag{A-25}$$

A general rate equation can also be written in terms of C_t,

$$\frac{dC_t(t)}{dt} = v_1 \cdot \frac{dC_1(t)}{dt} + v_2 \cdot \frac{dC_2(t)}{dt} . \tag{A-26}$$

Substituting the previous expression for the time derivative of C_2 one obtains,

$$\frac{dC_t(t)}{dt} = v_1 \cdot \frac{dC_1(t)}{dt} + v_2 \cdot k_{21} \cdot \left[C_1(t) - C_2(t)\right]. \tag{A-27}$$

If C_1 is known (for instance, available directly from a second measurement) then a solution exists. The solution can be obtained by solving equation A-19 for C_2 (9) which yields,

$$C_2(t) = k_{21} \int_0^t C_1(\tau) \cdot e^{-k_{21}(t-\tau)} \cdot d\tau + C_2(0) \cdot e^{-k_{21}t} . \tag{A-28}$$

If the initial concentration in compartment two is equal to zero then this simplifies to,

$$C_2(t) = k_{21} \int_0^t C_1(\tau) \cdot e^{-k_{21}(t-\tau)} d\tau . \tag{A-29}$$

Inserting the result into the original expression for the total concentration (equation A-24) one obtains,

$$C_t = v_1 \cdot C_1 + v_2 \cdot k_{21} \int_0^t C_1(\tau) \cdot e^{-k_{21}(t-\tau)} d\tau , \tag{A-30}$$

where τ is a dummy variable. This equation can be written with a convolution where the convolution operator $\otimes$ is defined as,

$$g(t) \otimes h(t) = \int_0^t g(t-\tau) \cdot h(\tau) d\tau . \tag{A-31}$$

This yields,

$$C_t(t) = v_1 \cdot C_1(t) + v_2 \cdot k_{21} \cdot e^{-k_{21}t} \otimes C_1(t) . \tag{A-32}$$

The two constants v_2 and k_{21} are confounded in this equation. They are thus often expressed as a single constant K^{trans}, the transfer constant (s^{-1}) from compartment one to two, where,

$$K^{trans} = k_{21} \cdot v_2 . \quad \text{(A-33)}$$

This yields the Tofts modified equation, commonly applied to DCE data,

$$C_t(t) = v_1 \cdot C_1(t) + K^{trans} \cdot e^{-k_{21} \cdot t} \otimes C_1(t) . \quad \text{(A-34)}$$

A.3. References

1. Tofts PS, Brix G, Buckley DL, Evelhoch JL, Henderson E, Knopp MV, Larsson HB, Lee TY, Mayr NA, Parker GJ, Port RE, Taylor J, Weisskoff RM. Estimating kinetic parameters from dynamic contrast-enhanced T(1)-weighted MRI of a diffusable tracer: standardized quantities and symbols. J Magn Reson Imaging 1999;10(3):223-232.
2. Jackson A, Buckley DL, Parker GJM, editors. Dynamic contrast-enhanced magnetic resonance imaging in oncology. Berlin Heielberg New York: Springer; 2005.
3. Larsson HB, Tofts PS. Measurement of blood-brain barrier permeability using dynamic Gd-DTPA scanning--a comparison of methods. Magn Reson Med 1992;24(1):174-176.
4. Tofts PS. Modeling tracer kinetics in dynamic Gd-DTPA MR imaging. J Magn Reson Imaging 1997;7(1):91-101.
5. St Lawrence KS, Lee TY. An adiabatic approximation to the tissue homogeneity model for water exchange in the brain: I. Theoretical derivation. J Cereb Blood Flow Metab 1998;18(12):1365-1377.
6. Tofts P, editor. Quantitative MRI of the brain : measuring changes caused by disease. Chichester, West Sussex ; Hoboken, NJ: Wiley; 2003.
7. Koh TS, Zeman V, Darko J, Lee TY, Milosevic MF, Haider M, Warde P, Yeung IW. The inclusion of capillary distribution in the adiabatic tissue homogeneity model of blood flow. Physics in Medicine & Biology 2001;46(5):1519-1538.
8. Weiss TF. Cellular biophysics. Cambridge, Mass.: MIT Press; 1996.
9. Boas ML. Mathematical methods in the physical sciences. New York: Wiley; 1983..

A.4. Figures and captions

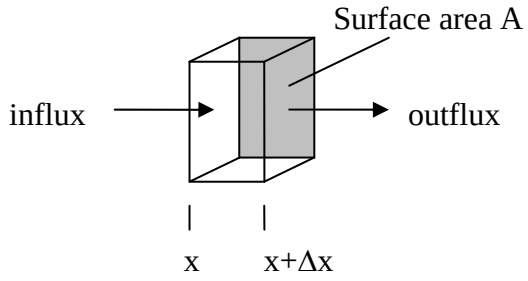

Figure A-1. a small voxel with influx and outflux(8)

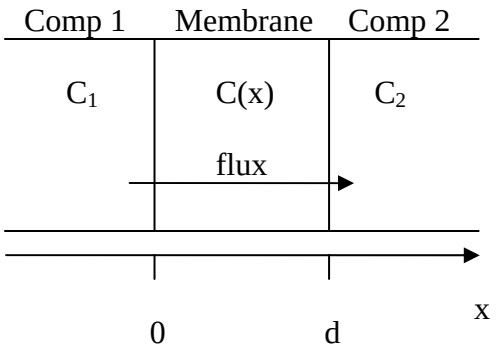

Figure A-2. a schematic of diffusion through a permeable membrane

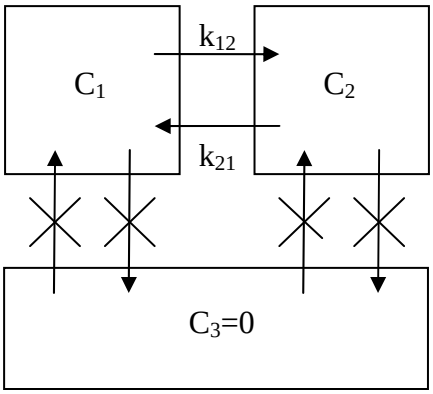

Figure A-3. A simple 3 compartment system with communication between only two of the compartments.

APPENDIX B. REPRINT OF MAGNETIC RESONANCE IMAGING DEFINES CERVICOVAGINAL ANATOMY, CANCER, AND VEGF TRAP ANTIANGIOGENIC EFFICACY IN ESTROGEN-TREATED K14-HPV16 TRANSGENIC MICE

B.1. Abstract

Noninvasive detection of dysplasia provides a potential platform for monitoring the efficacy of chemopreventive therapy of premalignancy, imaging the tissue compartments comprising dysplasia: epithelium, microvasculature, and stromal inflammatory cells. Here, using respiratory-gated magnetic resonance imaging (MRI), the anatomy of premalignant and malignant stages of cervical carcinogenesis in estrogen-treated K14-HPV16 transgenic mice was noninvasively defined. Dynamic contrast enhanced (DCE)-MRI was used to quantify leakage across premalignant dysplastic microvasculature. Vascular permeability as measured by DCE-MRI, K^{trans}, was similar in transgenic (0.053 ± 0.020 min^{-1}; n = 32 mice) and nontransgenic (0.056 ± 0.029 min^{-1}; n = 17 mice) animals despite a 2-fold increase in microvascular area in the former compared with the latter. DCE-MRI did detect a significant decrease in vascular permeability accompanying diminution of dysplastic microvasculature by the antiangiogenic agent, vascular endothelial growth factor Trap (K^{trans} = 0.052 ± 0.013 min^{-1} pretreatment; n = 6 mice versus K^{trans} = 0.019 ± 0.008 min^{-1} post-treatment; n = 5 mice). Thus, we determined that the threshold of microvessel leakage associated with cervical dysplasia was <17 kDa and highlighted the potential of DCE-MRI to noninvasively monitor the efficacy of antiangiogenic drugs or chemoprevention regimens targeting the vasculature in premalignant cervical dysplasia. [Cancer Res 2009;69(20):7945–52]

B.2. Publication information

B.2.1. Reference

Cancer Res 2009;69(20):7945–52

B.2.2. Title

Magnetic Resonance Imaging Defines Cervicovaginal Anatomy, Cancer, and VEGF Trap Antiangiogenic Efficacy in Estrogen-Treated K14-HPV16 Transgenic Mice

B.2.3. Authors

Joel R. Garbow,[1,4] Andrea C. Santeford,[2] Jeff R. Anderson,[3] John A. Engelbach,[1] and Jeffrey M. Arbeit[2,4]

B.2.4. Affiliation

Departments of [1]Radiology, [2]Urology, and [3]Chemistry and [4]Alvin J. Siteman Cancer Center, Washington University in St. Louis, St. Louis, Missouri

B.2.5. Note

Supplementary data for this article are available at Cancer Research Online (http://cancerres.aacrjournals.org/).

B.2.6. Request for Reprints

Joel R. Garbow, Washington University, Campus Box 8227, 4525 Scott Avenue, St. Louis, MO 63110. Phone: 314-362-9949; Fax: 314-362-0526; E-mail: garbow@wustl.edu.

B.2.7. Copyright

©2009 American Association for Cancer Research.

B.2.8. DOI

doi:10.1158/0008-5472.CAN-09-1271

B.2.9. Abstract

B.3. Introduction

Cervical cancer is the second most common malignancy affecting women worldwide (1). Although effective screening has markedly diminished cervical cancer incidence in the United States, dysplasia remains a common clinical challenge requiring surgical extirpation for high-grade lesions (1, 2). As such, noninvasive therapy for premalignant, but high-risk, dysplasias would be a tremendous boon to gynecologic care.

Dysplastic lesions are characterized by disorganized epithelial differentiation. The uterine cervical squamous epithelium can harbor dysplasia initiated by oncogenic human papillomaviruses (HPV), most frequently types 16 and 18 (1). Normal cervical epithelium is composed of a basal layer that is immature and proliferative and multiple suprabasal layers of differentiating squamous cells that are ultimately shed from the top of the epithelium into the cervical canal or vaginal lumen. Increasing grades of dysplasia are characterized by progressive occupation of the suprabasal layer by basaloid squamous cells (1). High-grade dysplasia, if untreated, has an extremely high incidence of conversion to malignancy (2). Cervical dysplasia and dysplastic lesions, in general, activate an angiogenic switch that both increases the subepithelial microvasculature and produces stromal inflammation (3, 4). Angiogenesis and inflammation are features that could be exploited for imaging by a technique measuring tissue vascularity and leakage, such as dynamic contrast enhanced (DCE)–magnetic resonance imaging (MRI). DCE-MRI, studied extensively in solid malignancies (5–7), uses bolus contrast agent administration to noninvasively visualize tumor microvasculature and quantify leakage across microvessels (8, 9). Time-resolved images, collected as contrast agent enters and exits tissue (10), are pharmacokinetically modeled (11, 12), providing quantitative measures of important physiologic parameters, such as tissue microvascular integrity (vascular permeability).

Here, we used respiratory-gated MRI to obtain high-resolution images of the entire mouse reproductive tract and delineated an invasive squamous carcinoma in a late-stage (13–15), estrogen-treated K14-HPV16 transgenic mouse. We also interrogated the microvascular biology associated with premalignant dysplasia using DCE-MRI with a 17-kDa contrast agent, Gadomer. No differential dysplastic microvascular leak was detectable, consistent with

experiments showing undetectable physical leakage of an i.v. injected marker protein, suggesting that dysplastic microvessels have a maximal permeability pore size <17 kDa. However, DCE-MRI detected a significant decrease in dysplastic vascular leak following treatment with the antiangiogenesis agent, vascular endothelial growth factor (VEGF) Trap (16, 17). Thus, DCE-MRI can serve as a platform for noninvasively monitoring antiangiogenic drug efficacy, potentially deployed with chemoprevention programs, for high-risk premalignant disease.

B.4. Materials and Methods

Transgenic mice. One-month-old female K14-HPV16:FVB/n congenic transgenic mice and nontransgenic littermate controls were treated for 3 or 6 months with s.c. insertion of 17β-estradiol pellets, 0.05 mg/60 day release (Innovative Research of America; ‘‘estrogen’’; refs. 13, 15). The Animal Studies Committee of Washington University in St. Louis approved all procedures in this study.

MRI. MR images were collected on a Varian NMR Systems 4.7T INOVA scanner described previously (18) using Stark Contrast 2.0 or 2.5 cm birdcage RF coils. Mice were anesthetized and maintained on isoflurane/O2 (1–1.25% v/v), and a 3-inch length of PE-10 tubing (Becton Dickinson) was inserted via the urethra into the bladder for drainage throughout data collection. Core body temperature was maintained at 37 ± 1°C by warm air circulation through the magnet bore.

For anatomic imaging, 500 μL Omniscan (gadodiamide; GE Healthcare) contrast agent, diluted 1:10 in saline to yield a 50 mmol/L solution, was administered i.p. immediately before placing the animal into the magnet. High-resolution images were collected using a respiratory-gated, two-dimensional, multi-slice spin-echo sequence (18), and all images were collected during post-expiratory periods. Imaging parameters were repetition time ~ 3 s, echo time 20 ms, field of view 2.5 x 2.5 cm^2 (transaxial)/4.0 x 4.0 cm^2 (coronal), 128 x 128 data points, and slice thickness 0.5 mm.

DCE-MRI data were collected using a T1-weighted, gradient spoiled, multi-slice gradient-echo sequence. Imaging parameters were flip angle 30°, repetition time 0.06 s, echo time 0.002

s, field of view 2.5 x 2.5 cm^2, number of slices 15, in-plane resolution 195 μm, and slice thickness 0.50 mm. The temporal resolution was ~ 15 s. Early DCE-MRI data were collected following i.v. injection of Omniscan. However, values of vascular permeability (K^{trans}) were all derived from experiments using Gadomer (Bayer Schering Pharma). Pre-contrast, T1 maps were produced using a variable flip-angle, three-dimensional, gradient-echo sequence (19, 20) with flip angles of 2.5°, 5.0°, 7.5°, 10.0°, and 15.0°. After 1 min of scanning (four images at 15 s/image), 60 μL of a solution of Gadomer that is 50 mmol/L Gd (a dose of 0.12 mmol Gd/kg body weight for a 25 g mouse) were injected over 10 s using a Harvard 2 dual syringe pump (Harvard Clinical Technology) via either a tail or a jugular venous catheter.

Modeling DCE data. The starting point for our analysis was the Patlak model containing independent parameters v_p (fractional blood-plasma volume) and (volume transfer constant between blood plasma and extravascular extracellular space; refs. 21, 22). Significant deviation from linearity in the Patlak plot led us to include a third independent parameter, v_e (fractional volume of extravascular extracellular space), to account for contrast agent efflux from extravascular extracellular space to blood plasma (21, 23). Conversion of signal intensity to concentration of contrast agent was achieved by standard methods (10). Negligible T_2* weighting of the images and the fast-exchange limit were both assumed (10, 12). Values of T_{10} were 1.6 s for cervix (24) and 1.4 s for leg muscle (see below; ref. 25); r_1 of Gadomer was taken to be 9.1 $mmol/L^{-1}s^{-1}$ (26).

The determination of v_p, v_e, and K^{trans} requires knowledge of contrast agent concentration in the blood plasma [arterial input function (AIF)] throughout the experimental time course. Traditionally, the AIF is measured from a large vessel within the image, carefully avoiding inflow and partial volume artifacts (10, 27, 28). However, direct AIF determinations in mice are often difficult due to small spatial dimensions and motion effects. Instead, we derived the AIF from leg muscle reference tissue (29, 30) using the following parameter values for muscle tissue: K^{trans} (Gadomer) = 0.002 min^{-1}, v_p = 0.021, and v_e =0.085 (31). To convert contrast agent concentration data into physiologic parameters, a region of interest (ROI) was drawn over the transformation zone of the cervix and the data were modeled in Matlab (Mathworks) using a variable projection

(VARPRO) nonlinear least-squares approach (32).

Detection of antiangiogenesis mediated by VEGF Trap. K14-HPV16 transgenic mice were scanned by DCE-MRI before treatment, treated biweekly for 2 weeks with 500 μg VEGF Trap (Regeneron Pharmaceuticals) or vehicle (5 mmol/L phosphate, 5 mmol/L citrate, 100 mmol/L NaCl, 0.005% Tween 20) via i.p. injection, and then rescanned to test therapy-associated microvascular permeability alterations.

Determination of microvessel density. Isoflurane anesthetized mice were i.v. injected with 50 μg FITC-conjugated *Lycopersicon esculentum* lectin (Vector Laboratories); after 3 min, the left ventricle was perfused with 10% formalin (Fisher Scientific International) for 3 min followed by 10% sucrose for 1 min (Perfusion One Rodent System; McCormick Scientific). The entire reproductive tract was removed, and the vaginal cavity was filled with OCT freezing medium, embedded in OCT (posterior-side down), flash-frozen using liquid nitrogen, and stored at -80°C. Cryosections (60 Am) were mounted using SlowFade Gold with 4',6-diamino-2-phenylindole (Invitrogen) and viewed under appropriate filter sets using an Olympus BX61 microscope equipped with a Fire Wire Colorview II camera (Olympus). Images of lectin-perfused vessels in the cervical transformation zone taken at x40 magnification were analyzed using Olympus MicroSuite Biological Suite software. For each image, four equally sized rectangular ROIs were identified along the epithelial-stromal border of the transformation zone. Subepithelial microvasculature was delineated by creating RGB color detection profiles to increase signal-to-noise and identify as many vessels as possible. These profiles were used for all images.

Determination of physical molecular leakage. ChromPure sheep IgG, Fc fragment, 50 μg in 50 μL PBS (Jackson ImmunoResearch Laboratories), was injected i.v. and allowed to circulate for 2 h followed by FITC-lectin injection, formalin perfusion, OCT whole-organ embedding, and 60 Am cryosectioning as described above. Air-dried sections were rinsed in PBS three times, blocked for 3 h with DAKO protein block, incubated overnight at 4°C with anti-sheep Cy3-conjugated AffiniPure Donkey IgG (Jackson Immuno Research Laboratories), diluted 1:100 in DAKO Antibody Diluent (DAKO), and mounted using SlowFade Gold with 4',6-diamino-2-phenylindole. For visualizing Fc Fragment leakage, images were captured using the Cy3 filter

from the sample with the highest signal, which was used to determine the optimal camera gain settings. A control image from a noninjected mouse was used to correct for the Cy3 background signal. A ROI obtained from the control image was used for background subtraction for analysis of signal intensity of Fc-injected experimental tissue sections using the MicroSuite software.

Statistical analysis. Data are mean ± SD. Mann-Whitney *U*, paired or unpaired Student's *t* tests were used to determine statistical significance (GraphPad Prism).

B.5. Results

Cervical transformation zone MRI and histopathologic correlation. First, we developed MRI techniques to visualize the entire mouse female reproductive tract, including the vagina, cervix, and lower uterus (Fig. 1*B*). High-resolution, in vivo respiratory-gated spin-echo coronal and transaxial MR images were obtained of a 3-month-old, estrogen-treated, nontransgenic mouse with an in-plane resolution of 150 μm (Fig. 1*A* and *C*). The coronal MR image (Fig. 1*A*) was a striking reproduction of the actual organ anatomy delineating the cervical isthmus, canal, outer cervix, and upper vagina (Fig. 1*B*). Transaxial images also delineated all three zones of the cervix: the upper cervical-uterine junction (data not shown), the mid-cervix with the transformation zone and isthmus division septum leading to the two uterine horns (Fig. 1*C*, *top*), and the lower cervix, here containing a single central canal and laterally bounded by the adjacent vaginal walls (Fig. 1*C*, *middle*), and the vagina (Fig. 1*C*, *bottom*).

Anatomic MRI also detected cervical cancer that occurs in 80% of K14-HPV16 transgenic mice treated with estrogen for 6 months (refs. 13, 15; Fig. 2*A* and *B*, multiple delineating *black* and *red* arrowheads, respectively). The malignancy was first evident in the mid-cervix both histologically and in the MRI (data not shown). Histologic analysis further showed spread of the cancer to the lower cervix, as determined by the single ''X''-shaped lumen (Fig. 2*A*, *green arrows* indicate upper vagina), which invaded almost through the anterior cervical wall adjacent to the bladder (Fig. 2*A*, six o'clock position), and effaced the right portion of the cervical canal. MRI delineated the same extent of tumor invasiveness (Fig. 2*B*, *red arrowheads*), but with the additional feature of obliteration of the right cervical lumen, not evident on the histopathology (Fig.

2*A*). This slight discordance of the MRI vis-à-vis histology is due either to volume averaging in the former or, more likely, tissue shrinkage during processing in the latter.

Differential histology and microvascular area in transgenic premalignant high-grade dysplasia. As high-grade dysplasia, usually arising from the cervical transformation zone, is the source of subsequent invasive cervical cancer in both humans (1) and this transgenic model (13) and is a potential target for chemoprevention, we focused our histopathologic (Fig. 3*A*-*D*), microvascular (Fig. 4*A*-*D*), and MRI analyses on this anatomic region and this stage of progression in the transgenic mice treated with estrogen for 3 months (13). Moderate to high-grade cervical dysplasia (Fig. 3*B* and *D*), but no cervical cancer, was evident, similar to our previous experience (13). Nontransgenic littermates treated with the same dosage and duration of estrogen evidenced hyperplasia without dysplasia (Fig. 3*A* and *C*).

Induction of angiogenesis and increased microvascularity has been documented previously in patients with cervical dysplasia and also in dysplastic skin lesions in K14-HPV16 transgenic mice (33). Thus, we first determined differences in microvascular morphology in transgenic cervical dysplasia (Fig. 4*A*, *top* and *bottom right*) compared with nontransgenic estrogen-induced hyperplasia (Fig. 4*A*, *top* and *bottom left*). There were two distinct zones of microvasculature in the mouse cervix: the subepithelial region and the deep stromal area (Fig. 4*A*, *top left*, *white arrowheads* and *arrow*). The subepithelial region was most affected by mouse genotype, with the transgenic microvasculature forming tufts and projections into the overlying dysplastic epithelium (Fig. 4*A*, *top right*, *arrowhead*, and higher-magnification image in *bottom right*). In contrast, nontransgenic microvasculature was flattened and linearly arrayed in the stroma immediately beneath the hyperplastic epithelium (Fig. 4*A*, *top* and *bottom left*). Image analysis revealed that the area of the subepithelial microvasculature in K14-HPV16 mice was 42.6 ± 8.8% compared with 24.3 ± 8.5% in nontransgenic cervices (Fig. 4*B*). These data were similar to immunohistochemical analysis of dysplastic microvessel density in this model (14).

Using DCE-MRI to detect vascular permeability changes in premalignant cervical dysplasia. The increased subepithelial microvascularity in 3-month-old, estrogen-treated transgenic cervices led us to investigate microvessel biology using DCE-MRI, particularly

because K14-HPV16 transgenic mice were known to accumulate activated stromal inflammatory cells that could, via chemokine/cytokine release, induce leakage even in premalignant dysplasia (14). Initially, we conducted these DCE-MRI experiments using Omniscan, a low-molecular weight, Gd-based contrast agent. Visual analysis of sequential temporal images from a DCE-MRI experiment using a nontransgenic mouse revealed a distinct pattern and distribution of Omniscan contrast agent over time (Fig. 5*A*; Supplementary Movie). Initial pre-injection images were dark (Fig. 5*A*, *left*). Immediately following injection, the pelvic branches of the internal iliac artery were visualized; coincidently, the luminal lining of the isthmus and cervical canal was brightly enhanced (Fig. 5*A*, *middle*). This compartment was presumably the subepithelial microvasculature. Finally, contrast was evenly distributed in the cervix, consistent with permeation throughout the deep cervical stroma (Fig. 5*A*, *right*). We observed a swift, large signal enhancement following Omniscan injection in both transgenic and nontransgenic animals, consistent with rapid extravasation, making it very difficult to collect high-resolution DCE-MRI data rapidly enough for determination of contrast agent kinetics.

As such, we switched to Gadomer, a 17-kDa, dendrimer-based contrast agent with permeability that was significantly lower than that of Omniscan, for DCE-MRI. Following data collection, ROIs were drawn in the cervical transformation zone (Fig. 5*B*, *left*) and image intensity versus time curves were derived from within these ROIs (Fig. 5*C*, *left*). Intensity versus time data were converted to concentration versus time curves, and physiologic parameters were derived, as described above. The red circles in Fig. 5*C* are experimental data points, whereas the red curve represents the modeling of this concentration versus time data using an AIF derived from a reference tissue, muscle (refs. 29, 30; Fig. 5*B*, *right*). A representative contrast agent concentration versus time curve for muscle is plotted as the blue circles, whereas the derived AIF is shown as the dashed blue curve (Fig. 5*C*, *left*). Based on our analysis of the DCE data, we determined the transfer constant (K^{trans}) for a ROI within the cervical transformation zone in 32 transgenic and 17 nontransgenic mice (Fig. 5C, right). Average K^{trans} values for the nontransgenic (0.056 ± 0.029 min^{-1}) and transgenic mice (0.053 ± 0.020 min^{-1}) were indistinguishable.

To investigate the possibility of low-level microvascular leak to which DCE-MRI was

insensitive, we determined the physical leakage (Fig. 5*D*). Injection of Fc fragments of 50-kDa molecular weight showed a robust microvascular leakage both within an invasive cancer (Fig. 5*D*, *left*) and within a dysplasia adjacent to the malignancy (Fig. 5*D*, *middle*). In contrast, we did not detect microvascular leak in dysplastic microvessels in 3-month-old, estrogen-treated transgenic mice (Fig. 5*D*, *right*). Thus, despite a 2-fold increase in microvascular density (Fig. 4*B*), the switch to leaky vessels occurred later in this model, possibly at the 4.5-month point wherein carcinoma *in situ* and microinvasive cancer first appear (15), or was restricted to frank invasive malignant lesions.

Anatomic response of microvasculature associated with premalignant cervical dysplasia to antiangiogenic therapy. Noninvasive detection of the response of dysplastic lesions to antiangiogenic or antineoplastic therapies would be a tremendous boon to assess efficacy of cancer prevention. We determined the morphologic response of the transgenic cervical microvasculature to VEGF Trap and then the sensitivity of DCE-MRI to detect alterations of microvascular leakage. We used VEGF Trap (16, 17), because VEGF has also been shown to be incrementally up-regulated in both human dysplastic and malignant cervix (34) and the cervical dysplasias and malignancies of estrogen-treated, K14-HPV16 transgenic mice (14).

Following a 2-week course of VEGF Trap, there was an obvious pruning of the epithelial tufting and a marked overall reduction in microvascular density in the treated mice (Fig. 6*A*, vehicle, *left*, and VEGF Trap–treated, *right*). Subepithelial microvascular area decreased 50% in VEGF Trap–treated mice compared with vehicle-treated transgenic mice (Fig. 6*B*), to a level below that of estrogen-treated nontransgenic controls (Fig. 4*B*). Despite the marked subepithelial microvascular pruning, there was no difference in the extent or grade of epithelial dysplastic histopathology in VEGF Trap–treated versus vehicle-treated transgenic mice (data not shown).

DCE-MRI detects antiangiogenic efficacy in premalignant dysplasia. Next, we tested the ability of DCE-MRI to detect a permeability response that potentially accompanied the VEGF Trap–mediated decrease in microvascular area in cervical dysplasia. Pre-and post-VEGF Trap DCE-MRI showed a significant 63% decrease in K^{trans} in all of the treated transgenic mice (0.052 ± 0.013 min^{-1} pretreatment versus 0.019 ± 0.008 min^{-1} posttreatment; n = 6 mice; Fig. 6*D*). DCE-

MRI data in vehicle control transgenic mice were heterogeneous and bivariant (Fig. 6*C*), but all values fell within the range that we previously determined for this group (Fig. 5*C*, *right*). Overall, there was no statistical difference in the pretreatment/post-treatment values either for each vehicle-treated mouse in a paired Student's *t* test (Fig. 6*D*) or within the entire vehicle-treated group (0.048 ± 0.015 min^{-1} baseline and 0.045 ± 0.021 min^{-1} after 2 weeks; *n* = 5 mice). The uniformity of K^{trans} reduction in VEGF Trap–treated mice compared with the variable response of vehicle-treated transgenic mice suggests that, at a 17-kDa cutoff, DCE-MRI was detecting the marked reduction in microvascular area in VEGF Trap–treated mice rather than an inherent effect on the microvessel stability of neoplastic vessels.

B.6. Discussion

The estrogen-treated K14-HPV16 transgenic mouse model of cervical carcinogenesis has been extensively studied since inception (14, 35–37), and its relevance for human disease has been validated by both detailed histopathologic and genome-wide expression analysis (15, 36, 38). Other work has shown angiogenesis induction coincident with high-grade dysplasia, similar to our findings (14). Moreover, dysplastic and malignant angiogenesis in this model has been linked to both macrophage and neutrophil expression of proteases and angiogenic factors (3, 14). Thus, the emerging importance of the K14-HPV16 transgenic mouse as a preclinical platform for testing drugs that target both malignant and dysplastic angiogenesis (3, 14) motivated us to undertake a detailed MRI-based analysis to both noninvasively determine cervicovaginal anatomy and interrogate microvascular biology associated with premalignant dysplasia.

Here, *in vivo* MRI at 4.7 T clearly distinguished epithelium and subepithelial microvasculature from the relatively avascular deep cervical stroma and detected cervical cancers in transgenic mice. The next challenge was determination of microvascular leak in premalignant cervical dysplasia using DCE-MRI. DCE-MRI of the lower female reproductive tract poses several unique data acquisition and analysis challenges, including the relatively small size of the target organs (only a few pixels in many images), bladder proximity, and respiratory motion

effects. Nonetheless, we successfully determined the transfer constant (K^{trans}), describing vascular permeability/leak in the cervical transformation zone. Within each of these groups of animals, we observed a wide range of K^{trans}, although the average values for transgenic and nontransgenic mice were indistinguishable. The DCE-MRI data were supported, in part, by the lack of detection of immunofluorescent analysis of Fc fragment leakage, although the molecular mass of this protein (50 kDa) was larger than Gadomer (17 kDa). Thus, the DCE-MRI data suggest that microvessels associated with dysplastic lesions at the midpoint of carcinogenic progression do not elaborate fenestrations or other leakage-associated structures (39) despite their increased density, abnormal morphology, and associated stromal inflammation (3, 4, 14).

In contrast, we were clearly able to detect and monitor the decrease in cervical microvasculature due to VEGF Trap (16, 17) in transgenic dysplasias. The antiangiogenic potency of VEGF Trap was highlighted by the marked 50% reduction in K^{trans} in VEGF Trap–treated compared with vehicle-treated transgenic mice. VEGF Trap also decreased dysplastic microvascular area to a level that was 25% lower than the estrogen-treated nontransgenic controls. These data suggested that VEGF was the predominant coordinator of angiogenesis of cervical dysplasia despite the documented contribution of platelet-derived growth factor-C and fibroblast growth factor-2 to this process in this model (4). These data also highlighted a correlation between K^{trans} and microvascular area within the 17-kDa pore size cutoff.

The lack of efficacy of VEGF Trap in ameliorating cervical dysplasia, despite its pronounced microvascular potency, suggests the need for combining antiangiogenic therapy with agents targeting dysplastic epithelium as in clinical scenarios for established malignancies (40). However, our study also highlights the ability of DCE-MRI to potentially detect reduction in the microvasculature that would likely accompany effective therapy for dysplasia. As a prominent goal of future prevention therapies is noninvasive ablation of high-risk dysplasia, DCE-MRI could become a valuable monitoring tool for treatment efficacy.

Disclosure of Potential Conflicts of Interest

No potential conflicts of interest were disclosed.

B.7. Acknowledgments

Received 4/17/09; revised 7/17/09; accepted 8/7/09; published OnlineFirst 9/29/09.

Grant support: NIH/National Cancer Institute Small Animal Imaging Resource Program grant U24 CA83060, Alvin J. Siteman Cancer Center at Washington University in St. Louis grant P30 CA91842, and Gynecological Cancer Division, Washington University in St. Louis School of Medicine.

The costs of publication of this article were defrayed in part by the payment of page charges. This article must therefore be hereby marked advertisement in accordance with 18 U.S.C. Section 1734 solely to indicate this fact.

We thank Justin Halder (University of Illinois-Urbana) for help with development of the Matlab-based analysis code, Gavin Thurston at Regeneron Pharmaceuticals for the generous gift of VEGF Trap, Krista Olsen and Aaron Lee for technical assistance, and Bayer Schering Pharma for the gift of Gadomer contrast agent.

B.8. References

1. Schiffman M, Castle PE, Jeronimo J, Rodriguez AC, Wacholder S. Human papillomavirus and cervical cancer. Lancet (N Am Ed) 2007;370:890–907.

2. Marshall K. Cervical dysplasia: early intervention. Altern Med Rev 2003;8:156–70.

3. Pahler JC, Tazzyman S, Erez N, et al. Plasticity in tumor-promoting inflammation: impairment of macrophage recruitment evokes a compensatory neutrophil response. Neoplasia (NY) 2008;10:329–40.

4. Pietras K, Pahler J, Bergers G, Hanahan D. Functions of paracrine PDGF signaling in the proangiogenic tumor stroma revealed by pharmacological targeting. PLoS Med 2008;5:e19.

5. Glunde K, Pathak AP, Bhujwalla ZM. Molecular-functional imaging of cancer: to image and imagine. Trends Mol Med 2007;13:287–97.

6. Herholz K, Coope D, Jackson A. Metabolic and molecular imaging in neuro-oncology. Lancet Neurol 2007;6:711–24.

7. Marcus CD, Ladam-Marcus V, Cucu C, Bouche O, Lucas L, Hoeffel C. Imaging techniques to evaluate the response to treatment in oncology: current standards and perspectives. Crit Rev Oncol Hematol. In press 2009.

8. Barrett T, Brechbiel M, Bernardo M, Choyke PL. MRI of tumor angiogenesis. J Magn Reson Imaging 2007;26: 235–49.

9. Jackson A, O'Connor JP, Parker GJ, Jayson GC. Imaging tumor vascular heterogeneity and angiogenesis using dynamic contrast-enhanced magnetic resonance imaging. Clin Cancer Res 2007;13:3449–59.

10. Jackson A, Buckley DL, Parker GJM, editors. Dynamic contrast-enhanced magnetic resonance imaging in oncology. Berlin: Springer; 2005.

11. Buckley DL. Uncertainty in the analysis of tracer kinetics using dynamic contrast-enhanced T1-weighted MRI. Magn Reson Med 2002;47:601–6.

12. Yankeelov TE, Rooney WD, Li X, Springer CS, Jr. Variation of the relaxographic ''shutter-speed'' for transcytolemmal water exchange affects the CR bolus-tracking curve shape. Magn Reson Med 2003; 50:1151–69.

13. ElsonDA, RileyRR, LaceyA,Thordarson G, Talamantes FJ, Arbeit JM. Sensitivity of the cervical transformation zone to estrogen-induced squamous carcinogenesis. Cancer Res 2000;60:1267–75.

14. Giraudo E, Inoue M, Hanahan D. An aminobisphosphonate targets MMP-9-expressing macrophages and angiogenesis to impair cervical carcinogenesis. J Clin Investig 2004;114:623–33.

15. Riley RR, Duensing S, Brake T, Munger K, Lambert PF, Arbeit JM. Dissection of human papillomavirus E6 and E7 function in transgenic mouse models of cervical carcinogenesis. Cancer Res 2003;63:4862–71.

16. Rudge JS, Thurston G, Davis S, et al. VEGF trap as a novel antiangiogenic treatment currently in clinical trials for cancer and eye diseases, and VelociGene-based discovery of the next generation of angiogenesis targets. Cold Spring Harbor Symp Quant Biol 2005;70:411–8.

17. Wachsberger PR, Burd R, Cardi C, et al. VEGF trap in combination with radiotherapy

improves tumor control in U87 glioblastoma. Int J Radiat Oncol Biol Phys 2007; 67:1526–37.

18. Garbow JR, Zhang Z, You M. Detection of primary lung tumors in rodents by magnetic resonance imaging. Cancer Res 2004;64:2740–2.

19. Christensen KA, Grant DM, Shulman EM, Walling C. Optimal determination of relaxation times of Fourier transform nuclear magnetic resonance. Determination of spin-lattice relaxation times in chemically polarized species. J Phys Chem 1974;78:1971–7.

20. Fram EK, Herfkens RJ, Johnson GA, et al. Rapid calculation of T1 using variable flip angle gradient refocused imaging. Magn Reson Imaging 1987;5: 201–8.

21. Buckley DL, Shurrab AE, Cheung CM, Jones AP, Mamtora H, Kalra PA. Measurement of single kidney function using dynamic contrast-enhanced MRI: comparison of two models in human subjects. J Magn Reson Imaging 2006;24:1117–23.

22. Tofts PS, Brix G, Buckley DL, et al. Estimating kinetic parameters from dynamic contrast-enhanced T(1)-weighted MRI of a diffusable tracer: standardized quantities and symbols. J Magn Reson Imaging 1999; 10:223–32.

23. Tofts PS. Modeling tracer kinetics in dynamic Gd-DTPA MR imaging. J Magn Reson Imaging 1997;7:91–101.

24. de Bazelaire CM, Duhamel GD, Rofsky NM, Alsop DC. MR imaging relaxation times of abdominal and pelvic tissues measured in vivo at 3.0 T: preliminary results. Radiology 2004;230:652–9.

25. Bottomley PA, Foster TH, Argersinger RE, Pfeifer LM. A review of normal tissue hydrogen NMR relaxation times and relaxation mechanisms from 1-100 MHz: dependence on tissue type, NMR frequency, temperature, species, excision, and age. Med Phys 1984;11:425–48.

26. Rohrer M, Bauer H, Mintorovitch J, Requardt M, Weinmann HJ. Comparison of magnetic properties of MRI contrast media solutions at different magnetic field strengths. Investig Radiol 2005;40:715–24.

27. Parker GJ, Roberts C, Macdonald A, et al. Experimentally-derived functional form for a population-averaged high-temporal-resolution arterial input function for dynamic contrast-enhanced MRI. Magn Reson Med 2006;56:993–1000.

28. Rijpkema M, Kaanders JH, Joosten FB, van der Kogel AJ, Heerschap A. Method for quantitative mapping of dynamic MRI contrast agent uptake in human tumors. J Magn Reson Imaging 2001;14:457–63.

29. Kovar DA, Lewis M, Karczmar GS. A new method for imaging perfusion and contrast extraction fraction: input functions derived from reference tissues. J Magn Reson Imaging 1998;8:1126–34.

30. Yankeelov TE, Luci JJ, Lepage M, et al. Quantitative pharmacokinetic analysis of DCE-MRI data without an arterial input function: a reference region model. Magn Reson Imaging 2005;23:519–29.

31. Faranesh AZ, Kraitchman DL, McVeigh ER. Measurement of kinetic parameters in skeletal muscle by magnetic resonance imaging with an intravascular agent. Magn Reson Med 2006;55:1114–23.

32. Golub GH, Pereya V. Separable nonlinear least squares: the variable projection method and its applications. Inverse Probl 2003;19:R1–26.

33. Smith-McCune K, Zhu YH, Hanahan D, Arbeit J. Cross-species comparison of angiogenesis during the premalignant stages of squamous carcinogenesis in the human cervix and K14-16 transgenic mice. Cancer Res 1997;57:1294–300.

34. Smith-McCune KK, Weidner N. Demonstration and characterization of the angiogenic properties of cervical dysplasia. Cancer Res 1994;54:800–4.

35. Arbeit JM, Howley PM, Hanahan D. Chronic estrogen-induced cervical and vaginal squamous carcinogenesis in human papillomavirus type 16 transgenic mice. Proc Natl Acad Sci U S A 1996;93:2930–5.

36. Lu ZH, Wright JD, Belt B, Cardiff RD, Arbeit JM. Hypoxia-inducible factor-1 facilitates cervical cancer progression in human papillomavirus type 16 transgenic mice. Am J Pathol 2007;171:667–81.

37. Shai A, Pitot HC, F. LP. p53 Loss synergizes with estrogen and papillomaviral oncogenes to induce cervical and breast cancers. Cancer Res 2008;68: 2622–31.

38. Brake T, Connor JP, Petereit DG, Lambert PF. Comparative analysis of cervical cancer in

women and in a human papillomavirus-transgenic mouse model: identification of minichromosome maintenance protein 7 as an informative biomarker for human cervical cancer. Cancer Res 2003;63:8173–80.

39. Nagy JA, Dvorak AM, Dvorak HF. VEGF-A and the induction of pathological angiogenesis. Annu Rev Pathol 2007;2:251–75.

40. Jain RK, Duda DG, Clark JW, Loeffler JS. Lessons from phase III clinical trials on anti-VEGF therapy for cancer. Nat Clin Pract Oncol 2006;3:24–40.

B.9. Figures and captions

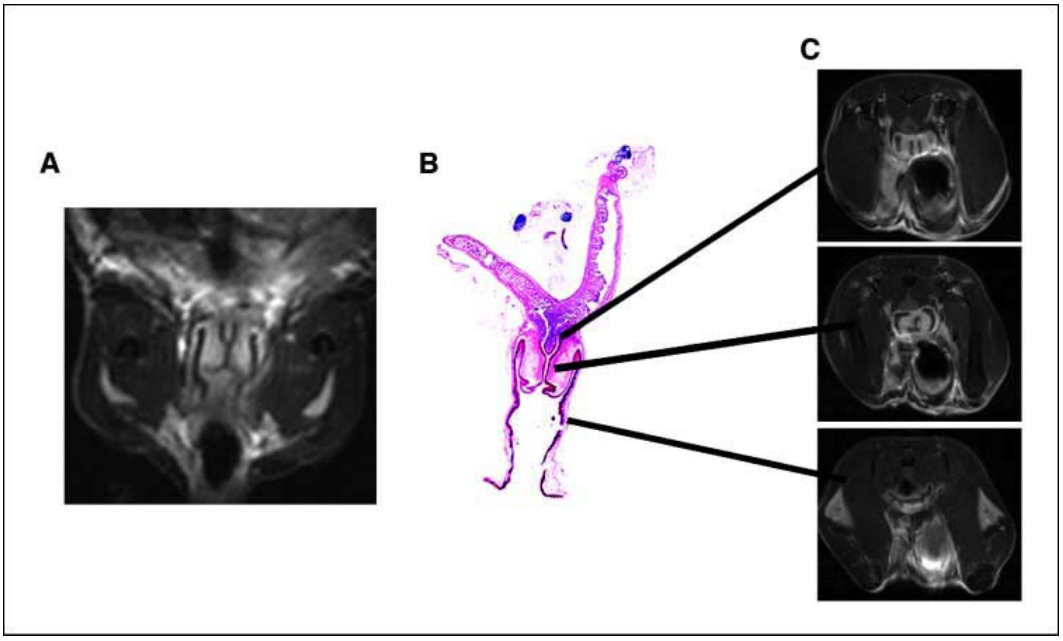

Figure 1. Development and histologic validation of MRI of the mouse female reproductive tact. Coronal MRI delineated the mouse reproductive tract, consisting of proximal cervical horns, cervix, and vagina (*A*). Low-power histology of the reproductive tract validated the coronal MR image and highlights the same regions (*B*). Axial MRI delineated the lower transformation zone (*C*, *top*), the cervical canal (*C*, *middle*), and the mid-vagina (*C*, *bottom*). Magnification, x12.5 (*B*).

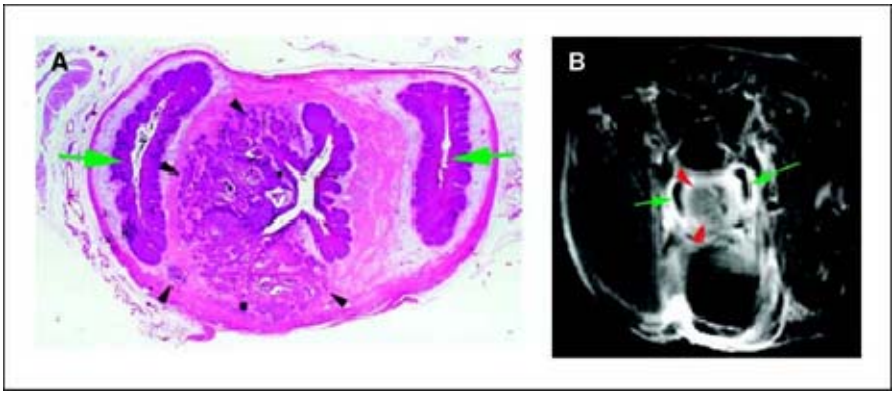

Figure 2. MRI detection of an invasive squamous cervical cancer. Paired transaxial MRI (*B*) and histologic cross-section of a cervix (*A*) obtained from a K14-HPV16 transgenic mouse treated with estrogen for 6 mo. A hyperintense lesion was detected extending from the upper to lower cervix on contrast agent–enhanced, T1-weighted images at the 6-mo time point (*B*, *red arrowheads*; *green arrows*, upper vagina). Matched cervical cross-sectional histology verified the cancer and distortion of the cervical canal (*A*, *black arrowheads*, cancer; *green arrows*, upper vagina). Magnification, x40 (*A*).

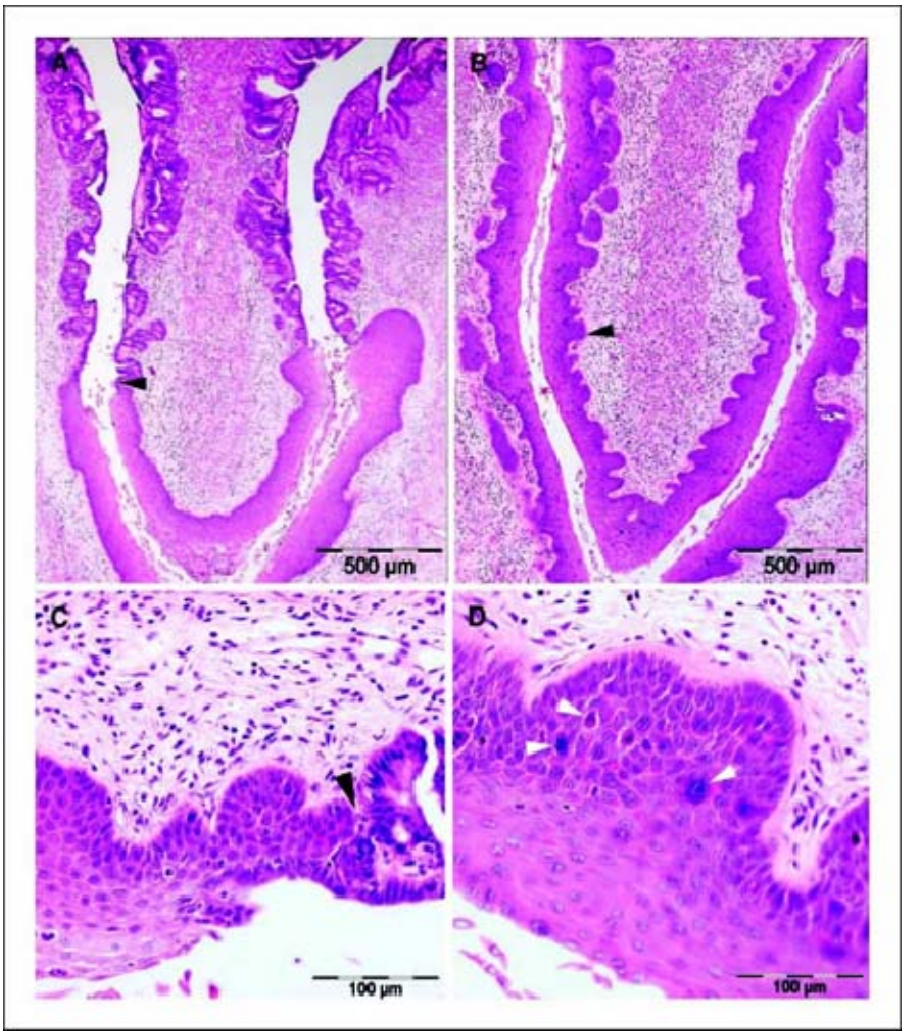

Figure 3. Histopathology of mid-to high-grade cervical dysplasia in estrogen-treated K14-HPV16 transgenic mice. Histologic images of transformation zones in 3-month-old, estrogen-treated nontransgenic (*A* and *C*) and transgenic (*B* and *D*) mice. The sharp demarcation of squamous with columnar epithelium in a nontransgenic mouse (*A* and *C*, *arrowheads*) contrasted with the squamous metaplasia of the transgenic cervix extending into the lower uterine horns (*B*). Papillation of the dysplastic transgenic epithelium was also evident (*B*, *arrowhead*). Mid-to high-grade dysplasia contained mitotic, apoptotic, enlarged, and anaplastic squamous epithelial cells (*D*, *white arrowhead* in clockwise orientation).

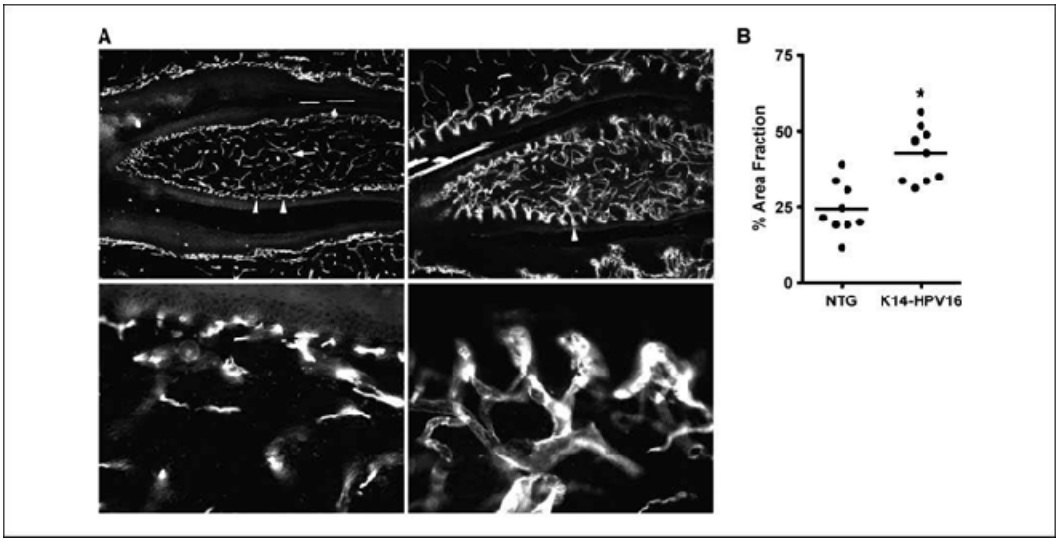

Figure 4. Microvascular anatomyand density in estrogen-treated cervices. Fluorescent images of FITC-conjugated L. esculentum lectin-perfused cervices from nontransgenic (*A*, *top* and *bottom left*) and transgenic (*A*, *top* and *bottom right*) mice revealed subepithelial and interior stromal microvascular compartments (*A*, *top left*, *arrowheads* and *arrow*, respectively). Subepithelial microvessels were linearly arrayed in nontransgenic (NTG) mice, whereas they formed tufts projecting into the neoplastic epithelium in transgenic mice (*A*, *top right*, *arrowhead*,and *bottom*). Microvessel quantification (see Materials and Methods) revealed a statisticallysignificant increase in subepithelial microvascular densityin the transgenic cervix (*B*).

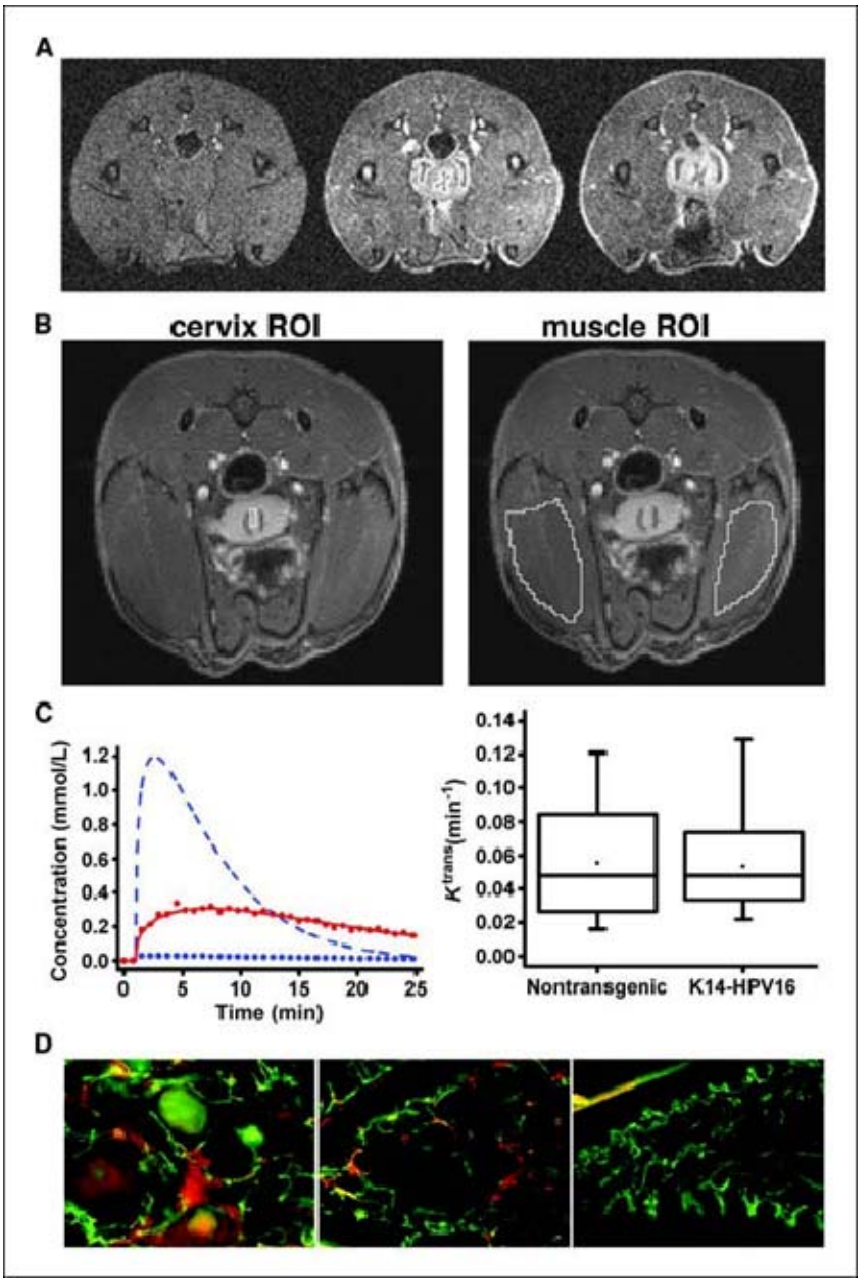

Figure 5. T1-weighted, gradient-echo images of the mouse female reproductive tract (*A*), showing the time course for contrast illumination of the pelvic internal iliac artery branches, the presumed epithelial/subepithelial tissue, followed by stromal permeation following i.v. injection of Omniscan (60 μL of 50 mmol/L contrast agent over 10 s). *A*, collected pre-contrast, 1-min post-contrast injection, and ~ 15 min post-injection. All other DCE-MRI data reported in this figure were collected following i.v. injection of Gadomer (60 μL of a solution that is 50 mmol/L Gd injected over 10 s). ROIs drawn in the cervical transformation zone (*B*, *left*) and in a reference muscle

region (*B*, *right*) were used to derive the AIF. For a typical mouse, the cervical transformation zone was defined by 30 to 50 pixels and the muscle region by 2,400 to 3,000 pixels. Contrast agent concentration versus time curves were constructed for a cervical transformation zone ROI: *red circles*, experimental data points; *red curve*, the model (*C*, *left*). The reference contrast agent concentration versus time curve for muscle, plotted with *blue circles*, and the derived AIF, shown as the *dashed blue curve* (*C*). K^{trans} values (*C*, *right*) for a ROI within the cervical transformation zone were statistically indistinguishable. *C*, *right*, the horizontal line within each box is the median value of K^{trans}, the dot at the middle of each box is the mean, the edges of the box are ± 1 SD, and the whiskers are the maximum and minimum values. Injection of sheep Fc fragment (50 kDa) and immunofluorescent analysis showed leakage in a large cervical cancer in a 6-month-old, estrogen-treated transgenic mouse (*D*, *left*), and adjacent dysplasia (*D*, *middle*), whereas leak was undetectable in the 3-month-old, estrogen-treated transgenic cervix (*D*, *right*).

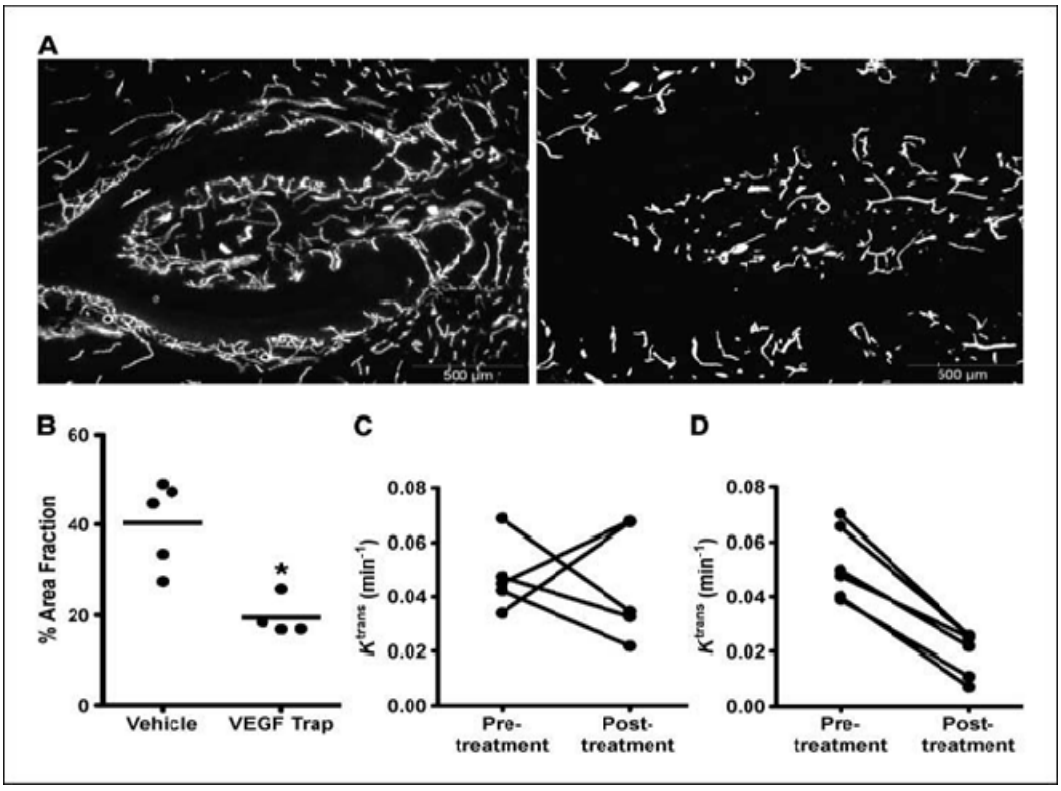

Figure 6. Effect of VEGF Trap on the transgenic cervical microvasculature. VEGF Trap treatment of transgenic mice produced a marked pruning of the cervical microvasculature in VEGF Trap (*A*, *right*), compared with vehicle control transgenic mice (A, left), with a statistically significant decrease in subepithelial microvascular area (*B*). DCE-MRI detected a significant decrease in microvessel leakage within VEGF Trap–treated transgenic mice (*D*) compared with lack of significance within the highly variant vehicle-treated transgenic group (*C*). *, $P < 0.05$, Mann-Whitney *U* test (*B*) or paired Student's *t* test (*C* and *D*).

APPENDIX C. REPRINT OF MAGNETIC RESONANCE IMAGING OF HYPOXIC INJURY TO THE MURINE PLACENTA

C.1. Abstract

Tomlinson TM, Garbow JR, Anderson JR, Engelbach JA, Nelson DM, Sadovsky Y. Magnetic resonance imaging of hypoxic injury to the murine placenta. *Am J Physiol Regul Integr Comp Physiol* 298: R312–R319, 2010. First published November 18, 2009; doi:10.1152/ajpregu.00425.2009.—We assessed the use of magnetic resonance imaging (MRI) to define placental hypoxic injury associated with fetal growth restriction. On embryonic *day 18.5* (E18.5) we utilized dynamic contrast-enhanced (DCE)-MRI on a 4.7-tesla small animal scanner to examine the uptake and distribution of gadolinium-based contrast agent. Quantitative DCE parameter analysis was performed for the placenta and fetal kidneys of three groups of pregnant C57BL/6 mice: *1*) mice that were exposed to $F_{I_{O2}}$ = 12% between E15.5 and E18.5, *2*) mice in normoxia with food restriction similar to the intake of hypoxic mice between E15.5 and E18.5, and *3*) mice in normoxia that were fed ad libitum. After imaging, we assessed fetoplacental weight, placental histology, and gene expression. We found that dams exposed to hypoxia exhibited fetal growth restriction (weight reduction by 28% and 14%, respectively, $P < 0.05$) with an increased placental-to-fetal ratio. By using MRI-based assessment of placental contrast agent kinetics, referenced to maternal paraspinous muscle, we found decreased placental clearance of contrast media in hypoxic mice, compared with either control group (61%, $P < 0.05$). This was accompanied by diminished contrast accumulation in the hypoxic fetal kidneys (23%, $P < 0.05$), reflecting reduced transplacental gadolinium transport. These changes were associated with increased expression of placental *Phlda2* and *Gcm1* transcripts. Exposure to hypoxia near the end of mouse pregnancy reduces placental perfusion and clearance of contrast. MRI-based DCE imaging provides a novel tool for dynamic, in vivo assessment of placental function.

C.2. Publication information

C.2.1. Reference

Magnetic resonance imaging of hypoxic injury to the murine placenta. *Am J Physiol Regul Integr Comp Physiol* 298: R312–R319, 2010.

C.2.2. Title

Magnetic resonance imaging of hypoxic injury to the murine placenta

C.2.3. Authors

Tracy M. Tomlinson[1], Joel R. Garbow[2], Jeff R. Anderson[3], John A. Engelbach[2], D. Michael Nelson[1], and Yoel Sadovsky[4]

C.2.4. Affiliation

[1]Department of Obstetrics and Gynecology, [2]Department of Radiology, [3]Department of Chemistry, Washington University, St. Louis, Missouri, and [4]Magee Womens Research Institute, Department of Obstetrics, Gynecology and Reproductive Sciences, University of Pittsburgh, Pittsburgh, Pennsylvania, USA.

C.2.5. Request for Reprints and other correspondence

Y. Sadovsky, Magee-Womens Research Institute, 204 Craft Ave. Rm. A608, Pittsburgh, PA 15213 (e-mail: ysadovsky@mwri.magee.edu).

C.2.6. Copyright

© 2010 by the American Physiological Society. ISSN: 0363-6119, ESSN: 1522-1490.

C.2.7. DOI

doi: 10.1152/ajpregu.00425.2009

C.2.8. Key words

Placenta; DCE-MRI; fetal growth restriction; hypoxia

C.3. Introduction

FETAL GROWTH RESTRICTION (FGR) complicates up to 8% of all pregnancies, adversely impacts perinatal outcome, and results in life-long complications for adult survivors (14). Placental insufficiency is the major cause of FGR in developed countries, where it remains prevalent despite improvements in obstetrical care. Diverse causes of placental injury, such as chronic hypertension, preeclampsia, connective tissue disease, diabetes, and abruption, alter placental perfusion and may cause hypoxic and reperfusion injury (42).

Doppler ultrasound is useful in assessing FGR-related blood flow changes in the preplacental (uterine) and postplacental (umbilical, fetal) vasculature (1, 21). While the detection of these changes has limited diagnostic value, changes in post-placental flow are presently used to assist clinicians in management and timing of delivery of pregnancies with an established diagnosis of FGR (1, 30). Notably, Doppler ultrasound detects umbilical vessel flow changes that result from parenchymal damage but cannot directly assess intraplacental per-fusion abnormalities (1, 28, 30).

Magnetic resonance imaging (MRI) offers superb visualization of anatomy and allows quantitative analysis of spatial and temporal changes in tissue morphology. MRI studies of placental anatomy and perfusion have been conducted in different species (16, 29, 31, 35, 36, 44, 51). Contrast agents (typically gadolinium-based chelates) were noted to easily cross the placental barrier in both the mouse and human placenta, and appeared in the fetal bladder soon after maternal intravenous administration (8, 49, 52). Dynamic contrast-enhanced (DCE) MRI is a powerful imaging technique for characterizing tissue vasculature. In DCE-MRI experiments, time-resolved images are collected as contrast agent washes in and out of the tissue, providing insight into blood flow, fractional blood volume, and vascular permeability (18, 53).

Mice are particularly useful for studying placental biology. Akin to the human placenta,

the mouse placenta is hemochorial, with maternal blood perfusing labyrinthine trophoblasts in a manner analogous to the branched villous tree that is bathed by the maternal human intervillous space (2, 10). In addition, the mouse is particularly amenable to targeted mutations, designed to analyze mechanisms underlying placental development and function (41). Not surprisingly, we previously found that several genes that are critical for murine placental development also regulate the differentiation of human trophoblasts (20, 39, 46, 47).

Hypoxia hinders the process of cytotrophoblast differentiation, induces apoptosis, and diminishes hormone production in the human placenta (9, 21, 25, 34). Exposure to hypoxia during murine pregnancy results in FGR (15, 27), although the precise mechanism underlying placental villous injury during hypoxia is unclear. Specifically, it is not known whether systemic hypoxia elicits preplacental hypoperfusion or causes placental parenchymal perfusion abnormalities. To elucidate mechanisms underlying placental hypoxic injury associated with FGR, we hypothesized that dynamic MR imaging could help to define hypoxia-induced placental dysfunction.

C.4. Materials and Methods

Animals. Care for the mice and all procedures were conducted in the Association for Assessment and Accreditation of Laboratory Animal Care-approved facility of Washington University School of Medicine in accordance with the standards set forth in the Guide for the Care and Use of Laboratory Animals of the National Institutes of Health. All experimental procedures were approved by the Animal Studies Committee of Washington University.

Experiments were performed using pregnant C57BL/6 mice. Timed matings were carried out by pairing strain-matched males and nulligravida females for one night, with the morning after mating designated as embryonic *day 0.5* (E0.5). Pregnancy was assumed based on a 10% weight gain on E10.5. Mice were kept under constant conditions until *day E15.5*. They were given a standard rodent chow and water ad libitum, and kept on a 12:12-h light-dark cycle in room air. Deliveries typically occur in these mice on E19.5. All procedures were initiated on E15.5, when the mice were allocated to one of three groups: *1*) exposure to $F_{I_{O2}}$ = 12% between E15.5 and E18.5 (hypoxic or Hpx group), *2*) exposure to normoxia with food restriction similar to the intake

of hypoxic mice between E15.5 and E18.5 (N-FR group), and *3*) exposure to normoxia with ad libitum feeding (N-AL group).

Body weight and food intake were recorded daily. Food matching between the N-FR and Hpx groups was based on daily assessment of food intake by mice in the Hpx group. For normobaric hypoxia exposure we used a Polymer Hypoxic Glove Box with a Purge Airlock system with CO_2 and O_2 control indicators (Coy Laboratory Products, Grass Lake, MI), which is specifically designed for experiments in live rodents and regulates ambient temperature, humidity, and gas composition. Oxygen concentration was maintained within a narrow preset range by introducing small amounts of nitrogen as required. The main chamber has a connected side chamber, equipped with a separate door to allow uninterrupted maintenance of a predefined F_{IO2} when the mice and their food were weighed daily. Dams were euthanized by CO_2 asphyxiation following MR imaging on E18.5 (see below). Embryos and placentas were collected immediately after death, weighed, and processed for further analysis (see below).

Imaging procedure. All MR images were collected and analyzed in Washington University's Biomedical MR Laboratory. Images were acquired with a small-animal MR scanner based on an Oxford Instruments (Oxford, UK) 4.7 tesla, 40-cm bore magnet. The magnet is equipped with Magnex Scientific (Oxford, UK) actively shielded, high-performance (10 cm ID, 60 gauss/cm, 100 μs rise time) gradient coils and Techron gradient power supplies and is interfaced with a Varian NMR Systems (Palo Alto, CA) INOVA console. Data were collected using a Stark Contrast (Erlangen, Germany) 3-cm diameter birdcage radio frequency (RF) coil. Prior to the imaging experiments, mice were anesthetized with isoflurane and were maintained on an isoflurane/O_2 inhalation mixture (1–1.5% vol/vol) throughout data collection. Animal core body temperature was supported at 37 ± 1°C by circulation of warm air through the bore of the magnet. Dams in the Hpx group were removed from the hypoxia chamber 1 h before imaging on the morning of E18.5. Hence, none of the dams were hypoxic during scanning.

Sagittal, axial, and coronal scout images were collected to ensure correct positioning of the animal within the RF coil, allowing visualization of all fetoplacental units. Images were acquired with a field of view of 30 × 30 mm^2 (transaxial) or 40 × 40 mm^2 (sagittal, coronal) and a

data matrix of 128 × 128, leading to an in-plane resolution of 234 μm (transaxial) or 313 μm (sagittal, coronal). Eighteen to twenty-two contiguous, 1-mm thick slices were acquired to cover all of the fetoplacental units.

DCE-MRI experiments were performed using a T_1-weighted two-dimension multislice gradient echo sequence. Typical imaging parameters were: repetition time (TR) = 100 ms, echo time (TE) = 2 ms, flip angle (α) = 30°, and eight signal averages; producing a temporal resolution of ~100 s. Two baseline images were acquired at the start of the time course and the contrast agent was administered prior to the collection of 28 additional images. Total imaging time for the DCE experiment was ~50 min.

Contrast agent*s* an*d* contras*t* distributio*n* control*s.* A standard gadolinium chelate (gadoversetamide, OptiMark; Covidien, St. Louis, MO) injected on a weight-based protocol was used throughout. Injection was performed via a 28-gauge catheter that was placed into the internal jugular vein prior to the start of imaging. To characterize placental transport to the fetus, a single bolus of 2.7 μl/g of undiluted contrast, corresponding to a gadolinium concentration of 2 mmol/kg, was administered over 10 s using a Harvard 2 dual syringe pump (Harvard Clinical Technology, South Natick, MA). To define the systemic distribution of contrast under different physiological conditions, DCE-MRI (1:10 dilution of contrast agent, 0.2 mmol/kg; 33 s temporal resolution) was performed on four groups of dams: normoxic pregnant, hypoxic pregnant, normoxic nonpregnant, and hypoxic nonpregnant. Gadolinium distribution was measured in the paraspinous muscles in these paradigms, and these data served as a reference for the placental flow results, as described below.

DCE data analysis. Regions of interest (ROIs) were drawn over the placentas, paraspinous muscle, and fetal kidneys by a single operator (T. M. Tomlinson) using ImageJ (http://rsbweb.nih.gov/ij). Although not blinded to the experimental group of the dam being analyzed, this operator followed standard procedures for unbiased ROI selection. These procedures were determined prior to data analysis. Placentas analyzed were those that could be easily visualized in sagittal images of the dam and around which ROIs could be clearly drawn. The coronal slice chosen for each placenta's time course analysis was the one having the largest

(midplacental) cross-section in the sagittal image. Similarly, for fetal kidney analysis, the kidney ROI was drawn on the coronal slice that provided the largest image of the kidney.

All subsequent image analysis calculations were performed in Matlab (Mathworks, Natick, MA) by using programs developed in our laboratory. Assuming the fast-exchange limit, signal intensity data for placenta and muscle were converted to concentrations by standard methods (18) using *Eq. 1* and *Eq. 2*.

$$\frac{1}{T_1(t)} = \frac{-1}{TR} \cdot \ln\left[\frac{\frac{S(t)}{S(0)} \cdot \left(e^{\frac{TR}{T_1(0)}} - 1 \right) - e^{\frac{TR}{T_1(0)}} + \cos(\alpha)}{\frac{S(t)}{S(0)} \cdot \left(e^{\frac{TR}{T_1(0)}} - 1 \right) \cdot \cos(\alpha) - e^{\frac{TR}{T_1(0)}} + \cos(\alpha)} \right] \quad (1)$$

$$\frac{1}{T_1(t)} = \frac{1}{T_1(0)} + r_1[CA(t)] \quad (2)$$

Here, S(t) is the signal at *time t*, S(0) is the signal in the absence of contrast agent (CA), $T_1(t)$ is the longitudinal relaxation rate constant at *time t*, $T_1(0)$ is the longitudinal relaxation rate constant in the absence of CA, TR and α are the repetition time and flip angle of the pulse sequence, respectively, [CA] is the concentration of the contrast agent, and r_1 is the relaxivity of the CA [4.4 mmol/s (40)]. Precontrast $T_1(0)$ values for both murine paraspinous muscles and term placentas were determined from a series of T_1-weighted spin-echo images.

In the fetal kidneys, in which $T_1(0)$ could not be measured, relative signal increase, itself proportional to contrast agent concentration, was calculated (18).

$$\frac{S(t) - S(0)}{S(t)} \alpha [CA(t)] \quad (3)$$

Intradam variations in image intensity (placenta and fetal kidney) were partly attributed to variations in RF coil sensitivity and to fetal position within the coil. To account for these variations, a straightforward normalization procedure was adopted. This normalization assumed the same vascular input function for all placentas/fetuses within a given dam, a reasonable assumption given that each dam received a single bolus injection of contrast agent. For each placenta, an individual concentration vs. time curve was calculated, and an average concentration curve for all

placentas within a specific dam was then computed. Next, each individual placenta's concentration vs. time curve was compared analytically, on a point-by-point basis, with the placental average concentration curve for its corresponding dam. A single scale factor was derived for each placenta by performing a linear, least-squares minimization of the variation between these curves. Finally, for each placenta, all data values were multiplied by its computed scale factor. This normalization procedure has the effect of scaling the overall intensity without altering the shape of the individual placental concentration curves. An analogous procedure was followed for normalizing the relative signal intensity curves for each fetal kidney within a given dam.

Complete characterization of the complex vasculature of the placenta, which contains multiple permeable barriers and compartments, is beyond the scope of small-animal DCE-MRI. While a full kinetic analysis is not possible, the time course DCE data can still be quantified using a model-free parameter approach (18). In all cases, analysis of DCE data requires accurate knowledge of the concentration of the CA in the blood throughout the time course experiment, a factor known as the arterial input function (AIF). Traditionally, the AIF is measured from a large vessel within the image, taking care to avoid inflow and partial volume artifacts (18, 37, 38). However, determining the AIF directly is difficult in mice, due to small spatial dimensions and the effects of motion. Instead, in analogy to our model-free analysis of the DCE data, we can derive a model-free vascular input parameter from a reference tissue, such as muscle (23, 55). As detailed below, we then computed the ratio of CA concentration in the placenta to that in the reference tissue, as previously described (13).

Quantification of dynamic data was achieved using three model-free parameters: initial area under the curve (IAUC), final slope, and area under the curve (AUC) (18). The IAUC was evaluated for the first 1,200 s postinjection ($IAUC_{1200}$) by calculating the areas under each placental concentration curve and the corresponding curve for paraspinous muscle from *time 0* to 1,200 s postinjection. Placental values were then referenced to the muscle signal by forming the ratio $IAUC_{1200,\ placenta}/IAUC_{1200,\ muscle}$ (13). The final slope was calculated by measuring the slope of each placental concentration curve from 1,300 s to 2,800 s postinjection. The complexity of

transport of contrast agent to the fetal kidneys, with numerous points of (bidirectional) transfer, prevents the calculation of CA concentration in these organs. Instead, AUC was calculated for each fetal kidney by calculating the area under its relative signal curve. As with IAUC in placenta, these values were normalized by forming the ratio $AUC_{kidney}/AUC_{placenta}$, where for each fetal kidney, $AUC_{placenta}$ is the area under the relative signal vs. time curve for its corresponding placenta.

Placental histology. Each placenta was divided in half by making a midline incision immediately adjacent to the cord insertion site, from the chorionic to the basal plate. One half was randomly selected for routine histology processing, following fixation overnight in fresh 4% paraformaldehyde. Tissues were dehydrated with alcohol, embedded in paraffin blocks, and cut into 5-[m sections. The sections were stained using standard hematoxylin and eosin staining and qualitatively evaluated for changes in the labyrinthine, spongiotrophoblast, and giant cell layers as routinely performed in our lab (47). To enhance assessment of the spongiotrophoblast layer, parallel slides from a portion of the placentas were stained with periodic acid Schiff staining (4, 47).

Assessment of gene expression using quantitative RT-PCR. The second half of each harvested placenta was snap frozen in liquid nitrogen and stored at -80°C for RNA isolation. RNA was extracted as previously described (47). Complementary DNA was prepared from 1 µg RNA in 50 µl reaction volume using the TaqMan Gold RT-PCR kit with the supplied random hexamer primers (Applied Biosystems, Foster City, CA). Quantitative PCR was performed in duplicate using 3 µl samples of cDNA and 12.5 µl SYBR Green PCR Master Mix (Applied Biosystems) in a total reaction volume of 25 µl that contained 300 nM of forward and reverse primers. Reactions were run and analyzed using Applied Biosystems Geneamp 7300 Sequence Detection Systems. Dissociation curves were performed on all reactions to ensure amplification of a single product with the appropriate melting temperature. The transcript levels were normalized to the housekeeping gene L32 RNA levels, and the data expressed as fold change relative to a single N-AL control placenta. The fold increase relative to control cultures was determined by the ΔΔCt method (26). All PCR primer pairs were checked for specificity using BLAST analysis. The list of

primers is provided in Table 1.

Statistics. We calculated our sample size based on attainment of 20% reduction in embryo weight in the Hpx group compared with the N-AL group. To achieve this difference at 80% power and $\alpha = 0.05$ required at least 12 dams in each paradigm. Data are expressed as means ± SD, and statistical significance was determined using the one-way ANOVA and Bonferroni post hoc test. Significance was determined at $P < 0.05$. For the data in Fig. 4, which are further analyzed in Table 2, we plotted binned data and confirmed symmetrical or near-symmetrical distributions about the means.

C.5. Results

Maternal food consumption and weight. We first sought to examine the effect of normobaric hypoxic environment on maternal food intake and weight gain. We exposed pregnant mice to $F_{I_{O2}}$ = 12% or to standard atmosphere over a period of 3 days at the end of pregnancy (E15.5–E18.5) with ad libitum supply of chow. We found that dams in the Hpx group (*n* = 22) exhibited lower food intake on the first day in hypoxia (Fig. 1*A*). Although food intake by hypoxic dams was increased in the subsequent 2 days in hypoxia, it remained lower than that of the N-AL dams (*n* = 25). Therefore, to control for food intake, we generated a third group, N-FR dams (*n* = 15), in which food was restricted to match exactly that of hypoxic dams (Fig. 1*A*). As expected, maternal weight gain in the N-AL group over the 3 days of the experiment was markedly higher than that of N-FR or Hpx groups (Fig. 1*B*).

Fetal and placental weights. As shown in Fig. 2*A*, murine pups (*n* = 126) harvested on E18.5 from Hpx dams were significantly smaller than pups from the N-FR dams (*n* = 99), which, in turn, were significantly smaller than those from N-AL dams (*n* = 113). We also observed a small, but statistically significant, difference in mean placenta weights from each of the three cohorts, with the largest placentas originating from the N-AL dams and the smallest from the N-FR dams (Fig. 2*B*). Not surprisingly, the placental-to-fetal ratio was greatest in the Hpx group (Fig. 2*C*). We found no significant differences in mean litter size (N-AL = 7.5, N-FR = 8.3, Hpx = 8.4). Fetal survival was > 95% in all three groups.

Fetoplacental MR and DCE imaging. Representative contrast-enhanced MR images of mouse fetuses and placentas placentas on E18.5 are shown in Fig. 3. Maximum placental enhancement by the contrast agent was observed at 7–10 min following contrast injection, with fetal enhancement lagging behind that of the placenta. Control experiments revealed that pregnancy did not noticeably impact the systemic distribution of contrast agent. Muscle-derived measures of vascular gadolinium concentration were used for referencing all of the placental data (see Materials and Methods).

DCE analysis of transplacental gadolinium distribution in each of the three experimental groups was limited to placentas that were reliably identified in coronal sections. $T_1(0)$ values for placenta (1.8 s) and paraspinous muscle (1.4 s) were computed from representative T_1 maps of the placenta and paraspinous muscle (reference tissue). CA concentrations, as a function of time, were calculated as described in Materials and Methods. Fig. 4 depicts representative concentration curves for one dam from each of the three experimental groups. IAUC was calculated for all placentas on a per dam basis. This calculation revealed a statistically significant difference in $IAUC_{1200}$ for the N-FR mice relative to the N-AL and Hpx groups (Table 2). Furthermore, while contrast concentration decreased in all placentas toward the end of the measurement period, the concentration in Hpx placentas decreased at a significantly slower rate compared with the other two groups (Table 2). Figure 5 highlights the difference in residual placentas and control. Together, these data point to greater washout of contrast from the N-AL and N-FR placentas compared with the Hpx placentas.

We anticipated that both maternal and fetal blood flow might contribute to contrast clearance from the placenta. Noting enhancement of the fetal kidneys early in the experimental time course, we sought to assess contrast accumulation in the fetal kidneys as a surrogate for fetal clearance of placental contrast. The adjusted fetal kidney AUC was lower in the Hpx group than in the N-AL group (Fig. 6), suggesting diminished transfer of contrast agent to the Hpx fetuses.

Placental histology and gene expression. To determine whether the perfusion changes assessed using DCE imaging were associated with discrete placental morphological changes, we

examined the placentas from the three experimental group using hematoxylin and eosin and periodic acid Schiff staining. While the placentas from the Hpx and N-FR groups were smaller than those from N-AL, we could not detect any differences in thicknesses of the labyrinth, spongiotrophoblast, or giant cell layers. Similarly, we did not identify any differences in labyrinth density, dilatation of the labyrinthine blood spaces, or any other discrete structural alterations (data not shown). To expand our assessment of region-specific changes, we measured the expression of several placental genes that are expressed in specific layers of the murine placenta. As shown in Fig. 7, the expression of labyrinthine *Gcm1* and *Phlda2* was increased in placentas from Hpx dams relative to those derived from the N-FR controls. No significant differences were found between these two groups in the expression level of spongiotrophoblastic Tpbpa and Mash2, or in the level of Plf (primarily giant cells), although some of the genes exhibited decreased expression in one or both injured groups relative to the N-AL controls.

C.6. Discussion

We used DCE-MRI with gadolinium contrast to assess placental perfusion in a mouse model of hypoxia at the end of pregnancy. We found that the initial uptake of contrast was similar for the Hpx and N-AL mice. The uptake was delayed in the Hpx mice compared with the N-FR mice, possibly reflecting reduced perfusion in hypoxia-exposed mice. Importantly, the clearance of contrast was reduced in the Hpx placentas, which manifested as a lower final slope of the gadolinium concentration vs. time curve in the Hpx group relative to the two normoxic controls. We emphasize that these results were normalized to the arterial input function, derived by assessing perfusion of a reference tissue, thereby correcting to general alterations in perfusion.

The initial appearance of contrast in the chorionic plate is consistent with rapid labyrinth perfusion by maternal blood, delivered directly from the uterine spiral arteries via central arterial canals into labyrinthine sinusoids (2). Our data suggest that the clearance of contrast from the adjacent labyrinth was slowed in Hpx placentas. Whereas our findings are consistent with the notion that hypoxia influences preplacental vasoconstriction (17), our data illuminate hypoxia-induced changes within the labyrinth, the site of maternal-fetal exchange in the murine placenta

(7, 32). Finally, we found that the accumulation of contrast in the kidneys of fetuses of Hpx dams was reduced. While we cannot rule out a direct influence of hypoxia on fetal renal function, our findings are consistent with diminished fetal perfusion.

We induced FGR using global maternal hypoxia for 3 days, as described previously (11, 48, 54). Importantly, the level of FGR, placental weight, and mean placenta-to-fetus ratio achieved in our studies was similar to that achieved by others (11, 22, 24). Furthermore, we did not observe an increase in fetal mortality, which might have introduced an additional variable. Because there is a plateau in murine placental growth after E14 (50), it is not surprising that we observed a minimal effect of E15.5 injury on placental size. We note that DCEMRI measurements were performed in standard atmospheric oxygen. Rather than hemodynamic changes that might be found during hypoxia, our results reflect tissue changes that were caused by hypoxia, but detected after the insult. We also did not rule out the possibility that some of the observed changes could have reflected reoxygenation injury, which might have taken place immediately prior to imaging. Nevertheless, we find it less likely that the FGR, CA dynamics changes, and altered gene expression could have been explained by changes that occurred over a brief reoxygenation period (2 h or less at the end of the experiment).

In vivo dynamic imaging of fetoplacental perfusion in mice poses a significant technological challenge (44, 51). First, high-quality DCE-MRI data must be acquired for several fetoplacental units within each pregnant dam. Second, these data must be referenced to an appropriate measure of vascular input, derived in our case from paraspinous muscle reference tissue. Third, a detailed evaluation of the fetus via imaging of the fetal kidney requires a higher dose of contrast agent than is commonly administered when imaging the dam. Despite these challenges, we were able to perform a quantitative analysis of temporal changes in contrast-medium concentration in both the placenta and fetal kidney. The accuracy of our measurements was limited by the subjective choice of ROIs, defined for analysis of the DCE images. In addition, partial volume effects could have contributed to errors in these measurements. Because of their small size and fetal movements, measurements of fetal kidney were particularly prone to this limitation. Finally, heterogeneity among mice within a given experimental group and among the

fetoplacental units within each dam accounts, in part, for the variability in measurements that was independent of the experimental paradigm.

Our analysis of placental histology was restricted to morphological changes that might be identified using standard staining techniques. The lack of clear evidence for tissue damage likely reflects the short duration of injury that was inflicted at a relatively late point in gestation, after the period of rapid placental growth. Using quantitative PCR to probe for tissue response to hypoxia, we found that the expression of *Phlda2*, a maternally imprinted gene that is expressed mainly in the labyrinth and negatively regulates placental growth (5, 43), was increased in placentas from the Hpx group compared with N-FR controls. In Hpx placentas we also detected a small yet statistically significant increase in the expression of *Gcm1*, a gene associated with labyrinthine layer branching and differentiation (3, 6, 33). In contrast, we did not detect any significant change in the expression of Tpbpa, Mash2, or Plf1 between the Hpx and N-FR groups (12, 19). Although the role of these gene products in placental response is presently uncertain, our results point to concomitant changes in expression of labyrinthine genes that are expressed in regions of placental exchange function. These changes might be a part of a placental adaptive response to hypoxic injury. Notably, our analysis was restricted to histological changes, and therefore, we cannot rule out mild changes in labyrinthine fetal or maternal blood spaces that might have been uncovered using more refined stereology or electron microscopy. Interestingly, using pregnant mice prior to full placental development (E7.5–E10.5), Schaffer et al. (45) showed that short-term normobaric hypoxia (6–24 h) influenced primarily the giant cells and spongiotrophoblasts, with no evidence for hypoxic changes in the labyrinth. These differences may reflect the fact that our mice were exposed to hypoxia for a longer interval during the embryonic maturation phase, not the developmental period.

Perspectives and Significance. Although placental insufficiency is one of the leading causes of perinatal morbidity and mortality worldwide, our limited understanding of its pathophysiology has hindered the development of new diagnostic tools for this condition or successful prophylactic or therapeutic interventions designed to mitigate fetoplacental injury. DCE-MR is a novel imaging tool for in vivo assessment of placental function. The combination of

DCE-MRI and gene-expression analysis in placentas exposed to hypoxic injury may illuminate unrecognized pathways in placental adaptation to hypoxic injury. In addition to its research use to interrogate patterns of blood flow in the injured placenta, DCE-MRI may have clinical utility for the detection of placental injury in women at risk for FGR.

C.7. Acknowledgements

We thank Joseph J. H. Ackerman and J. J. Neil, Washington University, St. Louis, MO, for helpful discussions, and S. L. Adamson, University of Toronto, for critically reading the manuscript. We also thank Lori Rideout for editorial assistance.

Present address of T. Tomlinson: Medical College of Wisconsin Maternal Fetal Care Center, Milwaukee, Wisconsin.

Data from this study were presented, in part, at the 29th meeting of the Society for Maternal Fetal Medicine, San Diego, CA, January 2009.

C.8. Grants

This project was supported by the ACOG/Ortho-McNeil Fellowship Training Grant (to T. M. Tomlinson), the National Institutes of Health/National Cancer Institute Small Animal Imaging Resource Program Grant U24-CA83060 (to J. R. Garbow and J. R. Anderson), and National Institutes of Health Grants R01-HD-29190 (to D. M. Nelson) and R01-HD-45675 and R01-ES-011597 (to Y. Sadovsky).

C.9. Disclosures

No conflicts of interest are declared by the author(s).

C.10. References

1. **Abramowicz JS, Sheiner E.** In utero imaging of the placenta: importance for diseases of pregnancy. *Placenta* 28, *Suppl A*: S14–S22, 2007.

2. **Adamson SL, Lu Y, Whiteley KJ, Holmyard D, Hemberger M, Pfarrer C, Cross JC.**

Interactions between trophoblast cells and the maternal and fetal circulation in the mouse placenta. *Dev Biol* 250: 358–373, 2002.

3. **Anson-Cartwright L, Dawson K, Holmyard D, Fisher SJ, Lazzarini RA, Cross JC.** The glial cells missing-1 protein is essential for branching morphogenesis in the chorioallantoic placenta. *Nat Genet* 25: 311–314, 2000.

4. **Antonson P, Schuster GU, Wang L, Rozell B, Holter E, Flodby P, Treuter E, Holmgren L, Gustafsson JA.** Inactivation of the nuclear receptor coactivator RAP250 in mice results in placental vascular dysfunction. *Mol Cell Biol* 23: 1260–1268, 2003.

5. **Apostolidou S, Abu-Amero S, O'Donoghue K, Frost J, Olafsdottir O, Chavele KM, Whittaker JC, Loughna P, Stanier P, Moore GE.** Elevated placental expression of the imprinted PHLDA2 gene is associated with low birth weight. *J Mol Med* 85: 379–387, 2007.

6. **Basyuk E, Cross JC, Corbin J, Nakayama H, Hunter P, Nait-Oumesmar B, Lazzarini RA.** Murine Gcm1 gene is expressed in a subset of placental trophoblast cells. *Dev Dyn* 214: 303–311, 1999.

7. **Brosens I, Robertson WB, Dixon HG.** The physiological response of the vessels of the placental bed to normal pregnancy. *J Pathol Bacteriol* 93: 569–579, 1967.

8. **Chapon C, Franconi F, Roux J, Le Jeune JJ, Lemaire L.** Prenatal evaluation of kidney function in mice using dynamic contrast-enhanced magnetic resonance imaging. *Anat Embryol (Berl)* 209: 263–267, 2005.

9. **Chen B, Nelson DM, Sadovsky Y.** N-myc down-regulated gene 1 modulates the response of term human trophoblasts to hypoxic injury. *J Biol Chem* 281: 2764–2772, 2006.

10. **Cross JC, Hemberger M, Lu Y, Nozaki T, Whiteley K, Masutani M, Adamson SL.** Trophoblast functions, angiogenesis and remodeling of the maternal vasculature in the placenta. *Mol Cell Endocrinol* 187: 207–212, 2002.

11. **de Grauw TJ, Myers RE, Scott WJ.** Fetal growth retardation in rats from different levels of hypoxia. *Biol Neonate* 49: 85–89, 1986.

12. **Dokras A, Hoffmann DS, Eastvold JS, Kienzle MF, Gruman LM, Kirby PA, Weiss RM, Davisson RL.** Severe feto-placental abnormalities precede the onset of hypertension and

proteinuria in a mouse model of preeclampsia. *Biol Reprod* 75: 899–907, 2006.

13. **Evelhoch JL.** Key factors in the acquisition of contrast kinetic data for oncology. *J Magn Reson Imaging* 10: 254–259, 1999.

14. **Gluckman PD, Hanson MA, Cooper C, Thornburg KL.** Effect of in utero and early-life conditions on adult health and disease. *N Engl J Med*
359: 61–73, 2008.

15. **Gortner L, Hilgendorff A, Bahner T, Ebsen M, Reiss I, Rudloff S.** Hypoxia-induced intrauterine growth retardation: effects on pulmonary development and surfactant protein transcription. *Biol Neonate* 88: 129 – 135, 2005.

16. **Gowland PA, Francis ST, Duncan KR, Freeman AJ, Issa B, Moore RJ, Bowtell RW, Baker PN, Johnson IR, Worthington BS.** In vivo perfusion measurements in the human placenta using echo planar imaging at 0.5 T. *Magn Reson Med* 40: 467–473, 1998.

17. **Howard RB, Hosokawa T, Maguire MH.** Hypoxia-induced fetoplacental vasoconstriction in perfused human placental cotyledons. *Am J Obstet Gynecol* 157: 1261–1266, 1987.

18. **Jackson A, Buckley DL, Parker GJM.** *Dynamic Contrast-Enhanced Magnetic Resonance Imaging in Oncology*. New York: Springer, 2005.

19. **Jackson D, Volpert OV, Bouck N, Linzer DI.** Stimulation and inhibition of angiogenesis by placental proliferin and proliferin-related protein. *Science* 266: 1581–1584, 1994.

20. **Kim HS, Roh CR, Chen B, Tycko B, Nelson DM, Sadovsky Y.** Hypoxia regulates the expression of PHLDA2 in primary term human trophoblasts. *Placenta* 28: 77–84, 2007.

21. **Kingdom JC, Kaufmann P.** Oxygen and placental vascular development. *Adv Exp Med Biol* 474: 259–275, 1999.

22. **Knight BS, Pennell CE, Shah R, Lye SJ.** Strain differences in the impact of dietary restriction on fetal growth and pregnancy in mice. *Reprod Sci*
14: 81–90, 2007.

23. **Kovar DA, Lewis M, Karczmar GS.** A new method for imaging perfusion and contrast extraction fraction: input functions derived from reference tissues. *J Magn Reson Imaging* 8: 1126–1134, 1998.

24. **Kruger H, Arias-Stella J.** The placenta and the newborn infant at high altitudes. *Am J Obstet Gynecol* 106: 586–591, 1970.

25. **Levy R, Smith SD, Chandler K, Sadovsky Y, Nelson DM.** Apoptosis in human cultured trophoblasts is enhanced by hypoxia and diminished by epidermal growth factor. *Am J Physiol Cell Physiol* 278: C982–C988, 2000.

26. **Livak KJ, Flood SJ, Marmaro J, Giusti W, Deetz K.** Oligonucleotides with fluorescent dyes at opposite ends provide a quenched probe system useful for detecting PCR product and nucleic acid hybridization. *PCR Methods Appl* 4: 357–362, 1995.

27. **Lueder FL, Bangalore SA, Glass S.** Experimental intrauterine growth retardation: prolonged maternal hypoxia reduces placental blood flow and retards fetal growth in the rat. *Pediatr Res* 33: 193, 1993.

28. **Madazli R, Somunkiran A, Calay Z, Ilvan S, Aksu MF.** Histomorphology of the placenta and the placental bed of growth restricted foetuses and correlation with the Doppler velocimetries of the uterine and umbilical arteries. *Placenta* 24: 510–516, 2003.

29. **Marcos HB, Semelka RC, Worawattanakul S.** Normal placenta: gadolinium-enhanced dynamic MR imaging. *Radiology* 205: 493–496, 1997.

30. **Miller J, Turan S, Baschat AA.** Fetal growth restriction. *Semin Perinatol* 32: 274–280, 2008.

31. **Moore RJ, Strachan BK, Tyler DJ, Duncan KR, Baker PN, Worthington BS, Johnson IR, Gowland PA.** In utero perfusing fraction maps in normal and growth restricted pregnancy measured using IVIM echo-planar MRI. *Placenta* 21: 726–732, 2000.

32. **Muntener M, Hsu YC.** Development of trophoblast and placenta of the mouse. A reinvestigation with regard to the in vitro culture of mouse trophoblast and placenta. *Acta Anat (Basel)* 98: 241–252, 1977.

33. **Nait-Oumesmar B, Copperman AB, Lazzarini RA.** Placental expression and chromosomal localization of the human *Gcm 1* gene. *J Histochem Cytochem* 48: 915–922, 2000.

34. **Nelson DM, Johnson RD, Smith SD, Anteby EY, Sadovsky Y.** Hypoxia limits differentiation and up-regulates expression and activity of prostaglandin H synthase 2 in cultured trophoblast

from term human placenta. *Am J Obstet Gynecol* 180: 896–902, 1999.

35. **Ong SS, Tyler DJ, Moore RJ, Gowland PA, Baker PN, Johnson IR, Mayhew TM.** Functional magnetic resonance imaging (magnetization transfer) and stereological analysis of human placentae in normal pregnancy and in pre-eclampsia and intrauterine growth restriction. *Placenta* 25: 408 –412, 2004.

36. **Panigel M, Dixon T, Constantinidis I, Sheppard S, Swenson R, McLure H, Campbell WE, Huddleston J, Polliotti B, Nahmias A.** Fast scan magnetic resonance imaging and Doppler ultrasonography of uteroplacental hemodynamics in the rhesus monkey (*Macaca mulatta*). *J Med Primatol* 22: 393–399, 1993.

37. **Parker GJ, Roberts C, Macdonald A, Buonaccorsi GA, Cheung S, Buckley DL, Jackson A, Watson Y, Davies K, Jayson GC.** Experimentally-derived functional form for a population-averaged high-temporalresolution arterial input function for dynamic contrast-enhanced MRI. *Magn Reson Med* 56: 993–1000, 2006.

38. **Rijpkema M, Kaanders JH, Joosten FB, van der Kogel AJ, Heerschap A.** Method for quantitative mapping of dynamic MRI contrast agent uptake in human tumors. *J Magn Reson Imaging* 14: 457–463, 2001.

39. **Roh CR, Budhraja V, Kim HS, Nelson DM, Sadovsky Y.** Microarraybased identification of differentially expressed genes in hypoxic term human trophoblasts and in placental villi of pregnancies with growth restricted fetuses. *Placenta* 26: 319–328, 2005.

40. **Rohrer M, Bauer H, Mintorovitch J, Requardt M, Weinmann HJ.** Comparison of magnetic properties of MRI contrast media solutions at different magnetic field strengths. *Invest Radiol* 40: 715–724, 2005.

41. **Rossant J, Cross JC.** Placental development: lessons from mouse mutants. *Nat Rev Genet* 2: 538–548, 2001.

42. **Salafia CM, Vintzileos AM, Silberman L, Bantham KF, Vogel CA.** Placental pathology of idiopathic intrauterine growth retardation at term. *Am J Perinatol* 9: 179–184, 1992.

43. **Salas M, John R, Saxena A, Barton S, Frank D, Fitzpatrick G, Higgins MJ, Tycko B.** Placental growth retardation due to loss of imprinting of Phlda2. *Mech Dev* 121: 1199–1210,

2004.

44. **Salomon LJ, Siauve N, Balvay D, Cuenod CA, Vayssettes C, Luciani A, Frija G, Ville Y, Clement O.** Placental perfusion MR imaging with contrast agents in a mouse model. *Radiology* 235: 73–80, 2005.

45. **Schaffer L, Vogel J, Breymann C, Gassmann M, Marti HH.** Preserved placental oxygenation and development during severe systemic hypoxia. *Am J Physiol Regul Integr Comp Physiol* 290: R844–R851, 2006.

46. **Schaiff WT, Bildirici I, Cheong M, Chern PL, Nelson DM, Sadovsky Y.** Peroxisome proliferator-activated receptor-gamma and retinoid X receptor signaling regulate fatty acid uptake by primary human placental trophoblasts. *J Clin Endocrinol Metab* 90: 4267–4275, 2005.

47. **Schaiff WT, Knapp FF Jr, Barak Y, Biron-Shental T, Nelson DM, Sadovsky Y.** Ligand-activated peroxisome proliferator activated receptor gamma alters placental morphology and placental fatty acid uptake in mice. *Endocrinology* 148: 3625–3634, 2007.

48. **Schwartz JE, Kovach A, Meyer J, McConnell C, Iwamoto HS.** Brief, intermittent hypoxia restricts fetal growth in Sprague-Dawley rats. *Biol Neonate* 73: 313–319, 1998.

49. **Shellock FG, Kanal E.** Safety of magnetic resonance imaging contrast agents. *J Magn Reson Imaging* 10: 477–484, 1999.

50. **Suzuki K, Kobayashi M, Kobayashi K, Shiraishi Y, Goto S, Hoshino T.** Structural and functional change of blood vessel labyrinth in maturing placenta of mice. *Trophoblast Res* 9: 155–164, 1997.

51. **Taillieu F, Salomon LJ, Siauve N, Clement O, Faye N, Balvay D, Vayssettes C, Frija G, Ville Y, Cuenod CA.** Placental perfusion and permeability: simultaneous assessment with dual-echo contrast-enhanced MR imaging in mice. *Radiology* 241: 737–745, 2006.

52. **Tanaka YO, Sohda S, Shigemitsu S, Niitsu M, Itai Y.** High temporal resolution dynamic contrast MRI in a high risk group for placenta accreta. *Magn Reson Imaging* 19: 635–642, 2001.

53. **Tofts PS, Brix G, Buckley DL, Evelhoch JL, Henderson E, Knopp MV, Larsson HB, Lee TY, Mayr NA, Parker GJ, Port RE, Taylor J, Weisskoff RM.** Estimating kinetic parameters from

dynamic contrast-enhanced T1-weighted MRI of a diffusible tracer: standardized quantities and symbols. *J Magn Reson Imaging* 10: 223–232, 1999.

54. **Van Geijn HP, Kaylor WM Jr, Nicola KR, and Zuspan FP.** Induction of severe intrauterine growth retardation in the Sprague-Dawley rat. *Am J Obstet Gynecol* 137: 43–47, 1980.

55. **Yankeelov TE, Luci JJ, Lepage M, Li R, Debusk L, Lin PC, Price RR, Gore JC.** Quantitative pharmacokinetic analysis of DCE-MRI data without an arterial input function: a reference region model. *Magn Reson Imaging* 23: 519–529, 2005.

C.11. Figures and captions

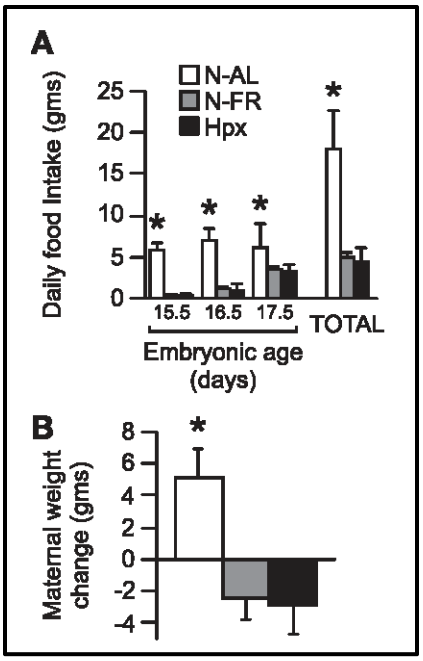

Fig. 1. Influence of hypoxia on dams' food intake and weight change. *A*: daily food intake in grams for each experimental group during the 3 experimental days (E15.5–E18.5, $n = 7$ for N-AL, $n = 15$ for N-FR, and $n = 16$ for Hpx). *B*: dams' weight change during the 3 experimental days (E15.5–E18.5, $n = 8$ for N-AL, $n = 11$ for N-FR, and $n = 8$ for Hpx). N-AL, normoxia ad libitum group; N-FR, normoxia food-restricted group; Hpx, hypoxic group. Values are means ± SD; $^*P < 0.05$ compared with the other paradigms (ANOVA with Bonferroni correction for multiple comparisons).

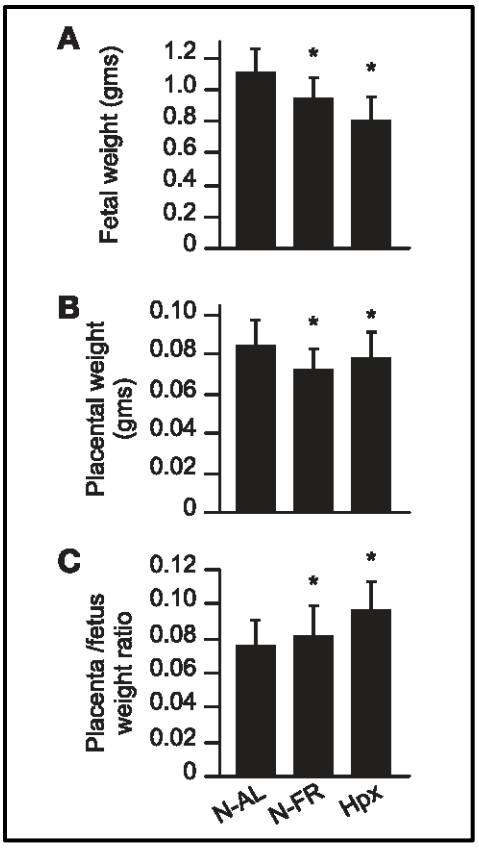

Fig. 2. Influence of hypoxia on fetal and placental weight. Measurements were performed during E15.5–E18.5 (n = 113 for N-AL, n = 99 for N-FR, and n = 126 for Hpx). Values are means ± SD; *P < 0.05 compared with the other paradigms (ANOVA with Bonferroni correction for multiple comparisons).

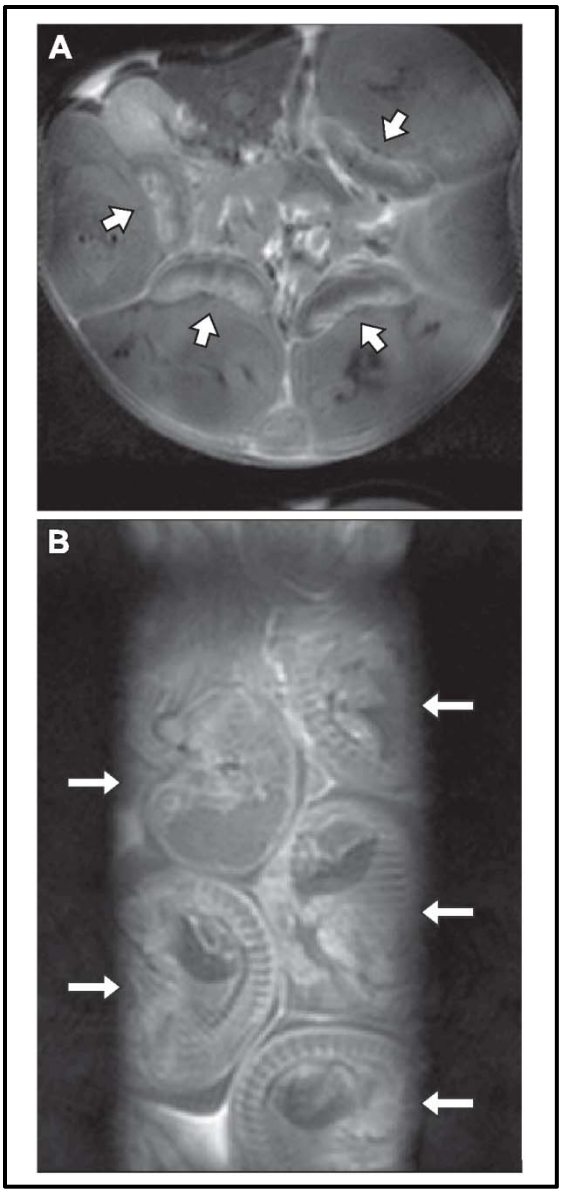

Fig. 3. Representative 4.7 tesla in vivo MRI images of control (N-AL) mice on E18.5. Respiratory-gated spin-echo images were collected following intraperitoneal administration of the contrast agent. Transaxial image of murine placentas (*A*; arrows) and coronal image of murine fetuses (*B*; arrows) are shown. Enhancement of the chorionic plate preceded enhancement of the remainder of the placental parenchyma and occurred within 30 s of contrast agent injection in all 3 experimental groups.

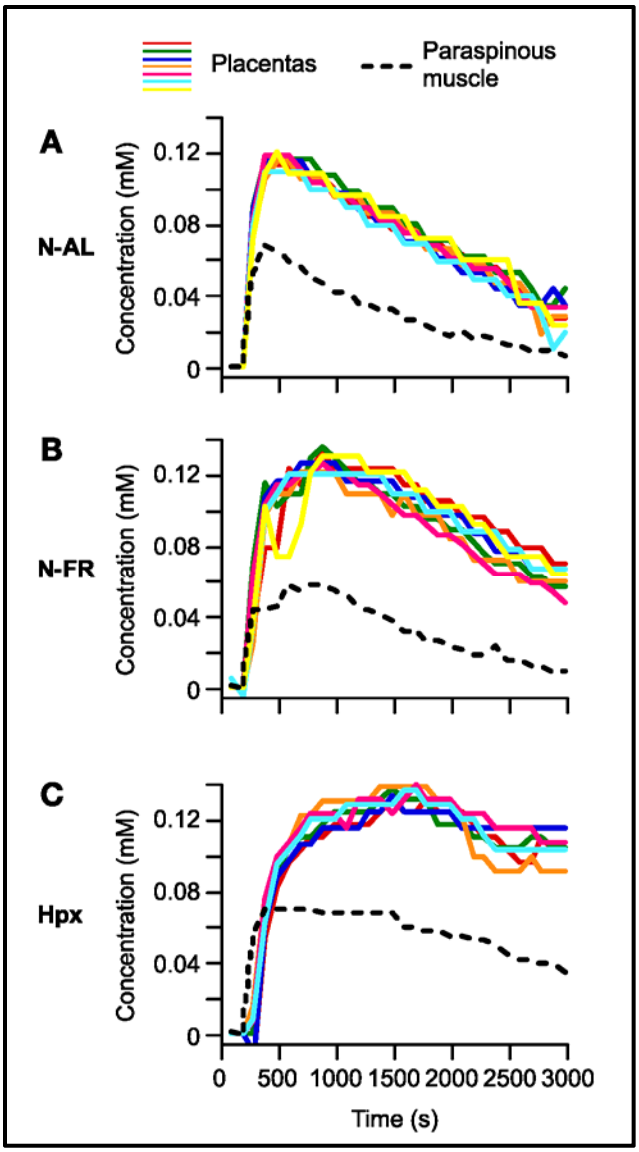

Fig. 4. Effect of hypoxia on placental and paraspinous muscle contrast kinetic curves. Each dynamic contrast-enhanced (DCE) time course curve represents 1 dam and a set of placentas from that dam for 1 of the 3 experimental groups, showing the concentration of gadolinium contrast in these tissues during the course of imaging. Solid color lines represent different placentas within each dam. For each dam, an average concentration vs. time curve was computed for all placentas in that dam. Individual placental concentration vs. time curves were normalized based upon this average concentration curve, as detailed in the text. Note that negative concentration values immediately after contrast administration stem from a T2* effect (signal loss due to magnetic susceptibility), associated with the bolus of gadolinium.

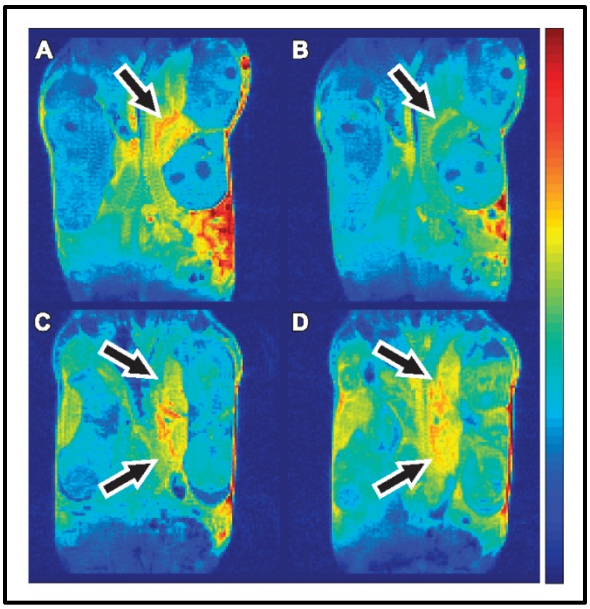

Fig. 5. DCE-MRI images (4.7 tesla) of control (N-AL) and hypoxic (Hpx) E18.5 mice. Images of a control mouse (*A* and *B*) and a Hpx mouse (*C* and *D*) are shown. *A* and *C* were collected at 400 s after injection of contrast agent [corresponding to 600 s (peak intensity) in the uptake curves of Fig. 4]. *B* and *D* were collected at 2,200 s postinjection. The diminished clearance of the contrast agent from placentas in the Hpx mouse (*D*) relative to the N-AL (*B*) is clearly evident in the later time images (arrows).

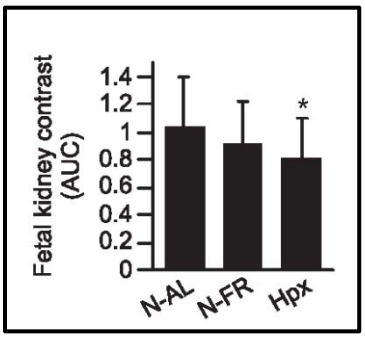

Fig. 6. Effect of hypoxia on contrast agent concentration in the fetal kidney. Values were determined as total area under the curve (AUC) calculated for each fetal kidney, normalized to the placental AUC of the same fetus as defined in MATERIALS AND METHODS. Values are means ± SD, n = 34 for N-AL, n = 32 for N-FR, and n = 38 for Hpx. *P < 0.05 compared with the N-AL paradigm (ANOVA with Bonferroni correction for multiple comparisons).

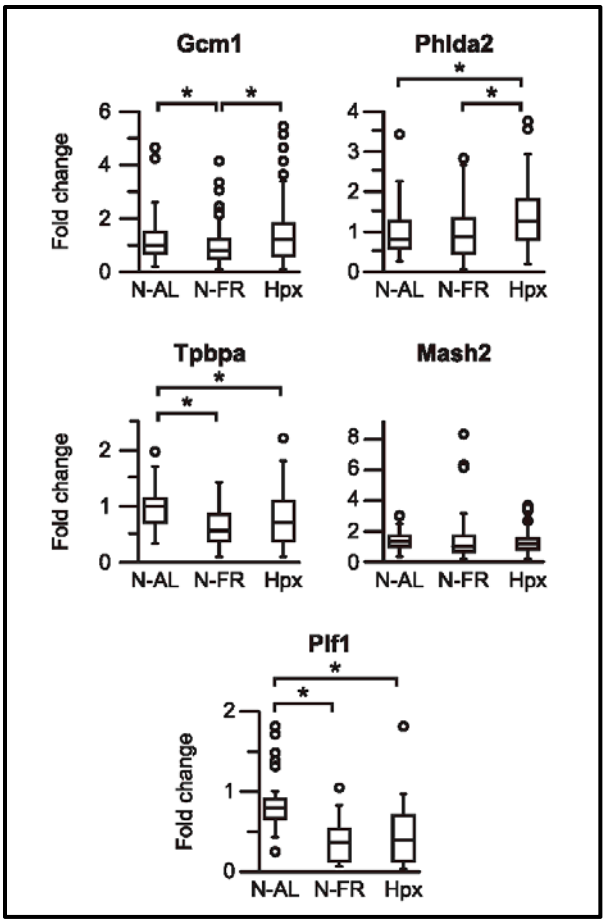

Fig. 7. Influence of hypoxia on placental gene expression. Quantitative RTPCR for genes expressed in the murine placenta performed on RNA prepared from E18.5 placentas from each experimental group (*n* = 74–98 for *Gcm1*, *Phlda2*, and *Mash2*; *n* = 32–47 for *Tpbpa* and *Plf1*). Each fold change was calculated as relative transcript expression in the placenta vs. control (N-AL). Data are expressed as box plots showing median value, upper and lower quartiles, range, and outliers. **P* < 0.05 (ANOVA with Bonferroni correction for multiple comparisons).

C.12. Tables

Table 1. Primer sequences used for standard PCR expression analysis

Name	Accession no.	Direction & site	Sequence
Gcm1	NM_008103	F(33-54)	AGAGATACTGAGCTGGGACATT
		R(149-129)	CTGTCGTCCGAGCTGTAGATG
Phlda2	NM_009434	F(209-231)	GAGCTGTTTTTCCACTCCATCCT
		R(267-289	GTTGGTGACGATGGTGAAGTACA
Tpbpa	*NM_009411*	F(120–139)	GGAGTGGCCTCAGCTGCTAT
		R(194–169)	AACTTCTTTATCCTTCTGCTCTTGCA
Mash2	*U77628*	F(394-415)	AACCGCGTAAAGCTGGTAAACT
		R(484-460)	TCTCCACCTTACTCAGCTTCTTGTT
Plf1	NM_031191	F(247-267)	AGCCCCATGAGATGCAATACT
		R(388-367)	CACTCACTAGATCGTCCAGAGG

F, forward; R, reverse

Table 2. Quantitative analysis of signal intensity in dynamic contrast-enhanced placentas

	N-AL	N-FR	Hpx
IAUC	1.87±0.35	2.28±0.40*	1.93±0.59
Final slope	$-2.59\times10^{-5}\pm0.86\times10^{-5}$	$-2.93\times10^{-5}\pm1.12\times10^{-5}$	$-1.34\times10^{-5}\pm1.67\times10^{-5}$

Values are ± SD; *n* = 56/group. N-AL, normoxic ad libitum; N-FR, normoxic food restricted; Hpx, hypoxic; IAUC, initial area under the curve; *P<0.05 vs. the other 2 experimental conditions.

APPENDIX D. REPRINT OF RGS4 CONTROLS RENAL BLOOD FLOW AND INHIBITS CYCLOSPORINE-MEDIATED NEPHROTOXICITY

D.1. Abstract

Calcineurin inhibitors (CNI) are powerful immunomodulatory agents that produce marked renal dysfunction due in part to endothelin-1-mediated reductions in renal blood flow. Ligand-stimulated Gq protein signaling promotes the contraction of smooth muscle cells via phospholipase Cβ-mediated stimulation of cytosolic calcium release. RGS4 is a GTPase activating protein that promotes the deactivation of Gq and Gi family members. To investigate the role of G protein-mediated signaling in the pathogenesis of CNI-mediated renal injury, we used mice deficient for RGS4 (*rgs4*$^{-/-}$). Compared to congenic wild type control animals, *rgs4*$^{-/-}$ mice were intolerant of the CNI, cyclosporine (CyA), rapidly developing fatal renal failure. *Rgs4*$^{-/-}$ mice exhibited markedly reduced renal blood flow after CyA treatment when compared to congenic wild type control mice as measured by magnetic resonance imaging (MRI). Hypoperfusion was reversed by coadministration of CyA with the endothelin antagonist, bosentan. The MAPK/ERK pathway was activated by cyclosporine administration and was inhibited by cotreatment with bosentan. These results show that endothelin-1-mediated Gq protein signaling plays a key role in the pathogenesis of vasoconstrictive renal injury and that RGS4 antagonizes the deleterious effects of excess endothelin receptor activation in the kidney.

D.2. Publication information

D.2.1. Reference

RGS4 Controls Renal Blood Flow and Inhibits Cyclosporine-Mediated Nephrotoxicity. *Am J Transplant* 9: 1–11, 2009.

D.2.2. Title

RGS4 Controls Renal Blood Flow and Inhibits Cyclosporine-Mediated Nephrotoxicity

D.2.3. Authors

A. Siedlecki[a,b], J. R. Anderson[c], X.Jin[a], J. R. Garbow[d],T.S.Lupu[a] and A. J. Muslin[a,e,*]

D.2.4. Affiliation

[a]Center for Cardiovascular Research, John Milliken Department of Internal Medicine; [b]Nephrology Division, John Milliken Department of Internal Medicine; [c]Department of Chemistry; [d]Biomedical Magnetic Resonance Laboratory, Mallinckrodt Institute of Radiology and [e]Department of Cell Biology and Physiology; Washington University School of Medicine, St. Louis, MO.

D.2.5. Request for Reprints and other correspondence

*Corresponding author: Anthony J. Muslin, amuslin@dom.wustl.edu.

D.2.6. Copyright

© 2009 The Authors Journal compilation

© 2009 The American Society of Transplantation and the American Society of Transplant Surgeons

D.2.7. DOI

doi: 10.1111/j.1600-6143.2009.02930.x

D.2.8. Key words

Cyclosporine, endothelin, G protein, nephrotoxicity, RGS4

D.2.9. Note

Received 05 August 2009, revised 05 October 2009 and accepted for publication 09 October 2009

D.3. Introduction

Vascular smooth muscle cells regulate renal blood flow depending on their contractile state (1). Extracellular ligands, such as endothelin-1 and angiotensin II, regulate vascular tone by binding to transmembrane receptors on smooth muscle cells (2,3). Calcineurin inhibitors were first demonstrated to induce renal vasoconstriction through the endothelin receptor by Lanese et al. (4). Several ligands thought to play a critical role in the regulation of vascular tone bind to seven transmembrane receptors (STRs), also called G protein coupled receptors (GPCRs) (5). When endothelin-1 binds to the endothelin type A (ET-A) GPCR, activated Gαq, finally stimulates cytosolic calcium levels to increase promoting contraction of smooth muscle cells (6,7). The Gq-coupled adrenergic receptor is also capable of phosporylating ERK1/2 in vascular smooth muscle cells (8– 11). This signaling pathway promotes the metabolic adaptation to increased mechanical load (8,12).

Regulator of G protein signaling (RGS) proteins are a family of GTPase activating proteins for heterotrimeric G proteins (13,14). They are differentially expressed in the renal cortex and medulla and include RGS1, RGS2, RGS4 and RGS13 (15). RGS4 is a small RGS protein that consists of an amino-terminal polybasic region and a single RGS core domain. It has GAP activity towards both Gi and Gq proteins when tested *in vitro* and *in vivo* (13,14). Its amino terminal sequence contains an N-degron degradation signal, which targets the protein for proteasomal degradation (16). RGS4 mRNA expression is present in both the cortex and the medulla, however the inner and outer medulla of the human kidney have relatively increased levels of expression (21).

Calcineurin inhibitors (CNI) are powerful immunomodulatory agents that are used by 98% of renal transplant recipients (17) to prevent transplant rejection, but often cause marked renal dysfunction (18). Several hypotheses seek to explain the mechanism of acute cyclosporine toxicity (19), including oxidant stress (20,21), the renin–angiotensin–aldosterone system (22), nitric oxide inhibition (23) and enhancement of endogenous ligands to GPCRs (24).

A longstanding explanation of acute cyclosporine renal toxicity is that cyclosporine-triggered endothelin-1 release by vascular endothelial cells promotes renal vasoconstriction and

reduced renal blood flow (4,25,26). Albig and Schiemann showed that RGS4 overexpression in endothelial cells prevented endothelin from activating extracellular signal-regulated kinase (ERK1/2) (27). Therefore, we proposed that RGS4 might play a critical role in limiting acute renovascular smooth muscle cell Gq activation after endothelin-1 release by endothelial cells. To test this model, mice deficient for RGS4 were generated and treated with cyclosporine. RGS4-deficient mice were highly sensitized to cyclosporine-induced renal failure and reduced renal blood flow.

D.4. Materials and Methods

Targeted disruption of the rgs4 gene

Murine 129/SvJ embryonic stem cells with targeted disruption of one allele of the rgs4 gene were generated. The details of this procedure are found in the online supplemental data.

Cell culture

Kidneys from rgs4$^{-/-}$ and congenic wild type control mice were procured after injecting mice with pentobarbital (0.05 mg/g). Tissue was washed in 10 mM PBS, cut in 2 mm sections and plated in endothelial cell media (Cell Applications, Inc., San Diego, CA) pretreated with endothelin (0.25 μM) (Sigma Aldrich; St. Louis, MO) or cyclosporine (20 μg/mL) (Sigma Aldrich). Tissue was then processed after a 10 minute incubation time.

Nephrectomy followed by Cyclosporine A and/or Bosentan Treatment in Mice

All research involving the use of mice was performed in strict accordance with protocols approved by the Animal Studies Committee of Washington University School of Medicine. At 12 weeks of age, wild type congenic and rgs4$^{-/-}$ C57/B6 mice were subjected to unilateral nephrectomy as previously described (28). After a 7-day recovery period, mice were administered a daily dose of intraperitoneal cyclosporine A (0.25 mg/g/day) (29), or cyclosporine + bosentan for 7 days. Intraperitoneal cyclosporine dose was determined by the smallest daily amount needed to achieve renal cortical vasoconstriction. Bosentan (Actelion Ltd, Switzerland) was administered through the animals' drinking water (2.35 mg/mL) to achieve a daily dose of 100 μg/g of body weight (30) based on an average urine output of 850 μL/day.

Renal histology and morphometry

Mice were weighed, and kidneys isolated. Tissue was fixed in 10% formalin, paraffin-embedded, microtome sectioned and stained with hematoxylin and eosin (H&E). Tissue slices with maximum longitudinal dimension were used to estimate glomerular number. Separate slices were prepared and stained immunohistochemically with phospho-ERK 1/2 (Thr183/Tyr185) (Ab-cam Inc.; Cambridge, MA). Tissue cross-sectional areas from medulla of four mice were measured at low power (2.5 times) and were calculated on an Axioskop microscope (Carl Zeiss, Inc., Jena, Germany) using ImageJ (version 1.24) software. Lean body mass was measured by EchoMRI 3-in-1 (Echo Medical Systems, Houston, TX) at 8 weeks after SIRI.

Gene expression analysis

Gene expression profiles were constructed using the GeneChip® Mouse Genome 430A 2.0 (Affymetrix, Southern Oaks, CA) high-density olignouncleotide microarray technique. mRNA purification and analysis were performed by the Siteman Cancer Center GeneChip Facility as previously described (31). Expression signaling was analyzed used Affymetrix Expression Console Software.

Quantitative real-time RT-PCR analysis on RNA extracted from kidney tissue lysates with Trizol reagent (Invitrogen Corp, Carlsbad, CA) was carried out with the Taqman master mix kit (Applied Biosystems, Foster City, CA) using RGS4 oligonulceotide primers (SABiosciences Corp., Frederick, MD) according to the manufacturer's specifications. The measured abundances of RGS4 mRNA were normalized to GAPDH in each sample as an internal loading control.

Protein analysis

Cytosolic protein lysates from kidney tissue were obtained as previously described (32). In brief, tissue was recovered from mice, and lysates were processed in the presence of protein lysis buffer. Once processed, protein bound to nitrocellulose filters were washed and incubated with murine monoclonal antiphospho-p44/42 (Thr202/Tyr204) and antitotal-p44/42 (Cell Signaling Technology, Inc., Beverly, MA). Bands were visualized by use of the ECL system (Amersham). Densitometry was performed using ImageJ software v1.24.

Vascular flow measurements

Transthoracic echocardiography and renal artery doppler sonography was performed in mice using a VEVO-770TTM Micro-Imaging System (Visual Sonic,Toronto, ON, Canada) equipped with a 15 MHz transducer. Before the imaging experiments, mice were anesthetized with isoflurane and were maintained on isoflurane/O_2 (1–1.25% v/v) throughout data collection. The sonographer was blinded in all cases to the transgenic status of the mice. Ten consecutive waveforms were averaged to obtain a mean systolic velocity for each animal.

Renal artery blood velocity was measured using an Advanced Laser Flowmeter 21 (ALF21, ADVANCE Co., Tokyo, Japan). Mice were anesthetized with a mixture of xylazine (16 mg/kg) and ketamine (0.080 mg/g). A sham procedure was performed exposing the right kidney but maintaining its blood supply. The flow meter probe was applied directly to the renal artery and then to the hilum.

A volume pressure recording (VPR) device (Kent Scientific Corp., Torrington, CT) was used for tail cuff blood pressure measurements of mice at baseline. Mice were trained for 2 days immediately followed by measurements on day 3. Mice were constrained in an adjustable plexiglass tube provided as a part of the VPR apparatus. A heating pad was placed under the tube to maintain a constant temperature between 31 and 33°C. Five training cycles were followed by five measurement cycles and then averaged.

Magnetic resonance imaging of renal blood flow in mice

MR images were collected using a dedicated small-animal MR scanner built around a 4.7 tesla, 40-cm bore magnet and interfaced with a Varian INOVA console. A home-built, actively decoupled volume coil (transmit)/surface coil (receive) pair were used for all image acquisitions. Before the imaging experiments, mice were anesthetized with isoflurane and were maintained on isoflurane/O_2 (1–1.25% v/v) throughout data collection. Animal core-body temperature was maintained at 37 ± 1°C via a heating pad formed with circulating warm water. Dynamic contrast enhanced (DCE) MRI (33,34) data were collected using a T1-weighted, gradient spoiled, multislice gradient-echo sequence. Further details of this procedure are found in the online supplemental data.

Quantitation of body fluid constituents

Levels of whole blood hemoglobin and serum blood urea nitrogen were measured in the Department of Comparative Medicine Diagnostic Laboratory at Washington University School of Medicine. Because of the imprecision of the Jaffe method in measuring mouse serum creatinine we collaborated with Satish Ramachandrarao at University of California, San Diego, California, to perform serum creatinine by HPLC as previously described (28,35).

Cyclosporine trough levels were measured with the automated Dimension® RxL Max® clinical chemistry system from Siemens. Healthcare Diagnostics, Ltd. using an immunoassay technique. The assay was performed using a Flex® reagent cartridge. Each sample of whole blood lysate was processed with the Dimension® system platform.

Statistical analysis

All data are presented as mean values ± standard error of the mean. Static group analysis was performed with SigmaStat® 3.1 (Systat Software, Inc., San Jose, CA). Statistical relationships were determined by the Student's *t*-test where significance was achieved when a population's mean value was separated from controls by two or more standard deviations ($p = 0.05$). All p-values calculated were two-sided. One-way ANOVA analysis was used in comparisons of greater than two groups, and Holm-Sidak pairwise comparisons were calculated between groups. Kaplan–Meier survival curves and Mantel Cox log-rank analysis was performed with SPSS v13.0 (SPSS Inc., Chicago, IL). Pearson's correlation coefficient was performed on signal intensities generated from two separate gene expression microarrays. The Bootstrap algorithm for error estimation of gene expression microarray data (36) was performed using the Wessa.Net server version 1.1.23-r4.

D.5. Results

To generate mice deficient for RGS4 we created a genetic construct that eliminated exons 3–5 of the *rgs4* gene, encoding the RGS box (Figure S1). *Rgs4*$^{-/-}$ mice appeared normal at birth and were fertile. Mating of *rgs4*$^{+/-}$ heterozygotes yielded live-born homozygotes with Mendelian frequencies. Analysis of *rgs4*$^{-/-}$ mice in the absence of provocative stimulation demonstrated that these animals had comparable physiologic parameters. Normalized kidney

weight was equal with no evidence of hypertension by noninvasive testing. These findings were correlated with equivalent glomerular number. Renal function as estimated by serum creatinine was nearly identical in *rgs4*$^{-/-}$ and wild type mice (0.106 ± 0.002 mg/dL vs. 0.105 ± 0.007 mg/dL, p = 0.89) (Table S1). Normalized mRNA expression of RGS2, RGS5, RGS10, RGS12 and RGS16 was not increased in *rgs4*$^{-/-}$ mice (Figure 2A and B; Table S2).

Calcineurin inhibitors are among the most commonly used immunomodulatory agents in transplantation, but they often cause marked renal dysfunction (18). Specifically, cyclosporine A (CyA) causes acute renal injury due to decreased intrarenal blood flow (4,25,26). Chronic injury mimics this mode of injury with histologic changes consistent with long term hypoxic injury described as striped fibrosis (37). To determine whether *rgs4*$^{-/-}$ mice were sensitized to cyclosporine-mediated renal injury, we subjected animals to unilateral nephrectomy followed 1 week later by treatment with CyA. Congenic wild type control mice developed renal dysfunction within 1 week following CyA administration. By HPLC, serum creatinine increased 108% (0.2201 mg/dL vs. 0.106 mg/dL) (Figure 1A) and BUN increased 274% (71 mg/dL) (Figure 1B) in *rgs4*$^{-/-}$ mice versus controls after 7 days of cyclosporine exposure while whole blood cyclosporine levels were equivalent between groups (Figure S3). Furthermore, there was no evidence that *rgs4*$^{-/-}$ mice metabolized cyclosporine less efficiently than congenic controls (Figure S4). Serum creatinine by HPLC approximates serum creatinine by the Jaffe method using a correction factor of 3.125. The Jaffe-equivalent measure in *rgs4*$^{-/-}$ given cyclosporine mice was 0.688 ± 0.044 mg/dL (35). Disruption of the apical membrane of proximal tubular cells, indicative of acute tubular necrosis, was seen by light microscopy and electron microscopy (Figure 2A and B). Renal artery blood flow to the kidney was decreased in cyclosporine-treated mice as measured by noninvasive Doppler sonography (Figure S5A and B), further implicating CyA exposure in the development of acute tubular necrosis. Noninvasive measurements could not differentiate the decrease in blood flow between *rgs4*$^{-/-}$ and controls, however, *rgs4*$^{-/-}$ mice had a decreased average renal artery flow velocity compared to congenic wild type control animals using invasive monitoring techniques (Figure S6). Smaller intrarenal vascular substructures could not be interrogated due to the limitations of current modalities of measuring in vivo renal blood flow.

To determine whether *rgs4*$^{-/-}$ mice developed more profound regional intrarenal vasoconstriction after CyA treatment, dynamic-contrast enhanced magnetic resonance imaging (DCE-MRI) (34,38,39) was used to quantitatively measure the uptake and clearance kinetics of a low molecular weight, Gadolinium-based MR contrast agent (CA). High-resolution, T1-weighted kidney images allowed clear visualization of the cortex, medulla and renal pelvis together with accompanying intrarenal vasculature (Figure 3). Selected images from the DCE time course and complete plots of adjusted signal intensity versus time allowed the CA kinetics to be accurately measured. A 42% decrease in blood flow was identified in the renal cortex (Figures 4A and 5A). In contrast to congenic wild type controls, $IAUC_{60}$ decreased by 62% in the medulla of CyA-treated *rgs4*$^{-/-}$ mice, indicative of a significant decrease in regional blood flow (Figures 4B and 5B). Blood flow was restored to both the medulla and the cortex with the coadministration of bosentan (5A, 5B). Cyclosporine's specific ability to activate an RGS-dependent signal transduction pathway is supported by the amelioration of its deleterious effect by administration of the endothelin receptor antagonist bosentan.

The ability of bosentan to reduce cyclosporine-mediated renal toxicity may be due to altered cyclosporine blood levels. To investigate this possibility, *rgs4*$^{-/-}$ mice were given escalating doses of cyclosporine with bosentan (100 µg/g/day) (see Figure S7). Cyclosporine blood levels increased with higher doses of cyclosporine and were not affected by coadministration of bosentan.

Mice were next observed for a month while being treated with cyclosporine. *Rgs4*$^{-/-}$ mice exhibited significantly reduced survival in response to treatment with CyA when compared to congenic wild type control mice (Figure 6). The mean survival time was 25 days for congenic wild type control mice in response to CyA administration, but *rgs4*$^{-/-}$ mice had a mean survival time of only 9 days (Mantel-Cox log rank test, $p = 0.002$). *Rgs4*$^{-/-}$ mice coadministered cyclosporine and bosentan exhibited a significantly increased survival rate compared to *rgs4*$^{-/-}$ mice given cyclosporine alone.

CyA renal toxicity is thought to be due to the action of endothelin-1. Given the reduced intrarenal blood flow observed in CyA-treated *rgs4*$^{-/-}$ mice, we hypothesized that the absence of

RGS4 protein would sensitize kidney to CyA-and endothelin-1-stimulated intracellular signal transduction. Sections of freshly obtained *rgs4*$^{-/-}$ and wild type congenic kidneys were treated in vitro with CyA or endothelin-1 for 10 minutes and processed for immunoblotting with an antiphospho-ERK1/2 primary antibody. *Rgs4*$^{-/-}$ kidney slices exhibited markedly increased ERK activation in response to endothelin-1 (Figure 7A and C). Similarly, *rgs4*$^{-/-}$ kidney slices exposed to CyA for 10 minutes showed increased ERK activation (Figure 7B and D). In vivo experiments demonstrated that ERK activation was increased in the kidneys of *rgs4*$^{-/-}$ mice treated with cyclosporine for 1 week (Figure 8A and B). Interestingly, RGS4 mRNA levels rose by 1.75-fold in wild type congenic kidneys after 7 days of CyA treatment (Figure 8C).

Rgs4$^{-/-}$ kidneys were sensitized to CyA-mediated reduction in renal blood flow and were also sensitized to endothelin-1 mediated ERK activation. Given that CyA-mediated acute renal toxicity correlates with increased endothelin-1 release, and that bosentan is a widely used ET-A/B receptor antagonist, mice were treated with this agent. Administration of bosentan to *rgs4*$^{-/-}$ mice abrogated the effect of CyA on blood perfusion in the kidney (Figures 4A, B and 5A, B) and ERK phosphorylation decreased to pre-cyclosporine levels in bosentan-treated animals (Figure 8A and B).

D.6. Discussion

Calcineurin inhibitors are the most commonly used immunosuppressive agents in the prevention of solid organ transplant rejection (17), but cause progressive renal toxicity (40,41). CNI nephrotoxicity is in part due to endothelin-1 release by vascular endothelial cells promoting renal vasoconstriction and reduction in renal blood flow. The mechanism by which cyclosporine causes endothelin-1 release is unclear. Although cyclosporine directly binds to L-type calcium channels *in vitro* (42), the secondary release of endothelin-1 stimulates Gq signaling that results in inositol triphosphate binding to L-type calcium channels (43). Therefore the direct link between calcineurin inhibition and elevated sarcoplasmic calcium levels is contested (44). However, after endothelin-1 is released acutely, cyclosporine initiates a maintenance phase of endothelin release and up-regulation of endothelin gene expression. Marsen and colleagues determined that

both cyclosporine and tacrolimus promote the transcription of preproendothelin-1 mRNA in human vascular endothelial cells (45).

In this work, we described for the first time, the *in vivo* vasoactive effects of cyclosporine A in a minimally invasive mouse model. Because the compact size of the mouse model system is more difficult to analyze than larger mammals, innovative methods are needed to analyze mouse renal and renovascular physiology in a reproducible manner. These adaptations are vital for the translation of animal studies to human therapy.

We hypothesized that RGS4 plays a key role in regulating renal vascular resistance through modulation of Gq activation. We found that *rgs4*$^{-/-}$ mice were uniquely susceptible to a reduction in renal medullary blood flow mediated by cyclosporine. Previous studies by Lee et al., Mazzali et al. and Neria et al. (29,46,47) could not demonstrate an increase in serum creatinine after exposure to cyclosporine and therefore relied predominantly on histologic markers of renal injury. In this study, we showed that *rgs4*$^{-/-}$ mice had a 108% increase in serum creatinine and 274% increase in BUN compared to congenic controls after both groups were exposed to cyclosporine for 1 week. These results link RGS4 deficiency and a susceptibility to renal failure.

The specificity of cyclosporine's action through the G-protein signaling cascade was demonstrated when bosentan, an endothelin A/B receptor antagonist, prevented the deleterious effect of cyclosporine on renal function. We also found that endothelin-1-mediated activation of ERK was enhanced in *rgs4*$^{-/-}$ kidney. This result follows the previous findings of Albig et al who showed that in vitro overexpression of RGS4 prevented ERK activation in the presence of endothelin-1 (27). These results establish that RGS4 is a key regulator of endothelin-1 action in the kidney, probably via effects on Gq.

The use of bosentan in transplantation is relatively contraindicated because of increased hypotension when coadministered with cyclosporine A. Only one human study to date by Binet et al. has evaluated the renal hemodynamic effects of endothelin receptor antagonists on calcineurin inhibitors (48). Binet et al. reported a mean systolic/diastolic blood pressure of 135 ± 6/80 ± 4mmHginseven patients given cyclosporine A alone which was comparable to internal controls given cyclosporine A and bosentan (136 ± 8/80 ± 7 mmHg). Limited animal studies

remain unclear (49,50). Further studies are needed to delineate the potentional hypotensive effects of calcineurin inhibitors when used in combination with endothelin receptor antagonists.

Our MRI results showed that CyA-treated *rgs4*$^{-/-}$ kidneys exhibited a greater decrease in signal intensity in the renal medulla than in the renal cortex, suggesting that RGS4 modulates vasoconstriction proximal to the vascular network of the medulla. Studies of CyA thus far have investigated the ligands responsible for initiating the intracellular signaling cascade that leads to smooth muscle vasoconstriction in the kidney (49,51–54). Lanese and colleagues were the first to show that cyclosporine was specific to the endothelin ligand (4). In our current study we describe a specific intracellular pathway that is activated by cyclosporine, and directs future studies to targeted inhibition of the G-protein signaling system or promotion of the inhibitory activities of RGS4.

To study the vasoconstrictive properties of cyclosporine we used a novel DCE-MRI, and were able to describe, in detail, contrast-agent uptake and clearance kinetics in the mouse kidney. Our studies focused on monitoring the regionalized effects of CyA treatment. These observed changes in CA kinetics following treatment with CyA reflect physiologic changes in the kidney that are consistent with a stepwise reduction of renal blood flow in the cortex and the medulla. While microbead radioisotope methods remain the gold standard for measuring end-organ perfusion (55,56), these methods can not be applied *in vivo*. Measuring alteration of organ blood flow with microbeads is limited by the need for postmortem tissue preparation. MR methods are non-invasive, enabling longitudinal, time-course studies of blood-flow patterns in response to interventions.

D.7. Conclusions

The large number of RGS family members implies that there is specific requirement for particular members in various cell types and organ systems. The role of RGS proteins in the management of renal vascular insult is not well understood. In this work, we demonstrated that RGS4 plays a specific role in modulating renal insults that occur as a consequence of overstimulation of the Gq signaling pathway. Increasing RGS4 protein levels by inhibiting pro-

teasomal degradation or increasing activity through in the kidney may be therapeutically beneficial for patients with renal dysfunction.

D.8. Acknowledgments

The authors had full access to the data and take responsibility for its integrity. All authors have read and agree to the manuscript as written. We acknowledge Dr. Joseph J.H. Ackerman for the generous contribution of his time spent on the conceptual design of this project. This work was supported by NIH grants RO1 HL061567, RO1 HL076670 and P01 HL057278 (A.J.M.). We thank the Alvin J. Siteman Cancer Center at Washington University School of Medicine and Barnes-Jewish Hospital in St. Louis, Mo., for use of the Center for Biomedical Informatics and Multiplex Gene Analysis Genechip Core Facility. The Siteman Cancer Center is supported in part by a NCI Cancer Center Support Grant #P30 CA91842. A portion of this data was presented at the 2009 American Transplant Congress, abstract 1703.

D.9. Fundings Sources

This work was supported by the Mallinckrodt Institute of Radiology and by NIH grants RO1 HL061567 (A.J.M.), P01 HL057278 (A.J.M.), RO1 HL 076670 (A.J.M.) and P30 DK079333 (A.S., A.J.M.) and U24 CA83060 (J.G., J. J. H. A.).

D.10. References

1. Pallone TL, Silldorff EP, Turner MR. Intrarenal blood flow: Microvascular anatomy and the regulation of medullary perfusion. Clin Exp Pharmacol Physiol 1998; 25: 383–92.

2. Arendshorst WJ, Brannstrom K, Ruan X. Actions of angiotensin II on the renal microvasculature. J Am Soc Nephrol 1999; 10: S149– S161.

3. Naicker S, Bhoola K. Endothelins: Vasoactive modulators of renal function in health and disease. Pharmacol Ther 2001; 90: 61–88.

4. Lanese DM, Conger J. Effects of endothelin receptor antagonist on cyclosporine-induced vasoconstriction in isolated rat renal arterioles. J Clin Invest 1993; 91: 2144–2149.

5. Lefkowitz R. Seven transmembrane receptors: Something old, something new. Acta Physiol 2007; 190: 9–19.

6. Wilson BA, Zhu X, Ho M, Lu L. Pasteurella multocida toxin activates the inositol triphosphate signaling pathway in Xenopus oocytes via G(q)alpha-coupled phospholipase C-beta1. J Biol Chem 1997; 272: 1268–1275.

7. Sternweis PC, Smrcka A. G proteins in signal transduction: The regulation of phospholipase C. Ciba Found Symp 1993; 176: 96– 106.

8. Ratz PH. Regulation of ERK phosphorylation in differentiated arterial muscle of rabbits. Am J Physiol Heart Circ Physiol 2001; 281: H114–H123.

9. Ishida M, Ishida T, Thomas SM, Berk BC. Activation of extracellular signal-regulated kinases (ERK1/2) by angiotensin II is dependent on c-Src in vascular smooth muscle cells. Circ Res 1998; 82: 7–12.

10. Adam LP, Franklin MT, Raff GJ, Hathaway DR. Activation of mitogen-activated protein kinase in porcine carotid arteries. Circ Res 1995; 76: 183–190.

11. Dikic I, Tokiwa G, Lev S, Courtneidge SA, Schlessinger J. A role for Pyk2 and Src in linking G-protein-coupled receptors with MAP kinase activation. Nature 1996; 383: 547–550.

12. Touyz RM, He G, Deng LY, Schiffrin EL. Role of extracellular signal-regulated kinases in angiotensin II-stimulated contraction of smooth muscle cells from human resistance arteries. Circulation 1999; 99: 392–399.

13. Berman DM, Wilkie T, Gilman AG. GAIP and RGS4 are GTPaseactivating proteins for the Gi subfamily of G protein alpha subunits. Cell 1996; 86: 445–452.

14. Bansal G, Druey KM, Xie Z. R4 RGS proteins: Regulation of G-protein signaling and beyond. Pharmacol Ther 2007; 116: 473–495.

15. Higgins JP, Wang L, Kambham N, Montgomery K, Mason V, Vogelmann SU. Gene expression in the normal adult human kidney assessed by complementary DNA microarray. Mol Biol Cell 2004; 15: 649–656.

16. Bodenstein J, Sunahara R, Neubig RR. N-terminal residues control proteasomal degradation of RGS2, RGS4, and RGS5 in human embryonic kidney 293 cells. Mol Pharmacol 2007; 71:

1040–1050.

17. Meier-Kriesche HU, Li S, Gruessner RW et al. Immunosuppression: Evolution in practice and trends, 1994–2004. Am J Transplant 2006; 6: 1111–1131.

18. Olyaei AJ, de Mattos A, Bennett WM. Nephrotoxicity of immunosuppressive drugs: New insight and preventive strategies. Curr Opin Crit Care 2001; 7: 384–389.

19. Naesens M, Kuypers DR, Sarwal M. Calcineurin inhibitor nephrotoxicity. Clin J Am Soc Nephrol 2009; 4: 481–508.

20. Krysztopik RJ, Bentley FR, Spain DA, Wilson MA, Garrison RN. Lazaroids prevent acute cyclosporine-induced renal vasoconstriction. Transplantation 1997; 63: 1215–1220.

21. Rezzani R. Exploring cyclosporine A-side effects and the protective role-played by antioxidants: The morphological and immunohistochemical studies. Histol Histopathol 2006; 21: 301–316.

22. Bobadilla NA, Gamba G. New insights into the pathophysiology of cyclosporine nephrotoxicity: A role of aldosterone. Am J Physiol Renal Physiol 2007; 293: F2–F9.

23. Ramzy D, Rao V, Tumiati LC et al. Role of endothelin-1 and nitric oxide bioavailability in transplant-related vascular injury: Comparative effects of rapamycin and cyclosporine. Circulation 2006; 114(1 Suppl): I214–I219.

24. Gabriëls G, August C, Grisk O et al. Impact of renal transplantation on
small vessel reactivity. Transplantation 2003; 75: 689–697.

25. Perico N, Dadan J, Remuzzi G. Endothelin mediates the renal vasoconstriction induced by cyclosporine in the rat. J Am Soc Nephrol 1990; 1: 76–83.

26. Kon V, Sugiura M, Inagami T, Harvie BR, Ichikawa I, Hoover RL. Role of endothelin in cyclosporine-induced glomerular dysfunction. Kidney Int 1990; 37: 1487–1491.

27. Albig AR, Schiemann W. Identification and characterization of regulator of G protein signaling 4 (RGS4) as a novel inhibitor of tubulogenesis: RGS4 inhibits mitogen-activated protein kinases and vascular endothelial growth factor signaling. Mol Biol Cell 2005; 16: 609–625.

28. Siedlecki AM, Jin X, Muslin AJ. Uremic cardiac hypertrophy is reversed by rapamycin but not by lowering of blood pressure. Kidney Int 2009; 75: 800–808.

29. Neria F, Castilla MA, Sanchez RF et al. Inhibition of JAK2 protects renal endothelial and epithelial cells from oxidative stress and cyclosporin A toxicity. Kidney Int 2009; 75: 227–234.

30. Sabaa N, de Franceschi L, Bonnin P et al. Endothelin receptor antagonism prevents hypoxia-induced mortality and morbidity in a mouse model of sickle-cell disease. J Clin Invest 2008; 118: 1924–1933.

31. Mahadevappa M, Warrington J. A high-density probe array sample preparation method using 10-to 100-fold fewer cells. Nat Biotechnol 1999; 17: 1134–1136.

32. DeBosch B, Treskov I, Lupu TS et al. Akt1 is required for physiological cardiac growth. Circulation 2006; 113: 2097–2104.

33. Knopp MV, Giesel F, Marcos H et al. Dynamic contrast-enhanced magnetic resonance imaging in oncology. Top Magn Reson Imaging 2001; 12: 301–308.

34. Tofts PS, Brix G, Buckley DL, Evelhoch JL, Henderson E, Knopp MV. Estimating kinetic parameters from dynamic contrast-enhanced T(1)-weighted MRI of a diffusable tracer: Standardized quantities and symbols. J Magn Reson Imaging 1999; 10: 223–232.

35. Dunn SR, Qi Z, Bottinger EP, Breyer MD, Sharma K. Utility of endogenous creatinine clearance as a measure of renal function in mice. Kidney Int 2004; 65: 1959–1967.

36. Brody JP, Williams BA, Wold BJ, Quake SR. Significance and statistical errors in the analysis of DNA microarray data. Proc Natl Acad Sci U S A 2002; 99: 12975–12978.

37. Myers BD, Ross J, Newton L, Luetscher J, Perlroth M. Cyclosporine-associated chronic nephropathy. N Engl J Med 1984; 311: 699–705.

38. Garbow JR, Mcintosh C, Conradi MS. Actively decoupled transmit-receive coil-pair for mouse brain MRI. Concepts Magn Reson 2008; 33: 252–259.

39. Evelhoch JL. Key factors in the acquisition of contrast kinetic data for oncology. J Magn Reson Imaging 1999; 10: 254–249.

40. Nankivell BJ, Borrows R, Fung CL, O'Connell PJ, Chapman JR, Allen RD. Calcineurin inhibitor nephrotoxicity: Longitudinal assessment by protocol histology. Transplantation 2004; 78: 557– 565.

41. European multicentre trial of cyclosporine in renal transplantation: 10-year follow-up.

Transplant Proc 25: 527–529.

42. Schuhmann K, Romanin C, Baumgartner W, Groschner K. Intracellular Ca2+ inhibits smooth muscle L-type Ca2+ channels by activation of protein phosphatase type 2B and by direct interaction with the channel. J Gen Physiol 1997; 110: 503– 513.

43. Takuwa Y, Kasuya Y, Takuwa N, Kudo M, Yanagisawa M, Goto K. Endothelin receptor is coupled to phospholipase C via a pertussis toxin-insensitive guanine nucleotide-binding regulatory protein in vascular smooth muscle cells. J Clin Invest 1990; 85: 653–658

44. Lo Russo A, Passaquin A, Andr ´e P et al. Effect of cyclosporin A and analogues on cytosolic calcium and vasoconstriction: Possible lack of relationship to immunosuppressive activity. Br J Pharmacol 1996; 118: 885–892.

45. Marsen TA, Weber F, Egink G, Suckau G, Baldamus CA. Differential transcriptional regulation of endothelin-1 by immunosuppressants FK506 and cyclosporin A. Fundam Clin Pharmacol 2000; 14: 401–408.

46. Lee S, Kim W, Kim DH et al. Protective effect of COMPangiopoietin-1 on cyclosporine-induced renal injury in mice. Nephrol Dial Transplant 2008; 23: 2784–2794.

47. Mazzali M, Hughes J, Dantas M et al. Effects of cyclosporine in osteopontin null mice. Kidney Int 2002; 62: 78–85.

48. Binet I, Wallnofer A, Weber C, Jones R, Thiel G. Renal hemodynamics and pharmacokinetics of bosentan with and without cyclosporine A. Kidney International 2000; 57: 224–231.

49. Prévot A, Semama D, Tendron A, Justrabo E, Guignard JP, Gouyon JB. Endothelin, angiotensin II and adenosine in acute cyclosporine A nephrotoxicity. Pediatr Nephrol 2000; 14: 927–934.

50. Soydan G, Tekes E, Tuncer M. Short-term and long-term FK506 treatment alters the vascular reactivity of renal and mesenteric vascular beds. J Pharmacol Sci 2006; 102: 359–367.

51. Binet I, Wallnofer A, Weber C, Jones R, Thiel G. Renal hemodynamics and pharmacokinetics of bosentan with and without cyclosporine A. Kidney Int 2000; 57: 224–231.

52. Bobadilla NA, Gamba G. New insights into the pathophysiology of cyclosporine nephrotoxicity: A role of aldosterone. Am J Physiol Renal Physiol 2007; 293: 2–9.

53. Perez-Rojas JM, Derive S, Blanco JA et al. Renocortical mRNA expression of vasoactive factors during spironolactone protectie effect in chronic cyclosporine nephrotoxicity. Am J Physiol Renal Physiol 2005; 289: 1020–1030.

54. Padi SS, Chopra K. Selective angiotensin II type 1 receptor blockade ameliorates cyclosporine nephrotoxicity. Pharmacol Ther 2002; 45: 413–420.

55. Sabto J, Bankir L, Gr ¨unfeld JP. The measurement of glomerular blood flow in the rat kidney: Influence of microsphere size. Clin Exp Pharmacol Physiol 1978; 5: 559–565.

56. Ofstad J, Morkrid L, Willassen Y. Diameter of the afferent arteriole in the dog kidney estimated by the microsphere method. Scand J Clin Lab Invest 1975; 35: 767–774.

D.11. Figures and captions

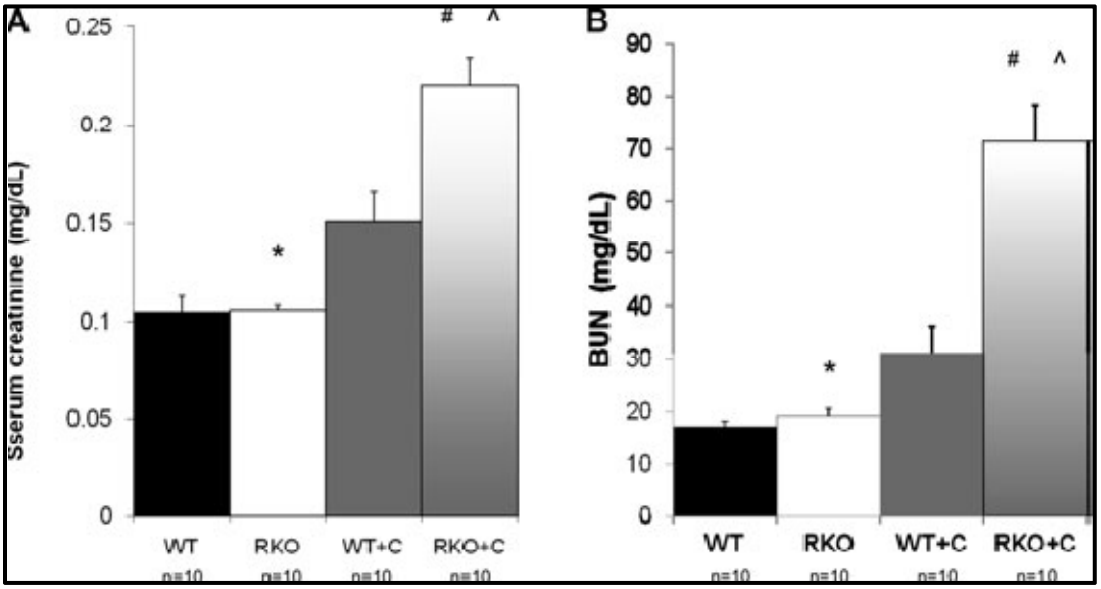

Figure 1: Increased renal injury in *rgs4*$^{-/-}$ mice treated with cyclosporine A. After 7 days of treatment with cyclosporine, (A) serum creatinine (sCr) was measured in *rgs4*$^{-/-}$ (RKO+C) (n = 10) and wild type congenic mice (WT+C) (n = 10). SCr was increased in RKO+C compared to other groups by one-way independent ANOVA: $F(3,31) = 43.88$, composite $p < 0.001$; WT versus RKO = *($p = 0.89$); RKO versus RKO+C = $^{\#}$($p = <0.0001$); WT+C versus RKO+C = $^{\wedge}$($p < 0.0001$), (B) Blood urea nitrogen (BUN) was increased in RKO+C(n = 10) compared to other groups by one-way independent ANOVA: $F(3,35) = 31.12$, composite $p < 0.0001$; WT versus RKO = *($p = 0.89$); RKO versus RKO+C = $^{\#}$($p = <0.0001$); WT+C versus RKO+C = $^{\wedge}$($p < 0.0001$)

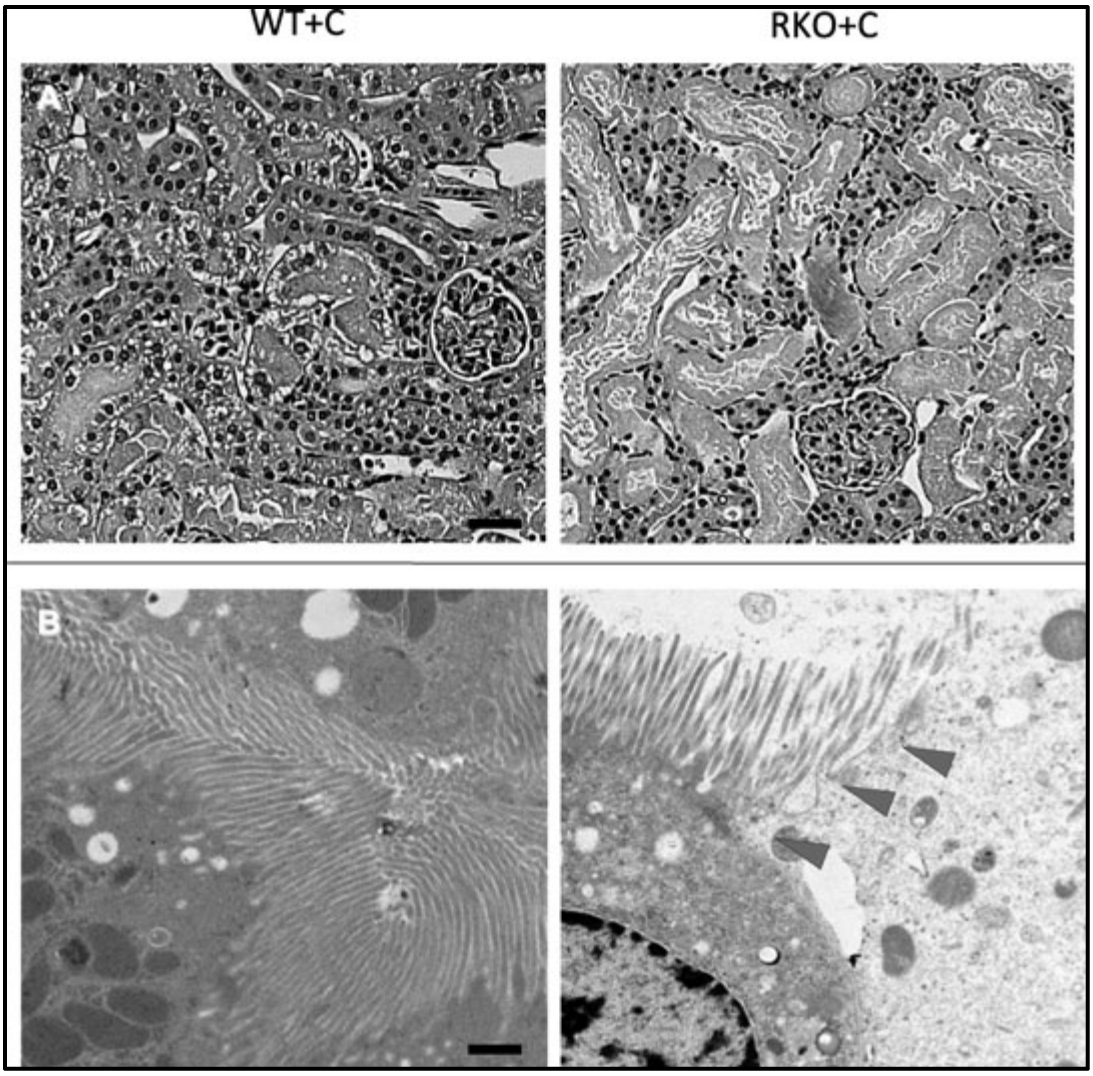

Figure 2: Light and electron microscopy of congenic wild type + cyclosporine (WT+C) (n = 4) and *rgs4*$^{-/-}$ + cyclosporine (RKO+C) (n = 4). (A) The lumenal membrane of proximal tubule cells is disrupted and intralumenal debris is present in RKO+C (arrows) (magnification 400×). Scale bar = 200 micron. (B) The ciliary brush border on the apical membrane of epithelial proximal tubule cells (arrows) is also disrupted in RKO+C mice (n = 4) compared to WT+C (n = 4) (magnification 7500×). Scale bar = 2 micron.

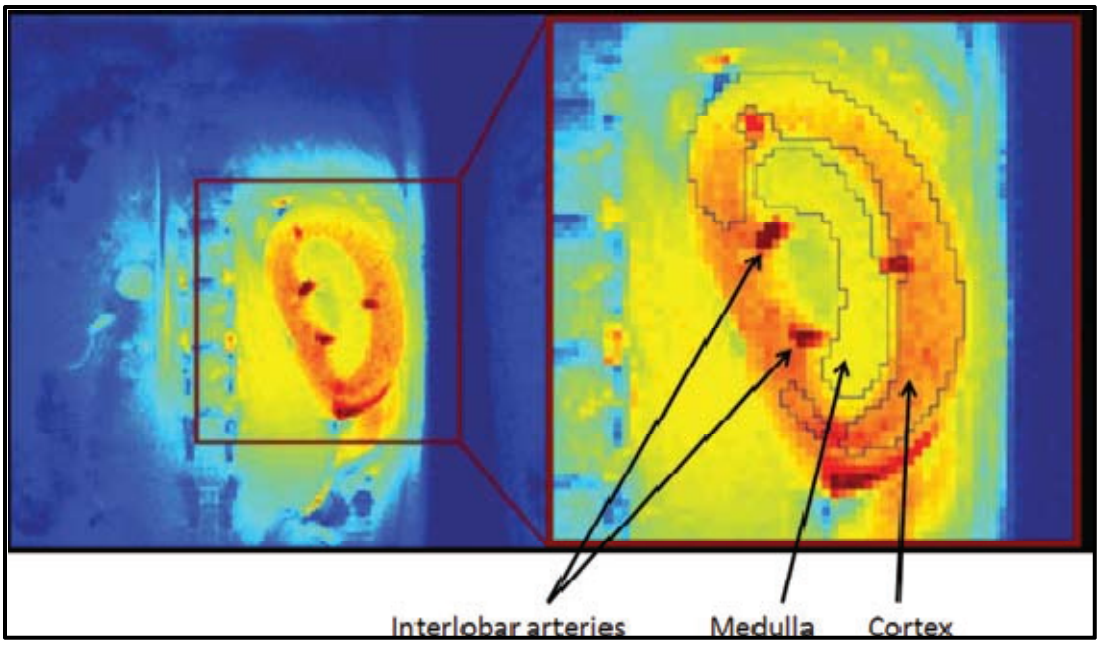

Figure 3: High-resolution, T1-weighted image of a kidney from an *rgs4*$^{-/-}$ mouse, allowing clear visualization of the cortex, medulla and renal pelvis and the intrarenal vasculature (intense red pixels).

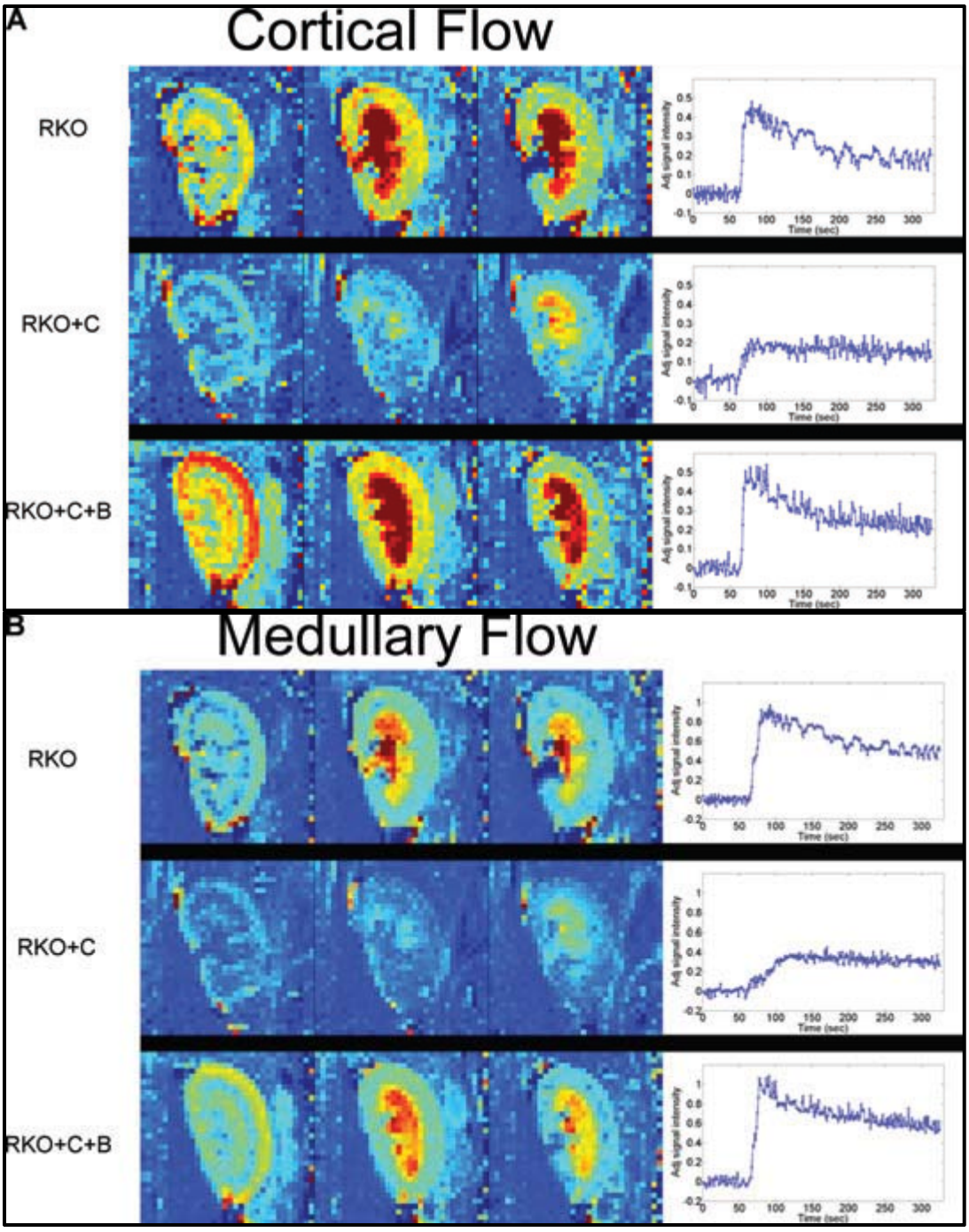

Figure 4: Dynamic-contrast enhanced magnetic resonance imaging (DCE-MRI) data collected following bolus injection of a low molecular weight, Gd-containing contrast agent (adjusted signal intensity). Selected images from the (A) cortical and (B) medullary regions of interest are shown for: (top) a *rgs4*$^{-/-}$ mouse (RKO); (middle) a *rgs4*$^{-/-}$ mouse treated with Cyclosporine (RKO+C); (bottom) and a *rgs4*$^{-/-}$ mouse treated with Cyclosporine and

bosentan (RKO+C+B). Images were collected 12 s (left panel), 38 s (middle panel) and 90 s (right panel) post-contrast injection. At the right, in each panel are the complete adjusted signal intensity versus time curves for a (A) cortical ROI and (B) medullary ROI for each of these mice.

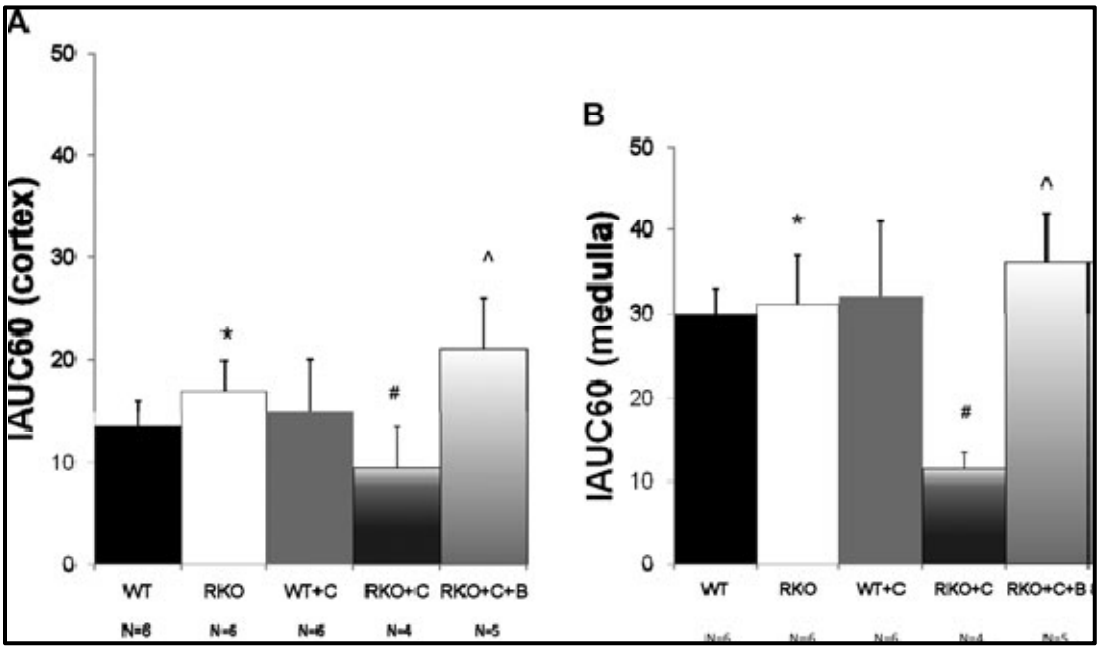

Figure 5: Average initial area under the curve ($IAUC_{60}$) values, computed for the (A) cortical cohorts of wild-type (WT) (n = 6), *rgs4*$^{-/-}$ (n = 6), Cyclosporine-treated wild-type (WT+C) (n = 6), cyclosporine-treated *rgs4*$^{-/-}$ (n = 4) and *rgs4*$^{-/-}$ + cyclosporine + bosentan mice (n = 5). Decreased rate of agent uptake in the cortex was evident in RKO+C by one-way independent ANOVA, F(3,61.7) = 5.5 (composite p = 0.009). Blood flow was then restored with bosentan cotreatment comparing RGS4KO + cyclosporine + bosentan (RKO+C+B) to WT, RKO and WT+C (one-way independent ANOVA, F(4,21) = 5.48 (composite p = 0.003). WT versus RKO, p = 0.79, *; RKO versus RKO+C, p = 0.01, #; RKO versus RKO +C+B, p = 0.10, ^. (B) Medullary cohorts of wild-type (WT) (n = 6), rgs4$^{-/-}$ (n = 6), Cyclosporine-treated wild-type (WT+C) (n = 6), cyclosporine-treated rgs4$^{-/-}$ (n = 4) and rgs4$^{-/-}$ + cyclosporine + bosentan mice (n = 5), showed a greater decrease in renal medullary blood flow than cortical blood flow in *rgs4*$^{-/-}$ mice after cyclosporine treatment (RKO+C). (One-way independent ANOVA, F(4,21) = 13.2.0 (composite p < 0.0001). Medullary blood flow was restored when *rgs4*$^{-/-}$ mice were cotreated with bosentan.

WT versus RKO, p = 0.49, *; RKO versus RKO +C, p = 0.0001, #; RKO versus RKO+C+B, p = 0.11, ^.

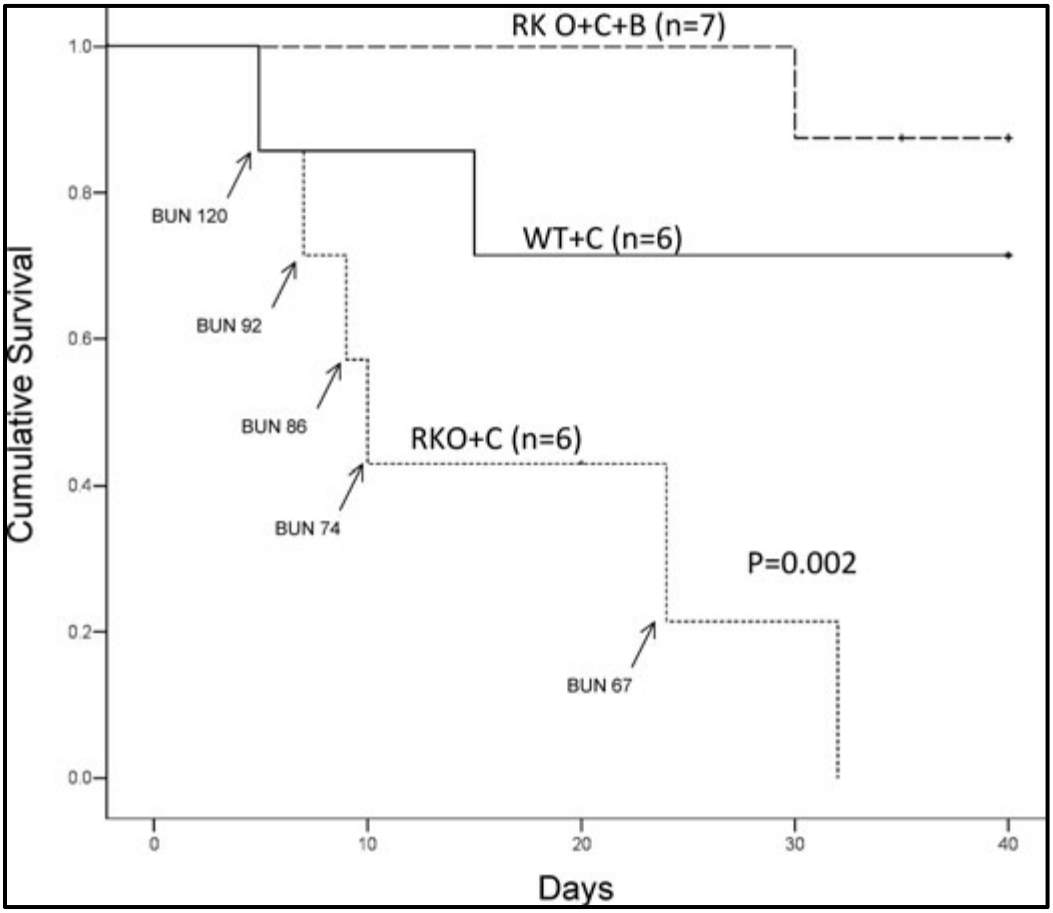

Figure 6: Increased mortality after daily cyclosporine treatment in *rgs4*$^{-/-}$ mice (n = 6) versus congenic wild type controls (n = 6) treated with cyclosporine and *rgs4*$^{-/-}$ coadministered cyclosporine and bosentan (n = 7). Survival with daily cyclosporine A treatment was monitored for 30 days (Mantel–Cox log rank test p = 0.002).

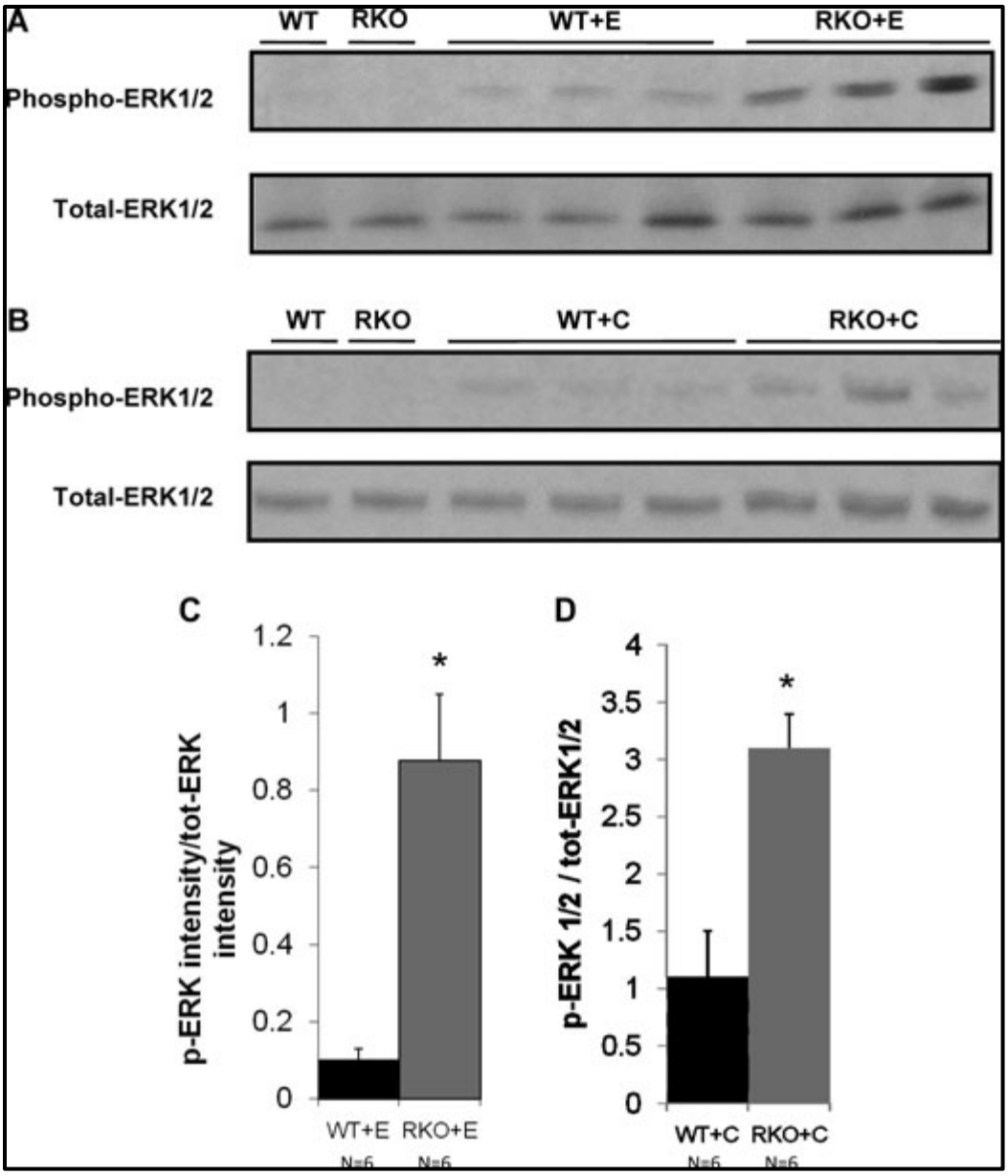

Figure 7: In vitro modulation of MAPK signaling in *rgs4*$^{-/-}$ after endothelin, or cyclosporine A treatment. Increased ERK1/2 activation in rgs4$^{-/-}$ kidney tissue after (A, C) endothelin-1 treatment ($p < 0.0001$, *) and after (B, D) cyclosporine A treatment ($p = 0.0003$, $^{\#}$). Kidneys were isolated from *rgs4*$^{-/-}$ (RKO) (n = 6) and wild type congenic mice (WT) (n = 6), quickly sliced into 2 mm sections and treated with endothelin-1 (E). Sections were used to generate protein lysates that were analyzed by antiphospho-ERK1/2 immunobloting. Membranes were re-probed with an antitotal-ERK1/2 primary antibody to control for protein loading. Densitometric analysis of immunoreactive bands identified in Figure 9 (A, B) was performed using ImageJ software 1.24.

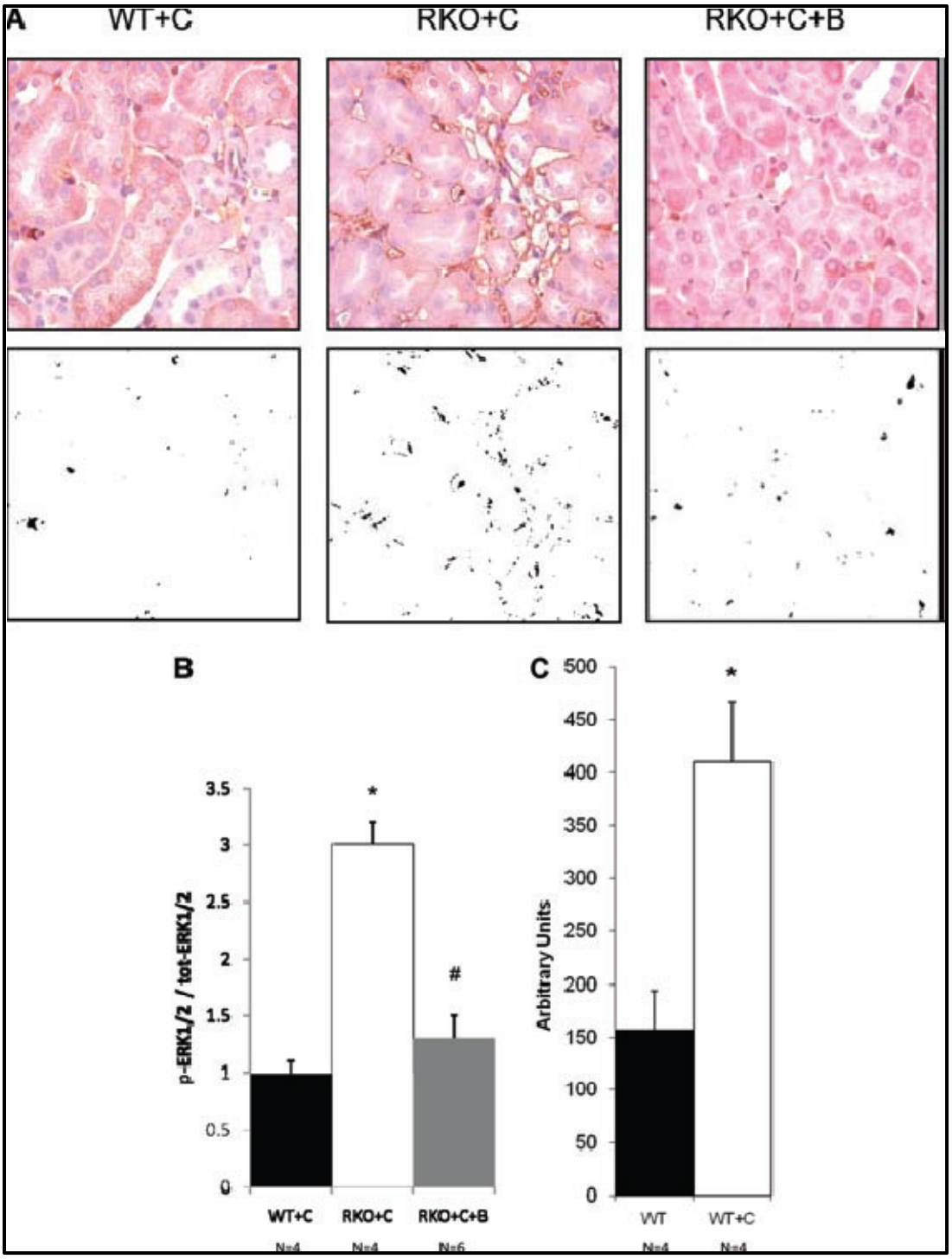

Figure 8: ERK1/2 activation in *rgs4*$^{-/-}$ mice induced by cyclosporine A is inhibited after 1 week of cotreatment with bosentan. (A) After 1 week of daily cyclosporine A treatment, WT+C (n = 4), RKO+C (n = 4) and RKO+C+B (n = 6) kidneys were isolated from wild type congenic mice *rgs4*$^{-/-}$ mice, fixed and embedded. Upper panels, embedded kidney tissue was analyzed by

immunohistochemical staining with antiphospho-ERK1/2 primary antibodies. Lower panels, digitized immunohistochemical images were converted to black-white contrast and analyzed with ImageJ software (B) to quantify ERK1/2 activation. ANOVA composite, p = < 0.0001; WT+C versus RKO+C, p = 0.0006, *;RKO+C versus RKO+C+B, p = 0 < 0.0001, #. (C) Increased renal RGS4 mRNA expression in wild type mice treated with C(n = 4) for 1 week compared to untreated wild type mice. Student's *t*-test, p = 0.0003.

D.12. Supporting Information

The following supporting information is available for this article online:

Supplemental Methods

Figure S1: Generation of *rgs4*$^{-/-}$ mice.

Figure S2: Analysis of gene expression in *rgs4*$^{-/-}$ mice compared to congenic wild type controls by gene expression microarray technique.

Figure S3: Cyclosporine blood levels after 7 days of daily administration is equivalent in RGS4$^{-/-}$ (n = 10) and wild type control mice (n = 10).

Figure S4: RGS4$^{-/-}$ mice metabolize cyclosporine at rates equal to congenic wild type control mice.

Figure S5: Renal artery (A) blood flow is reduced in the kidneys (K) of mice treated with cyclosporine for 1 week.

Figure S6: Renal artery (RA) blood flow in *rgs4*$^{-/-}$ (RKO+C) (n = 4) decreased after 1 week of daily cyclosporine A treatment compared to WT+C (n = 5).

Figure S7: Cyclosporine blood levels correspond with increasing dose of daily cyclosporine injection in the presence or absence of bosentan.

Table S1: Phenotypic comparison of congenic control (WT) (n = 10) and *rgs4*$^{-/-}$ mice (RKO) (n = 10).

Table S2: Expression of Regulators of G-protein Signaling (RGS) proteins in *rgs4*$^{-/-}$ mice compared to controls.